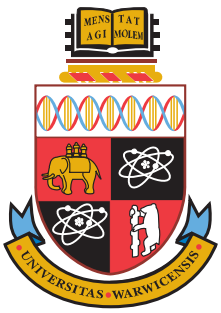

Exploiting the Properties of Diamond for Biosensing Applications: Electrochemical and Computational Approaches to Biomolecule Detection

by

Jennifer Rachel Webb

Thesis

Submitted to the University of Warwick

for the degree of

Doctor of Philosophy

Supervisors: Prof. Julie Macpherson, Dr. Rebecca Notman, Prof. Mark Newton

MOAC Doctoral Training Centre

September 2015

THE UNIVERSITY OF WARWICK

Table of Contents

List of Figures

List of Tables

Acknowledgements

Firstly, I would like to thank my supervisors, Prof. Julie Macpherson, Dr. Rebecca Notman and Prof. Mark Newton for their invaluable guidance, support and encouragement over the past few years. I'd also like to thank Prof. Pat Unwin for his support and scientific insights.

I would like to thank all members of the Warwick Electrochemistry and Interfaces Group, Notman Group, MOAC DTC, and the Theoretical and Computational Chemistry department for always offering help, support and a friendly face in times of need. I'd especially like to thank Zoë Ayres, Jonathan Newland, Robert Channon, Sophie Kinnear, Elizabeth Oseland, Max Joseph, Anthony Nash, Jasmine Desmond, Alaina Emmanuel and David O'Neill for their unwavering support and friendship throughout the ups and downs of PhD life. This thesis would not have existed without you all. I am also indebted to those further afield, especially Katharine Ashdown, Heather Alford and Hannah White, for always being there to listen and keep me (relatively!) sane.

A massive thank you to my housemates, Mike Irvine, Daniel Sprague, Philippe Le Goff, Dee Marco, Benjamin Collyer, Nick Binge and Allys Stafford for the fun we had and the great memories we shared over the past few years. Thank you for being a family to me throughout my PhD and making me laugh when I needed it the most. The infamous Portland/Gordon Street parties will never be forgotten. I'd also like to thank the MOAC 2010 cohort for the great times we had together and experiences we shared (both good and bad!) during our time together in MOAC.

Finally, I'd like to thank my parents who have always supported, encouraged and inspired me to fulfil my goals. Thank you for always being there for me and supporting me in whatever I do.

Declaration

I declare that the work contained in this thesis is entirely original and my own work, except where acknowledged. I confirm that this thesis has not been submitted in whole or in part for consideration for any other degree or qualification in this, or any other University.

The dopamine and serotonin models in Chapter 5 were built by Adam Hill, University of Manchester, U.K. The finite-element simulations in Chapter 6 were run by Sze-yin Tan, University of Warwick, U.K. The SECCM imaging in Chapter 6 was carried out by Dr. Hollie Patten and Dr. Laura Hutton, University of Warwick, U.K. The substrates in Chapter 7 were laser machined by Dr. Max Joseph, University of Warwick, U.K. and the pores fabricated by Dr. Aiden Martin, University of Technology, Sydney. The coarse-grained diamond models in Chapter 8 were built in collaboration with Dr. Syma Khalid, University of Southampton, U.K.

Parts of this thesis have been published as detailed below:

Patten, H. V., Hutton, L. A., Webb, J. R., Newton, M. E., Unwin, P. R., & Macpherson, J. V. (2015). Electrochemical "read–write" microscale patterning of boron doped diamond electrodes. *Chem. Comm.*, *51*(1), 164-167.

Thake, T. H., Webb, J. R., Nash, A., Rappoport, J. Z., & Notman, R. (2013). Permeation of polystyrene nanoparticles across model lipid bilayer membranes. *Soft Matter*, *9*(43), 10265-10274.

Abstract

Diamond exhibits many exceptional chemical, mechanical and electrical properties that make it ideally suited for use in biosensing devices. Insulating diamond offers an ideal platform in pore biosensing devices due to its robustness, biocompatibility, chemical inertness, and low dielectric constant (high signal to noise ratios). When doped with boron atoms to induce conductivity, boron-doped diamond (BDD) electrodes have unique electrochemical properties including a wide potential window, low background currents and reduced fouling. The ability for diamond to be easily modified between stable hydrophobic (H-terminated) and hydrophilic (O-terminated) surface functionalisation is particularly attractive as it enables the diamond surface to be tailored for specificity and selectivity in biosensing applications.

Work in this thesis aims to investigate, through the use of molecular dynamics (MD) simulations and electrochemical techniques, how the properties of diamond can be exploited in order to realise its full potential in electrochemical and pore biosensing technologies. MD simulations are employed to achieve a fundamental understanding of processes at the diamond-solution interface. In particular, the influence of the different crystal orientations and surface terminations of diamond on the structure and dynamics of biomolecules (water, ions, neurotransmitters, phospholipids) is investigated. Electrochemical techniques are used to probe the effect of surface termination and boron dopant concentration on the response of species in order to optimise electrochemical biosensing devices. In addition, the fabrication and sensing capability of a novel single crystal diamond pore device is presented.

Abbreviations

AC	Alternating current
AMBER	Assisted Model Building with Energy Refinement
BDD	Boron-doped diamond
CE	Counter electrode
CG	Conjugate-gradient energy minimisation algorithm
CG	Coarse-grained
CHARMM	Chemistry at HARvard Molecular Mechanics
CV	Cyclic voltammetry or cyclic voltammogram
CVD	Chemical vapour deposition
DAQ	Data acquisition card
DC	Direct current
DFT	Density functional theory
DNA	Deoxyribonucleic acid
DPPC	Dipalmitoyl phosphatidylcholine
e-beam	Electron Beam
EBIE	Electron beam induced etching
EDS	Energy-dispersive X-ray Spectroscopy
EM	Energy minimisation
ET	Electron transfer
fcc	Face centered cubic
FE-SEM	Field emission scanning electron microscopy
FEM	Finite element method
FIB	Focused ion beam
FIB-SEM	Focused ion beam scanning electron microscope
FWHM	Full width half maximum
GC	Glassy carbon
GROMACS	Groningen Machine for Chemical Simulations
GROMOS	Groningen molecular simulation
GSED	Gaseous secondary electron detector
H-terminated	Hydrogen terminated

HF	Hartree Fock
HOMO	Highest occupied molecular orbital
HOPG	Highly ordered pyrolytic graphite
HPHT	High-pressure high-temperature
HREELS	High resolution electron energy loss spectroscopy
IHP	Inner Helmholtz plane
IR	Infrared
LAMMPS	Large-scale Atomic/Molecular Massively Parallel Simulator
LINCS	Linear constraint solver
LJ	Lennard-Jones potential
LUMO	Lowest unoccupied molecular orbital
MD	Molecular dynamics
MM	Molecular mechanics
MSL	Micro-stereolithography
MspA	Mycobacterium smegmatic porin A
NAMD	NAnoscale Molecular Dynamics
NAPzT	Constant number, area, vertical pressure and temperature ensemble
NPT	Isothermal-isobaric ensemble
NVE	Microcanonical ensemble
NVT	Canonical ensemble
O-terminated	Oxygen terminated
OHP	Outer Helmholtz pane
OPLS	Optimised Potentials for Liquid Simulations
PBC	Periodic boundary conditions
PE	Potential energy
PME	Particle mesh Ewald
PMF	Potential of mean force
PS	Polystyrene
QM	Quantum mechanics
QM	Quantum mechanics
QRCE	Quasi-reference counter electrode
RE	Reference electrode
scBDD	Single crystal boron doped diamond

SCE	Saturated calomel electrode
SECCM	Scanning electrochemical cell microscopy
SEM	Scanning electron microscopy
SIMS	Secondary ion mass spectrometry
SPC	Simple point charge (water model)
SPM	Scanning probe microscopy
UFF	Universal Force Field
UME	Ultramicroelectrode
UV	Ultraviolet
vdW	Van der Waals
VMD	Visual Molecular Dynamics
WE	Working electrode
WLI	White light interferometry
XPS	X-ray photoelectron spectroscopy

Chapter 1

Introduction

1.1 Statement of the Problem

The use of diamond in biosensing devices has yet to realise its full potential. Electroanalytical sensors are already important for a wide range of applications in health care,[1] biosecurity,[2] and environmental monitoring.[3] However, there is still a need for platforms that can detect biomolecules quickly and to a high degree of accuracy, whilst ensuring cost-effectiveness, manufacturability and simplicity of use.[4] Diamond has recently emerged as a viable commercial material due to improvements in diamond synthesis techniques enabling lower costs to mass-produce and wider-availability.[5] In addition, diamond has ideal electrochemical, mechanical and optical properties to advance the field of biosensing. The work in this thesis uses theoretical and experimental techniques to reveal new understanding of interfacial processes at the diamond surface that advances knowledge and guides design of diamond electrochemical and pore-based biosensors (see section 1.5 for the significant contributions to knowledge from this thesis).

1.2 Introduction to Diamond

Diamond is most commonly recognised as a gemstone in jewellery, however it also has some of the most remarkable physical properties that makes it extremely attractive for industrial applications. In particular, diamond is the hardest known

material (*ca.* 90 GPa), has the highest thermal conductivity (*ca.* 2200 W m^{-1} K^{-1}) and the widest optical transparency range of all known solids (deep ultraviolet to far infrared).[6] However, the high cost and limited availability of natural diamond made it difficult to exploit the material. The situation changed with the development of techniques to synthesise diamond (see section 1.2.1) in the laboratory. These processes enable controlled, tailored growth of diamond for the required application.[7] Consequently, diamond has become more readily available and cost-effective in the last 10 years,[5] and is now employed in a wide range of products including, for example, high-quality speakers,[8] radiation detectors,[9] and bionic eyes.[10] Diamond can also be grown with different dopants incorporated into the lattice *e.g.* boron to provide defined electrical properties, as discussed in detail later (section 1.2.4).

1.2.1 Synthesis of Diamond

The first method for diamond growth was the *high-pressure high-temperature* (HPHT) method developed by General Electric in 1955.[11] This process works by mimicking the thermodynamically stable conditions for diamond formation in nature. Graphitic carbon is compressed to a pressure of ~ 5 GPa at 1800 °C in the presence of a metallic solvent (typically iron or nickel).[12] This process is well controlled enabling the formation of high purity single crystal diamonds of up to tens of millimetres in size.[6]

The second method for diamond growth is *chemical vapour deposition* (CVD). This method was first proposed in the 1950s,[13] although it was not until the 1980s that scientists developed the process for reproducible diamond growth.[14] The principle of CVD growth is outlined in several reviews.[15] In brief, the CVD growth process uses a substrate immersed in a mixture of heated (above 2000 °C) gas-phase

hydrocarbons (typically methane) and hydrogen in excess within the mix that are situated in a vacuum chamber under low pressure. Boron can also be incorporated by adding a small amount of B_2H_6 gas into the mix (typical ratios being 99.5% H_2, 0.5% CH_4 and B_2H_6).[16] The substrate can be any material that will withstand high temperatures and the plasma environment. These often include silicon, tungsten, titanium, or diamond itself. In order for the gases to react, energy is injected into the system, typically in the form of thermal (a hot filament)[14] or electric discharge (microwaves),[17] to form a plasma. The activation causes the hydrogen to convert into atomic hydrogen, which reacts with methane gas to form $CH_3^{\bullet}$ radicals in the plasma. Atomic hydrogen stabilises the diamond structure during growth by bonding to any dangling bonds on the surface to form C–H groups. Reaction of the radicals with the surface C–H sites causes carbon incorporation in the substrate, and a diamond lattice begins to form. In addition, atomic hydrogen will etch away sp and sp^2 carbon at a faster rate than diamond sp^3, thus removing any non-diamond carbon impurities during growth. The technique is slow (0.1 – 1 μm / hr),[18] but, unlike HPHT, CVD enables growth under low-pressure conditions, the ability to manipulate the material by incorporation of impurities and the formation of large surface area diamond through growth over silicon wafers. For example, 4" CVD diamond wafers (of ~ mm thickness) are commercially available at competitive prices.[5] The CVD process thus enables diamond to be brought to the market as a viable industrial material.

Two different diamond structures can be grown using CVD: (1) single crystal and (2) polycrystalline. Single crystal diamond is formed by homoepitaxial growth, where a single crystal diamond (natural or synthetic) is used as the growth substrate.[19] Polycrystalline diamond is formed using any suitable (as discussed above) non-diamond substrate material. Diamond crystals nucleate on the surface of

the substrate as seeds for diamond growth.[20] As each of these crystals grow, they eventually combine together to form a film of 'grains' that are terminated by a particular crystal growth face, as shown in **Figure 1.1**. The width of the growth faces is proportional to the height of the grains.[21] In addition, at the diamond-substrate interface sp^2 content can be high. Hence, thicker films display larger growth faces and fewer grain boundaries. *Ultrathin film, nanocrystalline diamond* (growth faces of width < 100 nm diameter), is thus often high in sp^2 content making them lower quality compared to *microcrystalline diamond* (growth faces of width > 1 μm diameter).[22] In this study, we use CVD polycrystalline *boron-doped diamond* (BDD) materials of thicknesses ~ 635 μm (growth faces of width 2 – 25 μm) and 880 μm (growth faces of width 7 – 100 μm), and dopant densities 3×10^{20} boron atoms cm^{-3} (conducting) and 2×10^{18} boron atoms cm^{-3} (semiconducting), respectively.

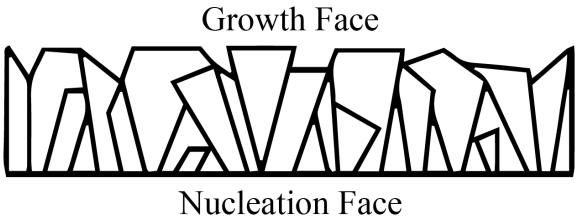

***Figure 1.1**: Schematic of CVD polycrystalline diamond*.[23]

1.2.2 Structural Properties of Diamond

Diamond consists of tetrahedrally bonded sp^3 carbon atoms that create a face centred cubic (fcc) lattice, as shown in **Figure 1.2**a. The carbon network consists of single C–C bonds of length 0.154 nm and C–C–C bond angles of 109.5°. This lattice forms the unit cell that is replicated to grow in three-dimensions to form diamond. The primary crystallographic orientations of diamond are the (100), (111) and (110). These orientations dominate the crystal growth faces in polycrystalline CVD

diamond. The planes of the (100), (111) and (110) faces with respect to the diamond lattice are displayed in **Figure 1.2**b.

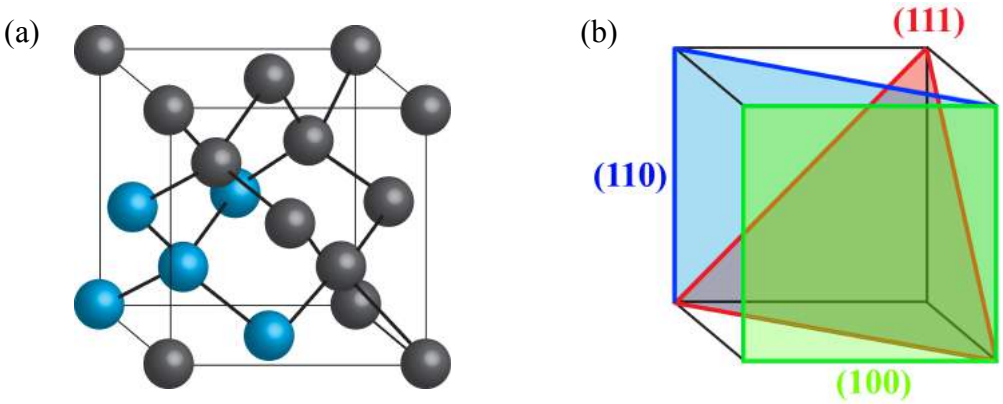

***Figure 1.2**: (a) The diamond crystal lattice and (b) the primary crystallographic faces of diamond.*

Each crystal orientation of diamond has a different surface arrangement of carbons. Diamond can exist with either hydrogen (–H) or oxygen (–O) termination, as diamond leaves the CVD reactor as H-terminated but reacts gradually with air (or can be surface treated) to become O-terminated, as discussed in section 1.2.3. Interestingly, the structures of the surface carbons favour particular termination groups on each face. Whilst H-termination introduces C–H groups to the surface, O-termination can introduce a range of groups including hydroxyl (C–OH), ether (C–O–C), carbonyl (C=O) and carboxyl (COOH).[24] The models for the surface structures of the (100), (111) and (110) diamond faces based on theoretical and experimental evidence (as described) are outlined below. Simple surface structure notation is used to denote the faces *i.e.* the surface is denoted 1 × 1 if the unit cell of the surface structure is exactly the same as the bulk unit cell, or 2 × 1 if the unit cell of the surface structure is twice as large along one major crystallographic axis compared to bulk.[25]

1.2.2.1 The (100) Surface

The (100) crystal plane is less susceptible to defects during growth making it the prominent face used in cutting tools due to its high resistance to stress.[26] Bare (100) has two dangling bonds per atom on the surface (**Figure 1.3**a).[27] This structure is extremely energetically unfavourable,[28] so these atoms typically form π-bonds with each other to create the more stable 2 × 1 geometry (**Figure 1.3**b).

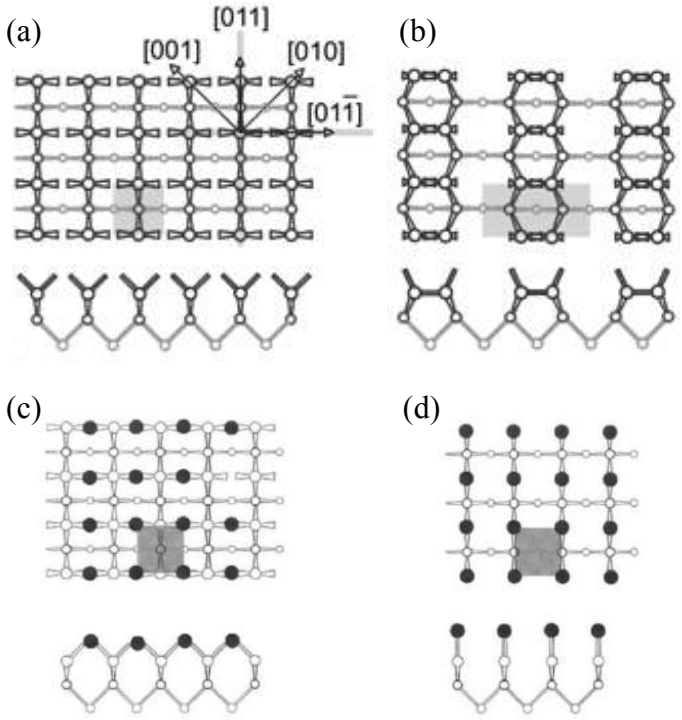

Figure 1.3*: Proposed top and side view models of the (100) diamond surface: (a) 1 × 1, which is typically surface reconstructed into (b) 2 × 1 structure.*[27] *The 2 × 1 model is either H-terminated as H groups attach to the dangling bonds, (c) O-ether- (bridge site) terminated or (d) ketone- (top site) terminated.*[29]

Upon H-termination, saturation of the dangling bonds in the 1 × 1 structure is prevented due to steric repulsion between the hydrogen atoms.[30] The hydrogen atoms lie far enough apart on the 2 × 1 surface that repulsion is not an issue and each hydrogen atom can bond to a surface carbon in a 1:1 ratio (**Figure 1.3**b). This is the most favourable model of the (100) H-terminated surface based on density functional theory (DFT) calculations.[31] When O-terminated, steric repulsion is no longer a

problem and oxygen groups can favourably bond to the 1 × 1 surface. Two models exist for the (100) O-terminated surface: (1) the ether or 'bridge site' model where each oxygen bonds to two neighbouring carbons to form C–O–C groups (**Figure 1.3**c), or (2) the ketone or 'top site' model where each oxygen forms a double bond with a surface carbon to form C=O groups (**Figure 1.3**d). DFT calculations report close to identical energetic stability of both of these groups on the (100) single crystal surface.[32] This is in agreement with experimental studies using X-ray photoelectron spectroscopy (XPS)[33] and high-resolution electron energy loss spectroscopy studies (HREELS)[34] that have also reported high proportions of both C–O–C and C=O groups on single crystal (100) surfaces. Furthermore, the proportion of each surface group is highly dependent on the type of surface treatment (as discussed in section 1.2.3). As the ether and ketone O-terminated models are considered of equal importance, they are both modelled in this study.

1.2.2.2 The (111) Surface

The (111) face is the natural cleavage plane of diamond.[27] Bare (111) diamond contains one dangling bond per surface carbon (**Figure 1.4**a). This structure can reconstruct so that the dangling bonds stabilise each other by forming π-bonds between nearest neighbours that creates a zigzag chain along the surface (**Figure 1.4**b). However, a high energy barrier exists for the transition of 1 × 1 to 2 × 1 to occur, as observed in both *ab initio*[35] and low-energy electron diffraction (LEED) studies.[36] H-termination stabilises the 1 × 1 structure by terminating each dangling bond with a hydrogen atom. During oxidation, the dangling bonds can be simply terminated with OH groups rather than H.[29] The 2 × 1 reconstructed (111) surface can also incorporate oxygen onto the bridge sites of the π-bonded chains.[32a] As ultraviolet photoelectron spectroscopy (UPS) studies of single crystal (111) surfaces

have reported a high abundance of single bond C–O groups on the (111) surface, the 1 × 1 (111) OH-terminated surface is considered the most stable structure.[35b] Consequently we focus in this study on models of the 1 × 1 H– and OH– terminated (111) surfaces.

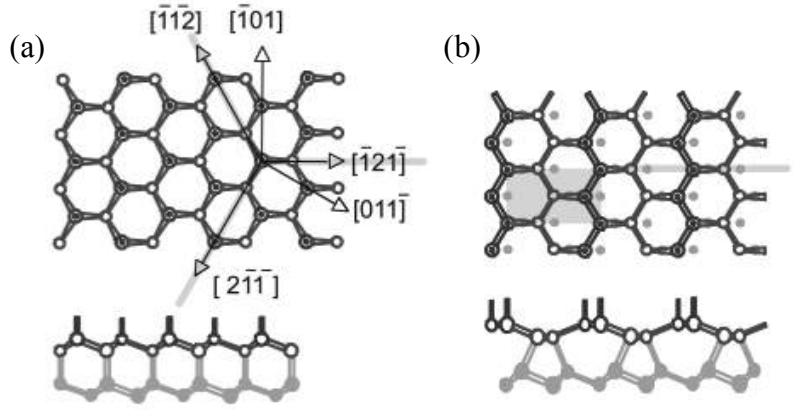

***Figure 1.4**: Proposed top and side view models of the (111) diamond surface: (a) 1 × 1 which can be H-terminated or OH-terminated by H/OH groups directly attaching on to the dangling bonds, and (b) the surface reconstructed 2 × 1 model.*[27]

1.2.2.3 The (110) Surface

Only a few results have been reported on the (110) surface to date. The bare (110) crystal plane contains zigzag chains running parallel to each other throughout the structure (**Figure 1.5**a).[29] In particular, each surface atom forms a double bond with a neighbouring carbon, and a covalent bond with an atom in a lower level chain. H-termination maintains the 1 × 1 structure but breaks the double bonds so that a hydrogen atom can covalently bond to each surface carbon (**Figure 1.5**a), as reported by Maier *et al.* using LEED, XPS and angle-resolved photoelectron spectroscopy (ARPES).[37] Three possible surface models (peroxide, ether and ketone) have been proposed by Mackey *et al.,* for the oxygen-terminated (110) surface based on multiple internal infrared spectroscopy (MIRIRS) and temperature-programmed desorption (TPD) analysis.[38] One of the possibilities is that the oxygen groups bridge between

the zigzags on the (110) surface to form an ether-terminated surface structure similar to the (100)-O-ether model (**Figure 1.5**b).[38] Furthermore, the presence of C–O–C groups has been observed in XPS studies of oxygen adsorption on single crystal (110),[38] providing support for this proposed model. The H- and O-ether-terminated (110) surfaces are modelled in this study.

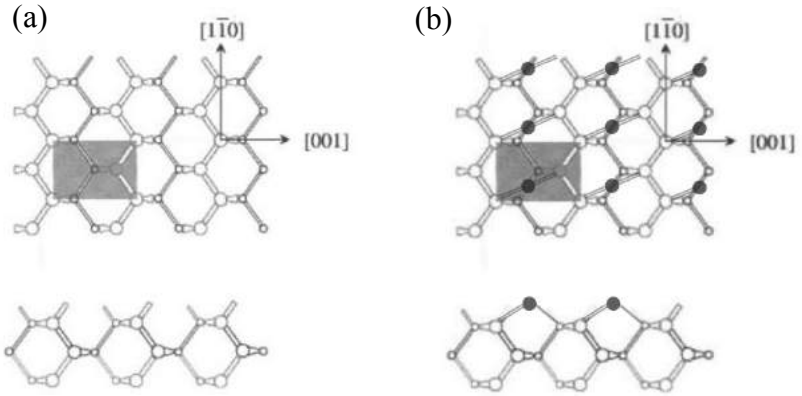

Figure 1.5*: Proposed top and side view models of the (110) diamond surfaces: 1 × 1 (a) H-terminated and (b) O-ether-terminated*.[29]

1.2.3 Surface Treatments

Treatments can be applied to the diamond surface to manipulate the surface termination. Due to the excess of hydrogen atoms during the CVD growth process, diamond leaves the chamber H-terminated. Whilst a H-terminated surface remains stable for months, it will gradually oxidise over time.[39] This places doubt on studies that utilise 'as-grown' diamond as a 'H-terminated' surface without confirmation of the surface state prior to the experiment (*e.g.* contact angles, see Chapter 3, section 3.11.3). Tracing the history of the sample is very important to understanding the surface termination. A sample that starts life as H-terminated is influenced by factors such as shelf life, packaging treatment and handling, cleaning procedures and experimental conditions that may all oxidise the surface.[40] Placing the sample into a hydrogen plasma serves to regenerate the H-termination layer (1 kW CVD reactor

operating at 500 Torr using H_2 gas for 10 mins, and left to cool for a further 10 mins under hydrogen flow at a rate of 500 sccm).[24a] It has been proposed that cathodic treatments to BDD *e.g.* applying a strong negative voltage in acidic solution (~ −3 V for 30 mins in 0.5 M H_2SO_4) can also hydrogenate the surface, as observed by a change in the electrochemical response.[41] However, complete characterisation of the surface post treatment was not performed to confirm that the hydrogen coverage is the same as if plasma treated (the best known way for hydrogenating the surface). For this reason, care must therefore be taken when interpreting data from studies that refer to a cathodically treated surface as H-terminated. Nebel *et al.,*[42] recognising the limitations of mild cathodic treatments advocated the use of an extremely harsh cathodic treatment (−35 V for 5 mins in 2 M HCl). However to be sure of reliably producing a fully H-terminated surface exposure to a hydrogen plasma or hydrogen dose is still the recommended procedure, as employed in studies herein.

In contrast, a variety of methods exist to oxygen terminate diamond including boiling in acid,[43] alumina polishing,[24a] anodic treatment (applying a strong positive potential),[44] exposure to an oxygen plasma,[24b, 45] photochemical oxidation,[46] or reactions with oxygen at high temperatures.[47] XPS studies of these surfaces have revealed differences in the chemical functionalisation after different oxidation treatments.[48] For example, anodic treatment has been shown by XPS to enhance highly polar groups *e.g.* C=O on a polycrystalline diamond surface,[49] whereas alumina treatment displays a mix of oxygen groups including C–O–C, C–OH and C=O.[24a] UV treatments have been shown to increase the amount of surface C–OH groups.[46] Oxygen plasma treated diamond has been reported by XPS[24b] and HREELS[34a] to display a high proportion of C–O–C groups. In this study, alumina-

polished O-terminated diamond surfaces are utilised, of which comparatively fewer electrochemical studies currently exist (compared to the other treatments).[24a, 50]

1.2.4 Electrical Properties: Diamond Doping

Intrinsic or undoped diamond is a wide band gap semiconductor (5.47 eV at 300 K).[5] This makes intrinsic diamond electrically insulating, although H-termination can induce p-type surface conductivity,[51] as discussed in section 1.2.5. Doping the material can modify the electronic band structure. Boron (p-type dopant) is similar in size to carbon, so it can easily take up the position of displaced carbon in the diamond lattice. Boron doping introduces an acceptor energy level (0.37 eV) above the valence band. Whilst nitrogen can also be used as a dopant, the concentration is too low to make the material sufficiently conductive for electrochemical studies.[52]

The degree of boron doping has a considerable effect on the boron acceptor level and resistivity of diamond,[53] as shown in **Figure 1.6**a. Diamond contains ~ 2×10^{23} C atoms per cm^{-3}. When diamond is doped with boron it exhibits p-type semiconductor behaviour.[54] At low boron dopant concentrations *i.e.* 10^{16} B atoms cm^{-3} (~ 1 in 10^7 C atoms replaced by B), the activation energy required to promote electrons from the valence into the acceptor level is still considerably large so that the material displays high resistance (**Figure 1.6**bi). As the boron dopant level increases towards 10^{19} B atoms cm^{-3} (~ 1 in 10^4 C atoms replaced by B), the distance between the boron atoms in the lattice decreases and the wave functions begin to overlap creating an impurity band (**Figure 1.6**bii).[54a] This lowers the activation energy, causing the resistivity of the material to decrease. At a dopant level of ~ 1.5×10^{19} B atoms cm^{-3}, the resistivity drops sharply as the boron atoms are in close enough proximity for hopping conductance to occur.[53] As the dopant concentration increases

above 10^{20} B atoms cm^{-3} (~ 1 in 1000 C atoms replaced by B), diamond exhibits 'metal-like' conductivity. This occurs as the overlap of the wave functions in the acceptor atoms is sufficiently high for hole propagation to occur without the need for activation energy to the valence band *i.e.* a continuum of occupied electron states exists between the acceptor level and the valence band (**Figure 1.6**biii).[55]

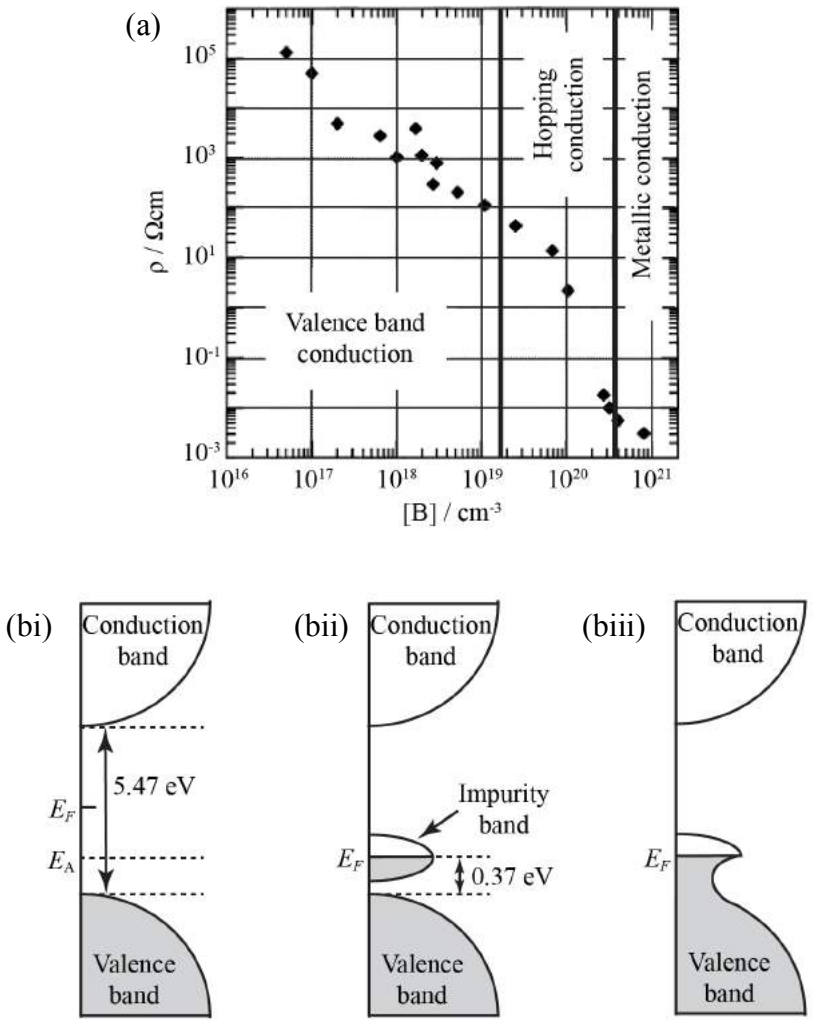

***Figure 1.6**: (a) Room temperature resistivity as a function of boron dopant concentration in diamond.*[53] *(b) Schematic of the electronic band structure at different boron concentrations: (i) Insulating (undoped) BDD, (ii) boron-doped semiconducting diamond (< 10^{20} boron atoms cm^{-3}), (iii) highly boron-doped 'metal-like' diamond (≥ 10^{20} boron atoms cm^{-3}).*[55]

As the existence of BDD in nature is rare,[56] for commercial applications it must be grown synthetically using the CVD process (see section 1.2.1). The

concentration of boron incorporated into the diamond lattice is highly dependent on the CVD growth conditions including the concentration of boron in the gas mixture,[57] temperature,[58] and surface properties of the substrate material.[59] Secondary ion mass spectrometry (SIMS) analysis can be used to determine the total boron concentration in BDD.[57b] The crystal orientation also influences boron uptake. The amount of boron incorporated into the (111) crystal face is an order of magnitude greater than the (100) face.[60] This causes heterogeneity in conductivity across the grains of a polycrystalline BDD sample, although the average behaviour will remain consistent.

1.2.5 Electrical Properties: Surface Conductivity of H-terminated Diamond

In 1989, Landstrass and Ravi were the first to observe surface p-type conductivity on H-terminated insulating (undoped) diamond surfaces.[61] For many years, this extraordinary phenomenon was believed due to sub-surface hydrogens.[62] However, in 2000, Maier *et al.,*[51] discovered the important role of atmospheric adsorbates in the conductivity. In particular, they observed that whilst hydrogenated insulating diamond displays surface conductance during exposure to air, conductance is not present under vacuum *i.e.* surface hydrogens are necessary but not sufficient for surface conductance. This led to the development of the theory of *surface transfer doping*.[51, 63]

H-termination of diamond causes a dipole layer of $C^{\delta+}$–$H^{\delta-}$ groups to form on the surface. H-termination induces a negative electron affinity of −1.3 eV (in vacuum) and $C^{\delta-}$–$O^{\delta+}$ groups on O-termination induce a positive electron affinity of +1.7 eV (in vacuum) causing the energy band structure to shift accordingly (**Figure 1.7**). Shielding from water molecules close to the surface slightly reduces the affinity to ~ −1.0 eV and ~ +1.3 eV, respectively.

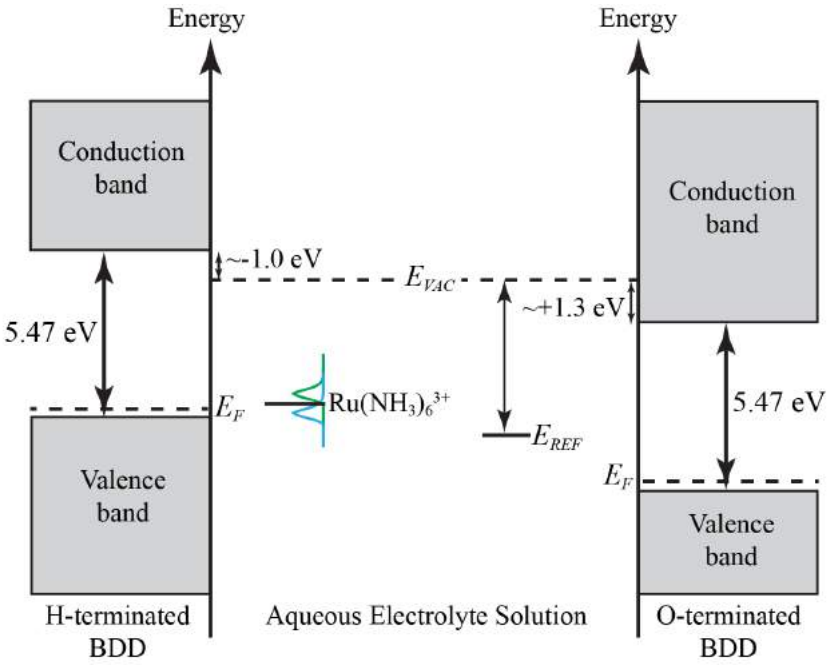

***Figure 1.7**: Schematic of the electronic band structures for H-terminated and O-terminated semiconducting BDD that induce a shift in electron affinity of ~ −1.0 eV and ~ +1.3 eV, respectively. In addition, the chemical potential in solution of a common mediator, $Ru(NH_3)_6^{3+}$ and the Ag/AgCl reference electrode, E_{REF}, which serves as a reference for any applied potential to the system.*

Importantly, the valence band maximum on H-terminated diamond is raised to just above the chemical potential of electrons, μ_e, in a mildly acidic water layer ($CO_2 + H_2O \rightleftharpoons HCO_3^- + H_3O^+$) physisorbed on the surface (**Figure 1.8**a).[40] ET between the diamond and water layer follows the redox reaction $2H_3O^+ + 2e^- \rightleftharpoons H_2 + 2H_2O$. This reaction is governed by the difference between μ_e and electrons in the diamond (E_F). As long as μ_e is below E_F, electrons will transfer to the acidic water layer causing the reduction of H_3O^+. This creates a sub-surface hole accumulation layer in diamond of density ~ 10^{13} holes cm^{-2}.[51] The accumulation layer forms a space charge region that induces a potential (surface band bending).[64] This causes μ_e to rise until equilibrium is reached (**Figure 1.8**b). The surface conductivity will remain as long as the positively charged holes are counterbalanced by the solvated anions (*i.e.* HCO_3^-). In fact, p-type transfer doping can also be established with neutral surface

adsorbates physisorbed on to the surface, provided they have a sufficiently high electron affinity (*e.g.* fullerenes).[65]

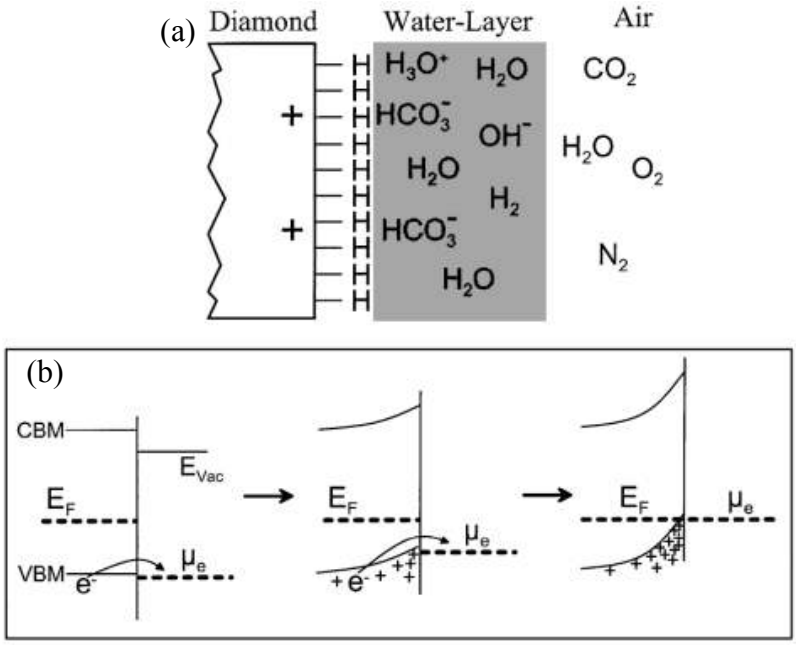

***Figure 1.8**: (a) Schematic of the H-terminated diamond surface and (b) evolution of band bending during the electron transfer process from diamond to a physisorbed acidic water layer.*[51]

Due to the large number of available charge carriers already present in highly doped 'metal-like' BDD, H-termination will have negligible effect on the electrochemical properties for outer-sphere species such as $Ru(NH_3)_6^{3+}$, but may influence the kinetics of surface sensitive species that follow an inner-sphere mechanism (see Chapter 3, section 3.5). Lower doped semiconducting BDD electrodes are depleted of charge carriers when driving to negative potentials.[64] In this case, the addition of surface charge carriers will decrease the potential drop in the electrical double layer (see Chapter 3, section 3.4) and noticeably enhance the ET kinetics relative to O-terminated semiconducting BDD. This means that a mediator (*e.g.* $Ru(NH_3)_6^{3+}$, whose redox potential lies close to the valence band (**Figure 1.7**) can display ET kinetics considerably faster than expected for that dopant density on a

H-terminated semiconducting BDD electrode.[66] Consequently, studies which report trends between O- and H- terminated BDD using low dopant levels (~ 10^{18} – 10^{19} B atoms cm^{-3}) may be observing effects due to charge depletion of the material instead of the different surface states. It is essential for diamond to be doped to the metallic level for the electrochemical response of outer-sphere mediators (Chapter 3, section 3.5) to be independent of the surface state.

1.3 Background to Biosensing Devices: Electrochemical and Pore

Biosensing technologies have become increasingly important in our modern lives. The ability to accurately and rapidly detect biomolecules has enabled significant advances in many fields including health care for early medical diagnostics,[1a, 67] security for the rapid identification of bio-warfare agents,[68] and environmental safety for detection of toxic contaminants.[69] Early detection of potentially dangerous chemicals can prevent harmful conditions for humans and enable fast response to medical problems. Biosensing devices are ideally: (1) accurate, (2) cheap, (3) easy to use, and (4) suitable for mass production. In particular, the ease of use is important for patients at home or workers in the field to implement the device. Biosensors that can be readily miniaturised to self-contained, handheld devices are particularly attractive for use as portable systems. This would enable the device to be used at the site of incident, reducing the time and cost of deliverables, and allow experts to work in the field, rather than in the confinement of the laboratory, for a direct point-of-contact.

A biosensor is an analytical device comprising a sensing element that detects a biological species and converts it into a measurable signal.[70] A variety of analytical tools exist to sense biomolecules.[71] These include: (1) optical techniques such as optical waveguide lightmode spectroscopy (OWLS) and surface plasmon resonance (SPR);[72] (2) gravimetric techniques such as quartz crystal microbalance (QCM);[73]

(3) imaging techniques such as atomic force microscopy (AFM);[74] (4) fluorescent techniques such as confocal microscopy;[75] and (5) electrical techniques such as electrochemistry (*i.e.* cyclic voltammetry)[71] and pore-based technologies.[76] These methods all work by probing biointerfacial properties and each have their advantages dependent on the study of interest. We also note hybrid technologies that combine these methodologies have also proven highly valuable for enhanced understanding of a system through the simultaneous extraction of biointerfacial properties.[77] However, in terms of the requirements discussed above, electrical biosensing techniques have enormous potential towards commercial application. These devices are typically simple and cheap to fabricate, robust, versatile, easy to miniaturise and have excellent detection limits at low analyte concentrations.[71]

In this study, we focus on two types of electrical biosensor: (1) electrochemical (detection of faradaic currents) and (2) resistive-pulse through a pore structure (detection of migration currents). *Electrochemical biosensors* measure the oxidation-reduction reactions of biological species on an electrode surface that generates a measurable electrical signal,[78] as illustrated in **Figure 1.9**. The measurement can be direct or indirect, as in the case of enzyme biosensors such as the commercial glucose biosensor that utilises the enzyme, glucose oxidase, for highly specific detection of glucose oxidation in solution.[79] The signal is often a characteristic voltammetric response for the biomolecule of interest.[71] The electrode material is chosen as a conducting material that can produce a signal with minimal background noise (due to interfering processes at the surface) and is biocompatible. Whilst this method enables detection of low concentrations of analytes *in vivo*,[80] selective detection in the presence of competing species can be challenging due to amalgamation of the responses. The electrode materials are often functionalised by a

biological species to enhance sensitivity and selectivity,[81] but to the detriment of device stability and reproducibility.[82] In addition, electrode materials often suffer from deactivation caused by fouling (*i.e.* favourable adsorption of the biomolecules) on the electrode surface.[83] Hence, the development of commercially viable electrochemical biosensors, that meet the requirements specified above, still remains challenging. A key aim of this study is to demonstrate the potential of diamond as an electrode material to meet these challenges, as discussed in detail later in this section.

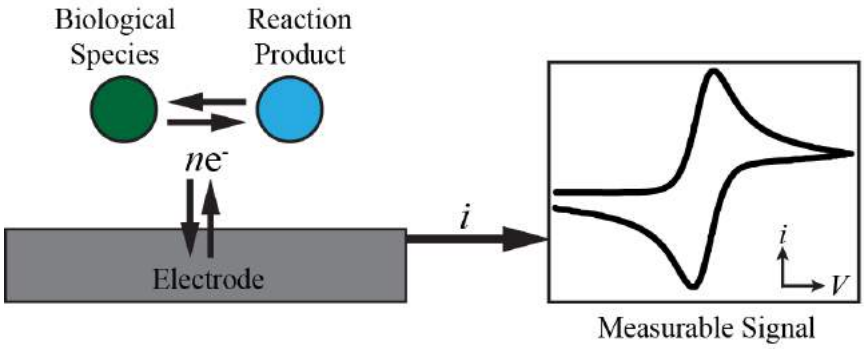

***Figure 1.9**: Schematic of an electrochemical biosensor. Chemical reactions at the electrode surface generate a measurable electrochemical response in the current-voltage trace.*

Another important type of biosensor is a *resistive-pulse device using a pore*. The principle of resistive-pulse sensing through a *solid-state* pore is similar to the conventional Coulter counter.[84] The detection occurs in real-time and relies on the measurement of conductivity signals across a very small pore fabricated in a synthetic material.[85] When a molecule passes through the pore, it can be identified by the characteristic way it blocks the ionic current described as its *unique current signature* (**Figure 1.10**), based on the size, shape and charge of the species. This method has led to the use of pore sensors for real-time, label-free detection of a wide range of species including particles,[86] polymers,[87] proteins,[88] and DNA.[89]

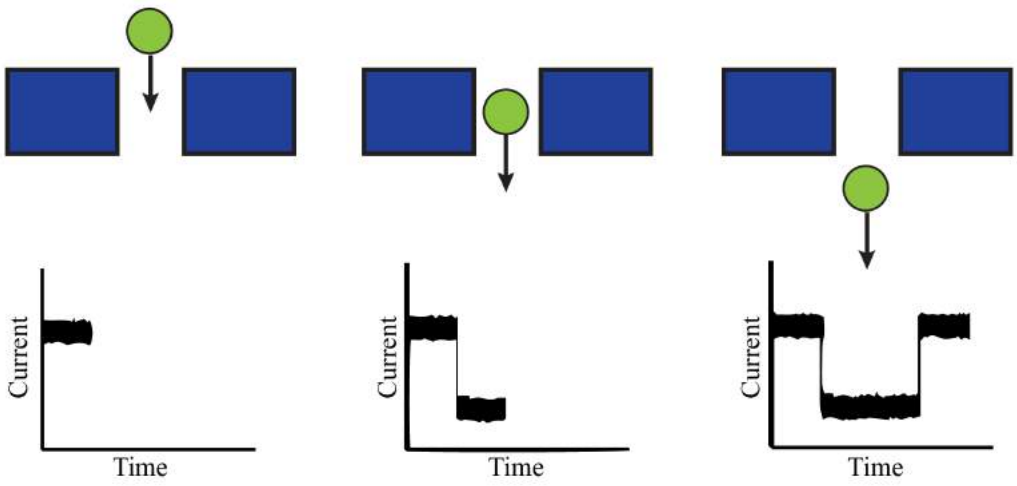

***Figure 1.10**: Schematic of pore biosensing. The particle creates a characteristic response in the current-time trace as it translocates through the pore.*[90]

The material properties of the pore biosensor platform will determine the detection capability and robustness of the device. Unfortunately, conventional platform materials such as silicon nitride,[86] silicon oxide,[91] and glass[92] all suffer from a lack of sensitivity and selectivity due to inherent capacitance (dielectric noise) that limits the achievable signal-to-noise and temporal resolution.[93] The pore thickness, size and geometry also play an important role in the sensing capability.[90] Conical shaped pores have proven highly advantageous as they provide a localised 'sensing zone' at the smallest orifice that facilitates high spatial resolution.[94] The width of the pore is typically fabricated to be comparable to the width of the analyte of interest to maximise the blockade signal *e.g.* micro-particles detected through micro-pores,[95] and nanoscale molecules such as DNA through nanoscale pores.[96] Pores are typically fabricated using electron-beam or focused ion beam milling, as summarised in the review by Healy *et al.*[97] However, there is considerable practical difficulty in making reliable, reproducible measurements with small pores due to blockage of species within the pore channel that is hard to remove on such a small scale, limiting the device to single use.[85]

The solid-state pore structure can be adapted into a *biological pore* device by functionalisation of the orifice with a lipid bilayer embedding a well-defined membrane protein.[76] The detection of single-stranded DNA through the channel of *Staphylococcal* alpha-hemolysin of smallest constriction 1.4 nm (**Figure 1.11**) has been highly influential towards the development of next generation sequencing devices.[98] Alpha-hemolysin is ideal for pore sensing devices as (1) it is always open and (2) it has a completely known internal geometry, so that the baseline open conductance reading is a known value as a function of KCl concentration.[99]

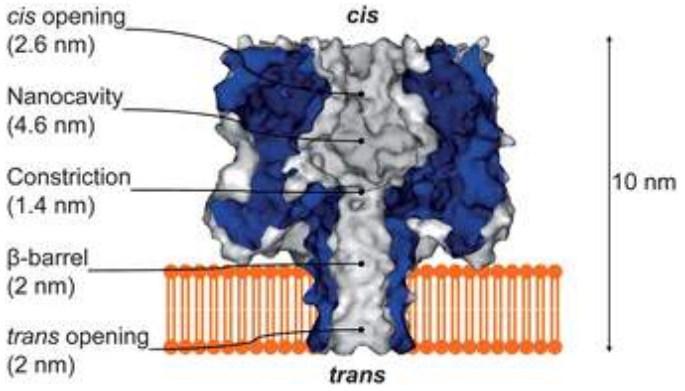

Figure 1.11: *Illustration of the staphylococcal alpha-hemolysin protein, commonly used in biological nanopore sensing devices.*[100]

The platform material of the pore biosensor has consequences on the structure and stability of the lipid bilayer. The orientation of the phospholipids with respect to the surface is crucial for the device stability. If they align in a supported bilayer conformation (**Figure 1.12**a),[101] the bilayer displays reduced stability (lasting only a few hours)[102] and is weakly bound by an interstitial water layer that gives rise to the leakage of current[101] and enables the protein to move away from the underlying pore, thus deactivating the device. For enhanced stability (lasting up to several months), the phospholipids align in a suspended bilayer formation (**Figure 1.12**b),[103] with the hydrophobic tails aligned towards the surface and hydrophilic heads facing away. The

ideal surface is required to be sufficiently hydrophobic for the phospholipids to orient into a suspended bilayer structure, whilst sufficiently hydrophilic to enable solution to wet the pore for the conductance measurements.[104] Whilst modification of the pore enables reproducibility and improved sensitivity by reduction of the pore dimensions, biological pore devices can suffer from low signal-to-noise ratios, complex manufacturability and poor stability.[105] There are two routes to explore when developing a pore device: (1) fabrication of nanopores that can hold the phospholipids and membrane protein stable for lengthy (~ months) time periods, and (2) fabrication of nanopores that are small enough to use as a solid-state devices without the need for biological modification.[85]

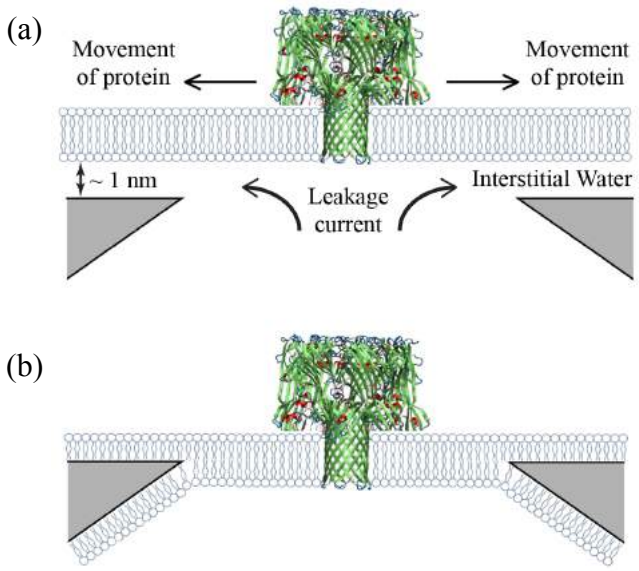

***Figure 1.12**: Schematic of two biological pore structures: (a) supported bilayer structure on (hydrophilic) glass, and (b) suspended bilayer structure on silanized (hydrophobic) glass. The latter displays greater stability (lasting months rather than hours). The synthetic pore is functionalised by a phospholipid bilayer containing the membrane protein staphylococcal alpha-hemolysin (PDB 7AHL).*

Diamond has huge potential in biosensing technologies. In terms of structural properties, diamond is robust, amenable to microfabrication,[106] chemically and

thermally inert, and can withstand extreme environments (high potentials, corrosive or high temperature/pressure conditions).[40] In terms of electrochemical properties, electrically conducting boron-doped diamond has the widest solvent window of all electrode materials, low background currents and high resistance to fouling.[40] Moreover, by using insulating diamond as a platform for pore structures, the resistance and capacitance properties will significantly reduce interfering signals to provide very high signal to noise ratios. Furthermore, diamond pores can be directly fabricated into the material making the methodology potentially simpler compared to other pore fabrication procedures.[90] Of key importance is the ability of diamond to be readily modified between stable hydrophilic O-terminated and hydrophobic H-terminated surface functionalisations (as discussed in section 1.2.3). This gives diamond a unique surface versatility that cannot be easily achieved by any other electrode material.

The exceptional physical and chemical properties of diamond, as outlined above, are well suited for biosensing technologies. As a consequence, investigation into diamond-based biosensing devices will help to further understanding and realise the full potential of the material in these devices.

1.4 Aims and Objectives

The overall aim of this study was to investigate the use of diamond in electrochemical and pore resistive-pulse biosensing devices. Whilst the detection capability of diamond electrochemical and pore structures can be addressed through experiments, interpretation requires a fundamental understanding of the processes at the biomolecule-diamond interface that cannot be accessed experimentally. Molecular dynamics (MD) simulations are ideally suited for this problem as they can successfully capture dynamic events at an atomistic resolution.

The main objectives was to: (1) achieve a fundamental understanding of how the different diamond surface orientations and terminations influence diamond-biomolecule interactions, (2) investigate how different surface terminations and dopant levels affect the electrochemical sensing capability of diamond electrodes, and (3) investigate the sensing capability of a novel diamond pore structure.

To meet these objectives, the plan of work is as follows. In Chapter 4, the first set of biocompatible diamond models of varying crystallographic orientation *i.e.* (100), (111), (110) and surface termination *i.e.* –H *vs.* –O are built. These models are employed in MD simulations to examine the influence of the different diamond surface orientations and terminations on the interfacial structure and dynamics of small molecules *i.e.* water and ions.

In Chapter 5, the diamond MD models are utilised to investigate the adsorption of larger biomolecules *i.e.* dopamine and serotonin, to different diamond surfaces. To do so, the free energy landscapes for the adsorption of dopamine and serotonin to each surface are revealed, and the conformational dynamics during the adsorption process are analysed. These studies will provide a molecular-level interpretation of biomolecule adsorption processes at different diamond surfaces and will help elucidate the ideal diamond surface that has the potential for selectivity of dopamine and serotonin in biosensing devices.

The focus then moves to experimentally investigate diamond electrochemical and pore resistive-pulse biosensing devices. In Chapter 6, the electrochemical response of a range of inner-sphere species on two high quality, well-defined H- and O- terminated conducting diamond electrodes is reported. In addition, the electrochemical response of an outer-sphere mediator when modifying the surface termination from –H to –O on a semiconducting diamond electrode is examined. The

application of localised diamond surface modification towards a novel electrode patterning technique is discussed.

In Chapter 7, fabrication of the first known diamond pore device is presented, and its sensing capability is demonstrated using polystyrene particles that can be detected by distinctive blockade events in the pore current.

In Chapter 8, development of coarse-grained MD models for polystyrene nanoparticles and diamond is presented, and preliminary investigation into the self-assembly of phospholipids on to model hydrophobic and hydrophilic diamond-like surfaces is discussed.

This thesis is structured in the following way: the theory behind the molecular simulations used in this study is outlined in chapter 2; the theory behind the experimental methodologies and instrumentation used in this study is outlined in chapter 3; the results for the simulation studies are presented in chapters 4 and 5; the results for the experimental studies are presented in chapters 6 and 7; preliminary work on coarse-grained molecular models is presented in chapter 8; and conclusions and future work are presented in chapter 9.

1.5 Significant Contributions to Knowledge in this Thesis

As a whole this thesis brings together experiments and computational studies to present, for the first time, an understanding of diamond interfaces that spans from the molecular-level to the microscale. The results are essential for driving forward the rational design and optimisation of diamond biosensors that could be used in applications such as healthcare (*e.g.* rapid DNA sequencing, screening and diagnosis of diseases), environmental science (*e.g.* detection of pollutants and toxins) and food safety (*e.g.* detection of harmful contaminants). The reader is referred to the overview sections at the beginning of Chapters 4 – 8 for a detailed account of the key advances

to knowledge in each research chapter. A broad view of the significant contributions to knowledge in this thesis and the critical linking between chapters is presented below.

1.5.1 Molecular Dynamics Simulations of Diamond-Water Interfaces

The first set of atomistic models of diamond surfaces with a range of crystallographic orientations and surface terminations were developed and validated against the available experimental data (Chapter 4). MD simulations enabled a detailed characterisation of water and ions at these different diamond surfaces and provided a fundamental molecular-level insight into the different diamond-solution interfaces, of which no prior knowledge exists. The analysis lays the foundation for explaining the role of interfacial water in diamond-water-biomolecule systems in the future and can help towards optimising an experimental surface process.

1.5.2 Molecular Dynamics Simulations of Diamond-Neurotransmitter Interfaces including a New Hypothesis for the Adsorption Pathway of Dopamine and Serotonin to Surfaces

The surface models developed in Chapter 4 were implemented in a real-life problem *i.e.* detection of neurotransmitters, dopamine and serotonin, through interaction with diamond surfaces (Chapter 5). This demonstrated how MD simulations of diamond could be used in practice for the study of diamond-water-biomolecule interfacial processes in order to optimise the experimental diamond electrode capability, but also detailed the limitations of these models when matching to electrochemical data. There was no prior knowledge of the pathway, strength or selectivity of dopamine/serotonin adsorption to different surfaces, hence these MD simulations revealed new and useful information that may also be generalised to other surfaces beyond diamond. The results enabled a proposed adsorption pathway and

reasons for the difference in the strength of adsorption to be postulated. The results will help the community to make informed decisions on the best electrode surface termination/orientation for improved detection of dopamine/serotonin in the future.

1.5.3 Electrochemical Analysis of Species on H- and O- terminated Conducting and Semi-Conducting Boron Doped Diamond

Existing electrochemical methodologies are used to reveal how changing the surface termination and boron dopant density of diamond can influence the detection of a range of different species (Chapter 6). The influence of surface termination was investigated for seven biologically relevant species including dopamine and serotonin, which were directly compared to the models in Chapter 5 to elucidate the role of the adsorption step in the electron transfer reaction. This work is the first to use well-defined and characterised diamond surfaces. The results were correlated to data of previous studies and a critique of the pre-existing data was provided. These new results are added to the bank of electrochemical information for each of these species on other surfaces to update the taxonomy, thus enabling the field to make a more informed decision on the ideal electrode material for detection of these species in future experiments. The results were utilised to demonstrate the concept of microscale 'read-write' diamond electrode surface patterning, which is an entirely new and original concept. This was shown to be a feasible and simple alterative to current surface patterning techniques and has enormous potential in the future to create microarrays on one surface that facilitate multiple experiments.

1.5.4 Fabrication and Use of a Novel Diamond Pore-Based Sensing Device

The existing concept of pore-based sensing was utilised and the idea extended to using single-crystal diamond as the platform material, which has never been used before (Chapter 7). A new methodology was demonstrated to fabricate individual

single-crystal diamond pores. The pores were applied in proof-of-concept studies to sense polystyrene particles. This is an entirely new device and the results served to demonstrate that diamond can be successfully applied in this technology. In addition, diamond offers several chemical, mechanical and electrical advantages over conventional pore-platform materials (*e.g.* extremely low background noise, chemical inertness, elimination of material hydration) that are highlighted throughout the Chapter 7. It is hoped that these results encourage the scientific community to use diamond in pore technology and thus more studies utilising diamond pore devices will follow in the future.

1.5.5 Development of New Coarse-Grained Molecular Dynamics Models

Bringing together the existing atomistic models in Chapters 4 – 5, and the larger scale experimental systems in Chapters 6 – 7, entirely new coarse-grained MD models of diamond and polystyrene nanoparticles were developed (Chapter 8). The feasibility of the models was tested using the self-assembly of phospholipids on different surfaces as a test system, that has not been modelled before. These new models are new and highly applicable for capturing a wide range of experimental systems and providing useful molecular-level insights in the future.

1.6 References

[1] a) L. C. Clark, C. Lyons, *Ann. N. Y. Acad. Sci.* **1962**, *102*, 29-45; b) G. Wang, B. Zhang, J. R. Wayment, J. M. Harris, H. S. White, *J. Am. Chem. Soc.* **2006**, *128*, 7679-7686.
[2] Z. Muhammad-Tahir, E. C. Alocilja, *Biosens. Bioelectron.* **2003**, *18*, 813-819.
[3] K. R. Rogers, *Biosens. Bioelectron.* **1995**, *10*, 533-541.
[4] P. T. Kissinger, *Biosens. Bioelectron.* **2005**, *20*, 2512-2516.
[5] R. Balmer, J. Brandon, S. Clewes, H. Dhillon, J. Dodson, I. Friel, P. Inglis, T. Madgwick, M. Markham, T. Mollart, *J. Phys. Condens. Matter* **2009**, *21*, 364221.
[6] P. W. May, *Philos. Trans. R. Soc. London A* **2000**, *358*, 473-495.
[7] A. Tallaire, J. Achard, F. Silva, O. Brinza, A. Gicquel, *C. R. Phys.* **2013**, *14*, 169-184.

[8] K. Sakamoto, A. Kasugai, M. Tsuneoka, K. Takahashi, T. Imai, T. Kariya, Y. Mitsunaka, *Rev. Sci. Instrum.* **1999**, *70*, 208-212.
[9] J. Kaneko, T. Tanaka, T. Imai, Y. Tanimura, M. Katagiri, T. Nishitani, H. Takeuchi, T. Sawamura, T. Iida, *Nucl. Instrum. Meth. A* **2003**, *505*, 187-190.
[10] N. Tran, S. Bai, J. Yang, H. Chun, O. Kavehei, Y. Yang, V. Muktamath, D. W. K. Ng, H. Meffin, M. Halpern, *IEEE J Solid-St. Circ.* **2014**, *49*, 751-765.
[11] F. Bundy, H. Hall, H. Strong, R. Wentorf, *Nature* **1955**, *176*, 51-55.
[12] F. Bundy, *J. Chem. Phys.* **1963**, *38*, 631-643.
[13] W. Eversole, *US Patents 3030187 & 3030188* **1958**.
[14] S. Matsumoto, Y. Sato, M. Tsutsumi, N. Setaka, *J. Mater. Sci.* **1982**, *17*, 3106-3112.
[15] a) P. K. Bachmann, D. Leers, H. Lydtin, *Diamond Relat. Mater.* **1991**, *1*, 1-12; b) J. E. Butler, R. L. Woodin, L. Brown, P. Fallon, *Philos. Trans. Roy. Soc. London Ser. A* **1993**, *342*, 209-224; c) J. C. Angus, A. Argoitia, R. Gat, Z. Li, M. Sunkara, L. Wang, Y. Wang, *Philos. Trans. Roy. Soc. London Ser. A* **1993**, *342*, 195-208.
[16] A. Fujishima, *Diamond Electrochemistry*, Elsevier, **2005**.
[17] K. Kobashi, K. Nishimura, Y. Kawate, T. Horiuchi, *Phys. Rev. B* **1988**, *38*, 4067.
[18] J. Xu, M. C. Granger, Q. Chen, J. W. Strojek, T. E. Lister, G. M. Swain, *Anal. Chem.* **1997**, *69*, 591A-597A.
[19] G. Janssen, W. Van Enckevort, W. Vollenberg, L. Giling, *Diamond Relat. Mater.* **1992**, *1*, 789-800.
[20] S.-T. Lee, Z. Lin, X. Jiang, *Mat. Sci. Eng. R* **1999**, *25*, 123-154.
[21] C. Chu, R. Hauge, J. Margrave, M. D'evelyn, *Appl. Phys. Lett.* **1992**, *61*, 1393-1395.
[22] A. Ferrari, J. Robertson, *Phys. Rev. B* **2001**, *63*, 121405.
[23] N. R. Wilson, S. L. Clewes, M. E. Newton, P. R. Unwin, J. V. Macpherson, *J. Phys. Chem. B* **2006**, *110*, 5639-5646.
[24] a) L. A. Hutton, J. G. Iacobini, E. Bitziou, R. B. Channon, M. E. Newton, J. V. Macpherson, *Anal. Chem.* **2013**, *85*, 7230-7240; b) H. Notsu, I. Yagi, T. Tatsuma, D. A. Tryk, A. Fujishima, *J. Electroanal. Chem.* **2000**, *492*, 31-37.
[25] G. A. Somorjai, Y. Li, *Introduction to Surface Chemistry and Catalysis*, John Wiley & Sons, **2010**.
[26] R. Telling, C. Pickard, M. Payne, J. Field, *Phys. Rev. Lett.* **2000**, *84*, 5160.
[27] J. Ristein, *App. Phys. A* **2006**, *82*, 377-384.
[28] Z. Zhang, M. Wensell, J. Bernholc, *Phys. Rev. B* **1995**, *51*, 5291.
[29] C. Nebel, J. Ristein, *Thin-Film Diamond II (Semiconductors and Semimetals), Vol. 77*, Elsevier B. V., Amsterdam, Netherlands., **2004**.
[30] a) T. Frauenheim, U. Stephan, P. Blaudeck, D. Porezag, H.-G. Busmann, W. Zimmermann-Edling, S. Lauer, *Phys. Rev. B* **1993**, *48*, 18189; b) Z. Jing, J. Whitten, *Surf. Sci.* **1994**, *314*, 300-306.
[31] a) C. Kress, M. Fiedler, W. Schmidt, F. Bechstedt, *Phys. Rev. B* **1994**, *50*, 17697; b) J. Furthmüller, J. Hafner, G. Kresse, *Phys. Rev. B* **1996**, *53*, 7334; c) P. Krüger, J. Pollmann, *Phys. Rev. Lett.* **1995**, *74*, 1155.
[32] a) X. Zheng, P. Smith, *Surf. Sci.* **1992**, *262*, 219-234; b) J. L. Whitten, P. Cremaschi, R. E. Thomas, R. A. Rudder, R. J. Markunas, *Appl. Surf. Sci.* **1994**, *75*, 45-50; c) S. Skokov, B. Weiner, M. Frenklach, *J. Phys. Chem.* **1994**, *98*, 7073-7082; d) D. Petrini, K. Larsson, *J. Phys. Chem. C* **2007**, *111*, 795-801.

[33] a) P. John, N. Polwart, C. Troupe, J. Wilson, *Diamond Relat. Mater.* **2002**, *11*, 861-866; b) S. Ghodbane, D. Ballutaud, A. Deneuville, C. Baron, *Phys. Status Solidi A* **2006**, *203*, 3147-3151.
[34] a) P. E. Pehrsson, T. W. Mercer, *Surf. Sci.* **2000**, *460*, 49-66; b) M. Z. Hossain, T. Kubo, T. Aruga, N. Takagi, T. Tsuno, N. Fujimori, M. Nishijima, *Surf. Sci.* **1999**, *436*, 63-71.
[35] a) D. Petrini, K. Larsson, *J. Phys. Chem. C* **2008**, *112*, 3018-3026; b) K. P. Loh, X. Xie, S. Yang, J. Zheng, *J. Phys. Chem. B* **2002**, *106*, 5230-5240.
[36] J. Cui, J. Ristein, L. Ley, *Phys. Rev. B* **1999**, *59*, 5847.
[37] F. Maier, R. Graupner, M. Hollering, L. Hammer, J. Ristein, L. Ley, *Surf. Sci.* **1999**, *443*, 177-185.
[38] B. L. Mackey, J. N. Russell, J. E. Crowell, P. E. Pehrsson, B. D. Thoms, J. E. Butler, *J. Phys. Chem. B* **2001**, *105*, 3803-3812.
[39] a) E. Vanhove, J. De Sanoit, J. Arnault, S. Saada, C. Mer, P. Mailley, P. Bergonzo, M. Nesladek, *Phys. Status Solidi A* **2007**, *204*, 2931-2939; b) G. R. Salazar-Banda, L. S. Andrade, P. A. Nascente, P. S. Pizani, R. C. Rocha-Filho, L. A. Avaca, *Electrochim. Acta* **2006**, *51*, 4612-4619.
[40] J. V. Macpherson, *Phys. Chem. Chem. Phys.* **2015**, *17*, 2935-2949.
[41] H. B. Suffredini, V. A. Pedrosa, L. Codognoto, S. A. Machado, R. C. Rocha-Filho, L. A. Avaca, *Electrochim. Acta* **2004**, *49*, 4021-4026.
[42] R. Hoffmann, A. Kriele, H. Obloh, J. Hees, M. Wolfer, W. Smirnov, N. Yang, C. E. Nebel, *Appl. Phys. Lett.* **2010**, *97*, 052103.
[43] F. Liu, J. Wang, B. Liu, X. Li, D. Chen, *Diamond Relat. Mater.* **2007**, *16*, 454-460.
[44] H. A. Girard, N. Simon, D. Ballutaud, E. de La Rochefoucauld, A. Etcheberry, *Diamond Relat. Mater.* **2007**, *16*, 888-891.
[45] S. Wang, V. M. Swope, J. E. Butler, T. Feygelson, G. M. Swain, *Diamond Relat. Mater.* **2009**, *18*, 669-677.
[46] R. Boukherroub, X. Wallart, S. Szunerits, B. Marcus, P. Bouvier, M. Mermoux, *Electrochem. Commun.* **2005**, *7*, 937-940.
[47] L. Ostrovskaya, V. Perevertailo, V. Ralchenko, A. Dementjev, O. Loginova, *Diamond Relat. Mater.* **2002**, *11*, 845-850.
[48] a) F. Klauser, S. Ghodbane, R. Boukherroub, S. Szunerits, D. Steinmüller-Nethl, E. Bertel, N. Memmel, *Diamond Relat. Mater.* **2010**, *19*, 474-478; b) S. Ghodbane, D. Ballutaud, F. Omnès, C. Agnes, *Diamond Relat. Mater.* **2010**, *19*, 630-636.
[49] C. H. Goeting, F. Marken, A. Gutiérrez-Sosa, R. G. Compton, J. S. Foord, *Diamond Relat. Mater.* **2000**, *9*, 390-396.
[50] a) L. Hutton, M. E. Newton, P. R. Unwin, J. V. Macpherson, *Anal. Chem.* **2008**, *81*, 1023-1032; b) A. G. Güell, K. E. Meadows, P. R. Unwin, J. V. Macpherson, *Phys. Chem. Chem. Phys.* **2010**, *12*, 10108-10114.
[51] F. Maier, M. Riedel, B. Mantel, J. Ristein, L. Ley, *Phys. Rev. Lett.* **2000**, *85*, 3472.
[52] R. Chrenko, *Phys. Rev. B* **1973**, *7*, 4560.
[53] J.-P. Lagrange, A. Deneuville, E. Gheeraert, *Diamond Relat. Mater.* **1998**, *7*, 1390-1393.
[54] a) E. Gheeraert, A. Deneuville, J. Mambou, *Diamond Relat. Mater.* **1998**, *7*, 1509-1512; b) T. Inushima, T. Matsushita, S. Ohya, H. Shiomi, *Diamond Relat. Mater.* **2000**, *9*, 1066-1070.

[55] X. Blase, E. Bustarret, C. Chapelier, T. Klein, C. Marcenat, *Nat. Mater.* **2009**, *8*, 375-382.
[56] J. E. Post, F. Farges, *Rocks & Minerals* **2014**, *89*, 16-26.
[57] a) H. Spicka, M. Griesser, H. Hutter, M. Grasserbauer, S. Bohr, R. Haubner, B. Lux, *Diamond Relat. Mater.* **1996**, *5*, 383-387; b) R. Locher, J. Wagner, F. Fuchs, C. Wild, P. Hiesinger, P. Gonon, P. Koidl, *Mat. Sci. Eng. B* **1995**, *29*, 211-215.
[58] D. Barbosa, F. Almeida, R. Silva, N. Ferreira, V. Trava-Airoldi, E. Corat, *Diamond Relat. Mater.* **2009**, *18*, 1283-1288.
[59] C. Nebel, J. Ristein, *Thin-Film Diamond I (Semiconductors and Semimetals), Vol. 76*, Academic Press, **2003**.
[60] K. Ushizawa, K. Watanabe, T. Ando, I. Sakaguchi, M. Nishitani-Gamo, Y. Sato, H. Kanda, *Diamond Relat. Mater.* **1998**, *7*, 1719-1722.
[61] a) M. Landstrass, K. Ravi, *Appl. Phys. Lett.* **1989**, *55*, 975-977; b) M. Landstrass, K. Ravi, *Appl. Phys. Lett.* **1989**, *55*, 1391-1393.
[62] K. Hayashi, S. Yamanaka, H. Watanabe, T. Sekiguchi, H. Okushi, K. Kajimura, *J. Appl. Phys.* **1997**, *81*, 744-753.
[63] J. Ristein, *J. Phys. D Appl. Phys.* **2006**, *39*, R71.
[64] A. W. Bott, *Curr. Sep.* **1998**, *17*, 87-92.
[65] P. Strobel, M. Riedel, J. Ristein, L. Ley, *Nature* **2004**, *430*, 439-441.
[66] a) M. C. Granger, M. Witek, J. Xu, J. Wang, M. Hupert, A. Hanks, M. D. Koppang, J. E. Butler, G. Lucazeau, M. Mermoux, *Anal. Chem.* **2000**, *72*, 3793-3804; b) H. V. Patten, L. A. Hutton, J. R. Webb, M. E. Newton, P. R. Unwin, J. V. Macpherson, *Chem. Comm.* **2015**, *51*, 164-167.
[67] J. Wang, *Biosens. Bioelectron.* **2006**, *21*, 1887-1892.
[68] R. Edelstein, C. Tamanaha, P. Sheehan, M. Miller, D. Baselt, L. Whitman, R. Colton, *Biosens. Bioelectron.* **2000**, *14*, 805-813.
[69] a) S. Rodriguez-Mozaz, M. J. L. de Alda, D. Barceló, *Anal. Bioanal. Chem.* **2006**, *386*, 1025-1041; b) J. Wang, G. Rivas, X. Cai, E. Palecek, P. Nielsen, H. Shiraishi, N. Dontha, D. Luo, C. Parrado, M. Chicharro, *Anal. Chim. Acta* **1997**, *347*, 1-8; c) L. D. Mello, L. T. Kubota, *Food Chem.* **2002**, *77*, 237-256.
[70] B. R. Eggins, *Biosensors: An Introduction*, Springer-Verlag, **2013**.
[71] D. Grieshaber, R. MacKenzie, J. Voeroes, E. Reimhult, *Sensors* **2008**, *8*, 1400-1458.
[72] a) X. Fan, I. M. White, S. I. Shopova, H. Zhu, J. D. Suter, Y. Sun, *Anal. Chim. Acta* **2008**, *620*, 8-26; b) J. Homola, *Anal. Bioanal. Chem.* **2003**, *377*, 528-539.
[73] K. A. Marx, *Biomacromolecules* **2003**, *4*, 1099-1120.
[74] G. Binnig, C. F. Quate, C. Gerber, *Phys. Rev. Lett.* **1986**, *56*, 930.
[75] D. J. Stephens, V. J. Allan, *Science* **2003**, *300*, 82-86.
[76] H. Bayley, P. S. Cremer, *Nature* **2001**, *413*, 226-230.
[77] a) A. Kueng, C. Kranz, B. Mizaikoff, *Sensor Lett.* **2003**, *1*, 2-15; b) G. A. Chansin, R. Mulero, J. Hong, M. J. Kim, A. J. Demello, J. B. Edel, *Nano Lett.* **2007**, *7*, 2901-2906; c) A. Baba, S. Tian, F. Stefani, C. Xia, Z. Wang, R. C. Advincula, D. Johannsmann, W. Knoll, *J. Electroanal. Chem.* **2004**, *562*, 95-103.
[78] D. R. Thévenot, K. Toth, R. A. Durst, G. S. Wilson, *Biosens. Bioelectron.* **2001**, *16*, 121-131.
[79] J. Wang, *Electroanalysis* **2001**, *13*, 983.
[80] G. S. Wilson, R. Gifford, *Biosens. Bioelectron.* **2005**, *20*, 2388-2403.

[81] a) M. Pumera, S. Sánchez, I. Ichinose, J. Tang, *Sensor Actuat. B Chem.* **2007**, *123*, 1195-1205; b) T. G. Drummond, M. G. Hill, J. K. Barton, *Nat. Biotechnol.* **2003**, *21*, 1192-1199.
[82] S. Park, H. Boo, T. D. Chung, *Anal. Chim. Acta* **2006**, *556*, 46-57.
[83] R. Trouillon, D. O'Hare, *Electrochim. Acta* **2010**, *55*, 6586-6595.
[84] R. DeBlois, C. Bean, *Rev. Sci. Instrum.* **1970**, *41*, 909-916.
[85] C. Dekker, *Nat. Nanotechnol.* **2007**, *2*, 209-215.
[86] J. Kong, H. Wu, L. Liu, X. Xie, L. Wu, X. Ye, Q. Liu, *J. Nanosci. Nanotechnol.* **2013**, *13*, 4010-4016.
[87] P. Rowghanian, A. Y. Grosberg, *J. Phys. Chem. B* **2011**, *115*, 14127-14135.
[88] E. C. Yusko, J. M. Johnson, S. Majd, P. Prangkio, R. C. Rollings, J. Li, J. Yang, M. Mayer, *Nat. Nanotechnol.* **2011**, *6*, 253-260.
[89] S. W. Kowalczyk, D. B. Wells, A. Aksimentiev, C. Dekker, *Nano Lett.* **2012**, *12*, 1038-1044.
[90] B. N. Miles, A. P. Ivanov, K. A. Wilson, F. Doğan, D. Japrung, J. B. Edel, *Chem. Soc. Rev.* **2013**, *42*, 15-28.
[91] A. Storm, J. Chen, X. Ling, H. Zandbergen, C. Dekker, *Nat. Mater.* **2003**, *2*, 537-540.
[92] B. Zhang, J. Galusha, P. G. Shiozawa, G. Wang, A. J. Bergren, R. M. Jones, R. J. White, E. N. Ervin, C. C. Cauley, H. S. White, *Anal. Chem.* **2007**, *79*, 4778-4787.
[93] V. Tabard-Cossa, D. Trivedi, M. Wiggin, N. N. Jetha, A. Marziali, *Nanotechnol.* **2007**, *18*, 305505.
[94] C. C. Harrell, Z. S. Siwy, C. R. Martin, *Small* **2006**, *2*, 194-198.
[95] R. Vogel, G. Willmott, D. Kozak, G. S. Roberts, W. Anderson, L. Groenewegen, B. Glossop, A. Barnett, A. Turner, M. Trau, *Anal. Chem.* **2011**, *83*, 3499-3506.
[96] A. J. Storm, C. Storm, J. Chen, H. Zandbergen, J.-F. Joanny, C. Dekker, *Nano. Lett.* **2005**, *5*, 1193-1197.
[97] K. Healy, B. Schiedt, A. P. Morrison, *Nanomedicine* **2007**, *2*, 875-897.
[98] J. Clarke, H.-C. Wu, L. Jayasinghe, A. Patel, S. Reid, H. Bayley, *Nat. Nanotechnol.* **2009**, *4*, 265-270.
[99] D. Fologea, J. Uplinger, B. Thomas, D. S. McNabb, J. Li, *Nano Lett.* **2005**, *5*, 1734-1737.
[100] L.-Q. Gu, J. W. Shim, *Analyst* **2010**, *135*, 441-451.
[101] R. J. White, B. Zhang, S. Daniel, J. M. Tang, E. N. Ervin, P. S. Cremer, H. S. White, *Langmuir* **2006**, *22*, 10777-10783.
[102] R. P. Richter, R. Bérat, A. R. Brisson, *Langmuir* **2006**, *22*, 3497-3505.
[103] A. E. Schibel, T. Edwards, R. Kawano, W. Lan, H. S. White, *Anal. Chem.* **2010**, *82*, 7259-7266.
[104] R. J. White, E. N. Ervin, T. Yang, X. Chen, S. Daniel, P. S. Cremer, H. S. White, *J. Am. Chem. Soc.* **2007**, *129*, 11766-11775.
[105] D. Branton, D. W. Deamer, A. Marziali, H. Bayley, S. A. Benner, T. Butler, M. Di Ventra, S. Garaj, A. Hibbs, X. Huang, *Nat. Biotechnol.* **2008**, *26*, 1146-1153.
[106] O. Auciello, J. Birrell, J. A. Carlisle, J. E. Gerbi, X. Xiao, B. Peng, H. D. Espinosa, *J. Phys. Condens. Matter* **2004**, *16*, R539.

Chapter 2

Simulation Theory

2.1 Introduction to Molecular Modelling

Linking molecular modelling and experimental data is highly relevant to this work. A key goal of this study is to utilise molecular dynamics (MD) models to elucidate various processes at the biomolecule-diamond interface that could help advance diamond-based biosensing technologies. In the following sections, we aim to introduce the fundamental concepts behind molecular simulation and the techniques used in this work: section 2.2 introduces statistical mechanics; section 2.3 introduces the theory of force fields to model the intra- and inter- molecular interactions of a molecular system; section 2.4 explains the technique of potential energy minimisation; section 2.5 reviews coarse-grained force fields; and section 2.6 explains the theory of MD and techniques relevant to this study.

2.2 Statistical Mechanics

Various experimental techniques exist to measure thermodynamic macroscopic bulk properties, time averaged over the large number of particles that constitute the system.[1] For example, cyclic voltammetry (CV) is used to determine the thermodynamic electrode potential of an electrochemical reaction based on the potential at which a faradaic peak current is measured (see Chapter 3, section 3.8.3).

However, as bulk measurements, these values cannot convey the full picture of a system. It is essential to turn to the atomic scale in order to elucidate the necessary components that build the foundations for the observed bulk property. Computer simulations are ideally suited for this purpose.

Simulation methods measure the atomic behaviour of an *N*-particle system by tracing the movement of the atoms and molecules. *Statistical mechanics* then links the microscopic information from computer simulations to the experimental macroscopic observations, by utilising probability theory to connect the two regimes.[2] For example, a measurable macroscopic property, *A*, will be dependent on the position and momenta of the *N* particles that constitute the system. The value of *A* will fluctuate over time due to the interactions of the particles in the system. However, a macroscopic system consists of a vast number of particles in the order of 10^{23} (Avogadro's number). It is unfeasible to calculate the time evolution of such a large number of particles in a single system. To overcome this problem, statistical mechanics uses the concept of *microstates* and *ensembles* of the system.

A microscopic configuration of the *N* particles in a thermodynamic system at a given instant in time is described as a *microstate*. In particular, each point in the 6*N*-dimensional *phase space* (three position coordinates and three components of momenta for each particle) of a thermodynamic system is a microstate, expressed by a set of values that describe the dynamic state of all *N* particles in the system ($\mathbf{r}_1$, $\mathbf{r}_2$, $\mathbf{r}_3$, … , $\mathbf{r}_N$; $\mathbf{p}_1$, $\mathbf{p}_2$, $\mathbf{p}_3$, … , $\mathbf{p}_N$), where $\mathbf{r}_i$ and $\mathbf{p}_i$ are the position and momentum of particle *i*, respectively. An *ensemble* is then defined as the collection of all possible microstates that are macroscopically indistinguishable *i.e.* all microstates that have a different configuration of the *N*-particles but share an identical thermodynamic property. Statistical mechanics works under the assumption that a macroscopic

property is the average of the corresponding ensemble. Hence, the time average of a single system can be replaced by the *ensemble average,* $\langle A \rangle$, of many microstates at a given instant in time:

$$\langle A \rangle = \iint d\mathbf{p}^N \, d\mathbf{r}^N A(\mathbf{p}^N, \mathbf{r}^N) \rho(\mathbf{p}^N, \mathbf{r}^N) \tag{2.1}$$

where $A(\mathbf{p}^N, \mathbf{r}^N)$ is the macroscopic property and $\rho(\mathbf{p}^N, \mathbf{r}^N)$ is the probability density of the ensemble *i.e.* the probability of finding the system in which the particles are in a microstate with particle positions $\mathbf{r}^N$ and momenta $\mathbf{p}^N$.

The *ergodic* hypothesis in classical statistical mechanics states that the time average equals the ensemble average *i.e.* that all accessible microstates are equally probable over a long time period.[3] For MD computer simulations, as employed in this thesis, the system is evolved over time to explore the phase space and calculate time-averaged properties. It is challenging to calculate an ensemble average using MD, as it would require the system to pass through all possible states corresponding to the required thermodynamic constraints. However, provided the system is ergodic, the time averages calculated in MD simulations match the ensemble averages calculated in experiments. Thus, computer simulations using the framework of statistical mechanics, such as MD, provide the means to relate the atomistic dynamics of a system to experimental observables.

2.3 Interaction Potentials

The design of a molecular model requires careful consideration of the appropriate time and length scales to capture the phenomena of interest. Quantum mechanics (QM) calculations can provide a full description of the behaviour of a system on the atomic and subatomic level, but requires a large amount of computational expenditure that, even with the most powerful computers, limits the

study to only a small number of particles. To capture biologically relevant events such as molecular adsorption or self-assembly, as of interest in this research, it is necessary to model systems comprising a relatively large number of particles (typically of the order of 10^6 atoms). *Molecular mechanics* (or *force field theory*) can achieve this by ignoring the electronic motions and studying the energy of a system as a function of the positions of the atomic nuclei over a single (typically ground-state) potential energy surface, based on the Born-Oppenheimer approximation that enables the separation of electronic and nuclear degrees of freedom.[1]

In force field theory, the interaction between atoms is described using equations and parameters that relate the chemical structure to the total system energy. A *force field* is the set of interaction potentials along with the necessary parameters that describe the forces acting on each type of atom within a system. The force field chosen in this research assumes that the potential energy of the system can break down into non-bonded and bonded potentials that correspond to the different inter- and intra-molecular forces between the atoms. The bonded interactions describe the energy penalties associated with the movement of bonds and angles away from their 'equilibrium' position. These include: (1) bond stretching (section 2.3.1), (2) angle bending (section 2.3.2) and (3) bond rotation or torsion angles (section 2.3.3). Non-bonded interactions describe how atoms that are not covalently bound to one another interact as a function of distance from each other. These include: (1) van der Waals (dipole-dipole, induced dipole-dipole and London dispersion) forces (section 2.3.4) and (2) electrostatic interactions (section 2.3.5). These interactions are illustrated in **Figure 2.1**. The total potential energy of the system, $U_{\text{total}}(\mathbf{r}^N)$, is assumed to be the sum of these interaction components as a function of the positions, $\mathbf{r}$, of the N particles in the system:

$$U_{\text{total}}(\mathbf{r}^N) = \sum_{\text{bonded}} U_{\text{bonded}}(\mathbf{r}^N) + \sum_{\text{nonbonded}} U_{\text{nonbonded}}(\mathbf{r}^N) \tag{2.2}$$

$$= \underbrace{\sum_{\text{bonds}} U_{\text{bonds}}(\mathbf{r}^N) + \sum_{\text{angles}} U_{\text{angles}}(\mathbf{r}^N) + \sum_{\text{dihedrals}} U_{\text{dihedrals}}(\mathbf{r}^N)}_{\text{Bonded interactions}} \tag{2.3}$$

$$\underbrace{+\sum_{\text{vdw}} U_{\text{vdw}}(\mathbf{r}^N) + \sum_{\text{electrostatics}} U_{\text{electrostatics}}(\mathbf{r}^N)}_{\text{Non-bonded interactions}}$$

$$= \underbrace{\sum_{\text{bonds}} \frac{k_{l_i}}{2}\left(l_i - l_{i,0}\right)^2}_{\text{Bond stretching}} + \underbrace{\sum_{\text{angles}} \frac{k_{\theta_i}}{2}\left(\theta_i - \theta_{i,0}\right)^2}_{\text{Angle bending}} + \underbrace{\sum_{\text{dihedrals}} \frac{k_{\omega_i}}{2}\left(1 + \cos(n\omega_i - \omega_{i,0})\right)}_{\text{Bond rotation (torsional angles)}} \tag{2.4}$$

$$\underbrace{+\sum_{i=1}^{N}\sum_{j=i+1}^{N}\left(4\varepsilon_{ij}\left[\left(\frac{\sigma_{ij}}{r_{ij}}\right)^{12} - \left(\frac{\sigma_{ij}}{r_{ij}}\right)^{6}\right] + \frac{q_i q_j}{4\pi\varepsilon_0 r_{ij}}\right)}_{\text{Van der Waals and Electrostatics}}$$

where all parameters are defined in the sections below.

While more specialised force fields may contain extra interaction components,[4] in general the most frequently used force fields take this form. In this study, two common force fields were used: the GROMOS96 53a6 united atom[5] and MARTINI coarse-grained (CG)[6] (discussed in section 2.5).

In the following sections, each of the interaction components in force fields will be discussed and their most common functional form (as presented in equation 2.4) explained.

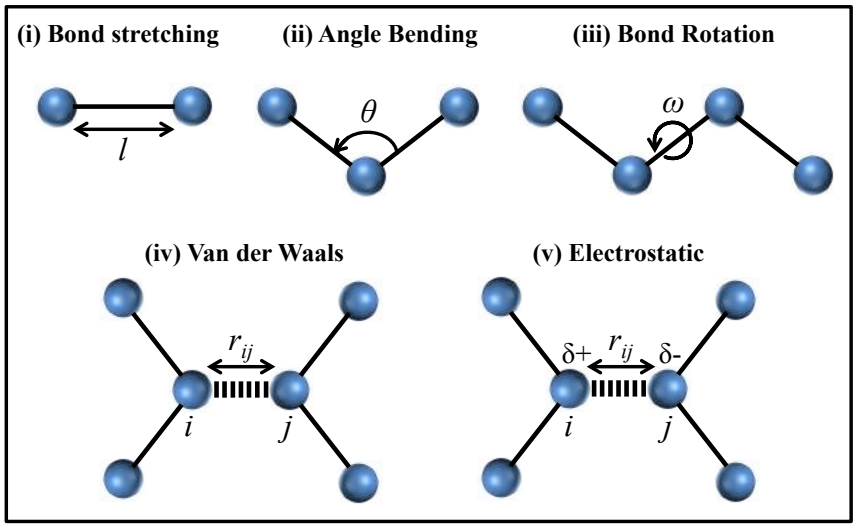

***Figure 2.1**: Schematic representation of the five interaction components that comprise the molecular mechanics force field chosen in this research: (i) bond stretching, (ii) angle bending, (iii) bond rotation or torsional angles (bonded interactions), and (iv) van der Waals, (v) electrostatic (non-bonded interactions).*

2.3.1 Bond Stretching

The *bond stretching* between two covalently bonded atoms can be approximated using the harmonic potential (**Figure 2.2**):

$$U_{\text{bond}}(l) = \frac{k_l}{2}(l - l_0)^2 \tag{2.5}$$

where $U_{\text{bond}}(l)$ is the bond energy as a function of bond length l, k_l is the bond force constant, and l_0 is the reference bond length (the choice of which is discussed below). The ½ term prevents double counting so that the bond stretching is only calculated for one of the atoms relative to the other. It is of note that bond stretching can be more accurately portrayed over a wider range of bond lengths using the Morse potential (**Figure 2.2**):

$$U_{\text{bond}}(l) = D_l(1 - e^{-\sqrt{k_l/2D_l}(l-l_0)})^2 \tag{2.6}$$

where D_l is the well depth. In particular, the Morse functional form captures the dissociation limit at large intermolecular separations where the particles are no longer

bound and prevents particle-particle overlap at small separations. This potential is useful for diatomic or very small molecules that have few bonds, but is computationally expensive to run over large systems (requiring three parameters per bond for the Morse compared to two for the simple quadratic harmonic). In addition, the harmonic potential is in close agreement with the Morse potential in the proximity of the energy minimum, which is of significance given that bonds typically display only small displacements from the reference bond length (**Figure 2.2**). For these reasons, the simple first-order harmonic potential is employed in this study to estimate bond stretching.

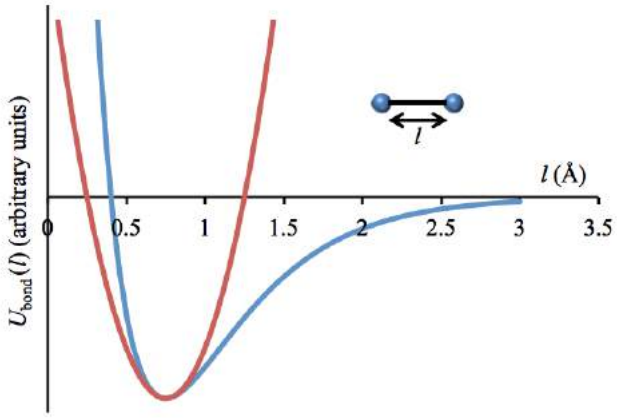

***Figure 2.2**: Bond energy as a function of intermolecular separation described by the Morse potential (blue) and the harmonic potential (red).*

The reference bond lengths in the Gromos53a6 parameter set were obtained from crystallographic and spectroscopic data for small molecules.[5] It is noted that there are uncertainties in the experimentally determined bond lengths (of up to 0.015 Å from X-ray methods) due to variations in the temperature or environment.[2] In addition, there will always be error contributions due to the vibrational motion of a molecule, and incidental shifts to compensate for other energy contributions in a system. Whilst these contributions are often negligible, they may become relevant if

measuring bond lengths to a high degree of accuracy. In this study, the parameters were adjusted to the reference bond lengths and angles of diamond from experimental and *ab-initio* studies. This serves to fine-tune the force field towards diamond (Chapter 4). These changes did not introduce extreme variations in the bond lengths, causing only slight shifts in the position of the reference length from that specified in the original force field (Chapter 4).

2.3.2 Angle Bending

The *angle bending* between three covalently bonded particles can be described by a cosine harmonic potential (**Figure 2.3**):

$$U_{\text{angle}}(\theta) = \frac{k_\theta}{2}(\cos(\theta) - \cos(\theta_0))^2 \tag{2.7}$$

with

$$\cos(\theta) = \frac{r_{ij} \cdot r_{kj}}{r_{ij} r_{kj}} \tag{2.8}$$

where $U_{\text{angle}}(\theta)$ is the energy as a function of the angle, θ, formed between the three bonded particles, k_θ is the angular force constant, θ_0 is the reference angle (chosen based on crystallographic and spectroscopic data for small molecules,[5] and r_{ij} and r_{kj} are the intermolecular separations (bond lengths) between particles *i*, *j* and *k*, *j*, respectively and *j* denoted by convention as the central atom. The ½ term prevents double counting. This functional form accurately reproduces the angle bending energy in the proximity of the energy minimum, which is sufficient for this study given that the angle does not deviate far from the reference value.

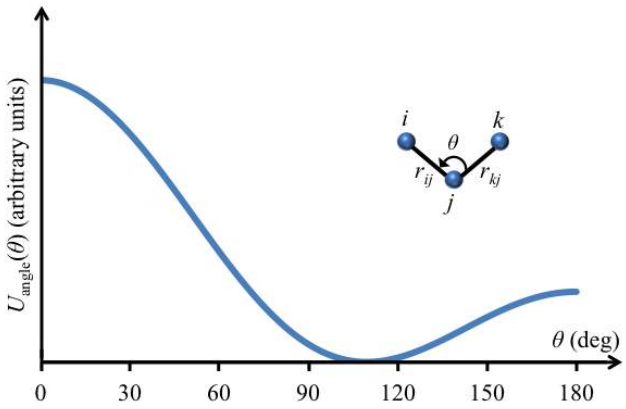

***Figure 2.3**: Angle bending energy as a function of bond angle described by a cosine harmonic potential with a reference angle of 109.5°.*

2.3.3 Bond Rotation (Torsional Angles)

For three consecutive bonds, or four covalently bonded atoms *i*, *j*, *k*, and *l*, the angle between the plane formed by *i*, *j* and *k* and the plane formed by *j*, *k* and *l* is defined as the (*proper) dihedral angle*. Whilst the bond stretching and angle bending terms do not deviate far from the reference value, the dihedral angle can fluctuate significantly. The dihedral angle can take any value to produce different geometrical conformations of a molecule. The molecule may have several favourable and unfavourable conformations, which are shown as minima and maxima in the energy landscape during torsional rotation. The energy potential can therefore be approximated by a cosine periodic function (**Figure 2.4**):

$$U_{\text{dihedral}}(\omega) = \frac{k_\omega}{2}\left[1 + \cos(n\omega - \omega_0)\right] \tag{2.9}$$

where $U_{\text{dihedral}}(\omega)$ is the energy as a function of the dihedral angle ω, k_ω is the force constant between the *i*-*j*-*k* and *j*-*k*-*l* planes, ω_0 is the reference dihedral angle, and *n* is the multiplicity defined as the number of minima in the function as the bond is rotated through 360°. This functional form was used to describe all proper dihedrals in this study.

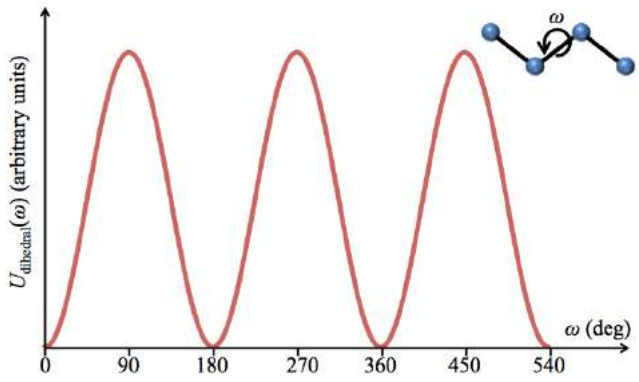

***Figure 2.4**: The torsional energy profile as a function of the dihedral angle.*

For certain molecules, groups are known to remain within a specific plane, for example the groups forming an aromatic ring always lie approximately planar. To achieve the desired geometry, *improper dihedral angles* are included in the force field. These use an out-of-plane bending component (typically involving atoms that are not bonded together in the standard order, or at all) to enforce the planarity. For example, in this study, each carbonyl group on the diamond surface requires an additional improper torsional angle to correctly model the planar rigidity enforced by the double bond, ensuring that C=O has minima at 0° and 180° (n = 2). The energy function for improper dihedral angles can be approximated by a harmonic potential:

$$U_{\text{improper}}(\omega) = \frac{k_\omega}{2}(\omega - \omega_0)^2 \qquad (2.10)$$

where $U_{\text{improper}}(\omega)$ is the energy as a function of the improper dihedral angle, ω, between four atoms, k_ω is the force constant of the angle between the two planes, n is the multiplicity and ω_0 is the reference angle. In this study, harmonic potentials were applied for all improper dihedrals.

2.3.4 Van der Waals Interactions

Forces between electrically neutral atoms can occur due to fluctuations in the positions of the electrons that can cause polarisation. This induces attractive permanent dipole-dipole, induced dipole-permanent dipole and London dispersion forces between non-bonded particles at relatively long-range separations. Moreover, at short-range distances, particles will experience repulsive forces due to overlap of the electron distribution. These attractive and repulsive intermolecular interactions are generally termed as *van der Waals* forces. The overall energy distribution of van der Waals interactions as a function of atomic separation can be approximated by the Lennard-Jones (LJ) 12-6 potential:

$$U_{\mathrm{LJ}}(r_{ij}) = 4\varepsilon\left[\left(\frac{\sigma}{r_{ij}}\right)^{12} - \left(\frac{\sigma}{r_{ij}}\right)^{6}\right] \tag{2.11}$$

where $U_{\mathrm{LJ}}(r_{ij})$ is the energy as a function of the intermolecular separation r_{ij} between two particles i and j, ε is the well depth and σ is the separation distance at which the potential is zero (the collision diameter), shown in **Figure 2.5**. The LJ potential is formed of attractive (αr^{-6}) and repulsive (αr^{-12}) components, where the energy minimum lies at position $r_m = 2^{1/6}\sigma$ with value of $-\varepsilon$.

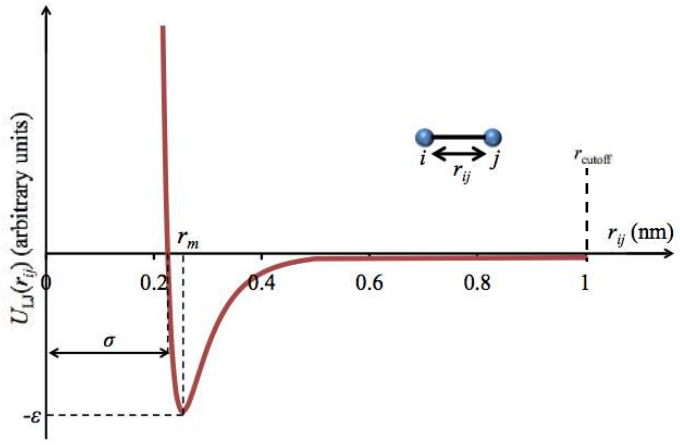

***Figure 2.5**: Schematic of the LJ potential. The plot falls off rapidly so that the typical cut-off value, r_{cutoff} = 1 nm, has a negligible effect on the interactions.*

In this study, the LJ 12-6 potential is used to describe all van der Waals interactions between atoms. In addition, the Lorentz-Berthelot mixing rules were applied to calculate the LJ parameters for cross-interactions:[5]

$$\sigma_{AB} = \frac{1}{2}(\sigma_{AA} + \sigma_{BB}) \tag{2.12}$$

$$\varepsilon_{AB} = \sqrt{\varepsilon_{AA}\varepsilon_{BB}} \tag{2.13}$$

where σ_{AB} and ε_{AB} are the collision diameter and potential well depth for two interacting particles *A* and *B*, respectively.

Calculating the non-bonded van der Waals interactions between each pair of atoms in a *N*-particle system (of the order N^2 interactions) can be extremely time consuming. The LJ potential falls off rapidly to zero with distance as the intermolecular separation becomes sufficiently large that the van der Waals forces are virtually negligible (**Figure 2.5)**. To improve the computational speed, a *cut-off,* r_{cutoff}, is frequently implemented. A sphere of radius r_{cutoff} is placed around each particle *i* in the system. If the distance to particle *j* is $r_{ij} \leq r_{\text{cutoff}}$, the non-bonded interactions between *i* and *j* are calculated. If $r_{ij} > r_{\text{cutoff}}$, the interactions are truncated to zero. A shift function is applied to the LJ potential to prevent a discontinuity at $r_{ij} = r_{\text{cutoff}}$. The potential is shifted upwards by $U_{\text{LJ}}(r_{\text{cutoff}})$ allowing the energy to increase continuously to reach zero exactly at r_{cutoff}. The choice of r_{cutoff} is essential; if the value is too large, particles may begin to interact with themselves due to the periodic boundary conditions (see section 2.6.3) but if it is too small, important interactions could be neglected.

2.3.5 Electrostatic Interactions

The electrostatic charge-charge interactions between two non-bonded, charged particles can be approximated using the Coulomb potential:

$$U_{\text{coulomb}}(r_{ij}) = \frac{1}{4\pi\varepsilon_0}\frac{q_i q_j}{\varepsilon_r r_{ij}} \tag{2.14}$$

where $U_{\text{coulomb}}(r_{ij})$ is the Coulombic interaction energy as a function of intermolecular distance r_{ij} between particles i and j, respectively and ε_0 is the permittivity of space. The Coulomb interaction energy decays slowly (r^{-1}) and covers a long range that is often greater than the size of the box (**Figure 2.6**). Similar to the van der Waals interactions, one could employ a simple cut-off to truncate the potential and reduce the computational cost; however this would lead to the exclusion of (likely) significant long-range electrostatic interactions and introduce artefacts into the simulations. More sophisticated methods are therefore required for accurate treatment of the long-range interactions. Several approaches have been developed to treat these forces, including the Ewald summation,[7] the reaction field,[8] or cell multipole methods.[9] In this work, the long-range electrostatic interactions were treated using the Particle-mesh Ewald (PME) summation method,[10] an implementation of the Ewald summation method. In a periodic system, particles interact with all other particles within the simulation box, as well as their images, in an infinite, periodic array. The sum of these contributions gives the total electrostatic energy, but the convergence to a solution is very slow and depends on the order of the summation. The Ewald summation method separates the total summation into a summation in real-space for the short-range interactions, and Fourier space for the long-range interactions.[1] The PME method speeds up the standard Ewald summation method through the use of Fast Fourier Transforms (FFT), whereby the charges are assigned to grid points using interpolation and a FFT algorithm is implemented to yield the reciprocal energy. The total long-range interaction energy is then obtained through inverse Fourier transformation and summation over the grid points. The

computational cost of the PME algorithm increases as $N\log N$ (compared to N^2 for standard Ewald) making it efficient for use in large systems.

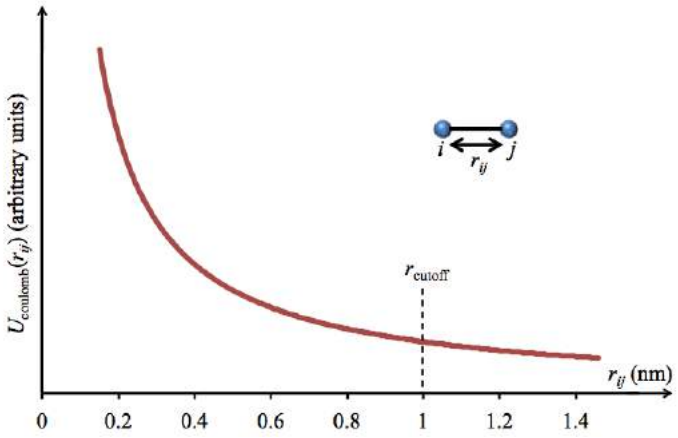

***Figure 2.6**: The Coulomb interaction between two charged particles in a system. The typical cut-off value, r_{cutoff} = 1 nm, has a considerable effect on the long-range interactions highlighting the need for the Ewald summation method.*

2.4 Potential Energy Minimisation

The potential energy of a system varies as a function of geometry to produce the complex, many-dimensional landscape known as the *potential energy surface.*[2] Locations of minimum energy exist on this surface that produce stable states of the system. These points are *local energy minima*, and the lowest point is the *global energy minimum*.

In our study, models of diamond surfaces and biomolecules (dopamine and serotonin) are initially built by arranging the atoms relative to each other based on known chemical structure information (as discussed in detail in Chapter 4). It is then necessary to minimise the potential energy between the atoms in each model in order to ensure the starting geometry of each model is optimal. This will also eliminate initial steric clashes between atoms that can be fatal to the simulation *i.e.* by generating large intermolecular forces that cause the time step integrator to fail. In this situation, the system is referred to as *blowing up*. *Minimisation algorithms* are

employed that move the system 'downhill' on the energy surface to locate the nearest (local) stable energy minimum, as shown in **Figure 2.7**. Methods commonly implemented for potential energy minimisation in molecular modelling are: (1) the steepest descent method[11] and (2) the conjugate gradients algorithm.[12] In this study, all starting systems were energy minimised using the *steepest descent method*, discussed herein.

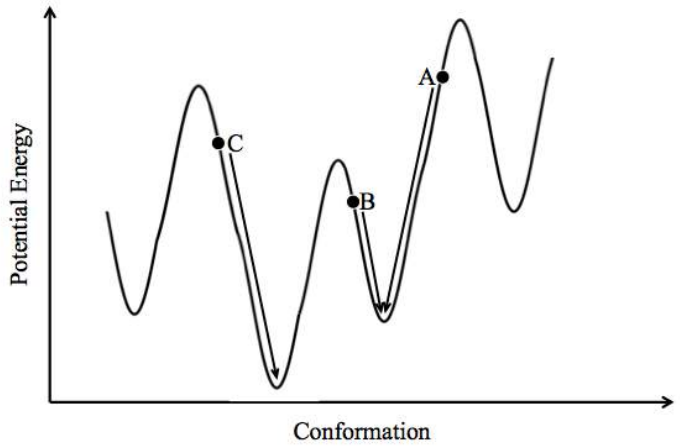

***Figure 2.7**: Illustration of a potential energy surface in one-dimension. Potential energy minimisation algorithms move the system downhill to the nearest local energy minimum from the starting conformation e.g. A, B or C.[2]*

The steepest descent algorithm iteratively adjusts the coordinates of the atoms to gradually move the system down the steepest local energy gradient. This method steps in the direction of the largest negative energy gradient *i.e.* the direction of the greatest force. The algorithm is given by:

$$\mathbf{r}_{n+1} = \mathbf{r}_n + \frac{\mathbf{F}_n}{\max(|\mathbf{F}_n|)} h_n \qquad (2.15)$$

where $\mathbf{r}_n$ and $\mathbf{r}_{n+1}$ are the positions of the atoms at the n^{th} and $n+1^{th}$ iteration steps, $\mathbf{F}_n$ is the forces on the atoms at the n^{th} iteration step (the negative gradient of the potential energy at the n^{th} iteration step, $\mathbf{U}_n$, calculated using the force field), $\max(|\mathbf{F}_n|)$ is the largest absolute value component of $\mathbf{F}_n$ and h_n is the maximum displacement

applied to positions of the atoms. An initial displacement value, h_0, is chosen (*e.g.* 0.01 nm). The potential energy of the atoms is calculated before, $\mathbf{U}_n$, and after, $\mathbf{U}_{n+1}$, each iteration using the force field. If $\mathbf{U}_{n+1} < \mathbf{U}_n$, the new coordinates are accepted and the displacement value is increased (*i.e.* $h_{n+1} = 1.2h_n$), otherwise they are rejected and the displacement value is reduced (*i.e.* $h_{n+1} = 0.2h_n$). The algorithm stops after a pre-defined number of iteration steps, or once max($|\mathbf{F}_n|$) falls below a specified value, so that the system is within close vicinity of a local minimum. In this study, all models were energy minimised using the steepest descent method prior to running the simulations.

2.5 Coarse-Grained Force Fields

Computer simulations are continually balancing the trade-off between accuracy and computational expense. With the computer power of today, all-atom and united-atom force fields can access time and lengths on the nano-scale typically up to 100s of ns and 10s of nm. However, certain biologically relevant events involve a large number of molecules or occur over time scales bordering the limits of atomistic models. For example, events such as protein folding,[13] translocation through proteins *e.g.* DNA in biological nanopore systems,[14] and molecular interactions with lipid bilayers[15] are currently beyond the scope of atomistic simulation. New methodologies are required to enable molecular models to reach the relevant time and length scales of these events in order to complement the experiments.

CG force fields provide a possible route to bridge the gap. In this approach, atoms are grouped together into relevant CG sites or 'beads'. For example, **Figure 2.8** shows how a DPPC phospholipid can be reduced to 12 CG beads. Effective potentials are developed for each of these beads based on thermodynamical information from experiments or appropriate atomistic systems. CG models can significantly reduce the

computational time of a simulation, enabling greater time and length scales to be achieved. CG simulations are faster than their atomistic counterparts for three reasons:[16] (i) the number of interaction sites is reduced and hence fewer force calculations are required at each step; (ii) CG beads have a greater mass which slows down the highest frequency motions in the system and enables the use of a larger time step; and (iii) CG potentials are softer than atomistic potentials, which results in a smoothing of the energy landscape and effectively reduces friction in the system. The CG empirical interaction potentials are combined with molecular mechanics force fields to enable biomolecular simulations. The MARTINI force field,[6] as used in the CG simulations in this study, has been parameterised so that the non-bonded interactions reproduce the partitioning free energies of a range of compounds, and the bonded interactions match to reference all-atom simulations. This force field has proven highly valuable for modelling the self-assembly and interactions of lipid bilayer systems, as relevant to this study.

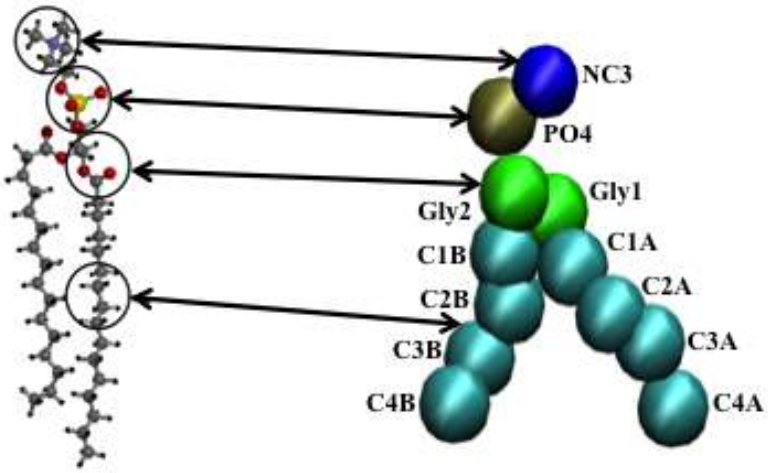

***Figure 2.8**: CG model of a DPPC phospholipid. The atomistic representation (left) is mapped to a CG representation (right).*

2.6 Molecular Dynamics

Molecular dynamics (MD) is a simulation technique that calculates the time-evolution of a system of interacting particles, from which time averages of properties can be determined. This technique produces the 'real' dynamics of an event that is not achievable from other simulation methods *e.g.* Monte Carlo.[2] Furthermore, the method is very similar to a real experiment *i.e.* the system is equilibrated and then run to measure a property over a long enough time period to achieve sufficient accuracy.[1] Alder and Wainwright performed the first MD simulation in 1957 to study the solid-liquid phase transition of a 'hard-sphere' system.[17] MD is a deterministic method, in which the state of the system at any point in time can be determined once the positions and velocities of the atoms are known. Successive configurations of the system are obtained using classical equations of motion that yield a trajectory of the system over time. **Figure 2.9** outlines an algorithm for a standard MD simulation.

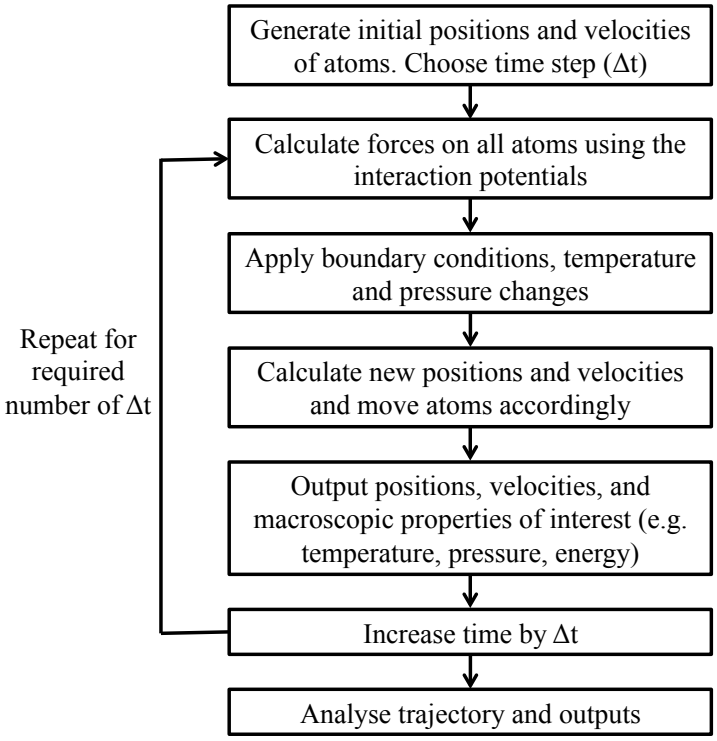

***Figure 2.9**: Algorithm for a standard MD simulation.*

The new positions and velocities of a particle *i* can be obtained by solving Newton's second law of motion:

$$\frac{d^2}{dt^2}\mathbf{r}_i(t) = \frac{d}{dt}\mathbf{v}_i(t) = \mathbf{a}_i(t) = \frac{\mathbf{F}_i(t)}{m_i} \tag{2.16}$$

where $\mathbf{r}_i(t)$ is the position, $\mathbf{v}_i(t)$ is the (constant) velocity, $\mathbf{a}_i(t)$ is the acceleration, m_i is the mass, and $\mathbf{F}_i(t)$ is the force exerted on particle *i* at time *t*. The force on particle *i* is calculated from the derivative of the potential energy, $\mathbf{U}_i$ determined from the sum of the non-bonded and bonded interaction potentials (see section 2.3):

$$\mathbf{F}_i = -\frac{d}{d\mathbf{r}_i}\mathbf{U}_i = m_i\frac{d^2}{dt^2}\mathbf{r}_i(t) = m_i\frac{d}{dt}\mathbf{v}_i(t) \tag{2.17}$$

It is clear from equation 2.17 that the force is coupled to the positions of all atoms in the system, making it impossible to calculate an analytical solution. Instead, the equations are discretised and solved using numerical time integration algorithms. The Verlet (leap-frog) integrator,[18] a modified version of the original Verlet algorithm,[19] was implemented in this study (see section 2.6.1).

2.6.1 Leap-Frog Algorithm

The *leap-frog algorithm* is a time integration method to numerically solve the equations of motion in a MD simulation. This method assumes that the position **r** of particle *i* at times $t + \Delta t$ and $t - \Delta t$ can be approximated by a Taylor expansion:

$$\mathbf{r}_i(t+\Delta t) = \mathbf{r}_i(t) + \Delta t\mathbf{v}_i(t) + \frac{\Delta^2 t}{2}\mathbf{a}_i(t) + \ldots \tag{2.18}$$

$$\mathbf{r}_i(t-\Delta t) = \mathbf{r}_i(t) - \Delta t\mathbf{v}_i(t) + \frac{\Delta^2 t}{2}\mathbf{a}_i(t) - \ldots \tag{2.19}$$

where $\mathbf{v}_i(t)$ and $\mathbf{a}_i(t)$ are the velocity [first derivative of $\mathbf{r}_i(t)$] and acceleration [second derivative of $\mathbf{r}_i(t)$], respectively. Summation of these expressions yields:

$$\mathbf{r}_i(t+\Delta t) = 2\mathbf{r}_i(t) - \mathbf{r}_i(t-\Delta t) + \Delta^2 t\mathbf{a}_i(t) \tag{2.20}$$

The velocity of particle *i* at the half-steps $t+\frac{\Delta t}{2}$ and $t-\frac{\Delta t}{2}$ is given by:

$$\mathbf{v}_i(t+\frac{\Delta t}{2}) = \frac{\mathbf{r}_i(t+\Delta t)-\mathbf{r}_i(t)}{\Delta t} \tag{2.21}$$

$$\mathbf{v}_i(t-\frac{\Delta t}{2}) = \frac{\mathbf{r}_i(t)-\mathbf{r}_i(t-\Delta t)}{\Delta t} \tag{2.22}$$

Rearranging equations 2.18 – 2.22 gives the relations of the leap-frog algorithm:

$$\mathbf{r}_i(t+\Delta t) = \mathbf{r}_i(t)+\Delta t\mathbf{v}_i(t+\frac{\Delta t}{2}) \tag{2.23}$$

$$\mathbf{v}_i(t+\frac{\Delta t}{2}) = \mathbf{v}_i(t-\frac{\Delta t}{2})+\Delta t\mathbf{a}_i(t) \tag{2.24}$$

$$\mathbf{v}_i(t) = \frac{1}{2}\left[\mathbf{v}_i(t+\frac{\Delta t}{2})+\mathbf{v}_i(t-\frac{\Delta t}{2})\right] \tag{2.25}$$

We see from these equations, that the particle velocity at time $t+½\Delta t$ can be calculated based on the velocity at time $t-½\Delta t$ and the acceleration at time t (equation 2.24). Then the particle position at time $t+\Delta t$ can be calculated using the position at time t and the calculated velocity at $t+½\Delta t$ (equation 2.23). Hence the velocities 'leap-frog' over the positions, as illustrated in **Figure 2.10**. The velocity at time t can subsequently be calculated based on the velocities at $t+½\Delta t$ and $t-½\Delta t$ (equation 2.25).

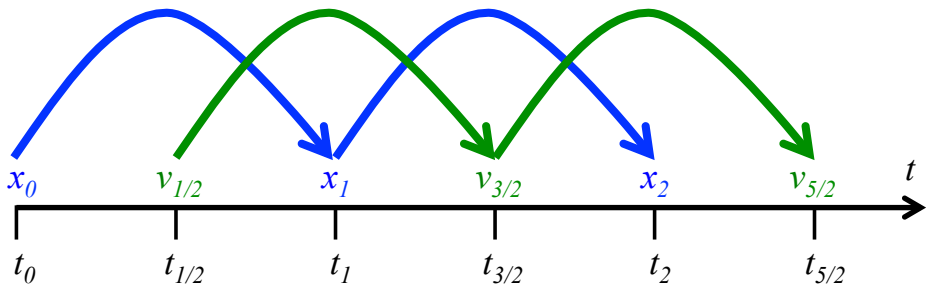

***Figure 2.10**: Schematic of the leap-frog integration method for calculating positions and velocities during a MD simulation with time step ½.*

Use of an appropriate time step is very important in MD simulations. If the time step is too small, not enough phase space will be sampled and the simulation would require high computational expense, but if it is too large the system will become unstable due to instabilities in the integration algorithm and eventually 'blow up'. The time step in an MD simulation must not be larger than the shortest period of motion in the system.[20] The fastest motion is typically the vibrations of bonds involving hydrogen with a ~ 2 fs oscillation period.[21] Constraints are often placed on bonds to eliminate vibrations that may be restricting the size of the time step (see section 2.6.4), in which case the shortest period of motion becomes the angle bending.

2.6.2 Ensembles

MD simulations were traditionally performed in the microcanonical (*NVE*) ensemble (*i.e.* constant number of particles *N*, volume *V* and total energy *E*). To match more closely to experimental conditions, it is more appropriate to maintain a constant temperature, *T*, and/or pressure, *P*, in the simulation. The canonical (*NVT*) and isothermal-isobaric (*NPT*) ensembles are commonly used for this purpose. The temperature of a system in the microcanonical ensemble is calculated by the average kinetic energy. However, in the canonical ensemble, the instantaneous kinetic energy per particle fluctuates within a system.[1] Whilst fixing the kinetic energy to the average would produce a constant temperature, it would also eliminate the variance and the true ensemble would not be simulated. To run MD simulations in the *NVT* and *NPT* ensembles, a *thermostat* or *barostat* is required to correctly maintain the constant temperature or pressure of the system.

2.6.2.1 Thermostats

Several thermostats exist that maintain the system temperature during a simulation that samples from a constant-temperature (*i.e. NVT*) ensemble. The most popular thermostats used in MD are the Nosé-Hoover[22] and Berendsen.[23] In this study, the Berendsen thermostat was implemented. The Berendsen thermostat works by rescaling the particle velocities at each time step, Δt :[20]

$$\mathbf{v}_i^{new}(t) = \lambda \mathbf{v}_i(t) \tag{2.26}$$

where the velocity rescaling factor, λ, is given by:

$$\lambda = \sqrt{1 + \frac{\Delta t}{\tau_T}\left(\frac{T_0}{T(t)} - 1\right)} \tag{2.27}$$

This ensures that the kinetic energy at each time step is scaled to produce the target temperature, T_0. The system is weakly-coupled to a 'heat bath' with coupling constant, τ_T, which describes the strength of the coupling of the system to the bath *i.e.* the larger the value of τ_T, the longer the system will take to adjust to T_0 from the instantaneous value $T(t)$:

$$\frac{dT(t)}{dt} = \frac{T_0 - T(t)}{\tau_T} \tag{2.28}$$

The advantage of the Berendsen thermostat is that it is relatively simple to implement and the strength of the coupling, *i.e.* the value of τ_T, can be easily adjusted to suit the requirement of the study, which is advantageous during system equilibration when large fluctuations are sometimes observed. Furthermore, the addition/removal of energy reduces energy drift caused by the accumulation of errors in the integration algorithm. However, the Berendsen method suppresses the fluctuations in the kinetic energy, which means the system never generates the true canonical ensemble. As the error scales by a factor $1/N$, the error in the ensemble averages will be small for large systems. However, the distribution of the kinetic energy will still be affected. This

means that any properties calculated from the fluctuation of the kinetic energy, *e.g.* the heat capacity, will not be correct. In this study, there is no interest in properties derived from the kinetic energy so the Berendsen thermostat is sufficient.

2.6.2.2 Barostats

Several barostats exist that maintain the system pressure during a simulation that samples from a constant-pressure (*i.e. NPT*) ensemble. These include: the Berendsen[23] and Parrinello-Rahman[24] barostats. Analogous to the Berendsen thermostat, the Berendsen barostat works by rescaling the volume of the box, **V**, at each time step, Δt :[20]

$$\mathbf{V}^{new}(t) = \eta^{\frac{1}{3}}\mathbf{V}(t) \tag{2.29}$$

where the volume rescaling factor, η, is given by:

$$\eta(t) = 1 - \frac{\Delta t}{\tau_P}\gamma(P_0 - P(t)) \tag{2.30}$$

Here, γ is the isothermal compressibility of the system. The box dimensions, box centre-of-mass, and coordinates of the particles are scaled at each time step by $\eta^{1/3}$ in each *x-, y-, z-* dimension to produce the target pressure, P_0. Similar to the Berendsen thermostat, the system is weakly-coupled to a 'pressure bath' with coupling constant, τ_P, which describes the strength of the coupling of the system to the bath *i.e.* the larger the value of τ_P, the longer the system will take to adjust to P_0 from the instantaneous value $P(t)$:

$$\frac{dP(t)}{dt} = \frac{P_0 - P(t)}{\tau_P} \tag{2.31}$$

Similar to the Berendsen thermostat, the Berendsen barostat is simple to use and enables adjustments in τ_P to cope with large fluctuations in pressure during equilibration. Whilst producing the correct average pressure, it does not generate the

exact *NPT* ensemble although it remains unclear what errors this may yield. When implemented together, the Berendsen thermostat and barostat display realistic fluctuations in the temperature and pressure of the system.[23]

In this study, the NAP_zT ensemble was utilised instead of the *NPT* ensemble, *i.e.* constant number of particles N, cross-sectional area A, perpendicular pressure P_z and temperature T. This enabled the area of the diamond surface to be fixed to its optimum (lowest energy structure) value while still allowing the density of the fluid phase to adjust to maintain a normal pressure of 1 bar.

2.6.3 Periodic Boundary Conditions

The aim of a molecular simulation is to provide information about the macroscopic properties of a system. In order to do so, the system size needs to be considerably large (in the order of Avogadro's constant ~10^{23}) which is challenging to simulate. *Periodic boundary conditions (PBC)* provide a solution to this problem. The simulation cell is replicated in all directions to form an infinite periodic lattice of identical cells, as illustrated in **Figure 2.11**. A given particle in the unit cell will now interact with all particles in both the primitive cell and the surrounding image cells (including its own image). Furthermore, any particle that leaves the simulation cell will be replaced by its periodic image from the opposite side. Short-range non-bonded interactions (provided the potential range is not too long) will now adopt a *minimum image convention*, where each atom interacts with any neighbouring atom or image in the periodic lattice within the interaction cut-off (see sections 2.3.4 and 2.3.5) specified by the force field. Long-range non-bonded interactions are treated by the PME summation method (see section 2.3.5). Importantly, the unit cell must be large enough to accommodate the cut-off to prevent an atom from interacting with itself.

By making the system essentially infinitely large, PBC removes any effects due to the boundaries to enable sampling of bulk macroscopic properties.

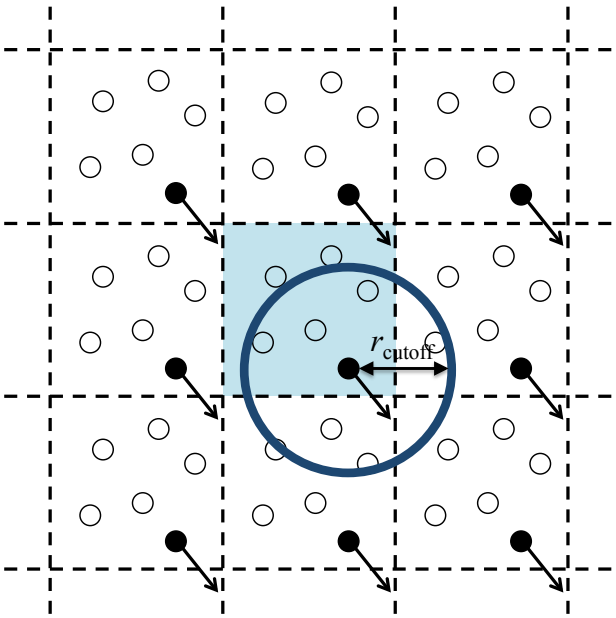

Figure 2.11*: Schematic representation of the periodic boundary condition in two–dimensions. The simulation cell (blue) is replicated in all directions to form an infinite periodic lattice. The particle experiences short-range interactions with all particles within the spherical region of radius* r_{cutoff}.

2.6.4 Constraints and Restraints

The highest frequency motions (typically the bond vibrations) in a system place an upper limit on the size of the time step. It is therefore beneficial to 'freeze out' the higher frequency motions that have negligible effect on the system. This would enable the time step to be increased without compromising on accuracy. *Constraints* are a method to fix the length of the bond (or angle) to a set value during a simulation. Constraints are applied using either the Linear Constraint Solver (LINCS)[25] or SHAKE[26] methodologies. Constraint algorithms apply corrections to reset the bonds back to their equilibrium lengths after each integration step. In this study, all bonds to hydrogens were constrained using the LINCS algorithm.

It is worth noting that constraints are different from *restraints*. In this study, harmonic position restraints were placed on molecules during equilibration to prevent deviation from the starting positions. Unlike constraints, restrained molecules are still able to move, but the deviation carries a large energy penalty:

$$U_{pr}(\mathbf{r}_i) = \frac{k_{pr}}{2}\left|\mathbf{r}_i - \mathbf{r}_0\right|^2 \tag{2.32}$$

where $U_{pr}(\mathbf{r}_i)$ is the energy penalty impeded by particle i for moving to position $\mathbf{r}_i$ from the reference position $\mathbf{r}_0$.

2.6.5 Potential of Mean Force (PMF)

Potential of mean force (PMF) calculates the change in free energy as a function of a chosen reaction coordinate connecting two groups of interest. In this study, free energy profiles for the adsorption of dopamine and serotonin to diamond surfaces are obtained using this technique (Chapter 5). The distance along the *z*-direction between the diamond surface and the centre of mass of the species was chosen as a suitable reaction coordinate. The PMF profile along the path *z'* can be calculated using:[27]

$$\Delta G(z) = \int_o^z \left\langle F(z') \right\rangle \, dz' \tag{2.33}$$

where $\Delta G(z)$ is the free energy change from $z' = 0$ to $z' = z$, and $\langle F(z') \rangle$ is the average force to constrain the species at z'.

A set of starting configurations along the reaction coordinate can be generated using steered MD or a normal MD simulation. In this study, *steered MD* was implemented. Steered MD applies an external force to the adsorbate to 'pull' it along the reaction coordinate towards the reference group (in this study, the diamond surface). Whilst these configurations could be generated by running an unconstrained MD simulation for long enough that the species will explore positions along the

chosen reaction coordinate on its own accord, this method accelerates the process and helps to overcome any energy barriers that might otherwise impede the path of the molecule.

A collection of starting configurations at varying adsorbate-surface separations along the reaction coordinate, in our case the *z*-direction, are chosen and the distance between the centres of mass of the two groups is constrained. Simulations are run allowing the adsorbate to adequately sample all possible configurations in phase space at each fixed separation, whilst outputting the constraint force at each time step. The average constraint force can then be calculated at each position, and cumulative integration of the average constraint forces along the reaction coordinate produces the free energy profile of adsorption (using equation 2.33), as illustrated in **Figure 2.12**. The method is suitable for this study, as dopamine and serotonin are small molecules with only a few internal degrees of freedom, so the mean force is a reasonably accurate description of the interaction with respect to the reaction coordinate.

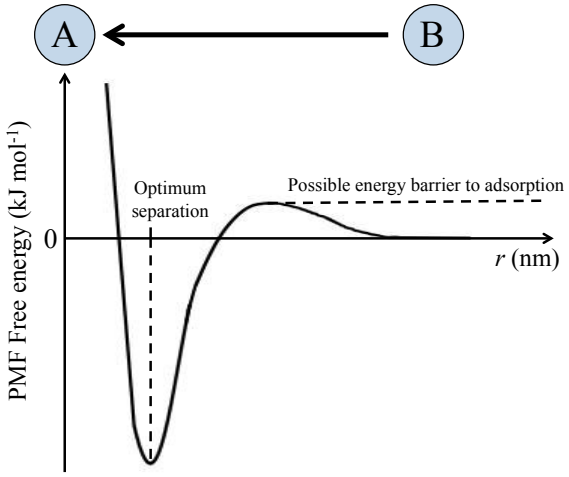

***Figure 2.12**: Schematic of a PMF free energy profile for the adsorption of species B to species A.*

2.7 References

[1] D. Frenkel, B. Smit, *Understanding Molecular Simulation: From Algorithms to Applications, Vol. 1*, Academic Press, **2001**.

[2] A. R. Leach, *Molecular Modelling: Principles and Applications*, Pearson Education, **2001**.

[3] M. P. Allen, D. J. Tildesley, *Computer Simulation of Liquids*, Oxford University Press, **1989**.

[4] J. W. Ponder, D. A. Case, *Adv. Protein Chem.* **2003**, *66*, 27-85.

[5] C. Oostenbrink, A. Villa, A. E. Mark, W. F. Van Gunsteren, *J. Comput. Chem.* **2004**, *25*, 1656-1676.

[6] S. J. Marrink, H. J. Risselada, S. Yefimov, D. P. Tieleman, A. H. De Vries, *J. Phys. Chem. B* **2007**, *111*, 7812-7824.

[7] P. P. Ewald, *Ann. Phys.* **1921**, *64*, 253-371.

[8] I. G. Tironi, R. Sperb, P. E. Smith, W. F. van Gunsteren, *J. Chem. Phys.* **1995**, *102*, 5451-5459.

[9] H. Q. Ding, N. Karasawa, W. A. Goddard III, *J. Chem. Phys.* **1992**, *97*, 4309-4315.

[10] U. Essmann, L. Perera, M. L. Berkowitz, T. Darden, H. Lee, L. G. Pedersen, *J. Chem. Phys.* **1995**, *103*, 8577-8593.

[11] J. Snyman, *Practical Mathematical Optimization: An Introduction to Basic Optimization Theory and Classical and New Gradient-based Algorithms, Vol. 97*, Springer Science & Business Media, **2005**.

[12] M. R. Hestenes, E. Stiefel, *J. Res. Nat. Bur. Stan.* **1952**, *49*, 409-436.

[13] M. Levitt, A. Warshel, *Nature* **1975**, *253*, 694-698.

[14] A. T. Guy, T. J. Piggot, S. Khalid, *Biophys. J.* **2012**, *103*, 1028-1036.

[15] P. J. Bond, J. Holyoake, A. Ivetac, S. Khalid, M. S. Sansom, *J. Struct. Biol.* **2007**, *157*, 593-605.

[16] S. Takada, *Curr. Opin. Struct. Biol.* **2012**, *22*, 130-137.

[17] B. Alder, T. Wainwright, *J. Chem. Phys.* **1957**, *27*, 1208.

[18] W. Van Gunsteren, H. Berendsen, *Mol. Simul.* **1988**, *1*, 173-185.

[19] L. Verlet, *Phys. Rev.* **1968**, *165*, 201.

[20] D. van der Spoel, E. Lindahl, B. Hess, A. Van Buuren, E. Apol, P. Meulenhoff, D. Tieleman, A. Sijbers, K. Feenstra, R. van Drunen, *GROMACS user manual version 3.3*, **2008**.

[21] S. P. Hau-Riege, *High-Intensity X-rays-Interaction with Matter: Processes in Plasmas, Clusters, Molecules and Solids*, John Wiley & Sons, **2012**.

[22] G. J. Martyna, M. L. Klein, M. Tuckerman, *J. Chem. Phys.* **1992**, *97*, 2635-2643.

[23] H. J. Berendsen, J. P. M. Postma, W. F. van Gunsteren, A. DiNola, J. Haak, *J. Chem. Phys.* **1984**, *81*, 3684-3690.

[24] M. Parrinello, A. Rahman, *J. Appl. Phys.* **1981**, *52*, 7182-7190.

[25] B. Hess, H. Bekker, H. J. Berendsen, J. G. Fraaije, *J. Comput. Chem.* **1997**, *18*, 1463-1472.

[26] J.-P. Ryckaert, G. Ciccotti, H. J. Berendsen, *J. Comput. Phys.* **1977**, *23*, 327-341.

[27] D. Trzesniak, A. P. E. Kunz, W. F. van Gunsteren, *Chem. Phys. Chem.* **2007**, *8*, 162-169.

Chapter 3

Experimental Methodology

In the following sections, the experimental techniques used in this study are presented: sections 3.1 – 3.7 outline key concepts of electrochemistry; section 3.8 introduces the techniques used in this study for electrochemical experiments; section 3.9 summaries the materials and chemicals of this study; section 3.10 outlines methods for diamond surface preparation; section 3.11 introduces diamond characterisation techniques; and section 3.12 explains the experimental instrumentation used in this study. Detailed methodology sections with the specific instrumentation and parameters can be found in Chapters 6 and 7, respectively.

3.1 Introduction to Electrochemistry

Electrochemistry is a tool for the study of charge transfer processes at an interface *i.e.* between a conductive material (the *electrode*) and a conductive ionic solution (the *electrolyte*).[1] In general, electrochemistry can either be performed under equilibrium conditions *i.e.* to measure thermodynamic properties of the system, or non-equilibrium conditions *i.e.* to measure dynamic processes by applying a current or potential to the system to drive chemical reactions at the interface. The latter is referred to as *dynamic electrochemistry* and is ideally suited for biosensing, as the species can be detected and quantified from the oxidation or reduction reactions that occur at the electrode interface under non-equilibrium conditions.

Two types of process occur at electrodes: *faradaic* and *non-faradaic*.[2] Non-faradaic current is typically due to the capacitance at the electrode interface (as discussed in section 3.4). Faradaic current is due to charge transfer reactions at the electrode. This is the current of interest in an electrochemical study.

3.2 Dynamic Electrochemistry

Let us consider a species with an oxidised form O and reduced form R. The electrode reaction is given by:[1]

$$O + ne^- \underset{k_{ox}}{\overset{k_{red}}{\rightleftarrows}} R \tag{3.1}$$

where n is the number of electrons transferred in the reaction, and k_{red} and k_{ox} are the rate constants of the oxidative and reductive reactions, respectively. The oxidation/reduction reaction at the electrode can be broken into a sequence of steps (**Figure 3.1**). These include: (1) mass transport of the reactant from bulk to the interface, (2) chemical reactions for the formation of necessary precursor complexes, (3) surface reactions *e.g.* adsorption, rearrangement of interfacial solvent and ion molecules, structural changes of the solvated complex, or reorganisation of the electronic structure into a transition state, and (4) electron transfer (ET). A similar process occurs in reverse as the reduced/oxidised product moves from the surface back into bulk solution (**Figure 3.1**). The overall rate of the reaction is governed by the rate of each of these steps, and is consequently limited by the slowest step in the process. In this study, the adsorption step for biomolecules (dopamine and serotonin) is investigated using molecular simulations (Chapter 5).

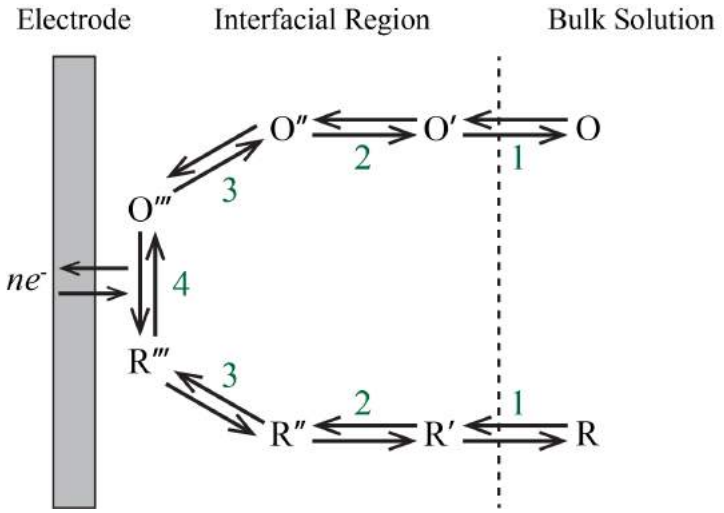

***Figure 3.1**: Schematic of the steps that constitute an electrode reaction: (1) mass transport, (2) chemical reactions, (3) adsorption and surface reactions, (4) ET.*[1]

Due to the difficulty of isolating the individual steps in an experiment, the observed rate of ET, k^0, typically represents the ET and all interfacial steps prior to ET. The overall reaction rate is limited by either the rate of ET at the electrode, (*kinetically limited*), or the rate of mass transport, (*mass transport limited*).[2] Molecular modelling can be used to investigate the adsorption and structural changes within the interfacial region to probe individual steps that cannot be accessed experimentally.

Applying an external potential to the electrode can drive non-spontaneous reactions at the surface.[3] A negative (positive) potential will increase (decrease) the electron energy. By driving the electrode to sufficiently negative potentials, the energy of the electrons will be high enough to transfer from the electrode to unoccupied energy states in the species inducing a *reduction current*. Similarly, by driving the electrode to sufficiently positive potentials the energy of the electrons will be low enough that electrons can transfer from the species to unoccupied energy states in the electrode causing an *oxidation current*. The standard reduction (oxidation) potential, E^0, of a redox species relates to the equilibrium, thermodynamic potential.[3]

By convention, E^0 is measured with respect to the standard hydrogen electrode (SHE) (of arbitrary potential 0 V) under standard thermodynamic conditions (298 K, 1 atm, unit activity). This enables effective comparison of the reducing (oxidising) ability of different redox species.[4]

3.3 Electron Transfer Kinetics

As mentioned in section 3.2, systems in dynamic electrochemistry are studied under non-equilibrium conditions. However, in mass transport limited systems *i.e.* when the ET kinetics are fast compared to the mass transport, the reactions can be regarded as being at equilibrium and the system is said to exhibit *reversible* or *Nernstian* behaviour.[1] In this case, the cell potential at the equilibrium, E_e, can be related to E^0 using the *Nernst equation*:

$$E_e = E^0 + \frac{RT}{nF} \ln \frac{a_O}{a_R} \tag{3.2}$$

where R is the molar gas constant, T is temperature, F is the Faraday constant and a_i is the activity of species i, where activity is the effective concentration of a species under non-ideal conditions.[1] In cyclic voltammetry (CV) experiments, a reversible n-electron transfer diffusion-limited reaction has a peak to peak separation of 59 mV / n, arising from consideration of the Nernst equation (see section 3.8.3).[5]

3.4 The Electrical Double Layer

The *electrical double layer* describes the layering of ions and molecules at the electrode-electrolyte interface, as shown in **Figure 3.2**.[6] The double layer consists of alternating layers of charge initiated by the electrostatic attraction between the charged electrode and oppositely charged ions in the solution. A layer of solvent molecules (and some ions) specifically adsorb to the electrode surface *i.e.* come into direct contact with the surface. The region extending from the surface to the centre of

the adsorbed ions is defined as the *inner Helmholtz plane* (IHP) (**Figure 3.2**). Solvated ions cannot penetrate the IHP. Hence, the centre of solvated ions at the distance of closest approach is defined as the boundary of the *outer Helmholtz plane* (OHP) (**Figure 3.2**). The ion structuring becomes more diffuse as a function of distance (*diffuse layer*) until it reaches bulk. The thickness of the double layer is dependent on the concentration and charge of ions in the solution (Debye length).[6] For high electrolyte concentrations (*i.e.* ≥ 0.1 M), the double layer is typically reduced to ≤ 1 nm in thickness with the OHP at ~ 10 – 20 Å dependent on the size of the solvated ions.

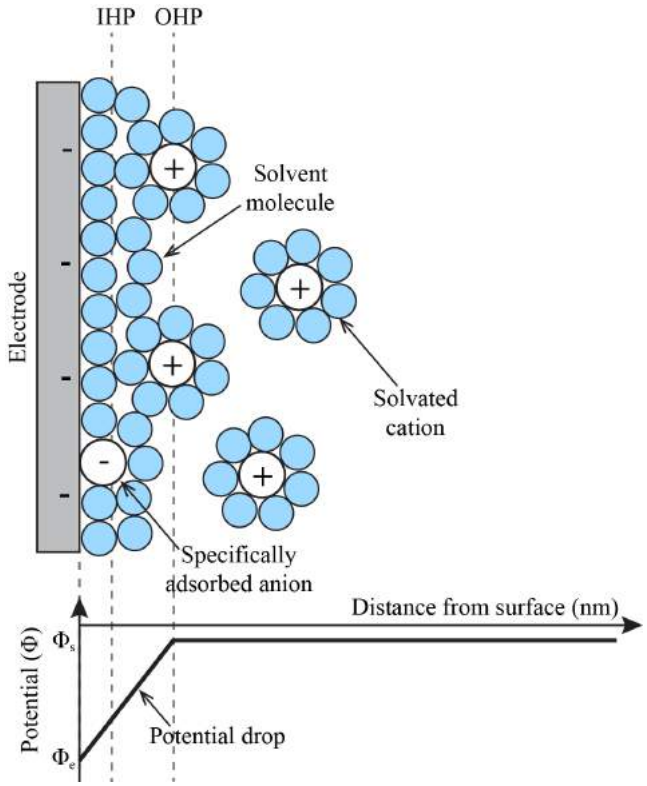

***Figure 3.2**: Proposed Helmholtz model of the electrical double layer. Solvated cations can only approach as close as the OHP and cannot penetrate the IHP. The charge layers cause the applied potential to drop close to the surface.*[1]

Importantly, when a potential is applied to the system, the double layer acts like a parallel-plate capacitor *i.e.* the separation of charge between the electrode

surface and the OHP causes a linear potential drop near the surface (**Figure 3.2**).[7] The *double layer capacitance,* C_d, can cause significant background currents during an electrochemical experiment. BDD exhibits the lowest C_d ($\leq$ 10 μF cm^{-2}) compared to other conventional electrode materials *e.g.* Pt and Au (~ 30 μF cm^{-2}) due its lower density of states and chemical inertness.[8] This makes it ideally suited for sensitive species detection in biosensor applications.

3.5 Inner *vs.* Outer Sphere Species

ET reactions can proceed by either an *inner-sphere* or *outer-sphere* process.[9] In an outer-sphere reaction, the species remain separate from the electrode throughout the entire ET process.[10] The species will only approach as close as the OHP (**Figure 3.3**) so that the electrons can tunnel through the space between the species and electrode (**Figure 3.3**a). In an inner-sphere reaction, the reactant, intermediate and/or product will bond directly with the electrode surface either by specific adsorption (**Figure 3.3**b) or formation of a ligand bridge between the surface and species.[10] Inner-sphere species are highly surface sensitive requiring strong interactions of the reactant, intermediates or product with the surface.[1] Hence, different surface groups can enhance or inhibit the ET reactions by influencing one or several of the interfacial electrode processes outlined in section 3.2.[11] Probing the influence of different diamond surface terminations on the adsorption mechanism (using molecular modelling) and the overall ET kinetics (using electrochemistry) for a range of inner-sphere species is a key aim of this study (see Chapter 1, section 1.4).

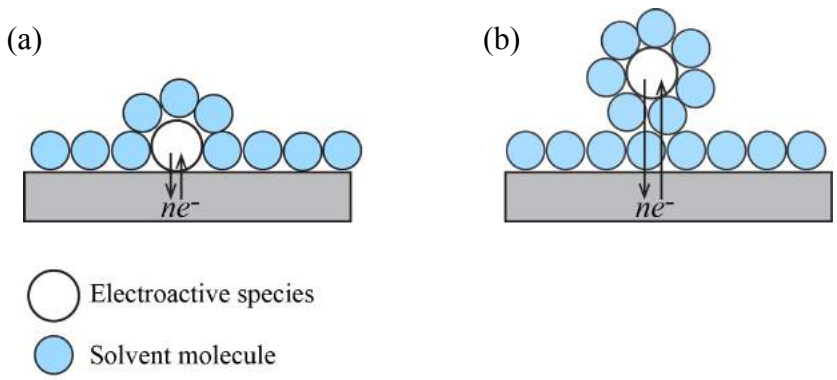

***Figure 3.3**: Schematic of (a) inner-sphere and (b) outer-sphere ET reactions.*

3.6 Mass Transport

Three different processes govern the mass transport of species from the bulk to the interface: (1) diffusion, (2) migration, and (3) convection. Diffusion is the most influential for electrochemical experiments, as migration and convection can be minimised in the experimental setup, as discussed in the sections below.

3.6.1 Diffusion

Diffusion is the movement of species down a concentration gradient.[1] In one-dimension, diffusion is described by Fick's first law:

$$j_{\mathrm{O}}(x,t) = -D_{\mathrm{O}} \frac{\partial c_{\mathrm{O}}(x,t)}{\partial x} \tag{3.3}$$

where j_{O} is the diffusional flux, D_{O} is the diffusion coefficient, and $\partial c_{\mathrm{O}} / \partial x$ is the concentration gradient at position x and time t for species O. In this study, equation (3.3) is used to describe the diffusive flux of ions through a model diamond pore (see Chapter 7).

The diffusion profile of a species at an electrode surface is dependent on the electrode size.[10] At a macroelectrode surface (of ~ mm dimensions), linear diffusion will dominate with negligible radial diffusion contributions at the sides (**Figure 3.4**a). This creates a planar diffusion profile, which generates a peak response in the current-

voltage trace. As the size of the electrode decreases, the radial diffusion contribution will become more significant creating a larger diffusion layer so that the system eventually changes from being diffusion to kinetically limited (**Figure 3.4**).[1]

For this study (Chapter 6), it is relevant to examine the diffusion profile of a ~ 50 μm electrode region accessed using a microcapillary (**Figure 3.4**b). The microcapillary forces planar diffusion to dominate within the meniscus, although there will be a greater contribution by radial diffusion than observed at macroelectrodes due to the wetting.

For a UME (of ~ 20 μm diameter), both radial and linear contributions exist that create a hemispherical diffusion profile (**Figure 3.4**c). In this case, there is greater flux to the surface that enables the system to reach steady state current-voltage behaviour after a sufficient time period.[1]

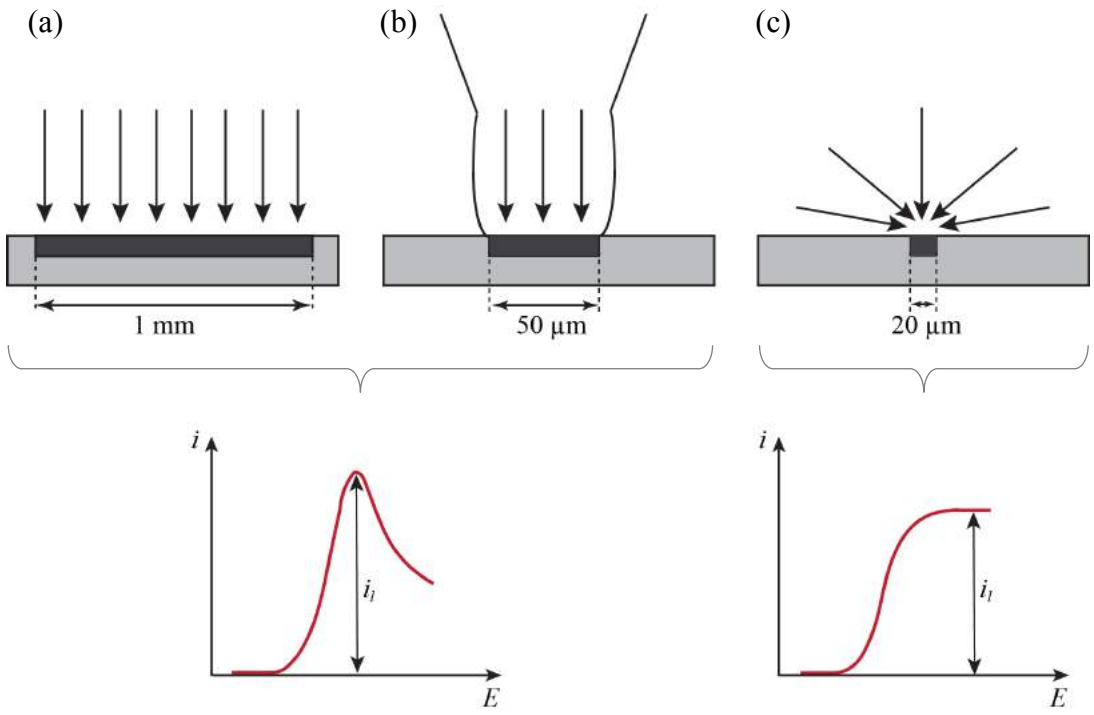

***Figure 3.4**: Diffusion profiles at different sized electrodes: (a) macroelectrode, (b) electrode constrained by a microcapillary, and (c) UME and their corresponding current-voltage responses both displaying limiting current, i_l, responses.*

The flux, j, of species to a surface a reaction is related to the faradaic current produced at the electrode by:[1]

$$i = nAFj \tag{3.4}$$

where A is the area of the electrode. Under kinetic conditions, j is directly proportional to k^0, and proportional to k^t when mass transport limits the reaction. It follows from equation (3.4) that k^t, is inversely proportional to the electrode area:[1]

$$k^t = \frac{i_l}{nAFc^*} \tag{3.5}$$

where c^* is the bulk concentration of species and i_l is the limiting current shown in **Figure 3.4**. Then, for the three different sized electrodes discussed, it is clear that:

$$k^t_{macro} < k^t_{microcapillary} < k^t_{UME} \tag{3.6}$$

where k^t_{macro}, $k^t_{microcapillary}$, and k^t_{UME} are the mass transport rate constants for a macroelectrode, microcapillary setup, and UME, respectively. Furthermore, if $k^0 > k^t$ in any of these systems, the system is reversible (mass transport controlled) and if $k^0 < k^t$ then it is non-reversible (kinetically limited).[6] The different rates of mass transport are particularly important for this study as we compare macroelectrode and microcapillary systems (Chapter 6).

3.6.2 Migration

Migration is the movement of charged species due a potential gradient. As the forces due to migration are electrostatic, migration can be eliminated by addition of an inert electrolyte solution that can carry the charge instead of the electroactive species.[1] Electrochemical experiments are therefore performed using excess supporting electrolyte in the solution *i.e.* at least 100 times larger than the concentration of the redox species.[6] The high electrolyte concentration also reduces the thickness of the double layer region, which confines the potential drop at the

interface to a small (< 1 nm) region close to the surface (see section 3.4). This enhances ET processes, as the species will experience the entirety of the applied potential at a closer approach to the electrode.

3.6.3 Convection

Convection is the movement of species by mechanical forces.[1] *Forced convection* is generated by external means *i.e.* stirring or heating can increase the mass transport of the system. *Natural convection* occurs when fluid motion is driven by density differences in the system due to temperature gradients. Convection is considered negligible in our study as all electrochemical experiments were performed under stable conditions and at short timescales in which temperature fluctuations were negligible.

3.7 Electrochemical Setup: Working, Reference, Counter Electrodes

A *two-electrode* electrochemical cell consists of three main components: a working electrode, a reference/counter electrode, and an electrolyte solution (**Figure 3.5**a).[12] The *working electrode* is the electrode at which the reaction of interest occurs. If the working electrode is solely used as a source or sink of electrons (as opposed to corrosion/film formation studies), the electrode material is required to be an inert conductor that does not exhibit competing side reactions (*e.g.* oxygen/hydrogen evolution) within the potential window of interest for the chosen electrolyte. Platinum, gold, mercury and carbon-based materials (glassy carbon, graphite, conducting diamond) are commonly employed for this purpose.[12] Conducting diamond is used as the focus of this study.

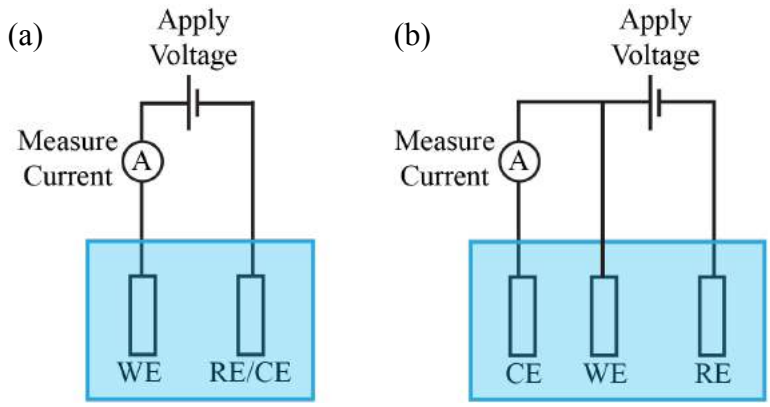

***Figure 3.5**: Electrochemical cell setups: (a) Two-electrode and (b) Three-electrode. Working (WE), reference (RE) and counter (CE) electrodes are immersed in an inert electrolyte solution.*

It is not possible to apply a potential to a single interface. Instead, a *potential difference* must be applied across two interfaces.[1] Typically, the potential at the working electrode is applied with respect to a *reference*. A reference electrode has a stable and well-known potential so any changes in the cell can be directly ascribed to processes at the working electrode. In this study, a silver-silver chloride (Ag/AgCl) electrode was used. Commercial Ag/AgCl electrodes maintain a constant potential due to the constant activity (concentration) of chloride ions present in the reference electrode set-up.[3] In this study, electrodeposited AgCl on a Ag wire was used. This functions as a quasi-reference electrode (QRE) as the local chloride activity depends on dissolution of the AgCl layer into the measurement solution. Failure to maintain a constant chloride concentration around the electrode results in potential drift, hence the QRE wire was always maintained in a chloride rich electrolyte in our experiments.

For larger currents where the ohmic drop could be problematic *i.e.* for ohmic losses > 1 mV, a *three-electrode* setup is required.[2] In this case a third electrode, the counter, must be added (**Figure 3.5**b). In this setup, the potential difference at the working electrode is applied with respect to the reference electrode, whilst current flows between the working and counter electrodes to balance the charge.[6] This

prevents large currents passing through the reference electrode that may generate significantly large ohmic drops in the cell, and may alter the electrode composition thus changing the reference potential. In this study, a commercial frit-based Ag/AgCl reference electrode with known and constant chloride activity was used with $E^{0'}$ = +0.22 V *vs.* SHE.[1] The counter electrode is typically required to be an inert metal with a large surface area to ensure the opposing reaction occurs sufficiently fast so that it does not limit the working electrode. A platinum gauze electrode is employed as the counter for all three-electrode experiments in this study.

In both the two and three electrode setups, the electrodes are immersed in a conducting electrolyte solution that has several functions mentioned throughout this chapter such as facilitating the flow of charge (3.2), reducing the size of the double layer (section 3.4), and mitigating migration (section 3.6.2).

3.8 Electrochemical Techniques

3.8.1 Solvent Windows

The solvent window describes the potential range in which no background processes occur (*e.g.* the potential range before water electrolysis occurs in the aqueous electrolytes used in this study). Solvent windows are run in the electrolyte solution of interest in absence of a redox mediator. Discussion on conducting diamond solvent windows can be found in Chapter 6.

3.8.2 Current-Time Traces

When a fixed potential is applied between a working and reference electrode, the resulting ionic conductance of the electrolyte solution can be monitored over time as an *i-t* trace.[10] This is useful to investigate the change in current through a pore due

to blockade events (see Chapter 1, Figure 1.10) and is employed in this study to investigate blockade events of diamond pores by polystyrene particles (Chapter 7).

3.8.3 Cyclic Voltammetry

Voltammetry is a technique in which the potential is varied linearly with time and the resulting current is measured directly to produce an *i-E* trace.[10] In *linear voltammetry*, the potential is swept from E_1 to E_2. In *cyclic voltammetry*, after reaching E_2 the potential sweep direction is reversed to return back to the initial potential E_1 (**Figure 3.6**a). The set period of time for each potential sweep is determined by the chosen *scan rate, v*. A typical cyclic voltammogram (CV) trace is shown in **Figure 3.6**b. The *i-E* trace displays CV peaks for a diffusion-controlled reaction. As the potential is swept from E_1 to E_2, an oxidation reaction occurs that causes an increase in the faradaic current and the diffusion layer begins to grow. Eventually, the diffusion layer has grown sufficiently large that the flux to the electrode is too slow to satisfy the fast ET kinetics at the surface. This causes a anodic limiting peak current, i_{pa}, at a potential, E_{pa}, before the current drops towards an equilibrium value. The same trend occurs as the potential is reversed from E_2 back to E_1 *i.e.* a reduction reaction occurs that produces a cathodic limiting peak current, i_{pc}, at a potential, E_{pc}, due to diffusion limited conditions.

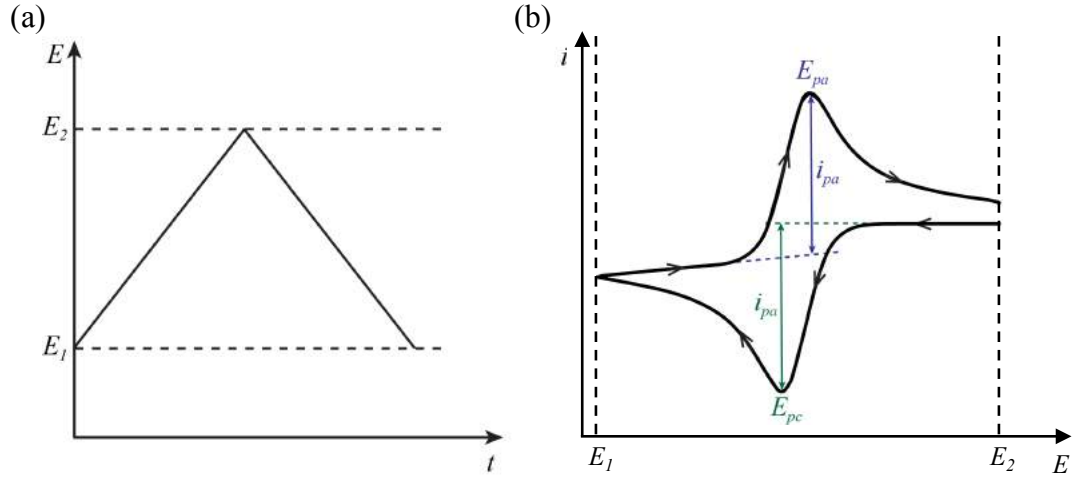

***Figure 3.6**: (a) E-t and (b) i-E traces during a cyclic voltammogram experiment. As E is swept over time from E_1 to E_2, an oxidation reaction occurs that generates i. i increases as a function of E until reaching an anodic limiting current, i_{pa}, at potential, E_{pa}, where the flux to the electrode limits the rate of the reaction. The same mechanism occurs in the reverse, when sweeping E from E_2 back to E_1, causing a reduction reaction with a cathodic limiting current, i_{pc}, at potential E_{pc}.*

The peak-to-peak separation, ΔE_p, of a CV is given by:

$$\Delta E_p = \left| E_{pc} - E_{pa} \right| \tag{3.7}$$

For a reversible one-electron transfer diffusion-limited reaction, this should have a value of 59 mV at 298 K as predicted by the Nernst equation (section 3.3, equation 3.2). The i_p can be related to the v using the Randles-Sevcik equation:[1, 13]

$$i_p = (2.69 \times 10^5) n^{3/2} A D^{1/2} c^* v^{1/2} \tag{3.8}$$

Substituting equation (3.8) into equation (3.5) enables the mass transport rate constant for a diffusion-limited CV to be calculated as:

$$k^t = \frac{(2.69 \times 10^5) n^{1/2} A D^{1/2} v^{1/2}}{F} \tag{3.9}$$

3.9 Materials and Chemicals

3.9.1 Diamond Samples

The diamond samples used in Chapters 6 and 7 of this work were grown and prepared by Element Six Ltd., Ascot, UK using either a commercial microwave plasma CVD process or the HPHT method (Chapter 1, section 1.2.1). The material properties are outlined in **Table 3.1**.

Table 3.1: *Properties of the diamond samples used in this study.*

Code	Type	Growth Method	[B] atoms cm^{-3}	Thickness (µm)	Surface Roughness (nm)
MR14	pBDD (EA)	CVD	5×10^{20}	630 ± 2	1 – 3
145-500-0233	Optical single crystal (100) intrinsic	HPHT	N/A	50 ± 2	< 5

3.9.2 Chemicals

All solutions were prepared using MilliQ water (Millipore Corp., resistivity 18.2 MΩ cm at 25 °C). All chemicals were weighed using a four-figure analytical balance (Sartorius A2008). The pH of phosphate-buffered saline (PBS) buffer solution used in Chapter 6 was measured using a pH meter (PHM201 Portable pH meter, Radiometer, Copenhagen). All chemicals used in Chapters 6 and 7 of this work are outlined in **Table 3.2**.

***Table 3.2**: Chemicals used in this study including purity and supplier.*

Chemical	Formula	Purity	Supplier
Chemicals for electroanalysis:			
Potassium Ferrocyanide	$K_4Fe(CN)_6.3H_2O$	99.99%	Sigma Aldrich, MO, USA
Iron (II) sulphate	$FeSO_4.7H_2O$	≥99%	Sigma Aldrich, MO, USA
Dopamine Hydrochloride	$C_8H_{11}NO_2$	≥98%	Sigma Aldrich, MO, USA
Serotonin Hydrochloride	$C_{10}H_{12}N_2O$	99%	Acros Organics, Geel, Belgium
Riboflavin	$C_{17}H_{20}N_4O_6$	≥98%	Sigma Aldrich, MO, USA
β-Nicotinamide adenine dinucleotide	$C_{21}H_{29}N_7O_{14}P_2$	95%	Sigma Aldrich, MO, USA
Europium (III) Nitrate Pentahydrate	$Eu(NO_3)_3.5H_2O$	99.9%	Sigma Aldrich, MO, USA
L-ascorbic acid	$C_6H_8O_6$	≥99%	Sigma Aldrich, MO, USA
Hexaammineruthenium (III) Chloride	$Ru(NH_3)_6Cl_3$	99%	Sigma Aldrich, MO, USA
Supporting electrolytes:			
Potassium Nitrate	KNO_3	99%	Fisher Scientific, Loughborough, UK
Perchloric Acid	$HClO_4$	70%	Acros Organics, Geel, Belgium
Potassium Chloride	KCl	99 – 100%	Sigma Aldrich, MO, USA
Phosphate-buffered saline (PBS):			
Sodium Chloride	NaCl	≥99%	Sigma Aldrich, MO, USA
Potassium Chloride	KCl	99 – 100%	Sigma Aldrich, MO, USA
Sodium phosphate dibasic	Na_2HPO_4	99.95%	Sigma Aldrich, MO, USA
Potassium phosphate monobasic	KH_2PO_4	≥99%	Sigma Aldrich, MO, USA
Chemicals for pore sensing:			
Triton X-100	$C_{14}H_{22}O(C_2H_4O)_n$	99%	Sigma Aldrich, MO, USA
Polystyrene Beads	$[-CH_2CH(C_6H_5)-]_n$	–	Sigma Aldrich, MO, USA
Solvents:			
Acetone	$(CH_3)_2CO$	99%	Fisher Scientific, Loughborough, UK
Sulphuric Acid	H_2SO_4	98%	Sigma Aldrich, MO, USA

3.10 Diamond Surface Preparation

All samples were acid cleaned prior to use by boiling in concentrated H_2SO_4 (95%, Fisher Scientific) supersaturated with KNO_3 for 1 hour. This removed any non-

diamond carbon or impurities on the surface produced during the fabrication procedure.[14]

3.10.1 Oxygen-termination

The BDD samples used in Chapter 6 were oxygen (–O) terminated by polishing with alumina (0.05 μm sized particles, micropolish, Buehler Ltd) on a microcloth polishing pad saturated with distilled water (Buehler Ltd).[15] To ensure complete removal of the alumina particles, the samples were then cleaned using a dry polishing pad and rinsed with distilled water. The single crystal diamond substrates used in Chapter 7 were acid cleaned prior to use (as discussed above), which also serves to oxygen-terminate the surface.[16]

3.10.2 Hydrogen-termination

The BDD samples used in Chapter 6 were hydrogen (–H) terminated by placing the substrates in a 1 kW hydrogen plasma CVD reactor operating at 500 Torr using H_2 gas for 10 mins (Department of Chemistry, University of Bristol, UK). The samples were then left to cool for a further 10 mins under a constant hydrogen flow at a rate of 500 sccm (standard cubic centimetres per minute).[17]

3.11 Diamond Characterisation

3.11.1 Optical Microscopy

An optical microscope is a tool to magnify micron-sized features on a sample using visible light.[18] Images of the diamond samples used in this study were taken using an optical microscope (Olympus BH2 light microscope, Olympus Corporation, Japan) with a magnification range of 20x. The images were captured using a 2 MP CMOS camera (Olympus Corporation, Japan) connected to a desktop computer.

3.11.2 Micro-Raman Spectroscopy

Raman spectroscopy is a technique to measure the rotational and vibrational modes of a molecule.[19] When monochromatic light (typically from a laser) of a chosen wavelength is directed at a sample, the photons are adsorbed, reflected or scattered. Whilst most of the photons experience elastic (Rayleigh) scattering, some are inelastically (Raman) scattered. The photon interacts with the molecule causing it to be excited to a higher "virtual" energy level. For inelastic scattering, the molecule relaxes to a different energy state than the original level. The emitted photon either has a lower energy (lower frequency) or higher energy (higher frequency) than the adsorbed photon. This shift is known as *Stokes shift* (for lower frequency) or *anti-Stokes shift* (for higher frequency), as illustrated in **Figure 3.7.** Importantly, the loss of energy can be directly related to the structural and chemical properties of the sample.

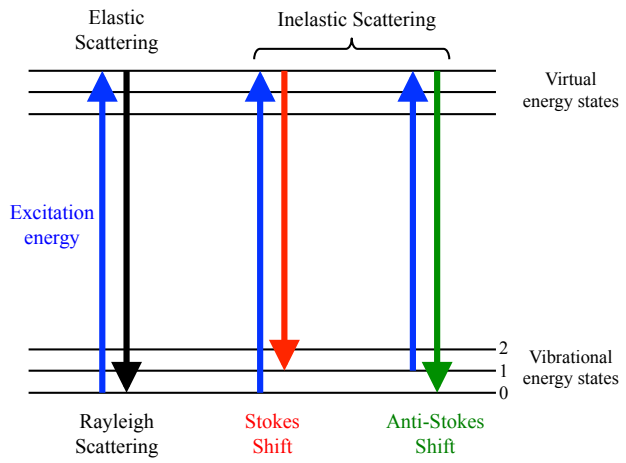

***Figure 3.7**: Schematic of the energy states involved in elastic and inelastic scattering. A photon excites the molecule from a vibrational energy state to a higher "virtual" energy state (blue arrows). Elastic (Rayleigh) scattering occurs if the molecule relaxes back to the original vibrational energy state (black arrow). Inelastic scattering occurs if it relaxes back to a lower frequency (Stokes shift) energy level (red arrow) or higher frequency (anti-Stokes shift) energy level (green arrow).*

As a non-destructive method, this technique is ideal for characterising diamond and carbon-based materials.[20] In this study, Raman spectroscopy was used to probe the carbon and boron content of our diamond samples. Characteristic features include: (1) a single sharp Raman line at 1332 cm^{-1} produced by the face-centered cubic lattice of sp^3 carbon, (2) broad peaks at 1355 cm^{-1} (the 'D peak') and 1575 cm^{-1} (the 'G-peak') produced by amorphous sp^2 carbon, and (3) asymmetry of the 1332 cm^{-1} peak due to Fano-type interference that can be attributed to boron at a concentration $\sim \geq 10^{20}$ B atoms cm^{-3}.[21] Raman measurements were conducted using a Renishaw inVia Raman microscope with laser wavelength of 514.5 nm generated from an Ar+ laser with 10 mV power.

3.11.3 Drop Shape Analysis

A simple method to determine whether a diamond surface is predominately H– (hydrophobic) or O– (hydrophilic) is by contact angle measurements.[22] Understanding whether the surface state (H– *vs.* O–) of BDD electrodes was extremely important in this study in order to compare the electrochemical responses of species on the different surfaces (Chapter 6). It was also used for validation of the diamond-water interactions in our MD models (Chapter 4). All measurements were taken using a drop shape analyser (Kruss drop shape analyser system DSA100). The sample stage was visualised using a camera connected to a desktop computer. The diamond substrate was placed on the sample stage. A 1 ml syringe with a needle attached to the end was filled with water and positioned directly above the sample using *x*-, *y*-, *z*- controllers. The syringe was gradually squeezed until a water droplet of volume 1 – 2 μl formed at the end of the needle (**Figure 3.8**a). The droplet was small enough (< 10 μl) to ensure that the drop volume did not have an effect on the wetting. The needle was then lowered to deposit the droplet on to the diamond

surface. Once deposited, the illumination was adjusted to provide maximum contrast and the image was frozen to prevent changes in the shape due to evaporation.

Drop shape analysis was applied to the image using the conic section (tangent) method.[23] In this method, the baseline *i.e.* the line at the interface between the substrate and droplet is identified and an ellipse is fitted along the drop shape profile. The contact angle, θ, is measured between the baseline and the tangent at the point where the profile of the droplet crosses the baseline, known as the *three-phase contact point* (**Figure 3.8**b). Two three-phase contact points exist where the droplet meets the surface; hence the final contact angle is calculated as an average of the two angles at these two contact points. In general, the diamond was considered hydrophilic (O-terminated) if $0.6 < \theta < 65°$ dependent on surface conditions *e.g.* roughness, type of surface treatment, and hydrophobic (H-terminated) if $\theta > 65°$, where ~ 90° is observed for insulating diamond.[8] Factors such as droplet volume, evaporation, substrate roughness, and the choice of profile fitting can all influence the contact angle measurement.[24]

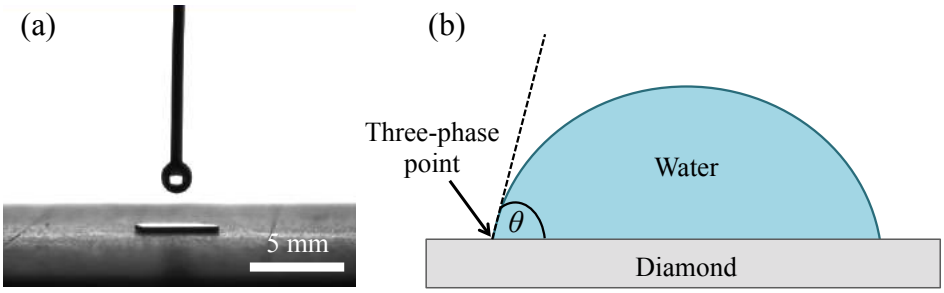

***Figure 3.8**: (a) Setup for contact angle measurements. A needle terminated by a ~ 1 µl water droplet is lowered towards the diamond sample. (b) Schematic of the conic section method to determine the contact angle, θ, at the point where the droplet profile (fitted to an ellipse), substrate and air meet (three-phase point).*[23]

3.12 Experimental Instrumentation

The instrumentation used in Chapters 6 and 7 are outlined below. Refer to these chapters for specific methodologies.

3.12.1 Laser Micromachining

Laser micromachining is a useful tool for high precision microfabrication of diamond.[25] The method utilises a high power laser beam focused on the underlying sample. Variation in the power, frequency and spot size enable precise control of the ablation depth and area. In addition, specific patterns can be formed on the surface by controlled movement of the sample stage during the laser process. All laser micromachining in this study (Chapters 6 and 7) was performed using the E-355H-3-ATHI-O system from Oxford Lasers, UK.

3.12.2 White Light Interferometry (WLI)

White light interferometry is an optical technique for measuring the surface topography of a sample.[26] White light is passed through a collimator and split into two beams – one that is reflected off a reference mirror and the second that is reflected off the sample. The two beams recombine to create an interference pattern that describes the surface topography captured by a CCD camera. This technique was used in this study during diamond pore fabrication to monitor the depth of laser ablation during sample thinning (Chapter 7).

3.12.3 Field-Emission Scanning Electron Microscopy (FE-SEM)

FE-SEM is a technique to image the surface topography and composition of a sample.[27] Electrons produced from a field emission source are accelerated through a column by applying voltages of 0.5 – 30 kV. The electron beam is then narrowed to focus on a small region of the sample using a series of electromagnetic lenses and apertures. Refinement of the electron beam enables higher spatial resolution imaging. Different types of electrons and photons are generated when the beam interacts with

the sample, as outlined in **Figure 3.9**. The secondary (SE) and back-scattered electrons (BSE) are of interest to this study.

Atoms of the sample absorb some of the electron energy (inelastic scattering) and emit low-energy SE. The level of SE emission is dependent on different atomic features of the sample. Detection will therefore carry important topographical information about the surface. The electrons are either captured using a conventional SE detector (located to the side of the chamber biased towards the SE path) or an in-lens detector (located inside the primary electron column). The position of the in-lens detector enables higher SE detection efficiency so that higher resolution images can be achieved at low accelerating voltages and short working distances.[28]

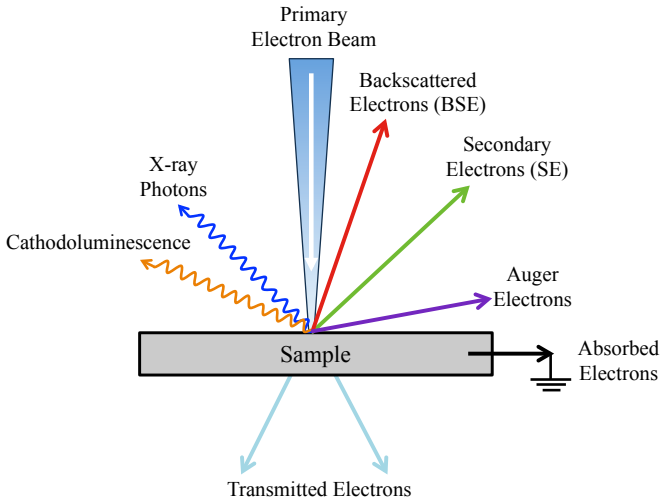

***Figure 3.9**: Schematic representation of the various signals produced when an electron beam interacts with the atoms of a sample.*[27]

BSE are high-energy electrons that have been elastically scattered by the sample. Since heavier elements will backscatter the electrons more efficiently than lighter elements, detection of BSE provides information about the chemical composition of the sample. In this study, FE-SEM was employed to monitor the formation of single crystal diamond pores (using BSE detection) and to image the

final pore structures (using SE detectors). The instrumentation and parameters used are detailed in Chapter 7.

3.12.4 Electron Beam Induced Etching (EBIE)

Pores were fabricated in single crystal diamond samples using water-mediated electron-beam induced etching (EBIE).[29] EBIE is a novel lithography technique that enables localised chemical dry etching of diamond and carbon-based materials. The method relies on electron-induced dissociation of precursor molecules on the surface. EBIE is performed at room temperature in an SEM chamber using a low vacuum (13 Pa) environment of water. Low-energy electron irradiation causes the surface-adsorbed water molecules to dissociate into fragments *e.g.* O* and OH* that proceed to react with the carbon to form volatile compounds *e.g.* CO and CO_2 (**Figure 3.10**).[30] These compounds desorb from the surface and are instantly removed by the pumping system. Other diamond fabrication techniques, such as focused ion beam (FIB) milling (see section 3.12.5) or laser ablation (see section 3.12.1) often cause surface damage and material redeposition artefacts due to ion implantation or sputtering. EBIE is a highly versatile and non-volatile technique.[30] The technique is presented in greater detail in Chapter 7.

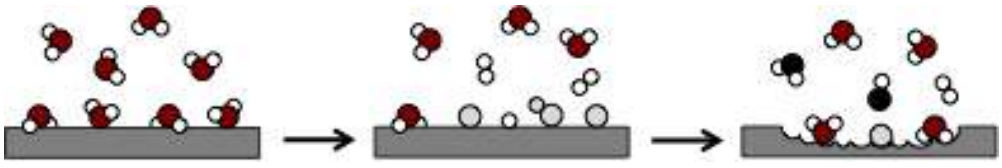

***Figure 3.10**: Schematic of water-mediated electron beam etching of diamond. (a) Water adsorption on the surface, (b) dissociation into O* and OH* fragments by electron beam irradiation, and (c) surface etching caused by the reaction of fragments with C to produce CO and CO_2.*[30]

3.12.5 Focused Ion Beam (FIB) Milling

FIB is a technique used for precise machining of materials down to the submicron level.[31] FIB operates under a similar setup to FE-SEM systems (section 3.12.3) but employs a focused beam of ions, usually gallium (Ga^+), instead of electrons. Ions are heavier than electrons so can achieve higher momenta making them more effective at milling. In addition, Ga^+ is typically chosen as it is liquid at room temperature, can be focused to < 10 nm in diameter and Ga^+ ion sources are readily available.[32] The beam is produced from a liquid-metal ion source (LMIS) that is accelerated through a column (5 – 30 keV) and narrowed using a series of electrostatic lenses and apertures. This enables FIB to reach a resolution of less than 10 nm. When the Ga^+ ion beam reaches the sample, ions are sputtered from the surface creating localised milling, as illustrated in **Figure 3.11**. For low beam currents, this sputtering is minimal and the sample can be imaged by detection of the secondary ions or electrons (FIB-SEM systems). The size and shape of the beam on the sample determines the micromachining precision and image resolution. Whilst FIB enables high precision milling, the method suffers due to Ga^+ ion implantation that can contaminate and damage the sample. Controlled FIB-SEM milling and imaging was employed in this study to cross-section a diamond pore (see Chapter 7).

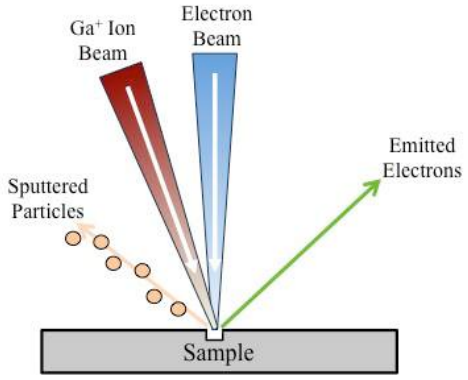

***Figure 3.11**: Schematic of the FIB-SEM setup. Milling (FIB) is achieved by the interaction of Ga^+ ions with the surface and can be imaged (SEM) using the secondary electrons that are emitted from both the ion and electron beams.*[31]

3.12.6 Dynamic Light Scattering (DLS)

DLS, or quasi-elastic light scattering, determines the size of hydrated particles within a solution by measuring the intensity fluctuations of (Rayleigh) scattered (see **Figure 3.7**) monochromatic (laser) light.[33] The scattered light intensity will fluctuate over time based on the Brownian motion of the particles *e.g.* smaller particles will diffuse faster causing greater fluctuations. The resulting time-dependent intensity trace is plotted as an autocorrelation function, $g(t)$, where the correlation exponentially decays from $g(0) = 1$, when the initial and scattered light intensities are equal, to $g(t) = 0$ when no correlation exists. The intensity-weighted diffusion coefficient, D_t, of the particle can then be determined by fitting a suitable algorithm to the data to measure the decay rate. The hydrodynamic radius, r_{DS}, can thus be determined using the *Stokes-Einstein* equation that describes the diffusion coefficient of a particle undergoing Brownian motion in a fluid at 298 K:[34]

$$r_{\mathrm{DS}} = \frac{kT}{6\pi\eta_v D_t} \tag{3.10}$$

where k_B is Boltzmann's constant and η_v is the viscosity of the solution. In this case, the size of the particle has been calculated by matching to a spherical particle that moves with the same translational diffusion coefficient as the particle in solution. In this study, the hydrodynamic radii of suspended polystyrene particles were determined using DLS (Chapter 7). Whilst DLS can provide the mean size and approximate the polydispersity of the particles in solution, the method can be erroneous in producing an accurate representation of the size distribution, especially for small particle sizes where shielding by larger particles can underestimate the scattering intensity. The particle sizes used in this study as considered large enough for this effect to be minimal.

3.13 References

[1] A. J. Bard, L. R. Faulkner, *Electrochemical Methods: Fundamentals and Applications, Vol. 2*, Wiley New York, **1980**.
[2] C. G. Zoski, *Handbook of Electrochemistry*, Elsevier, **2006**.
[3] R. G. Compton, G. H. Sanders, *Electrode Potentials*, Oxford University Press Oxford, **1996**.
[4] A. J. Bard, R. Parsons, J. Jordan, *Standard Potentials in Aqueous Solution, Vol. 6*, CRC press, **1985**.
[5] R. S. Nicholson, *Analytical Chemistry* **1965**, *37*, 1351-1355.
[6] C. M. Brett, A. M. O. Brett, *Electrochemistry: Principles, Methods, and Applications, Vol. 4*, Oxford University Press, Oxford, **1993**.
[7] J. Wang, *Analytical Electrochemistry*, John Wiley & Sons, **2006**.
[8] J. V. Macpherson, *Phys. Chem. Chem. Phys.* **2015**, *17*, 2935-2949.
[9] H. Taube, *Electron Transfer Reactions of Complex Ions in Solution*, Elsevier, **2012**.
[10] R. G. Compton, C. E. Banks, *Understanding Voltammetry*, World Scientific, **2007**.
[11] R. Marcus, *Annual Review of Physical Chemistry* **1964**, *15*, 155-196.
[12] D. Pletcher, *A First Course in Electrode Processes*, Royal Society of Chemistry, **2009**.
[13] J. E. B. Randles, *Trans. Faraday Soc.* **1948**, *44*, 327-338.
[14] C. Prado, S. J. Wilkins, P. Gründler, F. Marken, R. G. Compton, *Electroanalysis* **2003**, *15*, 1011-1016.
[15] L. Hutton, M. E. Newton, P. R. Unwin, J. V. Macpherson, *Anal. Chem.* **2008**, *81*, 1023-1032.
[16] P. E. Pehrsson, J. Long, M. J. Marchywka, J. E. Butler, *Applied physics letters* **1995**, *67*, 3414-3416.
[17] L. A. Hutton, J. G. Iacobini, E. Bitziou, R. B. Channon, M. E. Newton, J. V. Macpherson, *Anal. Chem.* **2013**, *85*, 7230-7240.
[18] H. Rühl, *The Optical Microscope–Some Basics*, Leica Microsystems, **2012**.
[19] D. A. Long, *New York* **1977**, 1-12.
[20] J. Filik, *Spectroscopy Europe* **2005**, *17*, 10.
[21] J. W. Ager III, W. Walukiewicz, M. McCluskey, M. A. Plano, M. I. Landstrass, *App. Phys. Lett.* **1995**, *66*, 616-618.
[22] A. Marmur, *Soft Matter* **2006**, *2*, 12-17.
[23] *Kruss Drop Shape Analysis (DSA100) Manual*, Kruss GmbH.
[24] a) C. Bourges-Monnier, M. Shanahan, *Langmuir* **1995**, *11*, 2820-2829; b) R. N. Wenzel, *The Journal of Physical Chemistry* **1949**, *53*, 1466-1467.
[25] W. T. Silfvast, *Laser Fundamentals*, Cambridge University Press, **2004**.
[26] C. O'Mahony, M. Hill, M. Brunet, R. Duane, A. Mathewson, *Measurement Science and Technology* **2003**, *14*, 1807.
[27] I. M. Watt, *The Principles and Practice of Electron Microscopy*, Cambridge University Press, **1997**.
[28] L. Reimer, *Image Formation in Low-Voltage Scanning Electron Microscopy, Vol. 12*, SPIE Press, **1993**.
[29] A. A. Martin, M. Toth, I. Aharonovich, *Sci. Rep.* **2014**, *4*.
[30] A. A. Martin, M. R. Phillips, M. Toth, *ACS App. Mater. Inter.* **2013**, *5*, 8002-8007.
[31] C. A. Volkert, A. M. Minor, *MRS Bull.* **2007**, *32*, 389-399.

[32] Z. Wang, *FIB Nanostructures*, Springer, **2014**.
[33] a) W. Goldburg, *Am. J. Phys.* **1999**, *67*, 1152-1160; b) R. Pecora, *Dynamic Light Scattering: Applications of Photon Correlation Spectroscopy*, Springer Science & Business Media, **2013**.
[34] J. T. Edward, *Journal of Chemical Education* **1970**, *47*, 261.

Chapter 4

Comparison of the Structure and Dynamics of Water at Model Hydrophobic and Hydrophilic (100), (111) and (110) Diamond Surfaces

4.1 Overview and Key Advances to Knowledge in this Chapter

Water is a ubiquitous solvent that participants directly or indirectly in interfacial chemical reactions at electrode surfaces. A detailed understanding of the water structure is an essential and necessary prerequisite to understanding, and ultimately predicting, interfacial interactions crucial for the function of diamond biosensor devices. This requires a fundamental understanding of the behaviour of water at the molecular level on different single crystal (or grains of polycrystalline) diamond surfaces, which is currently lacking in the scientific community.

In this chapter, we have developed the most realistic and extensive diamond molecular models to date, building on existing models of the (100) and (111) diamond surfaces by Netz *et al.,* through optimisation of the force field parameters and inclusion of the (110) crystal face. A set of single crystal diamond-water interfaces of different primary crystal orientations (110), (111), (100) with the most favourable hydrophobic (–H) and hydrophilic (C–O–C, C–OH, C=O) surface terminations were developed based on existing information from quantum calculations and experiments.

Our models were validated to experimental and theoretical data and good agreement was observed. The structure and dynamics of water and ions close to the different hydrophobic and hydrophilic diamond interfaces was revealed using molecular dynamics (MD) simulations. All diamond surfaces displayed distinct interfacial water ordering, with higher water densities and slower diffusion coefficients close to O-terminated surfaces and bulk-like water behaviour close to H-terminated surfaces. The influence of different geometrical and chemical surface features on the molecular-level structure and behaviour of the interfacial water was discussed. More specifically, differences in the water behaviour were linked to topographical and intermolecular interactions that alter the hydrogen bond networks.

No prior knowledge exists on how interfacial water compares on different single crystal diamond surfaces, hence the results of this chapter advance scientific knowledge in this field. The results assist the diamond community to better understand and interpret the role of interfacial water. This enables informed decisions to be made when selecting a diamond surface in future experiments, facilitating optimisation and rational design of diamond devices.

Our biocompatible diamond force field along with the set of surface models is a new tool to enable a wide range of diamond-biomolecule MD studies in the future that can assist a wealth of diamond experimental research. MD studies exploring diamond-biomolecule systems will need to consider the role of the interfacial water to fully elucidate the diamond-biomolecule interactions, which requires comparison to the diamond-water results in absence of biomolecules presented in this chapter. These results can also be compared to the water behaviour on other materials to assist the scientific community in technological design.

4.2 Introduction

The solid-liquid interface plays a fundamental role in a diverse range of environmental and technological fields including electrochemistry,[1] materials science,[2] biomedical technology,[3] and geology.[4] Due to its ubiquitous nature, water is typically present in these systems and often a key component to their functionality. It is therefore essential for advances in these fields to gain a fundamental understanding of how water and other solute molecules interact with surfaces.

The properties of water close to solid surfaces are known to vary significantly from those in bulk.[5] More specifically, layers of structured water have been shown to build up within close proximity to hydrophobic (that have weak to no affinity for water) and hydrophilic (that have a strong affinity for water) surfaces.[6] The influence of the surface typically extends to a few molecular layers (~ 1 – 6 nm from the interface),[7] with water ordering close to hydrophilic surfaces often extending to greater distances than hydrophobic.[8] For example, study of the different hydrophilic α-quartz surfaces showed at least two structured water layers forming close to these surfaces, with bulk water behaviour restored at 1.12 nm from the topmost layer of silicon atoms on all surfaces.[9] Hydrophobic surfaces have been shown to influence interfacial water in a similar way to air-water interfaces, where only weak hydrogen bonds exist to the surface and there is a strong ordering of the interfacial water.[10] This can be explained by the hydrophobic effect,[11] where the hydrophobic surface disrupts the hydrogen bonding network and causes the water to reassemble to maximise the number of water-water hydrogen bonds.[11]

In general, the arrangement and extension into bulk of the interfacial water is nontrivial, dependent not only on the surface nature but also on the topography of the

underlying surface *i.e.* the degree of protrusion, rigidity, surface density and lateral arrangement of the surface groups,[12] as well as structural features such as cavities and convexities,[13] that can all affect the degree of water affinity and adsorption. It was observed that voids in the $(10\bar{1}0)$ α-quartz surface were large enough for water to penetrate into and cause two-dimensional (2D) lateral ordering, whereas the smaller voids between the OH groups on the $(01\bar{1}1)$ and (0001) did not accommodate water.[9] Moreover, the surfaces with smaller voids were observed to have a greater water ordering effect. Facet selective binding has also been observed for other species besides water. These include amino acids on α-quartz surfaces,[14] metal formation on Cu,[15] surfactants on Ag,[16] and peptides on Pt.[17] Preferential molecular adsorption can lead to selective drug design based on the addition of facet recognition sites to peptides.[17]

The structure and properties of the interfacial water can be highly influential for surface phenomena including electron tunneling to facilitate electrochemical reactions,[18] and reduced friction and wear of substrates due to stable thin-layer water film formation.[19] Interfacial water is of particular relevance to molecules adsorbing onto a surface, as they must cross through the transition region from bulk to interfacial water in order to adsorb (see Chapter 3, section 3.2). Water at interfaces has shown an important role in the adsorption of amino acids,[20] peptides,[21] and proteins[22] to surfaces. Consequently, detailed knowledge of the structure and dynamics of the interfacial water is highly advantageous for a fundamental understanding of biomolecular adsorption and chemical reactions on surfaces, and would assist in the optimisation of electronic and nanotechnology biosensing devices that are reliant on a well-defined surface-water interface. This is discussed further in Chapter 5.

Diamond has emerged as an attractive material in biosensing applications due to its biocompatibility, resistance to fouling, and wide electrochemical potential window.[23] The strong crystal lattice of diamond provides it with excellent thermal stability, robustness, thermal diffusivity, and insulating properties (wide band gap of 5.5 eV).[24] Furthermore, carbon chemistry unlocks a wide variety of surface modifications, such as functionalisation of DNA and other biological species to the surface,[25] that makes diamond ideal as a robust, highly selective integrated biosensor.[26] Importantly, diamond surfaces can be easily modified to be hydrophobic (hydrogen (–H) terminated) by exposure to a hydrogen plasma, or hydrophilic (oxygen (–O) terminated) by boiling in acid,[27] exposure to an oxygen plasma,[28] or anodic electrochemical treatment.[29] Both –H and –O diamond surface terminations have chemical stability in aqueous environments. This unique ability to manipulate the surface groups of diamond enables it to be selective to different species *i.e.* that may bind more favourably to specific groups, as well as making it a useful platform material for electrochemical surface-dependent studies including localised chemical micropatterning of diamond surfaces,[30] and selectivity of redox species due to differing electron transfer (ET) kinetics on each surface.[31] Water plays an important role in the electronic properties of diamond, in which H-terminated surfaces exhibit p-type surface conductivity due to the influence of a mildly acidic physisorbed water layer on the surface.[32] A molecular-level interpretation of the diamond-solution interface is essential to fully utilise diamond in biosensing devices, as it would enable identification of the ideal surface state to enhance device stability and functionality.

In addition to its changeable surface chemistry, the various crystal orientations of diamond introduce topographical surface differences. The three primary crystal orientations of diamond are the (111), (110) and (100) faces (see Chapter 1, section

1.2.2). The different planes cause different arrangements of carbon on the surface, as shown in Chapter 1, section 1.2.2. Importantly, each diamond crystal face is closely linked to a preference for binding to different functional groups. X-ray photoelectron spectroscopy (XPS) and high resolution electron energy loss spectroscopy (HREELS) studies on single crystal diamond have reported a higher proportion of C–OH on the (111), C–OH and C–O–C on the (110), and C–O–C, C–OH and C=O on the (100) crystal faces (see Chapter 1, section 1.2.2). Hence, in order to fully understand molecular specificity of species to different diamond surfaces, it is important to investigate crystal orientation and surface chemistry in conjunction.

Due to the development of synthetic growth techniques, diamond has become more readily available in recent years for use in science and technology applications (see Chapter 1, section 1.2.1).[33] The most commonly used diamond surface for electrochemical biosensing experiments is synthetically grown polycrystalline boron doped diamond (BDD), which contains a mixture of crystalline faces and surface terminations.[34] By deconstructing this surface into the constituent facets, we can isolate the effect of the individual structural and chemical surface components on the interfacial properties. This would ultimately enable us to advise on the ideal diamond surface that could maximise biosensing capabilities for a particular system of interest.

Molecular dynamics (MD) simulations can provide a molecular-level insight into the diamond-solution interface. Experimental techniques which have been used to probe the diamond-solution interface include Raman and photoluminescence spectroscopy,[35] atomic force microscopy[36] and electrochemical impedance spectroscopy.[37] Whilst these can be used to deduce angstrom length scale data, they cannot reach the sufficient picosecond time scales to capture the dynamics of water molecules in the interfacial regions. MD simulations have been used to elucidate the

structure and dynamics of interfacial water close to other materials such as silica,[9, 38] quartz,[39] graphite,[40] carbon nanotubes,[41] and minerals.[42] Despite its significance, there exist only a few theoretical studies that investigate water interaction on diamond surfaces. These have been limited to the adsorption of water molecules on bare and hydrogenated (100) diamond surfaces. Manelli *et al*.,[43] Okamoto,[44] and Larsson *et al.*,[45] have implemented *ab-initio* calculations to investigate the interaction of water molecules with these surfaces. Netz *et al*.,[46] have utilised MD simulations to probe the water structure on hydrophobic and hydrophilic diamond-like surfaces (discussed in detail in section 4.3.3). To the best of our knowledge, this is the first study to build and compare the diamond-water interface for a complete set of biocompatible single crystal diamond surface models using all three primary faces and their principle H– and O– surface terminations, with previous MD and DFT studies only investigating up to two diamond surface systems at one time.

The aim of this work was to investigate the differences in water structure and dynamics close to model H– and O– terminated diamond surfaces. Through the use of MD simulations, we assess to what degree the interfacial properties of water, such as the density, lateral arrangement, orientation, hydrogen bonding, mobility, and diffusion, deviate from bulk. By studying a range of ideal diamond structures, we map any differences in the diamond-water interface to the crystal orientation and surface group responsible, and assess the impact that these variations may have in diamond-based technologies. Furthermore, as electrolyte solutions are used in electrochemical studies, we briefly examine how K^+, Cl^- ions of varying concentrations interact with water at each diamond surface and discuss the implications this may have on species adsorption in electrochemical studies.

4.3 Theoretical Methods

4.3.1 Structural Models

Seven diamond surface models were constructed to investigate the effect of the underlying diamond surface structure and chemistry on interfacial water adsorption. The three primary faces of diamond – (100), (110) and (111) – were chosen to probe structural differences. These were fully terminated with hydrogen (H) or oxygen (OH, C–O–C, C=O) groups dependent on the most common surface group identified by experimental analysis of single crystal H– and O– terminated diamond surfaces (see Chapter 1, section 1.2.2).

4.3.2 Model Building

Bulk diamond was built from the diamond crystalline unit cell consisting of eight carbon (C) atoms in a face-centered cubic lattice with lattice parameter a = 0.3567 nm (see Chapter 1, Figure 1.2). The unit cell was replicated in the *x-, y-* and *z-*directions to form a diamond crystal structure. The structure was cleaved along the (100), (111) or (110) planes, and rotated so that the surface of interest lay perpendicular to the *z*-axis of the simulation box. After rotation, the edges were trimmed along the *xz* and *yz* planes to create slabs that were fully periodic in the *x-* and *y-* directions. Side and aerial views of the model diamond surfaces are shown in **Figure 4.1**.

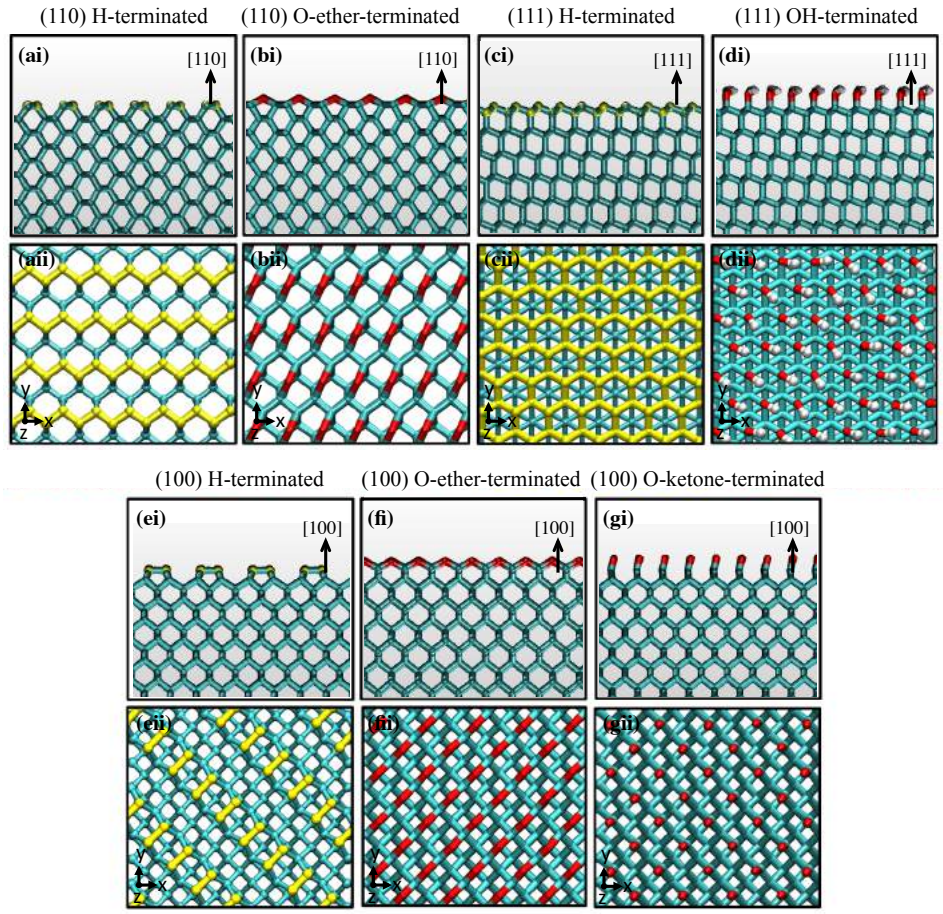

***Figure 4.1**: Snapshots of the diamond surfaces (a) – (g) used in the simulations from (i) side view and (ii) aerial view. Atoms are represented as beads with C = cyan, CH = yellow, O = red and H = white. Bonds are shaded with CH–CH = yellow C–O or C=O = cyan-red, C–CH = cyan-yellow, and O–H = red-white.*

All H-terminated surfaces were functionalised with CH groups in a 1:1 ratio at the position of each dangling surface carbon (**Figure 4.1**a, c and e).[47] The O-terminated (110) surface was functionalised by an ether conformation (see Chapter 1, section 1.2.2.3), where each O atom was bonded to two neighbouring surface carbons (**Figure 4.1**b),[48] and the O-terminated (111) slab terminated with hydroxyl (OH) groups (see Chapter 1, section 1.2.2.2) by bonding in a 1:1 ratio to each dangling surface carbon atom (**Figure 4.1**d).[49] The H-terminated (100) surface was first reconstructed into the more energetically favourable 2 × 1 surface geometry (see Chapter 1, section 1.2.2.1), where the uppermost dangling carbons were rearranged to

covalently bond to their neighbours (**Figure 4.1**e).[50] Two O-terminated (100) surfaces were built (see Chapter 1, section 1.2.2.1) – one O-ether-terminated where each O atom was bonded to two neighbouring surface carbons (**Figure 4.1**f),[51] and the other O-ketone-terminated where each O atom was double bonded to a surface carbon atom (**Figure 4.1**g).[52] Each surface was built with full coverage of only one type of termination in order to probe how the most favourable surface group influences adsorption. We note that a mix of terminations will exist on each surface however, for simplicity, it is considered the logical first step to investigate a single termination before increasing the surface complexity to additional groups. To minimise the potential energy of each diamond crystal lattice, the simulation box was varied systematically (1 Å steps) in the *x*- and *y*- directions and run for 1 ns (900 ps equilibration, 100 ps MD run) in the *NVT* (fixed number of particles N, volume V and temperature T) ensemble using a 0.5 fs time step. The potential energy was calculated after each change and the box dimensions that yielded the lowest potential energy were chosen. The final slabs had *xy*- dimensions of 7.578 × 7.491 nm^2, 7.568 × 6.999 nm^2, and 7.133 × 7.133 nm^2 for the (110), (111) and (100) respectively, consisting of 30240 C atoms with 2520 replaced as CH or 1260 O atoms added on the (110) surfaces, 28800 C atoms with 1920 replaced as CH groups or 1920 OH groups added on the (111) surfaces, and 27200 C atoms with 1600 replaced as CH groups or 1600 O atoms added on the (100) surfaces. These dimensions were chosen to be large enough for the models to be used in larger-scale simulations in the future *e.g.* phospholipid self-assembly, but not so large that they would run too slowly (*i.e.* requiring < 1 week of computational time). Each slab was approximately 3 nm thick (32 – 36 atomic layers) so that no interaction existed between the top and bottom faces.

All surfaces were solvated with explicit water molecules (14600 waters) making final equilibrated box dimensions of 7.578 × 7.491 × 11.337 nm^3 for the (110) H-terminated, 7.578 × 7.491 × 11.410 nm^3 for the (110) O-ether-terminated, 7.568 × 6.999 × 11.984 nm^3 for the (111) H-terminated, 7.568 × 6.999 × 12.212 nm^3 for the (111) OH-terminated, 7.133 × 7.133 × 12.273 nm^3 for the (100) H-terminated, 7.133 × 7.133 × 12.102 for the (100) O-ether-terminated, and 7.133 × 7.133 × 12.131 for the (100) O-ketone-terminated, as the starting structures for the simulations (**Figure 4.2**).

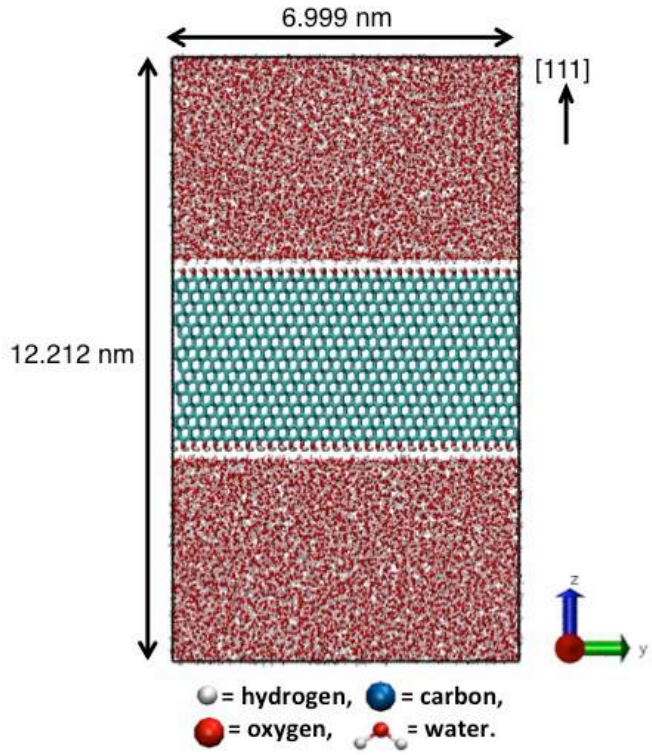

Figure 4.2*: Snapshot of a typical solvated model diamond slab used as the starting structure for molecular dynamics (MD) simulations of the diamond-water interface. The slab shown is (111) H-terminated model diamond. Each face of the slab is fully terminated by H atoms and the final dimensions of this equilibrated system are 7.568 × 6.999 × 12.212 nm*^{3}.

4.3.3 Force Field Parameters

There is significant difficulty in finding a force field that successfully reproduces self- and cross- interaction terms of inorganic surfaces and biomolecules. Our aim was to choose a force field that can capture the interaction of interfacial

water with diamond, and be utilised in future studies of diamond-water-biomolecule systems to further the understanding of biomolecular processes on diamond. With consideration of these requirements, parameters were taken from the GROMOS96 version 53a6 force field.[53] This force field has been parameterised for biomolecular systems, and has proven effective in reproducing solvation data for protein folding, membrane transport and peptide-surface interactions.[53] Compared to other force fields (*e.g.* CHARMM, AMBER, OPLS), GROMOS96 53a6 has been parameterised to reproduce the thermodynamic properties of pure liquids of 28 small polar molecules and the hydration and solvation free enthalpies of 14 representative amino acid analogues. Our model diamond surfaces, along with most biological compounds, consist of the functional groups found in these molecules. Furthermore, this force field (and specifically the 53a6 parameter set) with the SPC water model has been used previously to study the interaction of water with (100) diamond-like surfaces,[6] and the desorption of a mildly hydrophobic peptide from a hydrophobic, H-terminated (100) diamond surface with agreement to AFM experiments.[54]

To refine the force field for this study, small adjustments were made to the parameter set to optimise it for the different diamond surface functional groups. Detailed tables outlining the parameter choices for each system are presented in Appendix A1 – 7. The GROMOS96 force field treats aliphatic carbons (carbons bonded with hydrogens) as united-atoms to reduce the computational expense associated with simulating the hydrogens. All atom types and bonded interactions (bond lengths, angles and dihedrals), apart from the bulk C–C bonds, were assigned using parameters from the GROMOS96 force field. The choice of parameter was based on the order of atom types and most appropriate match, as outlined in Appendix A1 – 7. All bulk diamond C–C bonds were modified to the well-known experimental

(X-ray diffraction) value of 0.1545 nm at 298 K.[55] The model needs to be validated against experimental data in order to ascertain how well the force field captures properties of diamond. Validation of the force field is presented in section 4.4.1.

For the non-bonded interactions, Lennard-Jones (LJ) parameters were taken directly from the GROMOS96 force field. Partial atomic charges were adjusted based on quantum mechanical (QM) calculations of simple model compounds, based on the methodology by Lopes *et al.* used in the development of a silica force field.[56] Compounds were designed to contain the important functional groups for each surface, as shown in **Figure 4.3**.

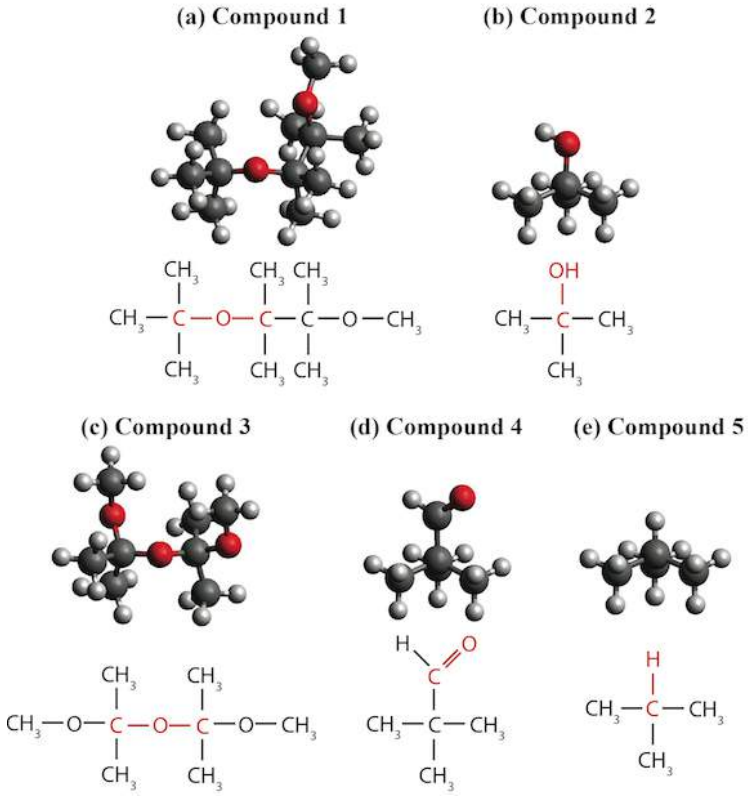

Figure 4.3*: Model compounds used for QM calculations of partial charge distributions. The compounds were designed to mimic important functional groups on each diamond surface (highlighted in red) and their immediate environment. Compounds 1 and 3 capture a C–O–C group on the (110) and (100) O-ether-terminated surfaces, respectively; Compound 2 captures an OH group on the (111) OH-terminated surface; Compound 4 captures a C=O group on the (100) ketone-terminated surface; and Compound 5 captures C–H groups on (110), (111), and (100) H-terminated surfaces.*

Geometry optimisation was performed and the five lowest energy conformers identified for each compound in **Figure 4.3** using Avogadro v.1.1.1 package.[57] *Ab-initio* QM calculations at the Hartree-Fock (HF) level with the HF/6-31G(d,p) basis set were performed using the Gaussian 03 package to determine the partial charge distribution for each conformer. The lowest energy conformer for each fragment was also subjected to a higher level of theory, the Møller-Plesset MP2/6-31G(d,p), and little difference was observed between the results, confirming the level of accuracy of HF was sufficient. The final partial atomic charges for each surface were calculated by averaging the charges of the five lowest energy conformers for each representative fragment. The first five conformers have the largest energy and therefore would have the biggest contribution to the partial charge distribution. Further conformers could have been included, but as they are less favourable they would have to be energy weighted based on the Boltzmann distribution to account for their smaller contribution to the average. Partial charges were calculated as (C, +0.345 e; O, −0.690 e) on the (110) O-ether-terminated surface, (C, +0.34 e; O, −0.76 e; H, +0.42 e) on the (111) OH-terminated surface, (C, +0.67 e; O, −0.67 e) on the (100) O-ether-terminated surface, and (C, +0.58 e; O, −0.58 e) on the (100) O-ketone-terminated surface. Differences observed in the partial charges were due to the different carbon arrangements on each surface that cause the partial charge distributions to vary (see Figure 4.1). All remaining partial atomic charges of bulk Cs were set to zero, as the bulk atoms lie far enough away from the surface to have a negligible contribution to the surface interactions. The charges were chosen to maintain electroneutrality of the system, ensuring that full electrostatics under periodic boundary conditions could be maintained. In addition, the partial charges on C–H were also calculated to test the methodology although these values are not used in our united-atom model (**Figure**

4.3). These produced small partial charges (C: −0.07, H: +0.07 e) as expected for C–H groups,[58] providing confidence to our results.

To ensure the force field captures the correct dihedral (torsional) angle energies, the force matching method could have been used to parameterise the bonded and non-bonded interactions,[59] by performing first-principle calculations of model hydrophobic/hydrophilic molecules interacting with each surface. However, the method of parameterisation used here was considered sufficient, as it is consistent with the parameterisation used for any new molecule in the GROMOS force field.

Both the SPC and SPC/E models have been used in previous water-diamond MD simulations.[60] In this study, the SPC water model was chosen as the GROMOS force field has been parameterized for use with this model, so we would expect it to produce the most reliable representation of the water interactions. The LJ potentials and table of LJ parameters for the diamond-diamond and diamond-water interactions are outlined in **Figure 4.4**. The potential depth, ε, and distance at which the potential is zero, σ, were calculated using the Lorentz-Berthelot combination rules as implemented in the GROMOS 53a6 force field.[53]

(a)

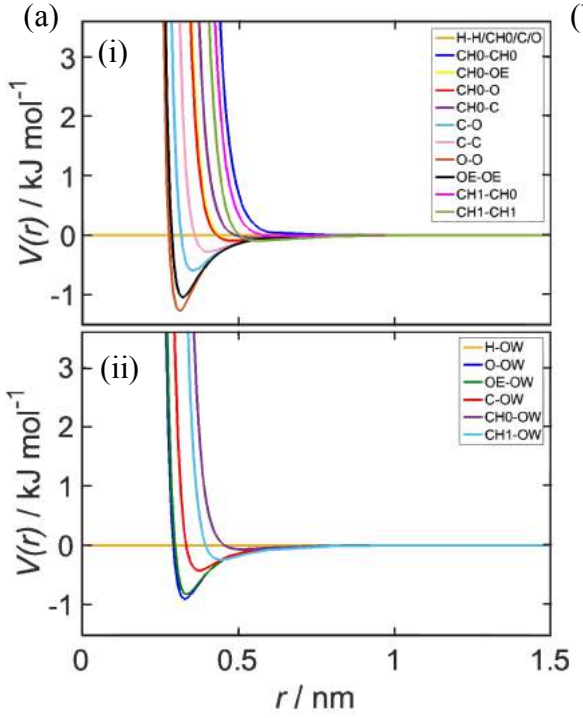

(b)

Atom Type	ε / kJ mol^{-1}	σ / nm
CH0	0.0070	0.6639
C	0.2774	0.2581
OE	1.0571	0.2849
O	1.2791	0.2760
H	0	0
OW	0.6502	0.3166
HW1/2	0	0
CH0-OW	0.0674	0.4585
C-OW	0.4247	0.3367
OE-OW	0.8290	0.3003
O-OW	0.9119	0.2956
H-OW	0	0
-HW1/2	0	0
OW-OW	0.6502	0.3166
H-H	0	0
C-C	0.2774	0.3581
CH0-CH0	0.0070	0.6639
CH0-OE	0.0860	0.4349
CH0-O	0.0946	0.4281
CH0-C	0.0441	0.4876
C-O	0.5957	0.3144
C-C	0.2774	0.3581
O-O	1.2791	0.2760
OE-OE	1.0571	0.2849

Figure 4.4*: (a) LJ potentials for (i) diamond-diamond and (ii) diamond-water van der Waals interactions, and (b) table of the LJ ε and σ parameters used to describe the van der Waals forces in the model diamond-water systems. Atom types are CH0 (bare sp3 carbon), C (bare carbon), OE (ether oxygen), O (carbonyl oxygen), H (hydrogen not bound to carbon), OW (water oxygen) and HW1/2 (water hydrogen 1 and 2).*

Whilst the GROMOS parameter choices (Appendix A1 – 7) mostly align with the previous bulk diamond model by Netz *et al.,*[46] there are two noteworthy differences to the models used in this study. Firstly, bulk diamond has been characterised by the atom type CH0 (bare sp^3 carbon) for aliphatic tetrahedral carbon.[53] This atom type was developed as the existing carbon atom type, C (bare carbon), was specifically parameterized for use in planar (carbonyl and aromatic) groups. Hence, the CH0 atom type is considered to provide a better representation of carbon within the tetrahedral structure of diamond. Secondly, previous studies typically vary the hydrophobicity of the diamond surface by adjusting the carbon-water interaction strength. In this study, Coulombic partial charges have been placed on each model surface to mimic the 'true' surface charge distribution for each

functional group (see Figure 4.3). Additionally, each diamond surface was built in accordance with the models outlined in the literature (Chapter 1, section 1.2.2). This enables us to have a set of comparatively realistic model diamond surfaces.

4.3.4 Simulation Parameters

All simulations were carried out using the GROMACS software package.[61] The diamond slabs were relaxed using a steepest descent algorithm (see Chapter 2, section 2.4) for 5000 steps or until the gradient was less than the tolerance of 1000 kJ mol^{-1} nm^{-1}. Water molecules (14600 waters) were inserted above and below each diamond slab. For the ion simulations, water molecules were replaced randomly by equal numbers of K^+ and Cl^- ions using the genion tool in Gromacs to ensure electroneutrality of each system that is required for MD simulations. Ionic solutions of concentration 0.01 M (4 K^+, 4 Cl^-, 14592 waters), 0.1 M (38 K^+, 38 Cl^-, 14524 waters), 0.2 M (76 K^+, 76 Cl^-, 14448 waters), 0.5 M (190 K^+, 190 Cl^-, 14220 waters) and 1.0 M (380 K^+, 380 Cl^-, 13840 waters) were produced. The solvated systems were energy minimized using the steepest descent algorithm (same conditions as above) and then equilibrated for 20 ps in the *NVT* (fixed number of particles *N*, volume *V* and temperature *T*) ensemble and 100 ps in the NAP_zT (fixed number of particles *N*, surface area *A*, vertical pressure P_z and temperature *T*) ensemble. The water and ion simulations were run for 20 ns in the NAP_zT ensemble, where the first 5 ns of all simulations were considered as the equilibration phase and the remaining 15 ns used as the MD run for subsequent analysis. MD simulations were performed using a time step of 2 fs with coordinates saved every 100 ps (50000 steps).

To capture fast hydrogen bond dynamics for the study of hydrogen bond lifetimes and lateral diffusion coefficients, all simulations were extended for a further 200 ps with system coordinates output every 10 fs. Hydrogen bond lifetimes were

calculated using the entire 200 ps run, whereas the lateral diffusion coefficients were calculated using the last 10 ps and only water molecules that existed at both $t = 0$ and $t = 10$ ps were considered in the calculation. The last 10 ps was chosen as the system will be fully equilibrated, and it is short enough for a suitable proportion of water molecules to remain in the region of interest throughout the time, whilst still long enough to allow sufficient capture of the water mobility. Given that this approach may cause bias towards water molecules of lower velocity, the mobility of bulk water was also calculated over the same timescale and compared to the interfacial mobility, so that any differences due to the methodology could be identified. Three-dimensional periodic boundary conditions (see Chapter 2, section 2.6.3) were used so that each slab appeared as infinite in the *xy*- plane. The system was coupled to a Berendsen thermostat and barostat (see Chapter 2, section 2.6.2)[62] with coupling constants τ_T = 2.0 ps and τ_P = 5.0 ps to maintain the temperature at 300 K and pressure at 1 bar. LJ interactions were cut-off at 1 nm, and electrostatics were treated using the particle mesh Ewald method (see Chapter 2, section 2.3.5) with a cut-off of 1 nm.[63] Bonds to hydrogen atoms were constrained using the LINCS algorithm implemented within GROMACS (see Chapter 2, section 2.6.4).[64]

4.3.5 Analysis

The simulations were analysed using tools available in GROMACS, VMD (visual molecular dynamics) and locally written scripts.[65] All MD trajectories were visualized using the VMD software. The average bond lengths and angles were measured using the g_bond and g_angle options in Gromacs, respectively. Density profiles of each group in the system were obtained by slicing the simulation box into 200 bins along the normal to the diamond surface and calculating the partial densities in each bin. The 2D lateral density profiles of the first layer of structured water were

further obtained by dividing the region into a grid and calculating the water density within each grid box. The average number of water-water and diamond-water hydrogen bonds per time frame (4 ps), made by polar and charged atoms, were stipulated under the standard geometric criteria for hydrogen bonds established by Jedlovszky *et al.*,[66] whereby the hydrogen-acceptor distance was required to be less than 0.3 nm and acceptor-donor-hydrogen angle cutoff less than 20°. Hydrogen bonds were analysed by counting the number formed at discrete time steps. The hydrogen bond time autocorrelation function, *C(t),* is defined by:[67]

$$C(t) = \frac{\langle h(0)h(t)\rangle}{\langle h\rangle} \tag{4.1}$$

where *h(t)* = 1 if a hydrogen bond that exists at $t = 0$ is still present at time *t,* and zero otherwise, and $\langle h\rangle$ is the average number of hydrogen bonds over all pairs in the simulation trajectory. The hydrogen bond lifetimes were calculated as the integral of the counted values in equation 4.1 with respect to time. The water orientation as a function of distance from the surface was obtained by dividing the system into bins along the *z*-axis and calculating $\langle\cos(\theta)\rangle$ for all water molecules within the bin, where θ is the angle between the water dipole vector and the normal to the surface. In this case, $\langle\cos(\theta)\rangle = 0$ indicates the average dipole vector of the water molecule lies parallel to the surface, and $\langle\cos(\theta)\rangle = 1$ indicates the dipole vector of the water lies perpendicular to the surface. This analysis does not distinguish conformations that are 360° rotation about the dipole vector. Further analysis of the water OH bond would need to be included to account for this. Lateral diffusion coefficients were calculated for the first layer of structured water from the lateral mean squared displacement using the Einstein relation (Chapter 3, equation 3.10). Only water molecules that

remained in the first water layer throughout the 10 ps run were included in the analysis.

4.4 Results and Discussion

4.4.1 Force Field Validation

The ability of the force field to reproduce structural information can provide validity to the diamond models. **Table 4.1** outlines the average bond lengths and angles of each of the energy minimised diamond surfaces. The topmost carbon atoms are denoted as C1, carbons directly below as C2, and bulk as C.

Table 4.1*: Average bond lengths and angles of the seven diamond surface models*.

Structure	(110)-H	(110)-O-ether	(111)-H	(111)-OH	(100)-H	(100)-O-ether	(100)-O-ketone
Bonds / Å							
O–H	–	–	–	0.10	–	–	–
O–O	–	3.56	–	2.47	–	2.50	2.49
C1–O	–	1.57	–	1.42	–	1.48	1.19
C1–C1	1.53	1.62	1.56	1.53	1.63	1.54	1.52
C1–C2	1.56	1.59	1.53	1.55	1.58	1.54	1.54
Bulk C–C	1.54	1.56	1.55	1.58	1.59	1.58	1.54
Angles / °							
C1–O–H	–	–	–	109.1	–	–	–
C1–C1–O	–	142.3	–	113.8	–	105.1	124.7
C1–O–C1	–	127.5	–	–	–	120.2	–
Bulk C–C–C	109.5	109.1	109.4	109.3	109.1	109.4	109.2

All models were able to successfully reproduce on average the bulk structural properties of diamond *i.e.* C–C: ~ 1.55 Å and C–C–C: ~ 109.5°. The geometry of each surface is in close agreement with various DFT studies. For the 2 × 1 (100) H-terminated model, the average C1–C1 bond length of 1.63 Å is also reported in DFT calculations of the same surface by Petrini *et al*.[68] Similarly, the C1–C2 bond length of 1.58 Å is in agreement with DFT C1–C2 values reported in literature for this surface of 1.59 Å,[69] 1.60 Å,[68] 1.53 Å,[70] and 1.54 Å.[71] For the (100) O-ether-terminated model, the average C1–O bond length of 1.48 Å and O–O separation

distance of 2.50 Å matches to DFT calculations of this surface by Sque[72] and Tamura.[73] The C1–O–C1 bond angle of 120.2° is in reasonably close agreement to that reported by Tamura *et al.,* (C–O–C: 115°). Similarly, for the (100) O-ketone-terminated surface, the average C=O bond length of 1.19 Å is in agreement with the DFT study by Sque *et al*.,[72] for the same surface. The O–O separation distance of 2.49 Å is in close agreement with Tamura *et al.,* (O–O: 2.52 Å).[73] The average bulk C–C bond length in our model falls close to the range of values (1.52 – 1.55 Å) reported from DFT calculations by Sque,[72] Tamura,[73] and Liu.[71]

For the 1 × 1 (111) H-terminated surface, Kern et al.,[70] have reported an increase in the C1–C1 bond length from 1.46 Å to 1.52 Å upon full coverage of H–groups. Our model produces a similar C1–C1 bond length of 1.56 Å with the extra distance likely accounted for by the use of CH united-atoms. DFT calculations by Sque *et al*.[72] report that all C–C bonds in 1 × 1 H-terminated (111) diamond are of similar length due to the lack of reconstruction (1.52 – 1.54 Å). Our model is in accordance with this *i.e.* all carbon bonds for this structure lie between 1.53 – 1.56 Å. For the (111) OH-terminated model, the average bond lengths of O–H: 0.10 Å, C1–O: 1.42 Å, and C1–C1: 1.53 Å are in agreement with DFT calculations of the same surface reported by Loh *et al*.[49] and Petrini *et al*.[74] The bare 1 × 1 (110) diamond surface has been reported by DFT studies to have C1–C1 bond lengths of ~ 1.43 Å[47a, 75] that increases to 1.51 Å upon hydrogenation.[47b] Our average C1–C1 value of 1.53 Å is in agreement with this result. Similar to reported for the (111) surface, the C–C bonds on (110) remain bulk-like (~ 1.55 Å) due to the lack of reconstruction. No DFT models exist for the (110)-O-ether-terminated surface. The closest comparison is to DFT studies of the 2 × 1 (111) O-terminated diamond surface that has a similar zigzag surface structure to (110). This reports a C1–O bond length of 1.45 Å,[74] which is

smaller than that obtained in our (110) model of C1–O: 1.57 Å, although (111) does have a more compact surface structure. Close agreement between the surface geometry of our models and DFT results provides confidence that our force field successfully captures the bonded interactions of diamond surfaces.

The capability of the force field to reproduce experimental diamond-water measurements can provide further confidence in the accuracy of the models. However, probing the water structure and dynamics at the nano-scale is experimentally challenging, facilitating the need for atomic level models in the first place. The effect of water adsorption on the diamond surface structure has been studied experimentally using high resolution electron energy loss (HREELS)[76] and infrared (IR) spectroscopies.[77] Most studies focus on the (100) surface with fewer studies on the (111) and (110) faces, likely owing to preferential CVD growth of diamond in the [100] plane for smoother surfaces.[78] Throughout our investigation, our findings are related to experimental and theoretical results where possible to reinforce the models.

Contact angle measurements of a water droplet on single crystal diamond surfaces are considered a useful validation tool for the models in this study, as they provide comparison between diamond-water interactions in experiment and simulation. The experimental contact angle of water on hydrophobic and hydrophilic diamond surfaces are typically ~ 90° and 0.6 – 65°, respectively,[79] with experimental variation due to differing surface functionalisation, roughness and type of diamond.[79] Here, water droplets were simulated on each model diamond surface and compared to experimental drop shape profiles on the corresponding single crystal diamond samples (see Chapter 1, section 3.11.3). These samples were acid cleaned prior to use, which served to clean and O-terminate the surface (see Chapter 3, section 3.10).

Whilst these samples have been polished to ~ nm roughness, the experimental surface area will still be affected more by roughness compared to the ideally flat simulated surfaces, and the surface groups will always be a mix of different terminations compared to the complete termination of only one group assumed in our models. This will cause discrepancies in the results.

Water boxes of approximately 2.5 × 2.5 × 2.5 nm^3 containing 428 water molecules were placed on each diamond surface and run for 5 ns in the *NVT* ensemble using a 2 fs time step. The surface coverage of each water droplet was monitored over time as shown in **Figure 4.5**. The surface was divided into 10 × 10 bins in the *xy*-direction and the number of bins containing water molecules at each time step was recorded to obtain the total surface coverage. All droplets reached equilibrium within the first 200 ps. The surface coverage fluctuated over time relating to the bin size and dynamic movement of the water molecules within the droplet. Droplets on the O-terminated (hydrophilic) diamond surfaces displayed greater surface coverage due to greater wetting, and vice versa for droplets on the H-terminated (hydrophobic) surfaces (**Figure 4.5**).

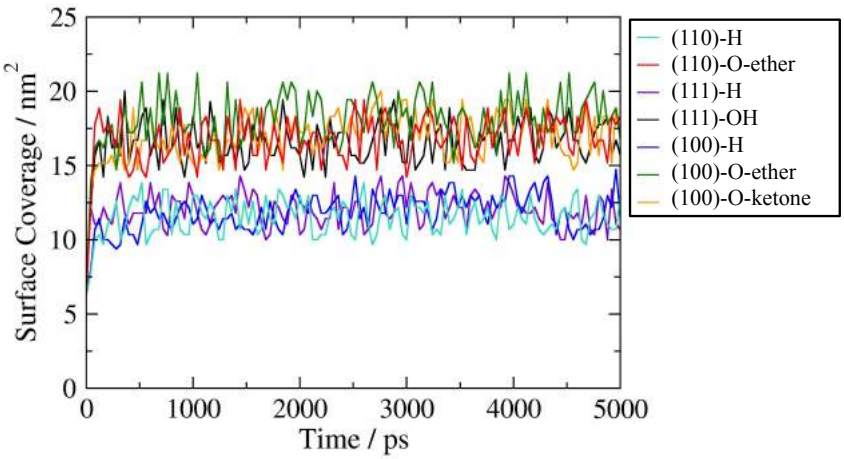

***Figure 4.5**: Surface coverage of a water droplet (428 water molecules) as a function of time on (110), (111) and (100) H-terminated (hydrophobic) and O-terminated (hydrophilic) diamond surfaces.*

Snapshots of the equilibrated water droplets were compared to the experimental profiles. The simulated and experimental water droplets on each surface are shown in **Figure 4.6** along with the contact angle for that snapshot. Both simulation and experiment displayed qualitatively similar drop shape profiles, with a clear difference in wetting observed on the O– (hydrophilic), compared to the H– (hydrophobic), terminated surfaces (**Figure 4.6**) *i.e.* greater wetting observed on the hydrophilic surfaces in accordance with the experiments. The average contact angle for each surface was measured on both the simulated and experimental profiles using the conic section method (see Chapter 3, section 3.11.3). Variance in the experimental values was calculated as the standard deviation over 5 repeats. Variance in the simulation was calculated as the standard deviation over 5 snapshots of the equilibrated droplet. The simulation and experimental contact angles were in agreement (**Table 4.2**) indicating that the chosen force field parameters capture the expected water behaviour on diamond.

Table 4.2*: Contact Angles of water droplets on simulated and experimental (110), (111) and (100) hydrophobic (H-terminated) and hydrophilic (O-terminated) diamond surfaces. Experimental and simulated H-terminated surfaces are terminated by a single (–H) group. Experimental O-terminated surfaces are a mixture of surface groups, whereas the simulated surface is a single termination as indicated.*

Surface	Simulation Contact Angle / deg	Experimental Contact Angle / deg
(110) H-terminated	84.1 ± 6.0	78.9 ± 6.6
(110) O-terminated (simulation: C-O-C)	47.8 ± 1.5	45.5 ± 6.0
(111) H-terminated	74.1 ± 7.1	77.5 ± 3.6
(111) O-terminated (simulation: OH)	39.2 ± 9.1	48.9 ± 3.5
(100) H-terminated	84.6 ± 3.7	89.2 ± 5.7
(100) O-terminated (simulation: C–O–C)	43.4 ± 4.9	38.3 ± 5.6
(100) O-terminated (simulation: C=O)	46.0 ± 5.6	38.3 ± 5.6

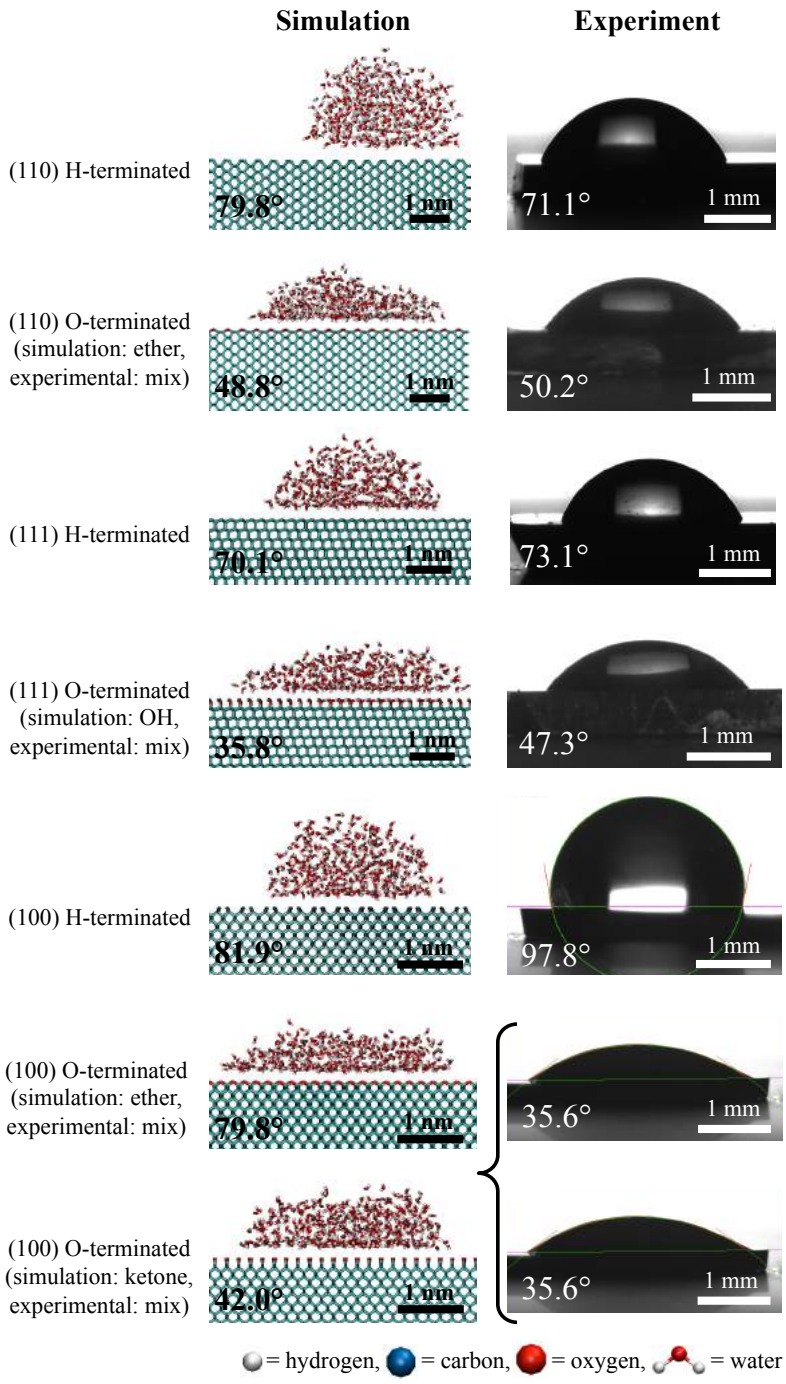

Figure 4.6*: Snapshots of typical water droplet profiles on simulated and experimental diamond surfaces with the corresponding contact angle. All experimental diamond surfaces were O-terminated by acid cleaning so that they constitute a mix of different –O groups.*

4.4.2 Snapshots of the Diamond Surfaces

Snapshots of the diamond-water interface for each model diamond surface are presented in **Figure 4.7**.

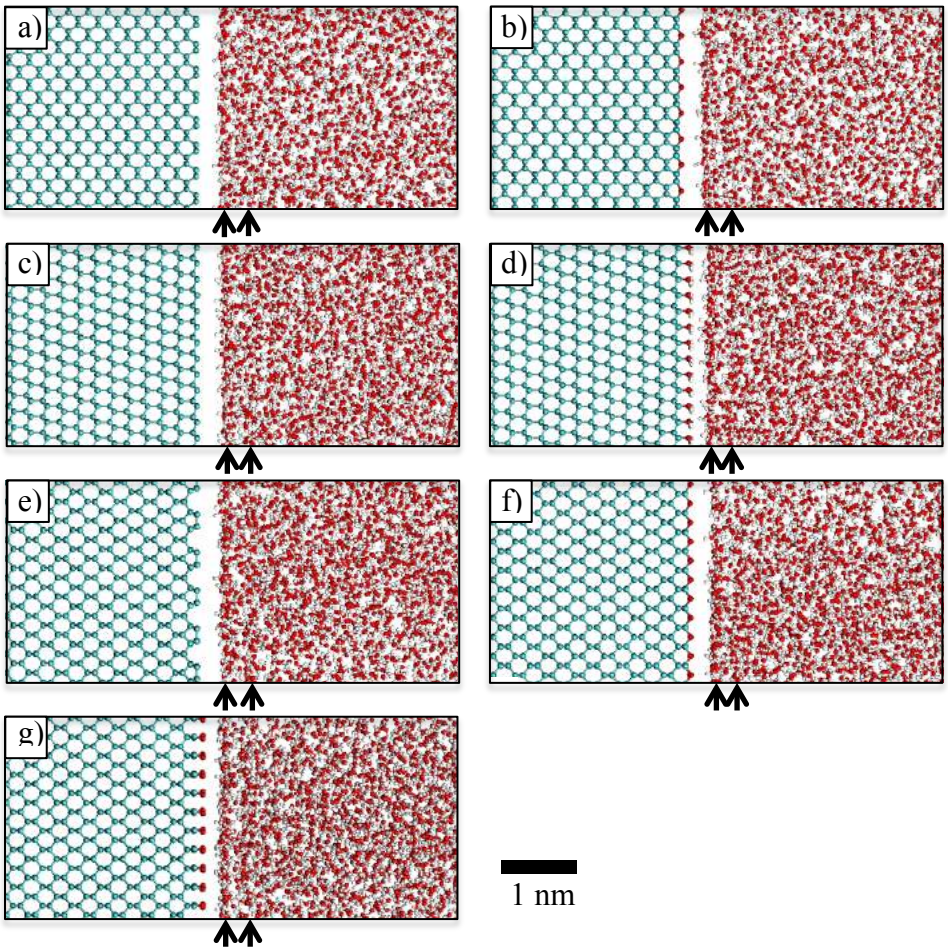

***Figure 4.7**: Snapshots of the diamond-water interface for (a) (110) H-terminated, (b) (110) O-ether-terminated, (c) (111) H-terminated, (d) (111) OH-terminated, (e) (100) H-terminated, (f) (100) O-ether-terminated, and (g) (100) O-ketone-terminated model diamond surfaces. Water ordering can be observed close to each diamond surface. Arrows indicate approximate positions of the first and second structured water regions.*

The lateral arrangement and extent of protrusion varies between each surface (see Figure 4.1). This results in each diamond slab presenting a different pattern and surface chemistry to the interfacial water causing the water to exist in different chemical and physical environments that influence the way it interacts. It is noted that the OH groups on the (111) OH-terminated surface provide the greatest protrusion from the surface, closely followed by the (100) O-ketone-terminated surface. Both of the (110) models have small cavities on their surfaces located between the zigzag chains of surface atoms. The (100) H-terminated surface has the most pronounced

indentations of all the surfaces, due to the surface reconstruction of dangling bonds along the diagonal within the plane creating extended cavities either side. In contrast, the (111) surfaces and (100) O-ether-terminated surface have very flat, closed geometries due to the closely packed OH groups on the (111), and C–O–C groups bridging the voids within the plane of the reconstructed (100) surface. All of the surfaces cause water to order into structured accumulation and depletion layers. The first two water accumulation regions for each surface have been highlighted as arrows in **Figure 4.7**. Water structuring near both hydrophobic and hydrophilic surfaces is a common phenomena that has been reported by experimental studies for numerous solid-water systems.[80] We observe that, similar to other surfaces, the mere presence of the diamond slab, independent of surface structure or chemistry, causes disruption in the bulk water network.

4.4.3 Water Structure perpendicular to Diamond Surfaces

Mass density profiles of the water structure as a function of distance away from each surface are shown in **Figure 4.8**. Mass density was chosen in order to compare the results to the experimental bulk mass density of water of 1000 kg m^{-3}. Error bars placed on the water density profiles were calculated by block averaging over 200 ps intervals. Uncertainties in the peak position were calculated as the standard deviation of the position in three separate 5 ns blocks of the MD run. The zero point of reference for each surface is the first peak in the diamond carbon density distribution (mean position of the uppermost layer of C atoms).

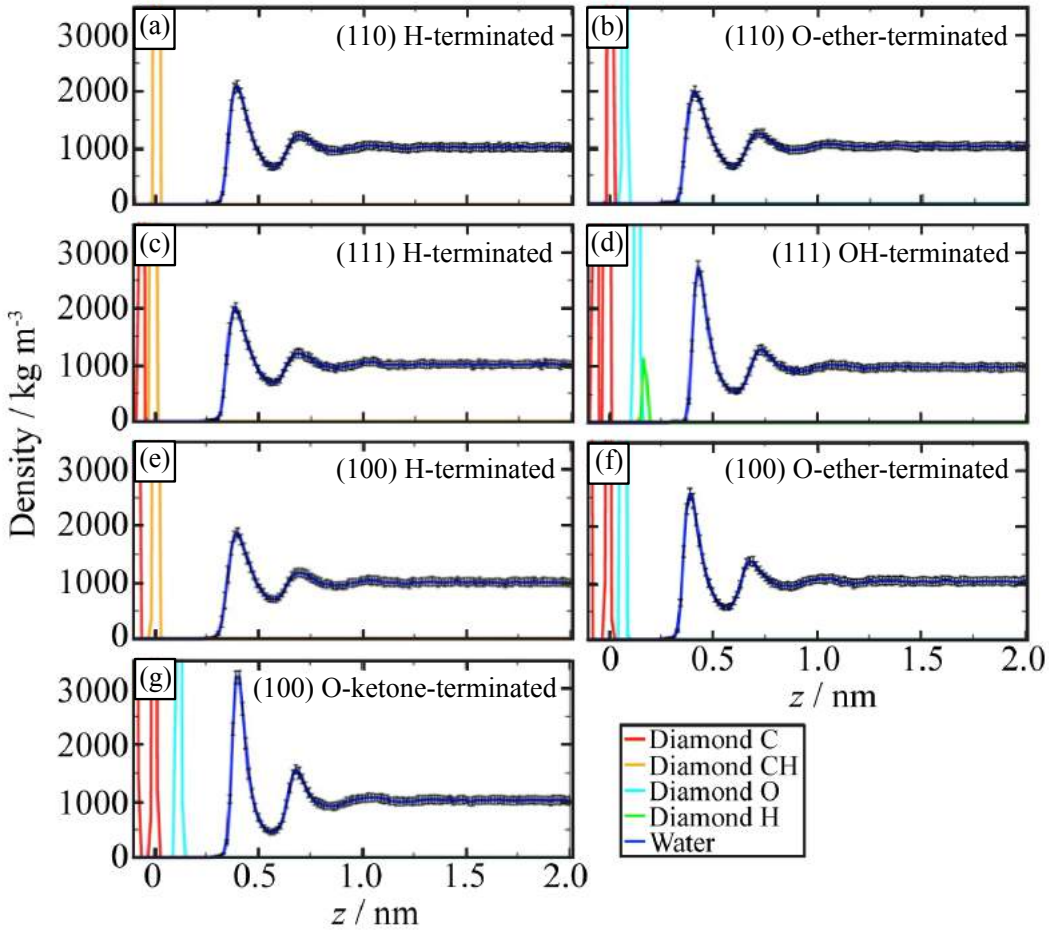

***Figure 4.8**: Density profiles of the diamond-water interface for (a) (110) H-terminated, (b) (110) O-ether-terminated, (c) (111) H-terminated, (d) (111) OH-terminated, (e) (100) H-terminated, (f) (100) O-ether-terminated, and (g) (100) O-ketone-terminated model diamond surfaces.*

All diamond surfaces display a similar trend in interfacial water ordering, namely, at least two distinct regions of alternating water accumulation and depletion exist when moving along the *z*-direction into bulk. We note that, for all surfaces, the density of water in the first and second structured layers is significantly greater than bulk, indicating that the structural properties of water are altered at diamond interfaces (**Figure 4.8**). The density profiles show interfacial layering of water exists within z = 1.3 nm away from all diamond surfaces. This is of a similar length-scale reported by MD studies of other surfaces, for example, features are reported up to 1.2

nm from α-quartz surfaces,[9], 1.25 nm from Pt(111),[81] and ~ 1.0 nm from a generic model hydrophobic surface.[82]

For each surface, the peak of the first layer of structured water lies between z = 0.390 nm and z = 0.429 nm and the density shows the greatest variation from bulk. This is followed by a depletion region where the water density is reduced below bulk density, and then a second peak in the water density for an additional layer of structured water between z = 0.678 nm and z = 0.735 nm. After a subsequent depletion region, a third structured water region can be observed with the peak existing between z = 1.005 and z = 1.093 nm. Any features beyond this are too weak to be classified, as the deviation in water density decreases along the z-direction until it settles at bulk value (1000 kg m^{-3}).

The existence of a ~ 1 nm adsorbed water region on both O– and H–terminated diamond surfaces is in agreement with HREELS experiments that have reported a thin (~ 1 nm) physisorbed water layer on diamond surfaces,[76, 83] that is responsible for an observable surface conductivity on H-terminated insulating diamond.[84] As physisorption is governed by non-bonded interactions, this agreement gives further confidence in the force field. It is also noted that the position of the first structured water peak near to the hydrophobic surfaces (~ 0.40 nm) is in agreement with neutron scattering experiments that measured the structured water peak to be < 0.5 nm away from a hydrophobic carbon surface.[85]

Whilst the density profiles show similar distributions, variations between each surface can be observed by (1) the position of the first structured water layer (section 4.4.3.1), (2) the water density within each structured layer (section 4.4.3.2), and (3) the prominence of the structured water regions (section 4.4.3.3).

4.4.3.1 Position of the Structured Water Layers

The positions of the first, second and third peak maxima in the water density, corresponding to the first, second and third layers of structured water, respectively, are outlined in **Table 4.3**, along with the width of each accumulation region and distance between them *i.e.* width of each depletion region.

Table 4.3*: Positions of structured water peaks, the width of each structured water region and distance between them for each diamond surface. The zero point of reference is defined as the position of the topmost carbon layer for each surface.*

Surface	Position of 1st water layer (nm)	Position of 2nd water layer (nm)	Position of 3rd water layer (nm)	Width of 1st water layer (nm)	Distance between 1st & 2nd peaks (nm)	Width of 2nd water layer (nm)	Distance between 2nd & 3rd peaks (nm)	Width of 3rd water layer (nm)
(110)-H	0.39 ± 0.01	0.70 ± 0.02	1.06 ± 0.02	0.13 ± 0.01	0.31 ± 0.02	0.16 ± 0.02	0.36 ± 0.02	0.21 ± 0.03
(110)-O-ether	0.41 ± 0.02	0.72 ± 0.02	1.05 ± 0.01	0.15 ± 0.02	0.31 ± 0.03	0.16 ± 0.02	0.33 ± 0.02	0.26 ± 0.04
(111)-H	0.40 ± 0.01	0.69 ± 0.01	1.03 ± 0.03	0.14 ± 0.01	0.29 ± 0.01	0.17 ± 0.01	0.34 ± 0.03	0.22 ± 0.02
(111)-OH	0.43 ± 0.01	0.73 ± 0.02	1.07 ± 0.03	0.13 ± 0.02	0.30 ± 0.02	0.16 ± 0.01	0.34 ± 0.03	0.25 ± 0.03
(100)-H	0.39 ± 0.01	0.69 ± 0.01	1.01 ± 0.02	0.15 ± 0.02	0.30 ± 0.01	0.16 ± 0.02	0.32 ± 0.02	0.21 ± 0.02
(100)-O-ether	0.39 ± 0.02	0.68 ± 0.01	1.06 ± 0.03	0.14 ± 0.01	0.29 ± 0.02	0.16 ± 0.02	0.38 ± 0.03	0.24 ± 0.02
(100)-O-ketone	0.41 ± 0.01	0.68 ± 0.02	1.03 ± 0.02	0.12 ± 0.02	0.27 ± 0.02	0.14 ± 0.02	0.35 ± 0.02	0.23 ± 0.02

It is of note that the position of the first water peak on (100) H-terminated diamond (0.39 nm) is in close agreement with DFT studies of this surface,[43, 45] where the optimal position for a physisorbed water molecule is calculated at a distance of 0.39 – 0.41 nm between water O and the topmost layer of carbon atoms.[43] In addition, the first structured water peaks lie at similar positions to the first water peaks observed by Netz *et al.*, near model diamond-like surfaces (*i.e.* ~ 0.32 – 0.41 nm).[6]

The position of the water relative to the surface is dependent on two factors: (1) topology of the surface that may cause spatial constraints, (2) intermolecular van der Waals and electrostatic interactions *e.g.* the different surface partial charges may influence the non-bonded interactions with water. In fact, there may be a tradeoff

between these phenomena *i.e.* by sitting at a further distance away from O-terminated surfaces the oxygen may be in an optimal position for C–O intermolecular interactions (and vice versa for optimal C–H intermolecular interactions). However, no significant difference is observed in the water positioning close to the different diamond surface (**Table 4.3**).

For the H-terminated surfaces, the partial charges are the same on all surfaces (CH united-atoms). This indicates that the differing surface topographies and van der Waals interactions do not have a strong influence on the water ordering. For the O-terminated surfaces, the first water peak lies slightly further away from the (111) OH-terminated surface compared to all other surfaces. This variation can be attributed to topography, where the protrusion in the *z*-direction of the C–OH group on this surface forces the nearest water to retreat further away. For the O-terminated surfaces, when measuring the distance from the surface O to the first water peak *i.e.* accounting for the different carbon-oxygen topographies, differences exist *i.e.* the first peak lies at a distance of 0.25 ± 0.01 nm on (110) O-ether–, 0.29 ± 0.01 nm on (111) OH–, 0.24 ± 0.02 nm on (100) O-ether-, and 0.29 ± 0.01 nm on (100) O-ketone-terminated surface away from the respective surface oxygen groups. This indicates that intermolecular forces must have a significant effect on the interaction with water, and in particular, strongly influences water close to (100) O-ketone-terminated and (111) OH-terminated surfaces.

The width of the structured water layers is observed to be over half the size of the interstitial depletion regions *i.e.* widths of 0.12 – 0.15 nm (first structured), 0.28 – 0.31 nm (first depletion), 0.14 – 0.16 nm (second structured), and 0.32 – 0.38 nm (second depletion). This indicates an approx. single layer of oriented water molecules in the first and second structured water regions, and ~ 1 – 2 molecular water layers in

the depletion regions. The regions increase in size as a function of *z*-distance from each diamond surface due to the water becoming more disordered as it approaches bulk. The width of the structured regions, in conjunction with the water density within them, can provide a first indication of the packing ability of the water related to hydrogen bond network. All surfaces display structured water regions of similar width, but containing water of varying densities. This suggests that certain diamond surfaces drive water molecules to pack more closely in these distinct regions. The water density is discussed in the following section.

4.4.3.2 Water Density within the Accumulation Peaks

The density of water in each structured accumulation region measured as the deviation away from bulk for each surface is presented in **Table 4.4**. Uncertainties in the water density in each region were calculated as the standard deviation in three separate 5 ns blocks of the MD run.

***Table 4.4**: Water densities within the three prominent accumulation regions close to different model diamond surfaces. The dimensions of the regions are outlined in Table 4.3, with the first corresponding to the closest region to the surface, and subsequent regions at greater distances along the z-axis towards bulk.*

Surface	Water density in first accumulation region (kg m^{-3})	Water density in second accumulation region (kg m^{-3})	Water density in third accumulation region (kg m^{-3})
(110)-H	2090 ± 100	1219 ± 70	1053 ± 62
(110)-O-ether	2154 ± 100	1244 ± 64	1059 ± 72
(111)-H	2011 ± 85	1202 ± 83	1056 ± 66
(111)-OH	2739 ± 123	1294 ± 88	1027 ± 80
(100)-H	1877 ± 84	1178 ± 72	1052 ± 73
(100)-O-ether	2567 ± 102	1380 ± 75	1076 ± 67
(100)-O-ketone	3200 ± 118	1564 ± 83	1068 ± 66

On all diamond surfaces, the water density is greatest within the first structured water layer and deceases as a function of increasing *z*-distance towards bulk water density (1000 kg m^{-3}) (**Table 4.4**). Furthermore, the density of the first layer of structured water is always observed to be greater close to the O– compared to

H– terminated surfaces (**Table 4.4**), and significantly higher on the (100) O-ketone-terminated surface (3200 ± 118 kg m^{-3}) compared to all other surfaces. The same trends were observed for the water density profiles close to hydrophobic and hydrophilic silica surfaces.[86] We note that the density of the first structured water layers close to the hydrophilic surfaces are in agreement with Netz *et al.*, who reported the density of the structured water peak near an ideal hydrophilic diamond-like surface to be ~ 2400 kg m^{-3}.[6]

As the density of water in the first structured region close to the O-terminated surfaces are on average higher than the H-terminated (**Table 4.4**), it is apparent that the O-terminated diamond surfaces may cause interfacial water to undergo a greater structural change compared to their H-terminated counterparts. The (100) O-ketone-terminated surface has the greatest impact on the local water environment, causing the largest first structured water density (3200 ± 118 kg m^{-3}) in the smallest region suggesting that the water must pack tightly. The water density drops to similar values in the second structured water layer for all diamond surfaces except the (100) O-ketone-terminated surface (**Table 4.4**), which does not align with the rest until the third structured layer. This indicates that diamond surfaces have a short range effect *i.e.* these surfaces may influence the binding energy of a species but not the diffusion as it approaches the surface.

The higher water densities on the (100) O-ketone-terminated surface are considered due to the strong non-bonded interactions (electrostatic and van der Waals) of the C=O functional groups with the surrounding water, given that it has a large partial charge distribution (± 0.58 e) and greatest LJ potential well depth, ε, of the surface functional groups (ε of 0.5957 kJ mol^{-1} for C=O) compared to all other surfaces (see Figure 4.4). This causes the greatest influence on the interfacial water

over the longest range. The presence of C=O on diamond surfaces has been reported to have a strong influence on the adsorption of inner-sphere species *i.e.* species that probe the interfacial water region to specifically adsorb with the surface.[87] It is possible that this strong water ordering may influence the adsorption. This is discussed further in Chapter 5.

4.4.3.3 Prominence of the Structured Water Regions

The prominence of a structured water region is distinguished by its projection from bulk in a well-defined manner *i.e.* the sharpness of the peak. We note that the (100) O-ketone-terminated surface has the most prominent interfacial water ordering, with all three structured peaks clearly defined and greatly pronounced from bulk. The (111) OH-terminated surface has the second most pronounced peaks. All of the H-terminated surfaces have similar, less-prominent profiles. Similar to ideas already discussed, it is clear that the degree of prominence is related to the ordering effect of the underlying surface groups, with the O-terminated surfaces showing, in general, more prominent water peaks but of varying degree due to their differing surface topology and charge, and H-terminated surfaces of lesser prominence. The similarity in the H-terminated water profiles (**Figure 4.8**) suggests that these surfaces may have a comparatively similar influence on the interfacial water. This is further explored in in the following sections.

4.4.4 Water Structure parallel to Diamond Surfaces

The structure of the underlying surface can influence the lateral ordering of interfacial water.[9] To investigate this property on diamond, lateral density profiles of the first layer of structured water were produced. **Figure 4.9** displays the water lateral

density profiles for the (100) H-terminated surface along with the lateral density profile and VMD snapshot of the surface carbon groups for comparison.

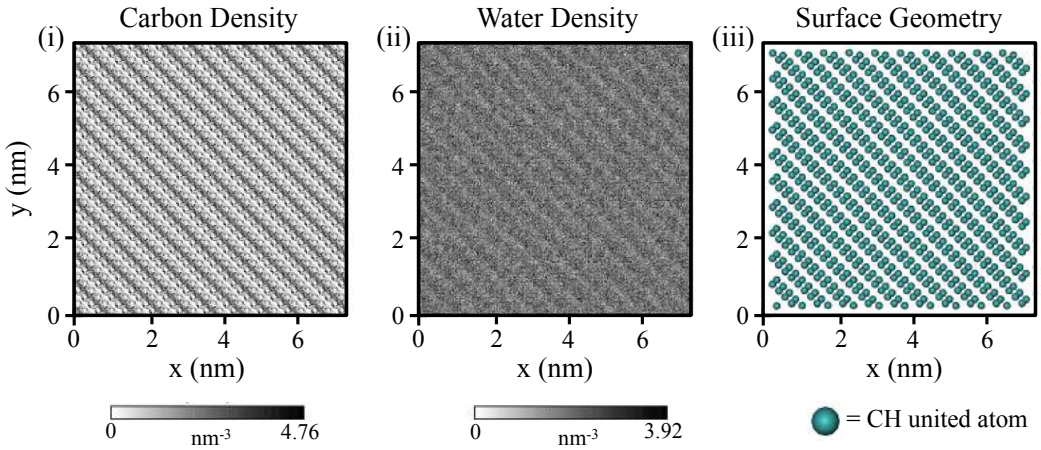

Figure 4.9*: Lateral density profiles of (i) uppermost surface layer of carbon atoms and (ii) first layer of structured water on the (100) H-terminated surface. For further comparison, (iii) displays the surface geometry captured using VMD.*

The water clearly orders into a diagonal pattern close to the (100) H-terminated surface (**Figure 4.9**). In particular, regions of high CH density match to regions of low water density, suggesting the interfacial water arranges to reduce contact with the hydrophobic surface groups. The reconstruction of (100) H-terminated diamond causes a distinct diagonal pattern of voids on the surface (**Figure 4.9**i and iii). This diagonal pattern is mirrored in the interfacial water that penetrates close enough to the surface *i.e.* within the first structured water region (**Figure 4.9**ii), which shows that the positioning of the CH groups does play a significant role in water arrangement on this surface. These results are supported by similar MD studies that have also reported the influence of crystallographic orientation, namely open voids, on interfacial water penetration.[9]

All of the H-terminated diamond surfaces display similar density profiles along the *z*-direction (shown in Figure 4.8), which suggests they have similar long

range interfacial water ordering. Therefore, the lateral ordering observed close to the (100) H-terminated surface is considered to be a short range ordering effect *i.e.* confined to the immediate proximity of the surface, without significant disruption to the long range water structure. Lateral water patterning was not observed on any of the other diamond surfaces. This suggests either that water cannot penetrate close enough to these surfaces to be laterally ordered by the underlying surface arrangement, not enough water can penetrate close enough for large-scale 2D ordering to be effective, or that the underlying surface pattern is not distinct enough to affect the water structure. Given that the (100) H-terminated surface has the most open void regions compared to the other diamond surfaces, yet the 2D water patterning is still relatively faint, it would not be unreasonable to expect water ordering to only occur on this surface.

4.4.5 Water Orientation close to Diamond Surfaces

To further understand the effect of diamond surface structure on local water arrangement, the orientation distribution of water molecules as a function of distance from each surface was calculated. **Figure 4.10** displays the water orientation plots for each diamond surface obtained by averaging over 0.02 nm intervals in the *z*-direction over the 15 ns run. Standard error bars were calculated for each profile by block averaging. The plots have been displayed on the same *z*-distance baseline as the density profiles, where $z = 0$ is the position of the uppermost carbon layer of each surface. To aid interpretation, each plot has been superimposed with the corresponding water density profile.

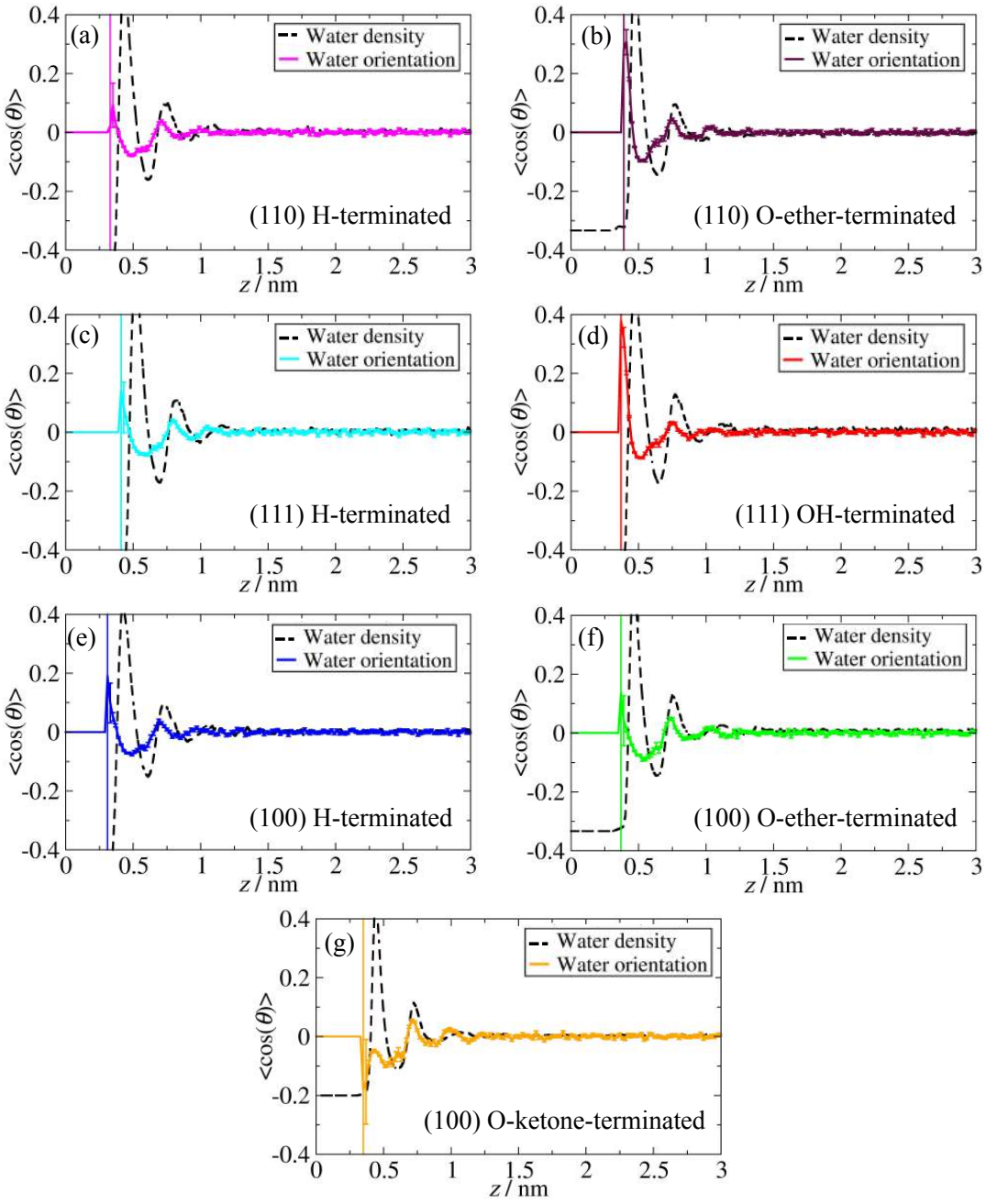

***Figure 4.10**: Orientation of water molecules close to each surface (a) – (g) (solid coloured) with respect to the surface normal. The corresponding water density profiles (black dashed) are outlined beneath each profile. The density profiles have been scaled in the y-axis to achieve comparison and are not representative of the true density values (kg m^{-3}) (scale factors: (a), (c), (d) by 2×10^3; (b), (f) by 3×10^3; and (g) by 5×10^3). Standard error bars are plotted on each profile. The largest error bar closest to each surface is due to poor sampling in that interval, with few water molecules penetrating into that region.*

In **Figure 4.10**, we observe that the orientational distribution of the water aligns with the density profiles *i.e.* on average, water in each accumulation layer can be associated with a particular orientation. We see that for all surfaces, the water orientation alternates between values greater and less than $\langle\cos(\theta)\rangle = 0$ as a function of z-distance from the surface. The value of $|\langle\cos(\theta)\rangle|$ decreases with increasing z-distance from the surface, until it converges to zero at bulk. Here, the water is randomly oriented causing the cosine values to average out.

For all surfaces, the first orientation peak occurs between $z = 0.31$ and $z = 0.41$ nm, lying in a region of low water density bordering the first layer of structured water (**Figure 4.10**). The orientation of the water molecules that penetrate this region are illustrated in **Figure 4.11**. It is noted that the water can exist at any 360° rotation about the dipole moment or reflection across the z-axis. However, the illustrated water orientation is considered most likely based on the underlying surface geometry.

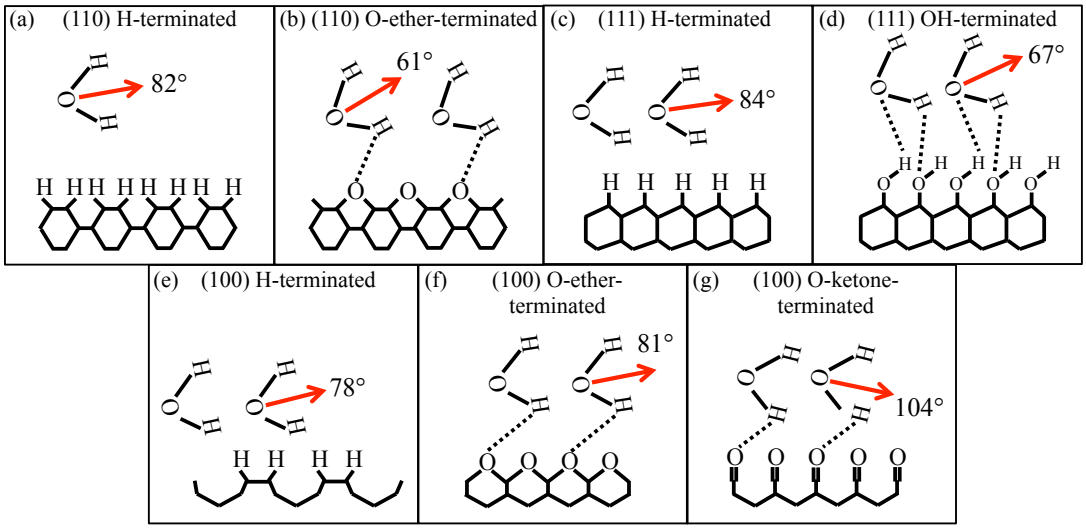

***Figure 4.11**: Illustration depicting the orientation, θ, of water molecules that penetrate closest to each of the diamond surfaces (a) – (g) for $0 < \theta < 180°$ i.e. the reflection in the y-plane is equally valid. The dipole vector is shown as a red arrow along with the angle of the dipole with respect to the surface normal (z-axis). Bonds shown are either covalent (solid black) or the hypothesized surface-water hydrogen bonds (dashed black). Not to scale.*

The water molecules close to the three H-terminated surfaces are arranged with one hydrogen pointing towards the surface and one towards bulk water *i.e.* (110): 82°, (111): 78° and (100): 84° relative to the surface normal (**Figure 4.11**). Given that the water cannot form strong hydrogen bonds with the surface hydrogens, the orientation of water molecules closest to these surfaces is considered dependent entirely on the underlying surface geometry. Due to the voids on the (100) H-terminated surface, the water molecules rotate to reduce clashes by slotting within the gaps between the underlying hydrogens (78° relative to the surface normal), as previously observed in the lateral density ordering (see section 4.4.4). Water molecules can thus penetrate closest to this diamond surface *i.e.* ~ 0.3 nm (see Figure 4.10**)**. Water molecules close to the (111) and (110) H-terminated diamond surfaces are orientated using a similar reasoning to the (100) H-terminated, with the water molecules penetrating to a lesser extent due to their closed surface geometries.

Water orientation close to the O-terminated diamond surfaces is influenced by the underlying surface structure and hydrophilic chemistry. The closest water molecules assemble into the ideal orientation and *z*-position to maximise hydrogen bonding to the surface O groups (**Figure 4.11**). The position of the water molecules is further determined by the surface structure, with water molecules able to penetrate closer to the flat (100) O-ether-terminated surface and further away from the (111) OH-terminated surface due to spatial restraints from the protruding OH groups. The dipole vector initially points away from all the surfaces except for the (100) O-ketone-terminated surface where the vector points towards the surface (104° relative to the surface normal) (**Figure 4.11**). This enables the water hydrogens to interact favourably with the underlying C=O groups.

We note that water orientation is also influenced by the surrounding waters, with the aim to maximise water-water hydrogen bonding to form the strongest possible hydrogen bonding network. This is particularly relevant in the region closest to the surface where fewer water molecules exist, so they must orientate themselves in such a way to ensure the greatest possibility for hydrogen bonding. For the O-terminated surfaces, there is a trade-off between bonding to the surface and to the surrounding waters. This is particularly noticeable on the (111) OH-terminated surface (67° relative to the surface normal), where the preferential water orientation can support the formation of two hydrogen bonds with the surface, whilst also maintaining a network of inter-water hydrogen bonds. As water cannot form hydrogen bonds with the H-terminated surfaces, the orientation distribution observed on these surfaces is due to water arranging in such a way as to maximise water-water hydrogen bonding. Hydrogen bonding is discussed in greater detail in the next section.

As a further aid to comparison of the surfaces, an overlay of the orientation profiles in Figure 4.10 is shown in **Figure 4.12**.

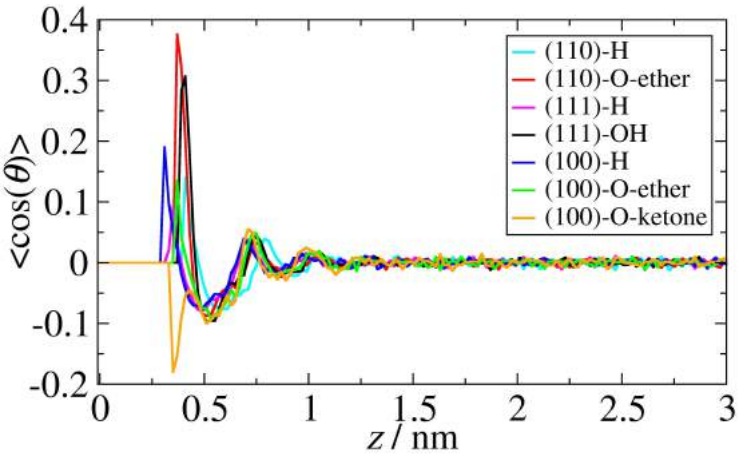

***Figure 4.12**: Water orientation close to different diamond surfaces as a function of distance along the z-axis, where z = 0 is the mean position of the topmost surface carbon layer for each surface and θ is the angle between the surface normal and dipole vector of each water molecule.*

Beyond the initial water ordering, the interfacial water orientation switches to negative <cos((θ)> values between z = 0.49 nm and z = 0.60 nm for all surfaces, corresponding to water in the first accumulation layer of the surfaces (**Figure 4.12**). Water molecules that occupy this region are oriented with the dipole vector pointing towards the surface so that one hydrogen atom is pointing towards the oriented water underneath and another points out into bulk (~ 95°). The water orientation closest to each surface has an impact on the subsequent orientational layers, causing the water to orientate relative to the initial configuration shown by the differing peak heights between the profiles (**Figure 4.12**). The water orientation continues to fluctuate between pointing towards and away from the surfaces with increasing z-distance but to a lesser extent each time as it tails to reach zero (**Figure 4.12**). All surfaces display similar orientation distributions beyond the first water peak but shifted to slightly different positions dependent on the packing of the water that will be a consequence of the initial water orientation. It is worth noting that the ordering effect is relatively weak on all surfaces *i.e.* the water orientation never deviates far from random.

Averaging was tested over seven different interval sizes ranging from 0.005 pm – 0.05 nm for each surface, shown in **Figure 4.13**. All plots displayed the same trend proving that the outcome is not affected by the interval size.

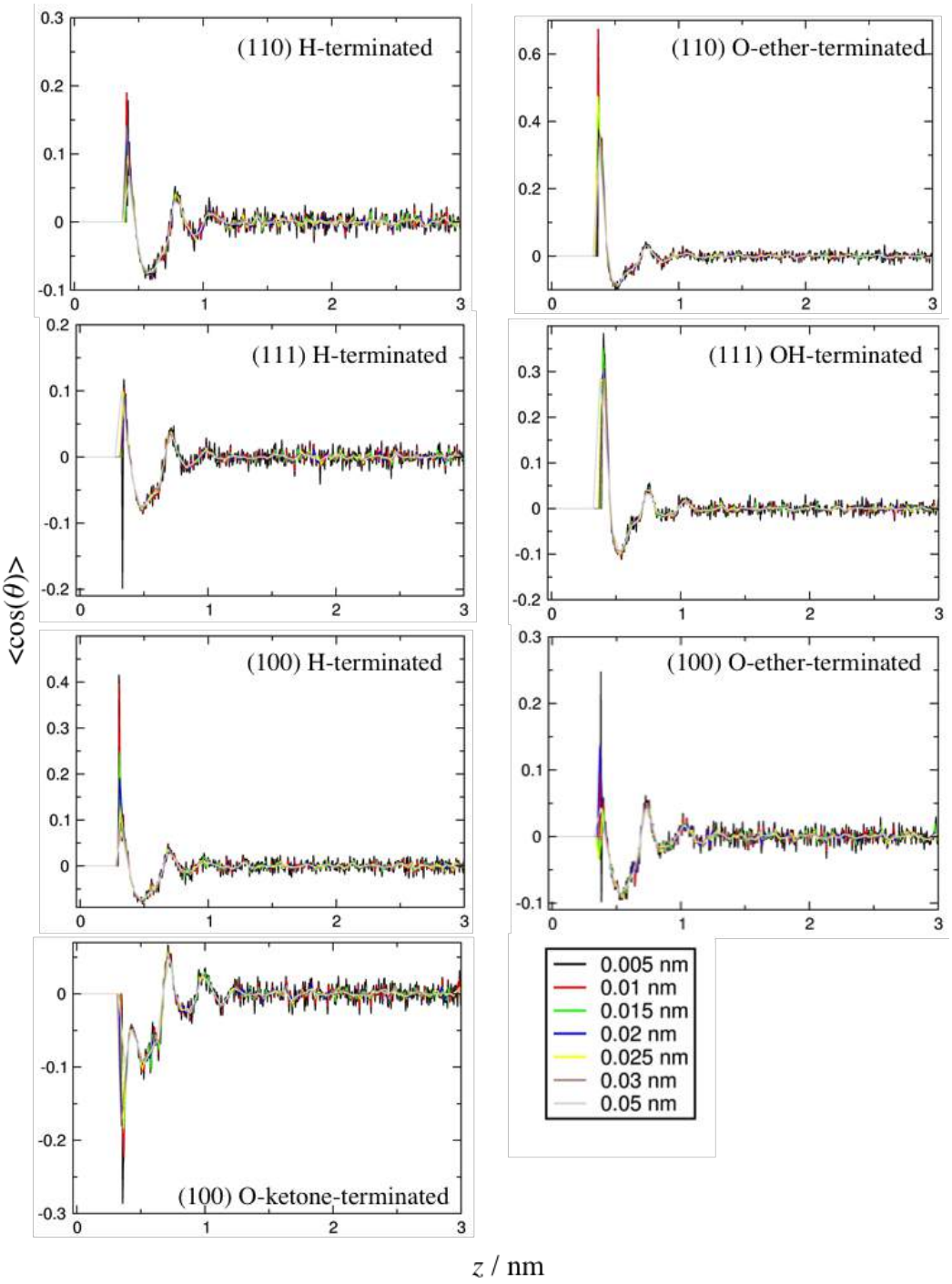

***Figure 4.13**: Water orientation plots for the seven different surfaces averaging over seven different interval sizes. The water structure follows the same trend for all surfaces confirming that the result is independent of the choice of interval.*

4.4.6 Hydrogen Bonding close to Diamond Surfaces

Hydrogen bonding frequently plays a key role in the adsorption of molecules to surfaces.[88] In terms of water adsorption, the reorganisation of hydrogen bonds at

surfaces is linked to the interfacial water orientation and dynamics. It has already been observed that the interfacial water orientation and density vary significantly from bulk properties (see Figure 4.10). Hence, the hydrogen bond network will also differ from bulk, as it is closely related to the water density.[89] An ordered network of water-water hydrogen bonds can be produced either as a consequence of hydrogen bonding between water and hydrophilic surfaces,[86] or due to the hydrophobic effect on water near hydrophobic surfaces.[90] The number of hydrogen bonds formed in four interfacial regions as a function of simulation time (15 ns) is shown in **Figure 4.14** and the average number of hydrogen bonds per water molecule detailed in **Table 4.5**. Uncertainties in the number of hydrogen bonds in each region were calculated as the standard deviation of number of hydrogen bonds in three separate 5 ns blocks of the MD run.

Table 4.5*: Number of hydrogen bonds per water molecule in each structured water region close to different diamond surfaces. Bulk is defined as a region between 2 and 2.2 nm from each surface. Surface-water hydrogen bonds have been omitted for the H-terminated diamond models, as these surfaces cannot form standard hydrogen bonds with water. Interfacial water is defined as any water molecule that exists per timeframe (4 ps) at a position between the surface and the peak of the first accumulation region. Water-water hydrogen bonds were calculated in the three structured water peaks at increasing z-distance from the surface (see Table 4.3 for the positions of each region).*

System	No. of Hydrogen Bonds per Water Molecule				
	Surface-Interfacial Water	Water-water in first structured region	Water-water in second structured region	Water-water in third structured region	Bulk
(110)-H	–	2.71 ± 0.10	1.55 ± 0.07	1.93 ± 0.08	3.75 ± 0.08
(110)-O-ether	0.14 ± 0.02	2.98 ± 0.10	1.57 ± 0.07	3.08 ± 0.10	3.74 ± 0.08
(111)-H	–	2.65 ± 0.09	1.47 ± 0.08	0.82 ± 0.06	3.74 ± 0.09
(111)-OH	0.30 ± 0.02	3.33 ± 0.12	1.49 ± 0.08	0.71 ± 0.05	3.68 ± 0.08
(100)-H	–	2.47 ± 0.10	1.46 ± 0.08	2.09 ± 0.09	3.77 ± 0.08
(100)-O-ether	0.04 ± 0.01	3.10 ± 0.12	1.54 ± 0.08	2.70 ± 0.11	3.77 ± 0.08
(100)-O-ketone	0.06 ± 0.01	3.43 ± 0.13	1.37 ± 0.08	2.44 ± 0.09	3.78 ± 0.08
				Overall Bulk:	1.75 ± 0.08

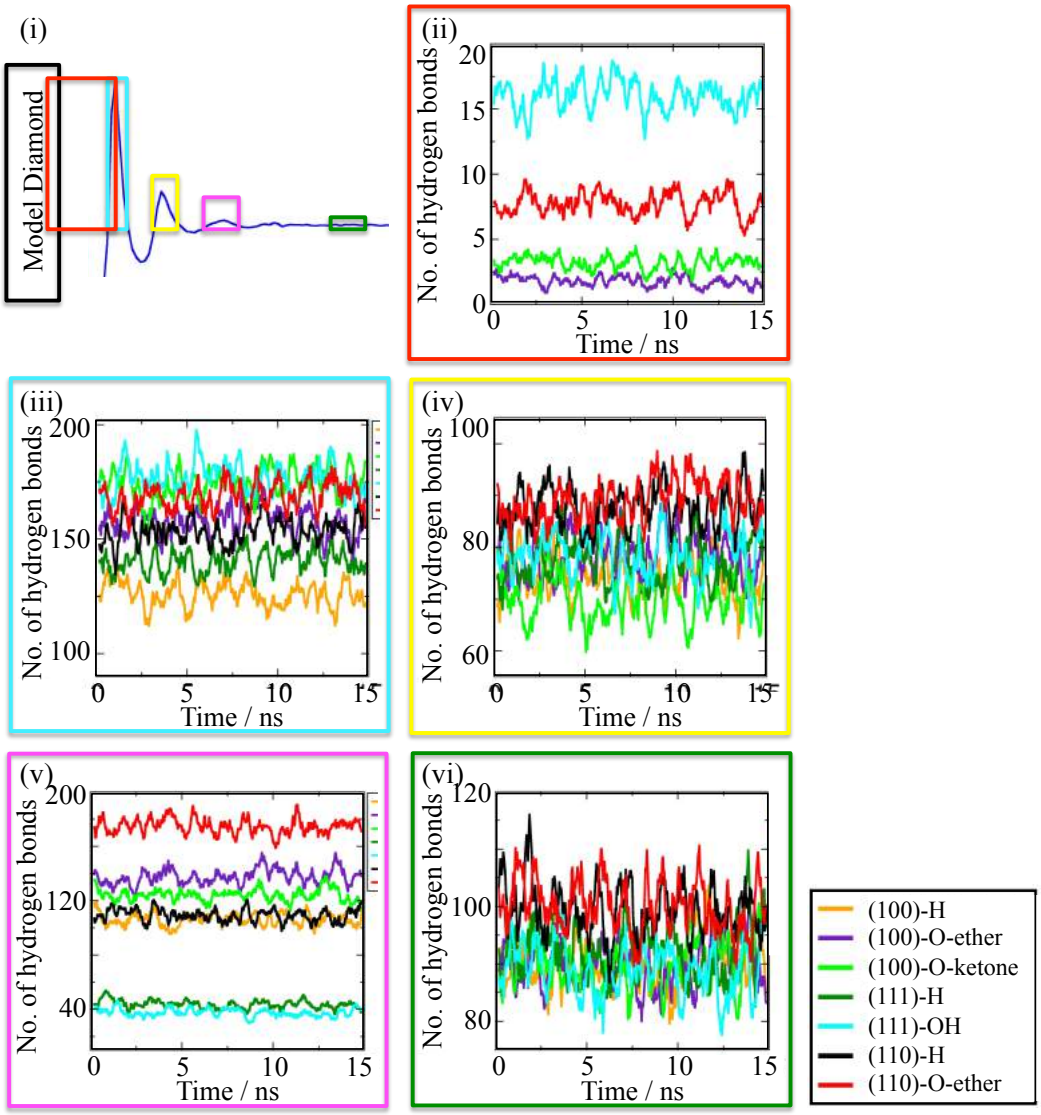

***Figure 4.14**: Plots displaying the number of hydrogen bonds over time in different interfacial water regions close to each model diamond surface. The number was calculated every timeframe (4 ps) over a 15 ns simulation run. The regions of interest are highlighted on the model density profile in (i). The number of diamond-water hydrogen bonds at each surface was calculated in (i), The number of water-water hydrogen bonds was calculated in the (iii) first, (iv) second, and (v) third layers of structured water, as well as (vi) in bulk.*

Hydrogen bonds in five different environments were considered: (1) surface-interfacial water, where interfacial water is defined as any water molecule that exists per timeframe (4 ps) at a position between the surface and the peak of the first structured region, (2) water-water in the first structured water region, (3) water-water in the second structured water region, (4) water-water in the third structured water

region, and (5) bulk defined as a 0.2 nm region starting at 2 nm away from each surface (**Figure 4.14**).

The number of hydrogen bonds per nm^2 is shown to vary from bulk in all of the four interfacial regions (**Table 4.5**). A significantly greater number of hydrogen bonds are observed in the first layer of structured water on all surfaces (**Table 4.5**), which corresponds to the higher density of water within this region. It is clear that the presence of any diamond surface disrupts the bulk water properties. This causes the water to order in such a way that they pack closely together creating a high density, structured hydrogen bond network in the immediate proximity of the surface.

Whilst O-terminated surfaces can form surface-water hydrogen bonds, water can only weakly hydrogen bond to H-terminated surfaces. Hence, the driving force for water ordering close to H-terminated diamond surfaces is to maximise the water-water hydrogen bonds, whereas water close to O-terminated diamond surfaces have a trade off between surface-water and water-water hydrogen bonding.

Significant differences are observed for the surface-water hydrogen bonding at O-terminated surfaces. The (111) OH-terminated surface has the greatest number of surface-water hydrogen bonds (0.30 nm^{-2}). This surface has double the number of available sites compared to the other surfaces, with both the O and H atoms available to bond, and has the highest density of surface sites (36.24 O/H atoms per nm^2). Interestingly, the number of hydrogen bonds to the (110) O-ether-terminated surface (0.14 nm^{-2}) is greater than to the (100) O-ether- (0.04 nm^{-2}) and O-ketone- (0.06 nm^{-2}) terminated surfaces despite fewer available sites *i.e.* (110)-O-ether-terminated: 22.23 O atoms per nm^2, (100)-O-ether/ketone-terminated: 31.45 atoms per nm^2. This is either due to fewer water molecules penetrating into this low density region within the simulation time, which is likely for the (100) O-ketone-terminated surface as the

water is positioned further away from the C=O groups, or that the topology of the (100) surface may hinder hydrogen bond formation.

All surfaces have a greater number of water-water hydrogen bonds in the first structured layer compared to bulk (~ 1.5 times bulk) (**Table 4.5**). This is a result of reorganisation of the water due to surface hydrogen bonding on the O-terminated surfaces, and the hydrophobic effect on the H-terminated surfaces. Furthermore, the O-terminated surfaces have a higher average number of water-water hydrogen bonds in the first structured region compared to the H-terminated surfaces (**Table 4.5**). This correlates with the higher water density close to O-terminated surfaces (see section 4.4.3) and indicates that the formation of surface-water hydrogen bonds on O-terminated surfaces has a greater influence on ordering than the hydrophobic effect.

Beyond the first water peak, the average number of hydrogen bonds in the second and third structured water regions oscillates rather than directly converging to a fixed bulk value (**Table 4.5**). This further highlights that the hydrogen bond network is closely linked to the varying water density (see section 4.4.3) and water orientation (section 4.4.5). It is believed that the hydrogen bond network will continue to fluctuate with increasing *z*-distance until it reaches bulk properties before or at 2 nm from the surface.

Curiously, despite the higher water density in the second structured region, the (110) and (100) surfaces display fewer water-water hydrogen bonds in the second compared to the third structured regions (**Table 4.5**). As well as bonding with each other, water in the second structured region will bond with water in the two surrounding depletion regions and orientate itself accordingly. These bonds are not counted in the analysis, which may account for the lower number of hydrogen bonds in this region. However, if this a real result it indicates that a region with a

particularly strong hydrogen bond network exists on the border of the interfacial water and bulk that may inhibit adsorption to the surface, as the molecule would have to break through this region in order to advance towards the surface. As a note, it can be postulated that the oscillation of the hydrogen bond network along *z* (fluctuating with water orientation) may have a different frequency for different surfaces depending on the ordering effect. This will likely correlate to the oscillation frequency of the orientation profiles (see Figure 4.10). These postulations are of considerable interest for future work.

4.4.7 Hydrogen Bond Lifetimes close to Diamond Surfaces

The strength and durability of the hydrogen bond network formed by the adsorbed water close to each diamond surface was explored by calculating the hydrogen bond time correlation functions for interfacial water hydrogen bonds over time. The data was then fit to a decaying exponential approximation in order to calculate hydrogen bond lifetimes.[91] The final time correlation functions for surface-water and water-water hydrogen bonds are shown in **Figure 4.15**. Three repeats of the correlation functions were run for each surface all of which generated close to identical exponential approximations. This displays the rate at which hydrogen bonds break over time and can thus provide an estimate for the lifetime of the interfacial hydrogen bonds.

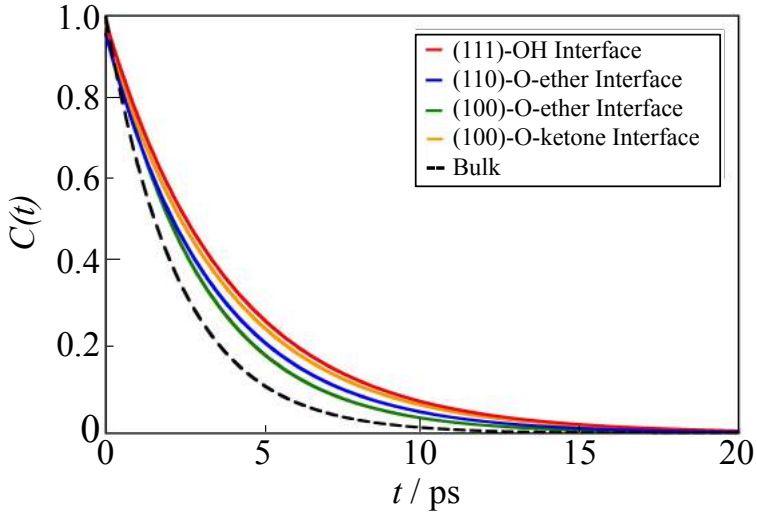

***Figure 4.15**: Typical time correlation function C(t) for the decay of surface-water hydrogen bonds for four O-terminated diamond surfaces compared to bulk water-water hydrogen bonds that exist at t = 0 and have all broken by t = 20 ps.*

The surface-water hydrogen bond correlation functions decay at a slower rate compared to the water-water hydrogen bonds in bulk. This suggests that hydrogen bonding of water to the O-terminated diamond surfaces lasts longer than the water-water hydrogen bonds in bulk, and indicates that surface-water hydrogen bonds have a significant influence on the dynamics of interfacial water. The variation between the bulk profiles is considered due to the error in bulk rather than long-range influence of the surface given that the bulk values are taken at 2 nm, which is a sufficiently large distance away from each surface.

The surface-water hydrogen bond lifetimes were calculated from the correlation functions and are presented in **Table 4.6**. Variances in hydrogen bond lifetimes were calculated from three independent repeats of the surface-water hydrogen bond correlation functions. We note that this methodology considers only hydrogen bonds formed in the region at $t = 0$ and does not include bonds that subsequently reform after breaking.

***Table 4.6**: Lifetimes of surface-water hydrogen bonds at O-terminated diamond surfaces, and water-water hydrogen bonds at bulk for all diamond surfaces averaged over five repeat simulations. Water molecules that exist at time t=0 within the region of interest were considered, where the first surface monolayer was defined as the region 0 – 0.45 nm from the surface. The zero point of reference was the uppermost layer of carbon atoms. The bulk monolayer was defined as a region of width 0.45 nm starting at 2 nm away from the surface. The overall bulk lifetime was obtained by averaging over the bulk monolayer lifetimes of all surfaces.*

System	Average Hydrogen Bond Lifetime of water in the first surface monolayer (ps)
(110)-O-ether	2.74 ± 0.19
(111)-OH	3.28 ± 0.14
(100)-O-ether	2.88 ± 0.23
(100)-O-ketone	3.14 ± 0.18
Bulk	2.37 ± 0.12

The surface-water hydrogen bonds have longer lifetimes compared to water-water hydrogen bonds in bulk (**Table 4.6**). Surface-water hydrogen bonds to the (111) OH-terminated surface last the longest (3.28 ps), followed by hydrogen bonds to the (100) O-ketone-terminated surface (3.14 ps), and the other two O-terminated diamond surfaces have relatively similar surface-water hydrogen bonds lifetimes *i.e.* 2.88 ps on (100) O-ether-terminated and 2.74 ps on (110) O-ether-terminated surfaces. The number of water-water hydrogen bonds close to O-terminated surfaces is connected to the increased lifetime of surface-water hydrogen bonds. For example, as the (111) OH-terminated surface has the greatest number of water-water hydrogen bonds, a highly ordered region is formed close to the surface that is less mobile than bulk (see section 4.4.8), causing less disruption to the surface-water hydrogen bonds, hence enabling them to last longer.

4.4.8 Lateral Diffusion Coefficients of Water close to Diamond Surfaces

The lateral diffusion coefficient of water in the first structured layer was calculated in order to ascertain the effect of diamond surface structure on the local water mobility (**Table 4.7**).

***Table 4.7**: Lateral diffusion coefficient of water molecules close to each model diamond surface and at bulk. Only water molecules that exist within the first surface monolayer at both time t = 0 and t = 10 ps were considered, where the first surface monolayer was defined as water molecules within 0.45 nm (first accumulation layer) of the surface and the zero point of reference taken as the topmost layer of carbon atoms. The bulk monolayer was defined as a region of width 0.45 nm starting at 2 nm away from the surface. The overall bulk lateral diffusion coefficient was obtained by averaging over the bulk lateral diffusion coefficients of all surfaces.*

System	Lateral Diffusion Coefficient of water in the first surface monolayer (1×10^{-5} cm^2 s^{-1})
(110)-H	4.75 ± 0.51
(110)-O-ether	1.20 ± 0.10
(111)-H	4.83 ± 0.53
(111)-OH	0.76 ± 0.03
(100)-H	4.06 ± 0.89
(100)-O-ether	0.90 ± 0.15
(100)-O-ketone	0.59 ± 0.05
Bulk	4.20 ± 0.13

It is clear that the lateral diffusion of water close to the three H-terminated surfaces is similar to bulk, whereas the lateral diffusion close to the four O-terminated surfaces is significantly reduced by over 70% of the bulk lateral diffusion coefficient. The interaction of water with the surface O groups thus causes considerably slower water mobility close to the surface.

The slower mobility can be ascribed to the formation of surface-water hydrogen bonds on the O-terminated diamond surfaces that have a stronger ordering effect on interfacial water (see section 4.4.6) compared to the hydrophobic effect on H-terminated surfaces. The surface-water hydrogen bonds are considered strong enough to impede interfacial water movement, causing slower lateral diffusion coefficients and longer hydrogen bond lifetimes. In particular, water close to the (100) O-ketone-terminated surface is the slowest. Although this surface has fewer surface-water hydrogen bonds (**Table 4.5**) of shorter lifetime (**Table 4.7**) compared to other O-terminated surfaces, it has the greatest water ordering effect *i.e.* highest water density within the narrowest structured regions (see Figure 4.8) compared to all other

surfaces. These factors combine to produce the slowest water mobility close to this diamond surface.

Despite significant water structuring close to H-terminated diamond surfaces, it appears the ordering due to the hydrophobic effect is not strong enough to modify the interfacial water dynamics. This is confirmed by the lowest water density and ~ 90° water orientation in the first structure water region of all H-terminated surfaces, suggesting the water properties were already tending closer to bulk. It is noted that the slower mobility and difference in strength of the interfacial hydrogen bonds on O- compared to H- terminated diamond may cause differences in the binding of species to these surfaces.

All surfaces the water still retain some degree of mobility, unlike titania[92] or highly hydroxylated silica,[93] where the water is known to freeze close to the surface. This indicates that the diamond-water hydrogen bonding on all surfaces is not strong enough to restrain the water into an ice-like configuration.

4.4.9 Ions near Diamond Surfaces

Aqueous solvents are regularly used as a supporting electrolyte in electrochemical reactions. To mimic the electrolyte solution, K^+ and Cl^- ions were added to the diamond-water simulations. Five different KCl concentrations were investigated, 0.01 M, 0.1 M, 0.2 M, 0.5 M and 1.0 M. These concentrations were chosen since they represent the typical range used in electrochemical experiments. The water density profiles in the presence of the different concentrations of KCl for each surface are shown in **Figure 4.16**.

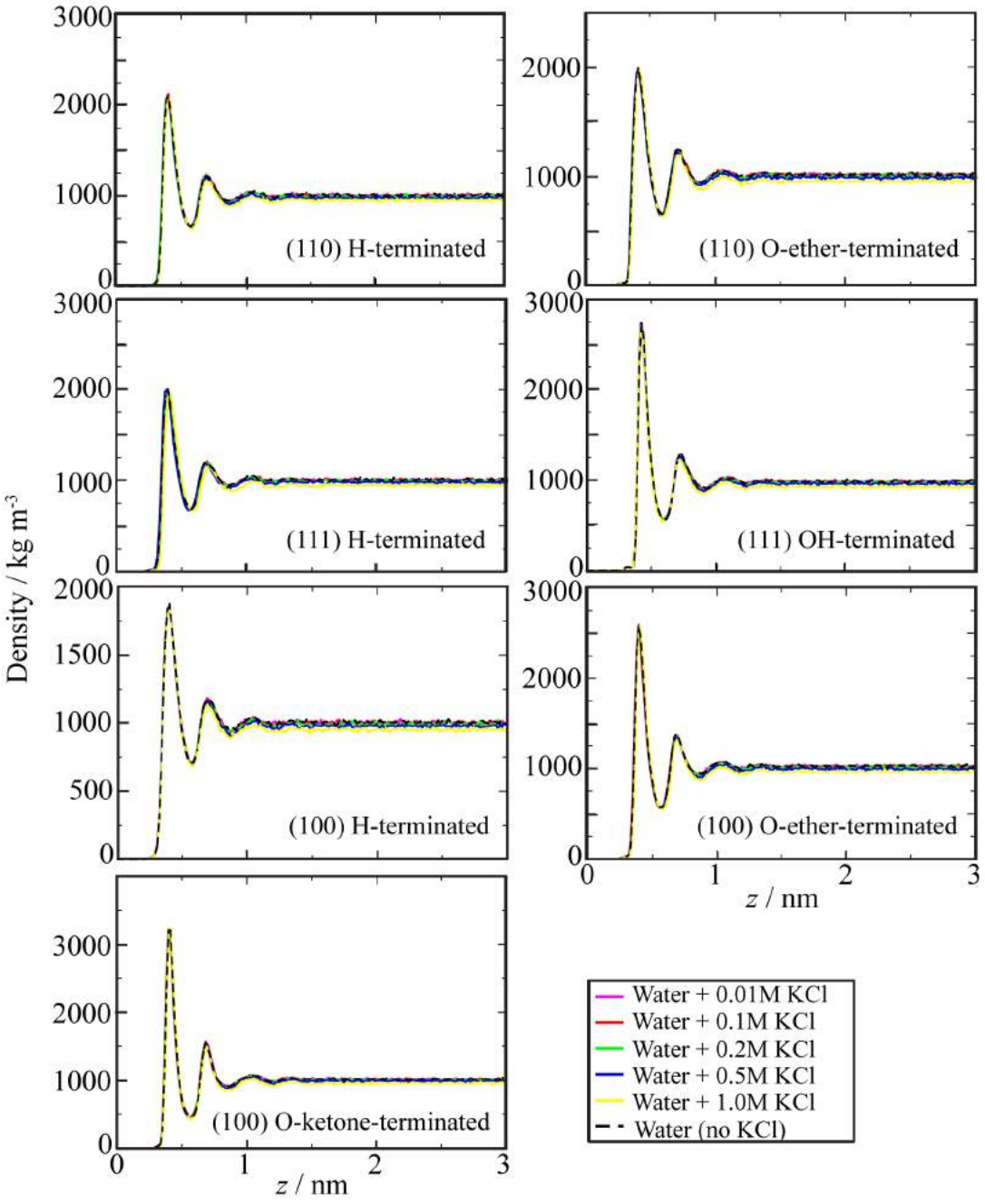

***Figure 4.16**: Water density profiles in the presence of none (dashed black), 0.01 M (pink), 0.1 M (red), 0.2 M (green), 0.5 M (blue), and 1.0 M (yellow) KCl for each diamond surface. No significant difference is observed between the profiles.*

The water density profiles in the presence of the ions are identical to the profiles without ions on all diamond surfaces (**Figure 4.16**). Thus, the diamond interfacial water structure is not affected by ions up to 1 M in concentration on this simulation scale.

The density profiles for K^+ and Cl^- ions close to each diamond surface for the five different KCl concentrations are displayed in **Figure 4.17**.

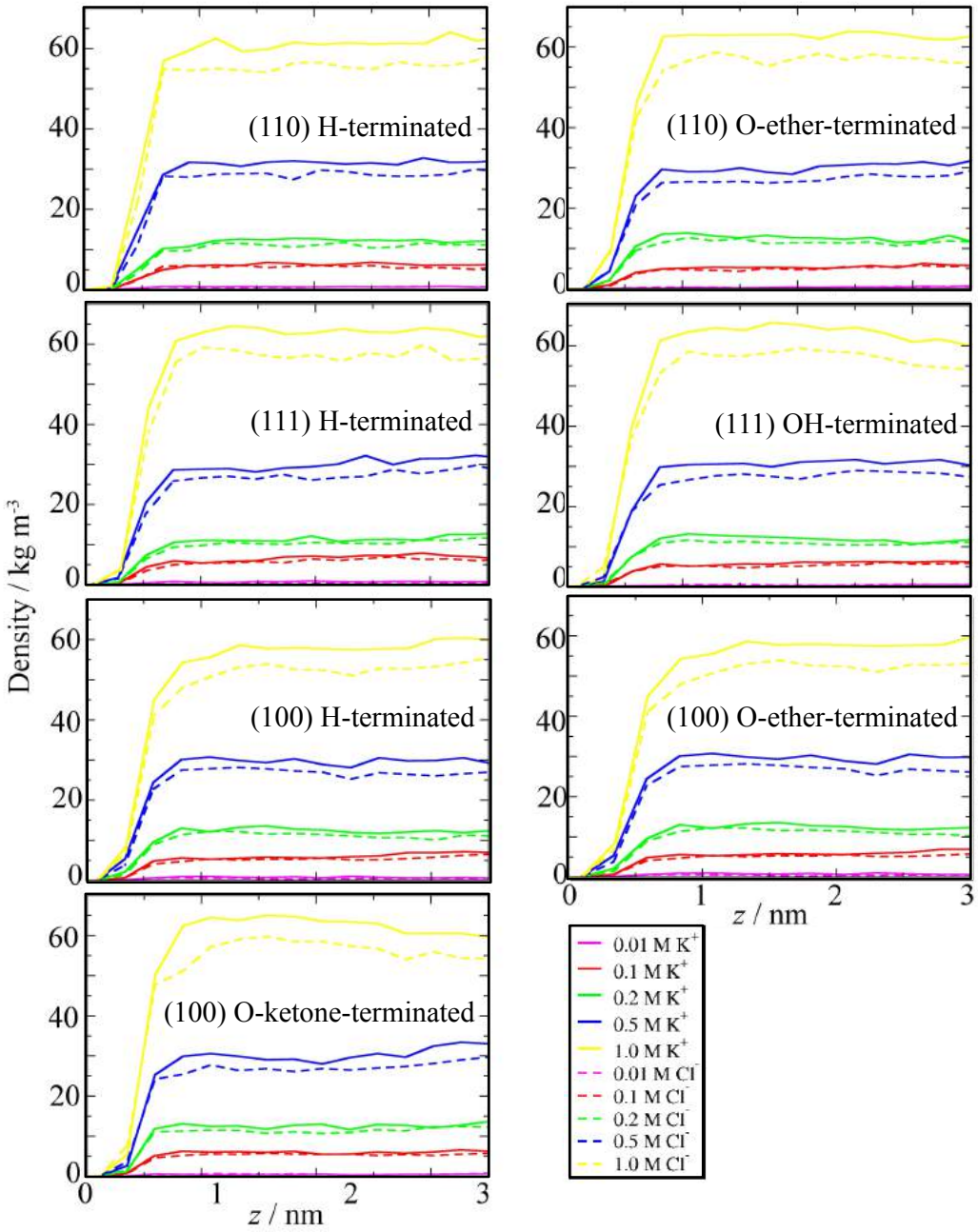

Figure 4.17: *Density profiles of K^+ (solid) and Cl^- (dashed) ions of varying concentrations close to each diamond surface, where z = 0 denotes the uppermost layer of carbons. Ion densities always increase at the position of the peak of the first structured water and then remain constant as a function of z-distance.*

We observe in **Figure 4.17** that both K^+ and Cl^- ions position themselves to the left of the peak of first structured water for each surface. This suggests that the

hydrogen bond network in the first layer of water is considerably strong to inhibit ion adsorption directly on to the diamond surfaces, and instead the ions sit where the first structured water layer tails off into the depletion region for all 0.01 M – 0.1 M ion concentrations. This aligns with the common model for electrolyte structuring on electrode surfaces, where a thin layer of water exists on the surface followed by the presence of solvated ions (see Chapter 3, section 3.4).

When diamond is used as an electrode, a potential is applied that charges the surface. This causes an electrical double layer to form *i.e.* for solvated ions to form charge layers (see Chapter 3, section 3.4). It appears that when diamond is electrically uncharged, there is insufficient drive for the ions to order themselves effectively in accordance with the surface charge. This may be particularly true for diamond surfaces as a chemically inert and catalytically unreactive material. Furthermore, whilst there will be some attraction between the surface partial charges and oppositely charged ions, it appears that these forces are not strong enough to induce observable layering effects. Decreasing the ionic concentration to < 0.01 M may help to elucidate ion layering effects *i.e.* at > 0.01 M, the ions exist in a compact region where all charges are compensated (see Chapter 3, section 3.4), whereas at < 0.01 M the electrolyte will be more diffuse thus more readily revealing ionic layering. However, whilst 'peaks' begin to appear for 0.01 M KCl, the concentration is too low for these to be considered as significant ordering (4 K^+, 4 Cl^-). It is therefore considerably difficult to capture ion structuring in our model. Applying electric fields of differing strength to the system may help to elucidate double layer formation on diamond electrodes, but this is beyond the scope of this study.

Once the ions appear, the ion density remains relatively constant out into bulk for these ion concentrations (**Figure 4.17**). Thus, the fluctuating water density along

the *z*-direction into bulk has no influence on the ion density for concentrations > 0.01 M. This suggests, for all surfaces, that the hydrogen bond network in the structured regions beyond the first is not strong enough to inhibit the movement of K^+ or Cl^- ions.

4.5 Conclusions

Atomistic MD models of diamond surfaces have been developed and utilized to provide a greater understanding of the water structuring and dynamics close to diamond surfaces. Significantly, the models have enabled comparisons of the diamond-water interface for surfaces of differing crystal orientations *e.g.* (110), (111), (100) and terminations *e.g.* H-, C-O-C, C-OH, C=O that has currently not been addressed in the literature. These include a comparison of the various properties of the interfacial water on the different diamond surfaces, such as the position of the structured water regions, density in the *z*-direction, lateral density, extension into bulk, hydrogen bonding networks, hydrogen bond lifetimes, water orientation and lateral diffusion coefficients. This information can help to optimize the surface for any diamond sensor where water plays a key role in its function (see section 4.1).

Our results show that two distinct layers of structured water exist close to all diamond surfaces, extending out by up to ~ 1.3 nm into bulk. The formation of hydrogen bonds appears to be an essential component to the interfacial water ordering. Water near H-terminated diamond surfaces experience a hydrophobic effect, where the water is forced to orient away from the surface to maximise water-water hydrogen bonding in solution. Similarly, water close to O-terminated diamond surfaces rotate into a favourable orientation and position to exploit both the surface-water and water-water hydrogen bonding capabilities. The co-operativity of hydrogen bonding extends to at least 1 nm on all diamond surfaces. The hydrogen bonding

network directly affects interfacial water dynamics, in particular there is slower water mobility and longer lifetimes of hydrogen bonds near to O-terminated diamond surfaces. Furthermore, the strength of the first structured water layer prevents K^+/Cl^- ions from adsorbing to the diamond surfaces.

Crystal orientation also effects water positioning close to the diamond surfaces. This is most pronounced on the (100) H-terminated surface, where water can penetrate into the voids on the surface causing lateral patterning. These regions of high and low density may affect the adsorption and aggregation of species to the surface since it would be easier for molecules to disrupt the regions of lower water density. Furthermore, bridging of voids by C–O–C groups prevents water from penetrating close to (100) and (110) O-ether-terminated diamond surfaces, and the protrusion of OH and C=O groups on surfaces forces water to sit further away. In general, the water sits at different positions due to a combination of topology and intermolecular interactions.

Finally, our simulations suggest that the (100) O-ketone-terminated diamond surface has the greatest influence on the interfacial water. In terms of water structure, the (100) O-ketone-terminated surface has the highest structured water densities and the most pronounced water structuring due to the favourable water orientation towards the surface to form both strong surface-water hydrogen bonds with the C=O groups and a large number of water-water hydrogen bonds in the structured regions. In terms of dynamics, this surface has a long hydrogen bond lifetime and the slowest surface-water mobility. It can be postulated that certain biomolecules may find it difficult to disrupt the strong hydrogen bond network close to diamond surfaces, in particular the (100) O-ketone-terminated diamond surface, which may influence the strength of adsorption. This is discussed further in the next chapter (Chapter 5).

4.6 Future Work

There is a wide range of possibilities for these models beyond this study. The clear extension to this work is the addition of an electric field, or corresponding surface charge induced by an applied potential, which would enable the study of the electrical double layer formation at diamond electrode-electrolyte interfaces. These models are also beneficial for a wide range of diamond-biomolecule systems in order to study the influence of diamond crystal orientation and surface termination on species adsorption.

4.7 References

[1] a) A. J. Bard, G. Denuault, C. Lee, D. Mandler, D. O. Wipf, *Acc. Chem. Res.* **1990**, *23*, 357-363; b) M. Williamson, R. Tromp, P. Vereecken, R. Hull, F. Ross, *Nat. Mater.* **2003**, *2*, 532-536; c) A. L. Barker, M. Gonsalves, J. V. Macpherson, C. J. Slevin, P. R. Unwin, *Anal. Chim. Acta* **1999**, *385*, 223-240.

[2] a) J. K. Nørskov, T. Bligaard, J. Rossmeisl, C. H. Christensen, *Nat. Chem.* **2009**, *1*, 37-46; b) G. M. Whitesides, P. E. Laibinis, *Langmuir* **1990**, *6*, 87-96.

[3] a) D. G. Castner, B. D. Ratner, *Surf. Sci.* **2002**, *500*, 28-60; b) A. Erdemir, *Tribol. Int.* **2005**, *38*, 249-256; c) B. Kasemo, *Curr. Opin. Solid St. M.* **1998**, *3*, 451-459.

[4] S. Paria, K. C. Khilar, *Adv. Colloid Interface Sci.* **2004**, *110*, 75-95.

[5] M. Maccarini, *Biointerphases* **2007**, *2*, MR1-MR15.

[6] F. Sedlmeier, J. Janecek, C. Sendner, L. Bocquet, R. R. Netz, D. Horinek, *Biointerphases* **2008**, *3*, FC23-FC39.

[7] J. N. Israelachvili, R. M. Pashley, **1983**.

[8] J. Janecek, R. R. Netz, *Langmuir* **2007**, *23*, 8417-8429.

[9] R. Notman, T. R. Walsh, *Langmuir* **2009**, *25*, 1638-1644.

[10] P. Jungwirth, D. J. Tobias, *Chem. Rev.* **2006**, *106*, 1259-1281.

[11] D. Chandler, *Nature* **2005**, *437*, 640-647.

[12] A. J. Pertsin, T. Hayashi, M. Grunze, *J. Phys. Chem. B* **2002**, *106*, 12274-12281.

[13] Y.-K. Cheng, P. J. Rossky, *Nature* **1998**, *392*, 696-699.

[14] L. B. Wright, T. R. Walsh, *J. Phys. Chem. C* **2012**, *116*, 2933-2945.

[15] C. Mottet, G. Tréglia, B. Legrand, *Phys. Rev. B* **1992**, *46*, 16018.

[16] P. S. Mdluli, N. M. Sosibo, P. N. Mashazi, T. Nyokong, R. T. Tshikhudo, A. Skepu, E. Van Der Lingen, *J. Mol. Struct.* **2011**, *1004*, 131-137.

[17] L. Ruan, H. Ramezani-Dakhel, C.-Y. Chiu, E. Zhu, Y. Li, H. Heinz, Y. Huang, *Nano Lett.* **2013**, *13*, 840-846.

[18] Y. Hong, J. Hahn, H. Kang, *J Chem. Phys.* **1998**, *108*, 4367-4370.

[19] J. Israelachvili, H. Wennerström, *Nature* **1996**.

[20] T. G. Trudeau, D. K. Hore, *Langmuir* **2010**, *26*, 11095-11102.

[21] A. A. Mungikar, D. Forciniti, *Biomacromolecules* **2004**, *5*, 2147-2159.

[22] J. Kim, P. S. Cremer, *Chem. Phys. Chem.* **2001**, *2*, 543-546.
[23] C. E. Nebel, B. Rezek, D. Shin, H. Uetsuka, N. Yang, *J. Phys. D Appl. Phys.* **2007**, *40*, 6443.
[24] L. Wei, P. Kuo, R. Thomas, T. Anthony, W. Banholzer, *Phys. Rev. Lett.* **1993**, *70*, 3764.
[25] A. Krueger, *Chem-Eur. J.* **2008**, *14*, 1382-1390.
[26] W. Yang, O. Auciello, J. E. Butler, W. Cai, J. A. Carlisle, J. E. Gerbi, D. M. Gruen, T. Knickerbocker, T. L. Lasseter, J. N. Russell, *Nat. Mater.* **2002**, *1*, 253-257.
[27] F. Liu, J. Wang, B. Liu, X. Li, D. Chen, *Diamond Relat. Mater.* **2007**, *16*, 454-460.
[28] H. S. Harned, B. B. Owen, *The Physical Chemistry of Electrolytic Solutions*, Reinhold, New York, **1959**.
[29] M. Werner, R. Job, A. Zaitzev, W. Fahrner, W. Seifert, C. Johnston, P. Chalker, *Phys. Status Solidi A* **1996**, *154*, 385-393.
[30] H. V. Patten, L. A. Hutton, J. R. Webb, M. E. Newton, P. R. Unwin, J. V. Macpherson, *Chem. Comm.* **2015**, *51*, 164-167.
[31] I. Yagi, H. Notsu, T. Kondo, D. A. Tryk, A. Fujishima, *J. Electroanal. Chem.* **1999**, *473*, 173-178.
[32] P. Strobel, M. Riedel, J. Ristein, L. Ley, *Nature* **2004**, *430*, 439-441.
[33] P. W. May, *Philos. Trans. A Math. Phys. Eng. Sci.* **2000**, *358*, 473-495.
[34] L. A. Hutton, J. G. Iacobini, E. Bitziou, R. B. Channon, M. E. Newton, J. V. Macpherson, *Anal. Chem.* **2013**, *85*, 7230-7240.
[35] T. A. Dolenko, S. A. Burikov, J. M. Rosenholm, O. A. Shenderova, I. I. Vlasov, *J. Phys. Chem. C* **2012**, *116*, 24314-24319.
[36] A. P. Sommer, D. Zhu, A. R. Mester, H.-D. Försterling, M. Gente, A. Caron, H.-J. r. Fecht, *Cryst. Growth Des.* **2009**, *9*, 3852-3854.
[37] J. A. Garrido, S. Nowy, A. Haertl, M. Stutzmann, *Langmuir* **2008**, *24*, 3897-3904.
[38] M. Sulpizi, M.-P. Gaigeot, M. Sprik, *J. Chem. Theory Comput.* **2012**, *8*, 1037-1047.
[39] A. Skelton, P. Fenter, J. D. Kubicki, D. J. Wesolowski, P. T. Cummings, *J. Phys. Chem. C* **2011**, *115*, 2076-2088.
[40] D. Argyris, N. R. Tummala, A. Striolo, D. R. Cole, *J. Phys. Chem. C* **2008**, *112*, 13587-13599.
[41] J. H. Walther, R. Jaffe, T. Halicioglu, P. Koumoutsakos, *J. Phys. Chem. B* **2001**, *105*, 9980-9987.
[42] a) S. Kerisit, D. J. Cooke, D. Spagnoli, S. C. Parker, *J. Mater. Chem.* **2005**, *15*, 1454-1462; b) J. Wang, A. G. Kalinichev, R. J. Kirkpatrick, *Geochim. Cosmochim. Acta* **2006**, *70*, 562-582.
[43] O. Manelli, S. Corni, M. Righi, *J. Phys. Chem. C* **2010**, *114*, 7045-7053.
[44] Y. Okamoto, *Phys. Rev. B* **1998**, *58*, 6760.
[45] K. Larsson, J. Ristein, *J. Phys. Chem. B* **2005**, *109*, 10304-10311.
[46] C. Sendner, D. Horinek, L. Bocquet, R. R. Netz, *Langmuir* **2009**, *25*, 10768-10781.
[47] a) D. R. Alfonso, D. A. Drabold, S. E. Ulloa, *Phys. Rev. B* **1995**, *51*, 14669; b) G. Kern, J. Hafner, *Phys. Rev. B* **1997**, *56*, 4203.
[48] B. L. Mackey, J. N. Russell, J. E. Crowell, P. E. Pehrsson, B. D. Thoms, J. E. Butler, *J. Phys. Chem. B* **2001**, *105*, 3803-3812.
[49] K. P. Loh, X. Xie, S. Yang, J. Zheng, *J. Phys. Chem. B* **2002**, *106*, 5230-5240.

[50] C. Kress, M. Fiedler, W. Schmidt, F. Bechstedt, *Phys. Rev. B* **1994**, *50*, 17697.
[51] G. Zilibotti, M. Righi, M. Ferrario, *Phys. Rev. B* **2009**, *79*, 075420.
[52] X. Zheng, P. Smith, *Surf. Sci.* **1992**, *262*, 219-234.
[53] C. Oostenbrink, A. Villa, A. E. Mark, W. F. Van Gunsteren, *J. Comput. Chem.* **2004**, *25*, 1656-1676.
[54] D. Horinek, A. Serr, M. Geisler, T. Pirzer, U. Slotta, S. Lud, J. Garrido, T. Scheibel, T. Hugel, R. Netz, *Proc. Natl. Acad. Sci.* **2008**, *105*, 2842-2847.
[55] J. Donohue, *Structures of the Elements*, Wiley, New York, US., **1974**.
[56] P. E. Lopes, V. Murashov, M. Tazi, E. Demchuk, A. D. MacKerell, *J. Phys. Chem. B* **2006**, *110*, 2782-2792.
[57] avogadro.openmolecules.net, *Avogadro: an open-source molecular builder and visualization tool. Version 1.1.1*, **2012**.
[58] C. Nebel, J. Ristein, *Thin-Film Diamond II (Semiconductors and Semimetals), Vol. 77*, Elsevier B. V., Amsterdam, Netherlands., **2004**.
[59] F. Ercolessi, J. B. Adams, *EPL-Europhys. Lett.* **1994**, *26*, 583.
[60] D. M. Huang, C. Sendner, D. Horinek, R. R. Netz, L. Bocquet, *Phys. Rev. Lett.* **2008**, *101*, 226101.
[61] a) H. J. Berendsen, D. van der Spoel, R. van Drunen, *Comput. Phys. Commun.* **1995**, *91*, 43-56; b) B. Hess, C. Kutzner, D. Van Der Spoel, E. Lindahl, *J. Chem. Theory Comput.* **2008**, *4*, 435-447; c) E. Lindahl, B. Hess, D. Van Der Spoel, *J. Mol. Model.* **2001**, *7*, 306-317; d) D. Van Der Spoel, E. Lindahl, B. Hess, G. Groenhof, A. E. Mark, H. J. Berendsen, *J. Comput. Chem.* **2005**, *26*, 1701-1718.
[62] H. J. Berendsen, J. P. M. Postma, W. F. van Gunsteren, A. DiNola, J. Haak, *J. Chem. Phys.* **1984**, *81*, 3684-3690.
[63] T. Darden, D. York, L. Pedersen, *J. Chem. Phys.* **1993**, *98*, 10089-10092.
[64] B. Hess, H. Bekker, H. J. Berendsen, J. G. Fraaije, *J. Comput. Chem.* **1997**, *18*, 1463-1472.
[65] W. Humphrey, A. Dalke, K. Schulten, *J. Mol. Graphics* **1996**, *14*, 33-38.
[66] P. Jedlovszky, J. Brodholt, F. Bruni, M. Ricci, A. Soper, R. Vallauri, *J. Chem. Phys.* **1998**, *108*, 8528-8540.
[67] A. Luzar, D. Chandler, *Nature* **1996**, *379*, 55-57.
[68] D. Petrini, K. Larsson, *J. Phys. Chem. C* **2007**, *111*, 795-801.
[69] S. H. Yang, D. A. Drabold, J. B. Adams, *Phys. Rev. B* **1993**, *48*, 5261.
[70] G. Kern, J. Hafner, J. Furthmüller, G. Kresse, *Surf. Sci.* **1996**, *352*, 745-749.
[71] F. Liu, J. Wang, B. Liu, X. Li, D. Chen, *Chin. Sci. Bull.* **2006**, *51*, 2437-2443.
[72] S. Sque, R. Jones, P. Briddon, *Phys. Rev. B* **2006**, *73*, 085313.
[73] H. Tamura, H. Zhou, K. Sugisako, Y. Yokoi, S. Takami, M. Kubo, K. Teraishi, A. Miyamoto, A. Imamura, N. Mikka, *Phys. Rev. B* **2000**, *61*, 11025.
[74] D. Petrini, K. Larsson, *J. Phys. Chem. C* **2008**, *112*, 3018-3026.
[75] a) M. De La Pierre, M. Bruno, C. Manfredotti, F. Nestola, M. Prencipe, C. Manfredotti, *Mol. Phys.* **2014**, *112*, 1030-1039; b) B. Davidson, W. Pickett, *Phys. Rev. B* **1994**, *49*, 11253.
[76] A. Laikhtman, A. Lafosse, Y. Le Coat, R. Azria, A. Hoffman, *Surf. Sci.* **2004**, *551*, 99-105.
[77] L. M. Struck, M. P. D'Evelyn, *J. Vac. Sci. Tech. A* **1993**, *11*, 1992-1997.
[78] H. Sasaki, M. Aoki, H. Kawarada, *Diamond Relat. Mater.* **1993**, *2*, 1271-1276.
[79] J. V. Macpherson, *Phys. Chem. Chem. Phys.* **2015**, *17*, 2935-2949.

[80] a) H. Yamauchi, S. Kondo, *Colloid Polym. Sci.* **1988**, *266*, 855-861; b) O. Dulub, B. Meyer, U. Diebold, *Phys. Rev. Lett.* **2005**, *95*, 136101; c) P. A. Thiel, T. E. Madey, *Surf. Sci. Rep.* **1987**, *7*, 211-385.
[81] M. Predota, A. Bandura, P. Cummings, J. Kubicki, D. Wesolowski, A. Chialvo, M. Machesky, *J. Phys. Chem. B* **2004**, *108*, 12049-12060.
[82] C. Y. Lee, J. A. McCammon, P. Rossky, *J. Chem. Phys.* **1984**, *80*, 4448-4455.
[83] R. Akhvlediani, S. Michaelson, A. Hoffman, *Surf. Sci.* **2010**, *604*, 2129-2138.
[84] F. Maier, M. Riedel, B. Mantel, J. Ristein, L. Ley, *Phys. Rev. Lett.* **2000**, *85*, 3472.
[85] M. C. Bellissent‐Funel, R. Sridi‐Dorbez, L. Bosio, *J. Chem. Phys.* **1996**, *104*, 10023-10029.
[86] S. H. Lee, P. J. Rossky, *J. Chem. Phys.* **1994**, *100*, 3334-3345.
[87] a) H. Notsu, I. Yagi, T. Tatsuma, D. A. Tryk, A. Fujishima, *J. Electroanal. Chem.* **2000**, *492*, 31-37; b) M. C. Granger, M. Witek, J. Xu, J. Wang, M. Hupert, A. Hanks, M. D. Koppang, J. E. Butler, G. Lucazeau, M. Mermoux, *Anal. Chem.* **2000**, *72*, 3793-3804.
[88] K. A. Melzak, C. S. Sherwood, R. F. Turner, C. A. Haynes, *J. Colloid Interface Sci.* **1996**, *181*, 635-644.
[89] M. A. Henderson, *Surf. Sci. Rep.* **2002**, *46*, 1-308.
[90] M. Ø. Jensen, O. G. Mouritsen, G. H. Peters, *J. Chem. Phys.* **2004**, *120*, 9729-9744.
[91] F. W. Starr, J. K. Nielsen, H. E. Stanley, *Phys. Rev. E* **2000**, *62*, 579.
[92] A. Skelton, T. Walsh, *Mol. Simul.* **2007**, *33*, 379-389.
[93] A. Anderson, W. R. Ashurst, *Langmuir* **2009**, *25*, 11549-11554.

Chapter 5

Biomolecular Adsorption at Model Hydrophobic and Hydrophilic Diamond Surfaces: Free-Energy Calculations of Dopamine and Serotonin Adsorption

5.1 Overview and Key Advances to Knowledge in this Chapter

Detection and treatment of neurodegenerative diseases in one of the greatest challenges for medicine in the 21st century. A key challenge in this area is the sensing of neurotransmitters *e.g.* dopamine and serotonin that are essential in the cause and cure of neurodegenerative conditions. Diamond electrochemical biosensors have the potential to simultaneously detect dopamine and serotonin to a high degree of accuracy. Optimisation of the diamond surface is essential in order to enhance the detection capability of the diamond device to its full potential *e.g.* using the ideal diamond surface that binds dopamine/serotonin strongly enough to facilitate reactions but weakly enough to reduce electrode fouling. This requires a fundamental understanding of the binding of dopamine/serotonin with different hydrophobic and hydrophilic diamond surfaces, which is currently not understood in the field, with no molecular studies probing the diamond-water-neurotransmitter interface in existence.

In this chapter, the diamond-water models developed in the Chapter 4 were extended to diamond-water-dopamine/serotonin systems. Potential of mean force

calculations were performed and free energy profiles were obtained for the adsorption of a single dopamine/serotonin molecule to different diamond surfaces with a range of crystal orientations and hydrophobic/hydrophilic surface terminations. The different diamond surfaces were ranked on how strongly they bind dopamine/serotonin, with C=O groups displaying the strongest binding and H-terminated surfaces the weakest for both molecules. Serotonin was observed to adsorb more strongly than dopamine to all diamond surfaces. Through careful structural analysis of dopamine functional groups during adsorption, the pathway of dopamine/serotonin adsorption was revealed. This cannot be obtained by any other means than molecular simulation. The results revealed the importance of the hydrophobic effect, with both molecules lying parallel to the surface at the free energy minima to enhance desolvation of the aromatic ring(s). The presence of dopamine/serotonin within the interfacial water region was also examined by comparison with the results in the Chapter 4 and the influence of the water disruption on the free energy of the system was discussed.

The results in this chapter advance scientific knowledge of the interaction of neurotransmitters with diamond that was not known prior to this study. The ranking of how strongly dopamine/serotonin bind on different diamond surfaces provides an essential guide to the diamond community for optimisation of the surface in a wide range of future diamond-neurotransmitter experiments *e.g.* poly(dopamine/serotonin)-functionalised surfaces (strong binding), non-fouling surfaces (weak binding), templates, and rational design of sensors. As the first ever MD study of dopamine/serotonin adsorption on any surface, the results in this chapter can be generalised to other materials and similar biomolecules. Hence, the results will be useful in the future to interpret and guide any neurotransmitter-surface experiments in the wider scientific field.

5.2 Introduction

Dopamine and serotonin are biological molecules that play an important role as neurotransmitters in the brain. Dopamine (3,4-dihydroxyphenethylamine) assists in movement, motivation and cognition, and a deficiency of the molecule has been linked to several neurodegenerative conditions including schizophrenia, addiction, attention deficit hyperactivity disorder (ADHD) and Parkinson's disease.[1] Serotonin (5-hydroxytryptamine) regulates physiological processes such as mood and sleep, and has been linked to psychological disorders such as depression, anxiety and obsessive-compulsive disorder.[2] Studies have shown that neuronal interactions between dopamine and serotonin molecules are closely linked.[3] The effect of serotonergic therapeutics on dopamine neurotransmission has been highlighted in schizophrenia,[4] ADHD[5] and cocaine usage.[6] Similarly, the interaction of dopamine and serotonin in antidepressant drugs, such as the influence of selective serotonin reuptake inhibitors on extracellular dopamine levels,[7] has helped to advance understanding of antidepressant function and assist in the development of new targeted drugs.[8] Accurate detection of these compounds in solution is therefore important for early medical diagnosis, and an understanding of their interaction is essential in order to develop more effective treatments.

As dopamine and serotonin can be readily oxidised, electrochemical sensors have emerged as one of the most promising techniques to detect the concentration of each species both *in vitro* and *in vivo*. The simultaneous detection of dopamine and serotonin has been reported using a range of carbon-based electrodes including edge plane pyrolytic graphite,[9] carbon nanotubes,[10] carbon fibre,[11] and surface-modified glassy carbon (GC) electrodes.[12] However, co-detection of species is often limited by the overlap of voltammetric responses, with the choice of electrode dependent on the

material that produces well-defined voltammetric peaks for the species of interest. This is of particular relevance for dopamine and serotonin that are often oxidised at similar potentials (oxidation potential at ~600 mV on GC electrodes, pH > 6),[13] making them difficult to distinguish due to signal amalgamation.

Electrode fouling is also problematic in biomolecule detection. Whilst carbon-based electrodes are often chosen due to their biocompatibility and chemical stability, they are known to suffer from species adsorbing to the surface. Reports have shown that GC and carbon-fibre electrodes used in serotonin measurements suffer from electrochemical fouling that causes limited detection sensitivity and reduced lifetime of electrode functionality.[14]

Conducting diamond has superior properties as an electrode such as low background currents, wide potential window, chemical inertness and biocompatibility, making it an attractive substrate for highly sensitive and selective electroanalytical measurements in biosensing and electrocatalytic devices.[15] Polycrystalline boron-doped diamond (BDD) electrodes have already proven successful in detecting dopamine in the presence of other competing species including ascorbic acid[16] and NADH.[17] Dopamine and serotonin have been detected down to a limit of 50 nM[18] and 10 nM,[19] respectively, using BDD electrodes. Furthermore, diamond has the highest resistance to fouling by neurotransmitters compared to all other carbon-based electrodes.[19-20] As inner-sphere electron transfer (ET) species (see Chapter 3, section 3.5), dopamine and serotonin both require adsorption to the electrode surface for the chemical reaction to proceed. The need is thus for an optimised BDD surface that selectively absorbs dopamine and serotonin for the chemical reaction to proceed, but with a binding strength that is weak enough for the reactant and oxidised product to desorb once formed.

Diamond is well suited for selective binding, as it is the only carbon-based material, due to its sp^3 nature, that can be readily modified between hydrophobic *i.e.* hydrogen (–H) and hydrophilic *i.e.* oxygen (–O) surface terminations, both of which are stable in air and aqueous electrolytes.[21] Different termination procedures are discussed in Chapter 1, section 1.2.3. Consequently, diamond electrodes have the potential to be appropriately functionalised to enhance dopamine/serotonin electrochemical detection and reduce fouling.

In addition to the functionalisation, the surface crystal structure also has an influence on electrochemical behaviour. Due to the development of controlled growth techniques, most notably the chemical vapour deposition (CVD) method (see Chapter 1, section 1.2.1), BDD has become widely available in recent years, enabling its electrochemical potential to be realised.[22] Polycrystalline BDD consists of different crystallographic faces, or grains, on the diamond surface, of which the primary orientations are the (100), (110) and (111) planes (see Chapter 1, section 1.2.2). These crystal faces introduce different topographical features (*e.g.* protrusions, voids) at the molecular level that may influence the adsorption of molecules.[23]

Single crystal (sc) BDD can also be synthetically grown but with greater difficulty than polycrystalline,[24] and thus scBDD has been scarcely utilised in biosensing to date.[25] However, as technologies improve, scBDD samples may become more widely available, so an understanding of the biomolecule-surface interactions at each crystal face would be highly advantageous for optimising BDD and future scBDD technologies.

Species such as dopamine/serotonin that react through an inner-sphere ET pathway are affected by a range of interfacial processes including adsorption of the molecule, formation of necessary precursor complexes, reorganisation of the adsorbed

complex into a transition state, and desorption of the resulting products (see Chapter 3, section 3.2). Any of these stages can limit the rate of the reaction. Furthermore, studies have reported that certain inner-sphere species are sensitive to the surface termination on BDD.[26] In the case of dopamine and serotonin, reports have been inconsistent. Studies have suggested dopamine to have faster ET on H-terminated BDD,[27] O-terminated BDD (Chapter 6), or to be unaffected to surface termination.[20] Serotonin has been reported to have faster ET on H-terminated BDD (Chapter 6), or to be surface insensitive.[19] However, caution must be taken to these results as the H-terminated surface oxidises over time and may no longer be fully hydrogenated. As different treatments influence the predominant surface groups on diamond (see Chapter 1, section 1.2.3), the experimental BDD surfaces are a combination of surface terminations. Understanding how each surface termination affects the adsorption step may have a significant influence on the reaction kinetics, and help to realise the ideal diamond surface for optimum dopamine/serotonin binding that could improve the neurotransmitter sensing capabilities of diamond.

Molecular dynamics (MD) simulations are ideally suited to elucidate many of the important steps in the process of dopamine/serotonin adsorption to diamond, including the mechanism during adsorption, the strength of binding to the diamond surface, and the interfacial dynamics of the species once adsorbed. In order for dopamine/serotonin to adsorb onto a diamond surface, it must cross through the transition region from bulk to interfacial water. This process occurs on the nano-length and time scales that can be captured by MD models. The advantage of classical MD over DFT or combined MD-DFT systems is the ability to study the structural and dynamical changes of the molecule over the biologically relevant time scales through use of classical (Newtonian) force-fields.[28]

The interaction between biomolecules and solid surfaces has been the focus of numerous MD studies.[29] MD simulations have provided useful insight into the adsorption of biomolecules onto solid substrates of varying surface structure and chemistry. Studies of particular note include the investigation by Wright *et al.,*[30] of the differences in the free energy of adsorption of amino acid analogues to the hydrophobic (100), (001) and (011) orientations of α-quartz, finding the species to configure differently on each of the faces with preferential binding by nonpolar aromatic compounds to the surfaces; examination by Ghiringhelli *et al.,*[31] of the role of interfacial water in the binding affinity of oligopeptides on a hydrophilic Pt(111) surface; an extensive study by Qin *et al.,*[32] into the adsorption behaviour of L-leucine to a graphene sheet using a combination of DFT and MD simulations; and a study into the free energy of adsorption of 20 amino acids to a hydrophilic Au(111) surface by Hoefling *et al*.[33] As well as providing fundamental information about the respective interface, we note that investigation into biomolecule-solid systems is also useful towards the development of new biohybrid materials[34] and non-fouling surfaces in medical technologies.[35] This is highly relevant for this work, as the results could help optimise the neurotransmitter-diamond interface in poly(dopamine)– coated diamond biosensors[36] and diamond-coated medical devices used in neurological studies.[37]

Despite its importance, only two MD studies on the diamond-biomolecule interface currently exist and no studies exist of the solid-neurotransmitter interface to the best of the author's knowledge. These studies are the binding of a hydrophobic spider silk peptide to (100) H– and OH– terminated diamond surfaces by Horinek *et al*.,[38] and the binding of three small peptides (Arg–Gly–Arg, Arg–Gly–Phe and Phe–Gly–Phe) in combination with DFT to a bare and doped (111) diamond surface by Borisenko *et al*.[39] Here, for the first time, the neurotransmitter-diamond interface is

investigated and the influence of seven different model diamond surfaces is screened to assess facet-selective adsorption.

In this study the aim is to elucidate the free energy of adsorption of a single dopamine and serotonin molecule onto ideal hydrophobic and hydrophilic (100), (110) and (111) diamond surfaces by means of potential of mean force calculations. By deconstructing BDD, we will be able to systematically elucidate the influence of each surface on dopamine/serotonin adsorption, with the ultimate goal to advise on the ideal diamond surface that will enhance dopamine/serotonin selectivity. The adsorption mechanism of dopamine and any key structural changes will be investigated in detail. In addition, the adsorption mechanism of serotonin will also be discussed in comparison to dopamine.

5.3 Theoretical Methods

5.3.1 Diamond Models

Seven diamond surface models were utilised to explore the effect of different crystal orientations and surface terminations on selective biomolecule adsorption. The methodology used to build and validate these models is presented in detail in Chapter 4. In brief, the three primary crystallographic faces of diamond were investigated – (100), (110) and (111). These faces have distinctly different surface topographies (see Chapter 4, Figure 4.1). Surface groups were added to render each diamond slab as hydrophobic or hydrophilic. The faces were fully terminated with either hydrogen (H) or a single oxygen group (OH, C–O–C, C=O) dependent on the most favourable group as detailed in experimental and theoretical studies (outlined in Chapter 1, section 1.2.2).[40] This produced seven diamond models: the (100) H-terminated, O-ether-terminated and O-ketone-terminated, (111) H-terminated and OH-terminated,

and (110) H-terminated and O-ether-terminated (pictured in Chapter 4, Figure 4.1). It is noted that these models are of intrinsic diamond instead of boron-doped that is used in electrochemical experiments. However, these models are appropriate for the aim to understand the effect of different diamond surface terminations on adsorption.

5.3.2 Dopamine and Serotonin Models

Dopamine and serotonin molecules were built using the PRODRG server.[41] These models were built by Adam Hill, University of Manchester (see Declaration). Given the physiological pH of the blood (pH 7.4)[42] and the pKa value of their amine groups (9.61 and 10.4 for dopamine[43] and serotonin,[44] respectively), the molecules were built with the amine groups in the protonated state. Snapshots of the dopamine and serotonin models are shown in **Figure 5.1**. For the adsorption simulations of dopamine and serotonin on diamond, an additional counter Cl^- ion was added to the solution (of 14600 waters) to maintain the electroneutrality of the system.

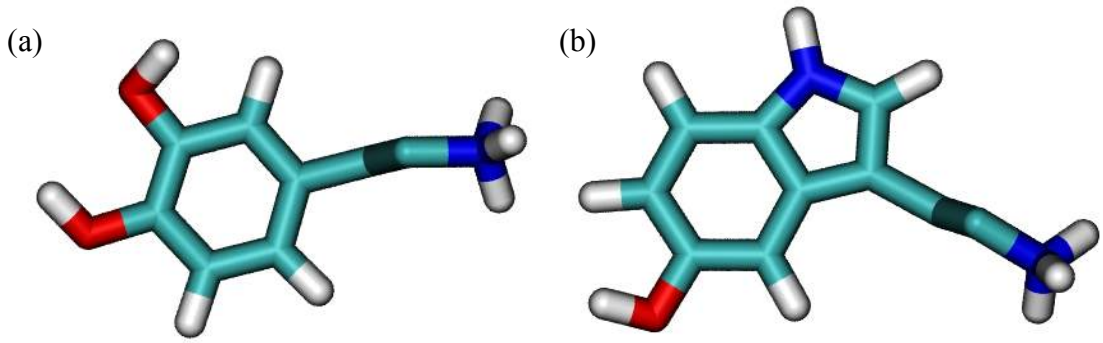

Figure 5.1*: Snapshots of the (a) dopamine and (b) serotonin molecules used in the simulations. Bonds are coloured to represent carbon (cyan), oxygen (red), nitrogen (blue) and hydrogen (white).*

5.3.3 Force Field Parameters

A modified version of the GROMOS96 version 53a6 force field was utilised in this study.[45] This force field has been previously discussed and implemented to

investigate the interfacial water structure close to the seven different model diamond surfaces (see Chapter 4, section 4.3.3). The GROMOS96 53a6 parameters have been fit to reproduce thermodynamic properties of a range of pure liquids and the free enthalpies of hydration and solvation of 14 amino acid analogs in simple point charge (SPC) water and cyclohexane.[45] This is highly advantageous for this study given the similarity between dopamine and serotonin with tyrosine and tryptophan, respectively. None of the other biomolecular force fields (AMBER, CHARMM, OPLS) have been parameterized to reproduce solvation free enthalpies, therefore this force field is considered the most reliable to accurately capture the solvation of polar groups on dopamine and serotonin. In addition, the GROMOS 53a6 force field has been previously used in diamond MD studies to reproduce atomic force microscopy data for the desorption force of a mildly hydrophobic peptide on model (100) hydrophobic and hydrophilic diamond surfaces.[38] The modified GROMOS 53a6 force field used in this study has been fine tuned to specifically capture the different diamond surfaces, where the bonded parameters were adjusted to the known diamond bond lengths and angles for each model, and the partial charges on each functional group determined by *ab-initio* calculations of representative compounds. This was presented in detail in Chapter 4 (see Chapter 4, section 4.3.3).

The six lowest energy conformers of dopamine and serotonin were identified using the Avogadro v.1.1.1 package,[46] allowing the C–C and C–N bonds to rotate about their axis during the conformational search. Similar to the parameterisation of the diamond surfaces (see Chapter 4, section 4.3.3), the first six conformers were chosen as they had the largest energy and therefore would have the biggest contribution to the partial charge distribution. The partial atomic charges for each conformer were calculated using QM theory at the Hartree-Fock (HF) level with

HF/6-31G(d,p) basis set (Gaussian 03 package) and then averaged to obtain the final partial atomic charges on dopamine and serotonin. The partial charges have magnitude and direction of dipole moment comparable to the values for the similar amino acids (tyrosine and tryptophan) in the GROMOS96 53a6 parameter set,[45] providing confidence in the results. All other bonded and non-bonded parameters for dopamine and serotonin were taken from the tyrosine and tryptophan, respectively. Both the diamond and neurotransmitter models were built using united atoms to ensure compatibility with the force field.

The parameterisation for dopamine/serotonin does assume that the force field parameters are transferable from tyrosine/tryptophan. A comparison of the dihedral angles could be performed to check the force field conserves torsional angle energetics. However, the method of parameterisation used was considered sufficient, as it is consistent with the parameterisation used for any new molecule in the GROMOS force field. In addition, the dopamine/serotonin models could have been validated against experimental (*e.g.* crystal structure) data. However, in this case, validation of the dopamine/serotonin models was considered to be how well the interaction of dopamine/serotonin with diamond matches to theoretical and experimental data, as it is more important to ensure the diamond-water-neurotransmitter interface is successfully captured (discussed in the results section).

5.3.4 System Setup and Simulation Parameters

All simulations were carried out using the GROMACS version 4.6.5 software package.[47] The diamond slabs and biomolecules were energy minimised separately using a steepest descent algorithm for 5000 steps or until the gradient is less than the tolerance of 1000 kJ mol^{-1} nm^{-1} (see Chapter 2, section 2.4). Dopamine and serotonin structures were equilibrated for 500 ps in vacuum (using a time step of 2 fs) in the

NVT ensemble. Each biomolecule was then placed in a 15 nm^3 water box and further equilibrated for 500 ps in the *NVT* ensemble and 1 ns in the NAP_zT ensemble using a 2 fs time step with coordinates saved every 10 ps (5000 steps). A single pre-equilibrated dopamine or serotonin molecule was inserted into the simulation box at a distance of at least 3.5 nm from the diamond surface. The box was then solvated with 14600 water molecules and one Cl^- counterion using the Gromacs genion tool. The systems were energy minimised using the steepest descent algorithm (5000 steps or until the gradient is less than the tolerance of 1000 kJ mol^{-1} nm^{-1}) and then equilibrated for 20 ps in the *NVT* ensemble followed by 100 ps in the NAP_zT ensemble. Throughout the equilibration, harmonic restraints of 1000 kJ mol^{-1} nm^{-2} were placed on the dopamine or serotonin molecule to ensure they remained at a fixed distance from the surface (see Chapter 2, section 2.6.4). The system parameters were the same as those used in the previous study of interfacial water on diamond surfaces (Chapter 4), thus the results can be directly compared to outcomes of that study.

5.3.5 Free Energy Calculations

Free energy profiles for the adsorption of the neurotransmitters, dopamine and serotonin, to each diamond surface were obtained using the potential of mean constraint force (PMF) method (see Chapter 2, section 2.6.5). Each molecule was pulled along the coordinate axis, in this case the *z*-axis, from bulk water towards the surface using steered MD to generate initial starting configurations. The separation distance between the surface and molecule was calculated by the difference between the center of mass of the molecule and the center of mass of the diamond in the *z*-direction. For separation distances between 0 and 1.2 nm, configurations were selected at every 0.05 nm intervals, whereas at separation distances > 1.2 nm, configurations were selected at 0.1 nm intervals along the coordinate axis. At each

position, the molecule was constrained in the *z*-direction but allowed to freely explore in the *xy*- directions. Each PMF constraint window (20 – 30 per system) was equilibrated for 100 ps in the NAP_zT ensemble using harmonic position restraints (1000 kJ mol^{-1} nm^{-2}) placed on the species. The restraints were then removed (but the constraints remained in place on the molecule) and simulations were run for 20 ns in the NAP_zT ensemble, exporting the constraint force and position on the molecule in each configuration every 2 ps. The first 5 ns were discarded as equilibration with the remaining 15 ns used in the subsequent analysis. The free energy profile was obtained by cumulatively integrating the constraint force obtained at each *z*-position over the distance moved along the *z*-axis (Chapter 2, equation 2.33).

5.3.6 Analysis

The simulations were analysed using tools available in GROMACS,[48] VMD (visual molecular dynamics),[49] and locally written scripts. Snapshots of the dopamine and serotonin molecules at the energy minimum and during adsorption to the diamond surfaces were taken using VMD. Detailed structural analysis was performed on dopamine during adsorption. The average number of diamond-water, water-water, dopamine-water and diamond-dopamine hydrogen bonds per time frame (4 ps), made by polar and charged atoms, were stipulated under certain geometric criteria,[50] whereby the hydrogen-acceptor distance was required to be less than 0.35 nm and acceptor-donor-hydrogen angle cut-off less than 30°. Hydrogen bonds were analysed by counting the number formed at discrete time steps. In order to ascertain the mechanism of adsorption, the orientation of functional groups on dopamine, relative to the surface normal, was calculated as a function of surface-species distance. This was considered necessary to realise the important adsorption sites and to elucidate the role of the key functional groups in adsorption. The angle of the meta

OH, para OH, CN and ring on dopamine was determined within each PMF constraint window. The distribution of angles was calculated over the last 5 ns within each constrained *z*-position. The distance between the para O or meta O atoms, and the uppermost C atoms of each diamond surface was measured using the Gromacs g_dist code, where the atom position was calculated by averaging over the last 5 ns of each PMF constraint window. The frequency distributions were then obtained using the Gromacs g_analyze code. The distribution of bond and ring angles at discrete distances away from the surface was determined by calculating the angle (over the last 5 ns of simulation) between the bond vector or ring plane, and normal to the surface at each time frame (4 ps) for each PMF constraint window.

5.4 Results and Discussion

5.4.1 Free Energy Calculations of Dopamine on Diamond Surfaces

The final PMF free energy profiles were obtained by monitoring the profile over increasing simulation time intervals until the plots had converged to a time-independent profile for each diamond surface. **Figure 5.2** shows the profiles calculated over 9 different simulation times ranging from 2 – 15 ns, with a convergent profile achieved by 15 ns. An additional well at ~ 1.3 nm can be observed during adsorption to the H-terminated diamond surfaces for shorter (< 12 ns) simulation times (**Figure 5.2**). This is an artefact of not sampling for long enough and disappears when sampling data over longer (> 12 ns) time periods. Eleven profiles were calculated using simulation times of 14 – 15 ns in 0.1 ns intervals (**Figure 5.2** insets). These plots overlay each other confirming PMF convergence has been reached. This means that no significant differences would be gained from running the simulations for longer than 15 ns. The zero point of reference for each surface is the average

position of the uppermost layer of C atoms. Error in the force data was calculated for the (111) H-terminated surface using the block averaging method outlined by Wright and Walsh.[30]

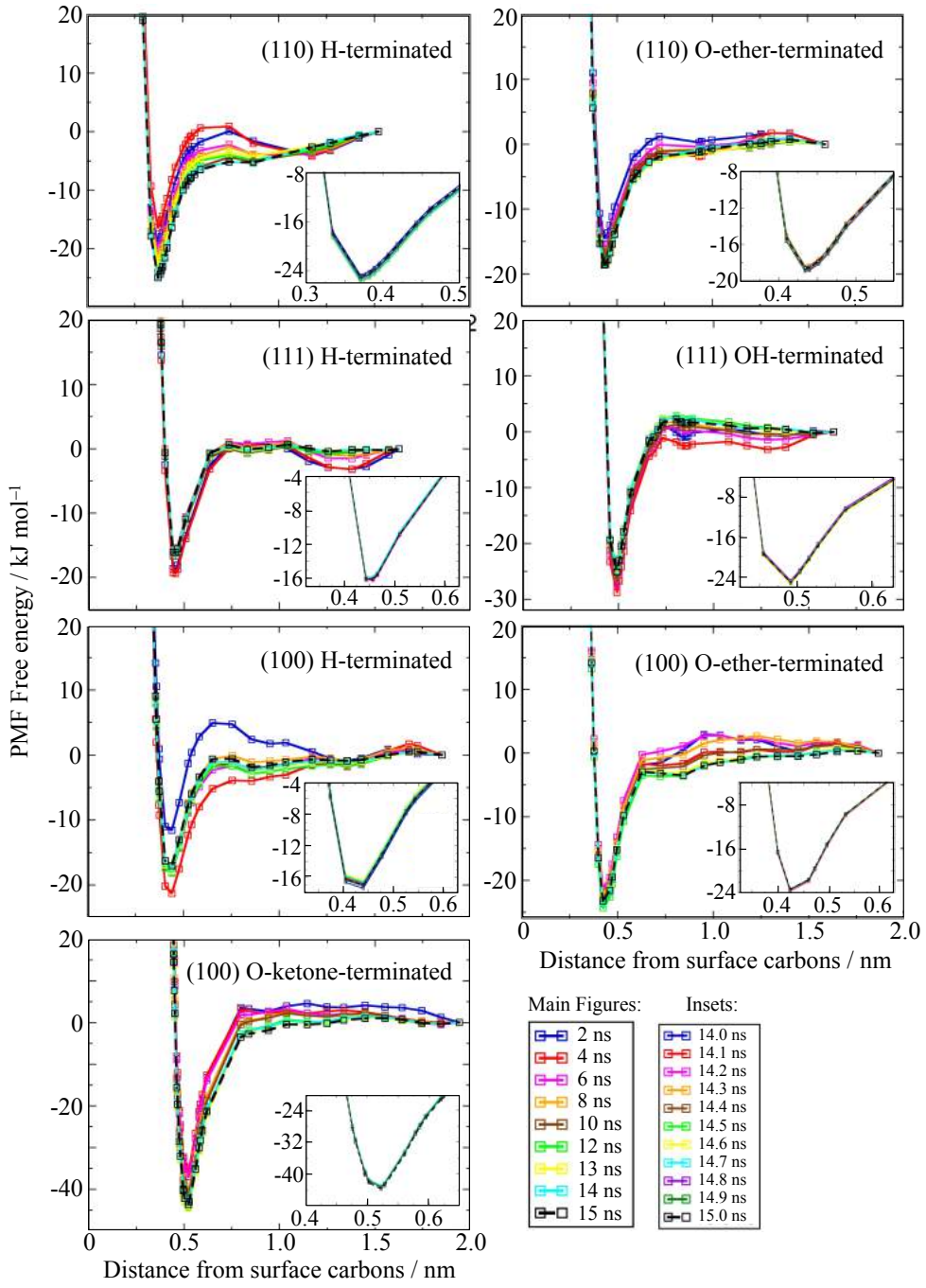

***Figure 5.2**: Convergence plots over time for the free energy of dopamine adsorption as a function of z-distance from surface carbons on seven different model diamond surfaces. Profiles were calculated by averaging over increasing simulation time, and shown to converge by 15 ns (black --). Insets show zoom-ins of the free energy minimum for each surface averaged over 14 – 15 ns with 0.1 ns spacings. All inset profiles overlay each other confirming convergence.*

The optimum PMF free energy minimum for each surface, and the *z*-position at which it occurs, is outlined in **Table 5.1**. Uncertainties in the optimum position were calculated from the positions either side of the minima. It is of note that the calculated PMF free energy of adsorption is a combination of enthalpic and entropic contributions, as discussed in detail in section 5.4.14.

***Table 5.1**: Optimum PMF free energy of adsorption and the z-position at which it occurs for dopamine on different (100), (111) and (110) diamond surfaces.*

Surface	Optimal PMF Free Energy of Dopamine Adsorption (kJ mol^{-1})	Optimum dopamine-surface separation (nm)	Distance away from the peak of first structured water (optimum position – peak position) (nm)
(100)-H	−16.99 ± 1.43	0.44 ± 0.05	+0.05
(100)-O-ether	−23.24 ± 1.34	0.43 ± 0.04	+0.04
(100)-O-ketone	−35.15 ± 1.27	0.52 ± 0.02	+0.12
(111)-H	−16.04 ± 1.25	0.45 ± 0.02	+0.06
(111)-OH	−25.13 ± 1.40	0.48 ± 0.03	+0.05
(110)-H	−17.65 ± 1.18	0.36 ± 0.04	−0.03
(110)-O-ether	−18.60 ± 1.79	0.42 ± 0.02	+0.01

For all surfaces, the optimum free energy minimum lies in the average range of [−16.04, −35.15] kJ mol^{-1} (**Table 5.1**). This indicates that dopamine adsorption is favourable on any diamond surface. These values are in a similar range to other biomolecule-surface free energy minima reported by MD studies in literature *e.g.* [−2.82, −11.96] kJ mol^{-1} of numerous peptides on silica[30] and [−17.5, −44.2] kJ mol^{-1} for amino acids on (111) gold,[33] providing confidence in the models. Furthermore, the optimal binding strength varies between the different diamond surfaces (**Table 5.1**), indicating that dopamine adsorption is surface specific. On average, dopamine adsorbs more favourably on the hydrophilic (O-terminated) rather than hydrophobic (H-terminated) surfaces. The binding strength of dopamine is most favourable to the (100) O-ketone-terminated surface with a well depth of −35.15 ± 1.27 kJ mol^{-1} and no energy barrier for adsorption, and least favourable to the (111) H-terminated surface with an energy minimum of −16.04 ± 1.25 kJ mol^{-1}.

Besides the energetic differences, there is also variation in the optimum dopamine-surface separation *i.e.* the *z*-position at which the free energy minima occurs (**Table 5.1**). For all surfaces, the optimum dopamine-surface separation lies within the first structured water region, which indicates that dopamine must disrupt the strong interfacial hydrogen bonding in this region.

5.4.2 Adsorption of Dopamine on (100) Diamond Surfaces

The PMF free energy profile for the adsorption of dopamine along the *z*-axis to the (100) diamond surfaces is shown in **Figure 5.3**. The centre of mass of dopamine was constrained at different separations away from the surface carbons, but the molecule was allowed to explore all possible configurations in the *xy*- direction (see Chapter 2, section 2.6.5). Dopamine attains random configurations in bulk but converges to a preferential orientation at each free energy minimum, displayed in **Figure 5.3** (orientation is analysed in greater detail in section 5.4.6).

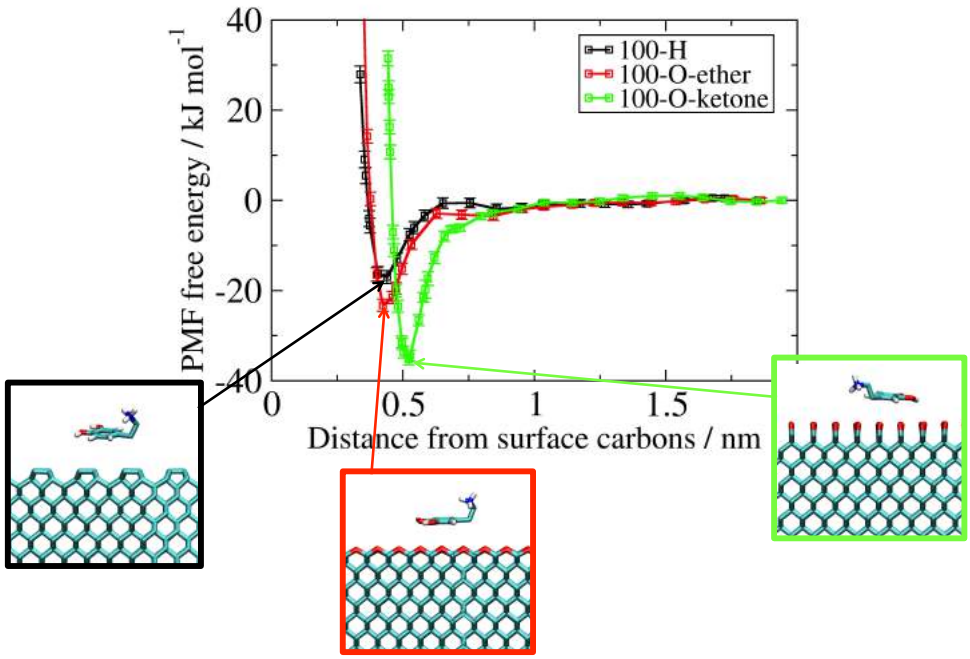

***Figure 5.3**: PMF free energy of adsorption of dopamine on (100) H-terminated, O-ether-terminated and O-ketone-terminated diamond surfaces as a function of surface separation.*

We observe that the adsorption of dopamine to the (100) O-ketone-terminated surface is approx. 1.5 × stronger (−35.15 ± 1.27 kJ mol^{-1}) than to the other hydrophilic (100) surface *i.e.* the (100) O-ether-terminated with a well depth of −23.24 ± 1.34 kJ mol^{-1} (**Table 5.1**). This suggests that the C=O groups must play a key role in adsorption. Adsorption to the hydrophobic (100) H-terminated surface is the weakest, compared to the other (100) surfaces, with a well depth of −16.99 ± 1.43 kJ mol^{-1}. We also note that the (100) H-terminated and (100) O-ether-terminated surfaces have slight energy barriers to adsorption, which is not observed on the (100) O-ketone-terminated surface (**Figure 5.3**).

The free energy of dopamine during adsorption begins to deviate from bulk at ~ 0.65 nm on both the (100) H-terminated and (100) O-ether-terminated surfaces, but at a further distance of ~ 1.03 nm on the (100) O-ketone-terminated surface (**Figure 5.3**). This is mirrored by the position of the stable adsorption minima, which exist at a similar distance away from the (100) H-terminated (0.44 ± 0.05 nm) and (100) O-ether-terminated (0.43 ± 0.04 nm), and a greater distance away from the (100) O-ketone-terminated surface (0.52 ± 0.02 nm), highlighting that the profiles have shifted in the *z*-direction based on the different underlying surfaces. DFT studies of dopamine adsorption on a (100) O-ketone-terminated and (100) H-terminated surface also found the optimum position for dopamine to be further away from the ketone-terminated surface (0.41 nm) compared to the H-terminated surface (0.29 nm),[51] in agreement with these models. A detailed analysis of the orientation of dopamine during adsorption is presented in following sections 5.4.5 – 5.4.8, with the proposed pathway to adsorption based on these findings displayed in Figure 5.9.

The positional differences are due to a combination of the topology and intermolecular forces of the underlying surface. The protrusion of the C=O groups on

the (100) O-ketone-terminated surface forces dopamine to sit further away from the surface carbons compared to the relatively flat structure of the other (100) surfaces. In addition to topology, the polar groups on dopamine can interact with O-terminated surfaces via hydrogen bonding and intermolecular forces. We note that: (1) hydrogen bonding could be affected by the direction of the C–O bond vector *i.e.* hydrogen bonds are stronger when linear, (2) the O on the O-ketone-terminated surface carries a less negative charge compared to the ether (O-ketone: −0.58 e *vs.* O-ether: −0.67 e), which means that there will be less attraction between C=O and the polar groups on dopamine (OH, NH_3^+), (3) there may be steric clashes from the C=O groups with the polar groups on dopamine, (4) π–π interactions between the C=O groups on diamond and dopamine aromatic ring, and (5) the O on the O-ketone-terminated surfaces has either the same or stronger LJ interactions[45] (van der Waals, dispersive forces) with the atoms on dopamine compared to O-ether and H- terminated surfaces. These differences all contribute to the ideal *z*-position for dopamine on the (100) O-ketone-terminated surface. Furthermore, the *z*-separation may be ideal to enable favourable surface hydrogen bonding that would enhance the binding strength to the O-terminated surfaces compared to the H-terminated.

It is important to note that for all (100) surfaces, the optimum dopamine-surface separation lies within the first ordered water layer (**Table 5.1**). It is hypothesised that dopamine positions itself at the ideal proximity to maximise hydrogen bonding and enhance hydrophobic shielding. In particular, hydrophobic shielding can either occur directly *i.e.* where the surface itself acts to shield the hydrophobic functional groups from water, or indirectly *i.e.* where the presence of dopamine will reduce the water density close to the surface and thus reduce the number of unfavourable hydrophobic-hydrophilic interactions. Whilst disruption of

the strong hydrogen bonding water network close to the surface is unfavourable, the counterbalance of favourable processes also needs to be accounted for such as improved solvation of the dopamine polar groups, desolvation of the nonpolar groups, and potentially stronger diamond-dopamine or dopamine-water interactions compared to water-diamond or water-water interactions. The success of this interplay between favourable and unfavourable interactions, along with positional constraints from the underlying surface topology, is considered to be the reason why all three surfaces have favourable binding strengths but to differing degrees.

The configuration of the dopamine molecule further supports the important role of hydrophobic shielding. At the adsorption minima, the dopamine ring sits approx. parallel to the surface with the NH_3^+ group pointing upwards towards bulk (**Figure 5.3**). The flattening of the ring against the surface is believed to enhance desolvation, whereas the polar NH_3^+ group points upwards into a region of higher water density to maximise solvation. This conformation is seen on all three (100) surfaces. Detailed investigation into the orientations of the dopamine functional groups during adsorption and the influence on the interfacial hydrogen bond network is presented later.

5.4.3 Adsorption of Dopamine on (111) Diamond Surfaces

The PMF free energy profiles for the adsorption of dopamine to the (111) diamond surfaces are shown in **Figure 5.4.** Dopamine attains random configurations in bulk but converges to a preferential orientation at each free energy minimum, displayed in **Figure 5.4** (orientation is analysed in greater detail in section 5.4.6).

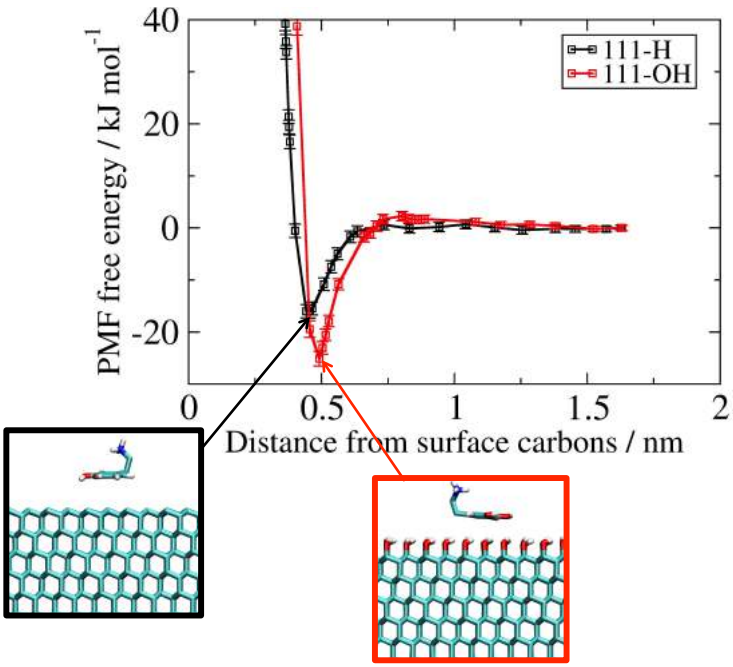

***Figure 5.4**: PMF free energy of adsorption of dopamine on (111) H-terminated and OH-terminated diamond surfaces as a function of surface separation.*

The (111) diamond surfaces display similar trends to the (100) surfaces. We observe that dopamine adsorbs more strongly to the hydrophilic (111) OH-terminated surface with energy minima at −25.13 ± 1.40 kJ mol^{-1} compared to the hydrophobic (111) H-terminated surface with energy minima at −16.04 ± 1.25 kJ mol^{-1} (**Table 5.1**). Dopamine also sits within the first structured water layer, at distances of 0.45 ± 0.02 nm (~ 0.06 nm beyond the first structured water peak) and 0.48 ± 0.03 nm (~ 0.05 nm beyond the first structured water peak) for the (111) H– and (111) OH–terminated surfaces, respectively. Given that the expected distance in the *z*-direction for π-π stacking is ~ 0.34 nm,[52] this indicates that π–π interactions are not influential to the optimal dopamine-diamond separation. Despite their differing surface topographies *i.e.* the presence of voids on the (100) H-terminated, the optimum position and strength of binding is similar for the (111) and (100) H-terminated surfaces. As the dopamine molecule is larger than the orifices in the (100) H-

terminated surface, it is of little surprise that the lateral surface structure does not influence the adsorbed species.

Interestingly, the optimum binding strength is lower on the (111) OH-terminated compared to the (100) O-ketone-terminated diamond surface, despite the fact that the surface OH can act as a hydrogen bond donor and acceptor making it more likely to form hydrogen bonds. This suggests that the disruption to the water ordering is least favourable on this surface compared to the others, as the (111) OH-terminated surface has the greatest number of surface-water hydrogen bonds (0.30 ± 0.02 nm^{-2}) and the largest first structured water density (2739.32 ± 123.79 kg m^{3}) of all the model diamond surfaces (outlined in Chapter 4), as well as the presence of surface-surface hydrogen bonds between the OH groups that is not possible on any other surface. Consequently, the presence of dopamine will likely cause considerably unfavourable disruption to the surface-surface, surface-water and water-water hydrogen bonding, thus lowering the favourable binding strength.

In addition, whilst (100) O-ketone-terminated surface can also interact via π–π interactions, the optimal dopamine-diamond position on (100) O-ketone-terminated (0.53 nm) is greater than the optimal *z*-separation for π–stacking (0.34 nm), suggesting that π–stacking does not contribute significantly to the interaction.

It is noted that the surface O on the OH-terminated surface has a larger partial charge than the O on the O-ketone-terminated (OH: −0.76 e *vs.* O-ketone: −0.58 e), which means it has stronger electrostatic attraction to the dopamine polar groups. This may explain why dopamine sits closer to the uppermost carbons on the (111) OH-terminated surface. Dispersive forces between the surface groups and dopamine will also contribute to the binding strengths, with the O on O-ketone-terminated surfaces

always having the same or stronger interactions with the dopamine groups compared to the other surfaces.[45]

The (111) OH-terminated surface also exhibits a small energy barrier to adsorption, which is not observed on the (111) H-terminated surface and likely connected to the unfavourable reorganisation of the hydrogen bonding network as the dopamine enters the first structured water layer. The energy minima lies at a further *z*-distance away from the uppermost surface carbons on the (111) OH-terminated surface (0.48 ± 0.03 nm) compared to the (111) H-terminated surface (0.45 ± 0.02 nm), and the position at which the energy begins to deviate from bulk is also shifted accordingly (~0.73 nm for OH-terminated, ~0.63 nm for H-terminated). The positional difference is a consequence of spatial constraints due to the larger size and greater protrusion of the OH compared to H groups, given the surface topographies are otherwise the same. Dopamine is observed to adopt the same conformation at the free energy minima on the (111) surfaces as observed on the (100) surfaces.

5.4.4 Adsorption of Dopamine on (110) Diamond Surfaces

The PMF free energy profiles for the adsorption of dopamine to the (110) diamond surfaces are shown in **Figure 5.5.** Dopamine attains random configurations in bulk but converges to a preferential orientation at each free energy minimum, displayed in **Figure 5.5** (orientation is analysed in greater detail in section 5.4.6).

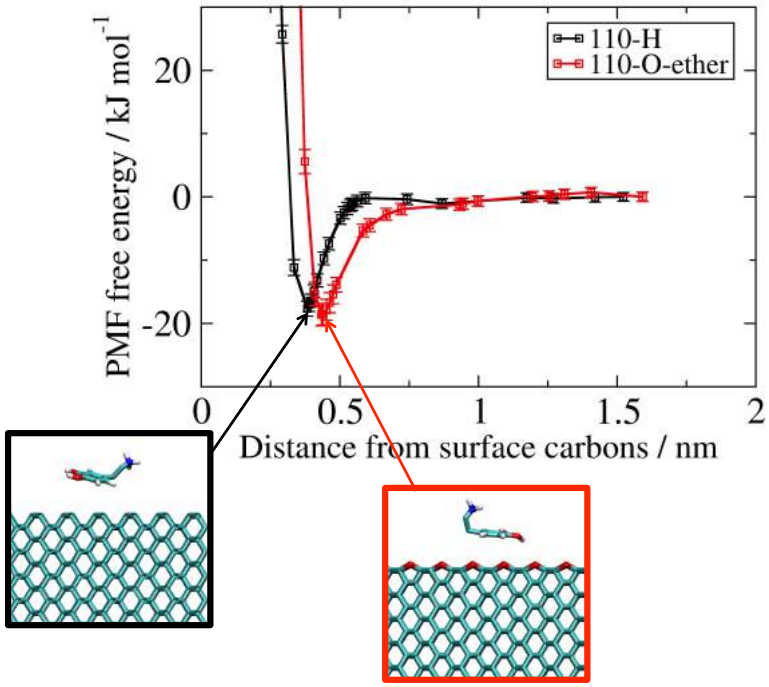

***Figure 5.5**: PMF free energy of adsorption of dopamine on (110) H-terminated and O-ether-terminated diamond surfaces as a function of surface separation.*

The energy minima on the (110) H- and (100) O-ether- terminated surfaces are relatively close to each other (−18.60 kJ mol^{-1} on the O-ether-terminated, −17.65 kJ mol^{-1} on the H-terminated) suggesting that there is no preferential (110) adsorption surface. The energy drops on the (110) O-ether-terminated surface over a longer *z*-distance compared to the other diamond surfaces with the energy beginning to fall at around 0.9 nm and reaching a minimum at 0.42 nm. Dopamine also penetrates closest to the (110) H-terminated of all the surfaces, lying within the first structured water region, 0.03 nm before the peak. This surface has the flattest topology compared to the others, and the partial charge on the surface O of (110)-O-ether is larger than the O-ketone-terminated surface (O-ether: −0.67 e, O-ketone: −0.58 e) enabling strong attraction between the polar surface and dopamine groups. The dispersive forces for the O-ether groups with dopamine atoms are stronger than the H groups with the

dopamine atoms,[45] which will also contribute the greater binding strength to the (110) O-ether-terminated surface.

The similarity in the optimum binding strengths suggests that favourable and unfavourable processes are cancelling out, likely for the (110)-O-ether-terminated surface *i.e.* it can be hypothesised that the very close proximity that dopamine sits to this surface may introduce unfavourable interactions in addition to the favourable desolvation. It is noted that thorough checking has eliminated technical errors. The configuration dopamine attains at the free energy minima is the same as that observed on all other diamond surfaces.

5.4.5 Hydrogen Bonding during Dopamine Adsorption

Hydrogen bonding often plays an influential role in the adsorption of a species to a surface.[38, 53] The average number of dopamine-water, diamond-dopamine, diamond-diamond, water-diamond and water-water hydrogen bonds per time frame (4 ps) were calculated at the adsorption minima, ~ 0.1 nm above the adsorbed position, ~ 0.2 nm above the adsorbed position and bulk (~ 1.5 nm) for each system, shown in **Table 5.2**a – g. Interfacial water-water hydrogen bonds were also calculated for each surface using water that lies in the region between the uppermost layer of surface carbons (z = 0) and z = 0.4 nm. This was considered necessary to interpret how the presence of the dopamine molecule disrupts the hydrogen bond network within the first structured water layer. As the H-terminated surfaces cannot form strong hydrogen bonds with water, dopamine or itself, these have not been included in the analysis.

***Table 5.2**: The average number of dopamine-water (Dop – Water), diamond-dopamine (Dia – Dop), diamond-diamond (Dia – Dia), water-diamond (Water – Dia), interfacial water-water and total water-water hydrogen bonds formed on each diamond surface (a) – (g) calculated at the adsorption minima, ~ 0.1 nm above the minima, ~ 0.2 nm above the minima, and in bulk (~ 1.5 nm). Interfacial water-water hydrogen bonds were calculated for water molecules that lie within 0.4 nm of the surface during the trajectory (15 ns).*

(a)	**Groups**	**Average No. of Hydrogen Bonds: (100) H-terminated diamond**			
		Minima (0.44 nm)	**~ 0.1 nm above minima (0.54 nm)**	**~ 0.2 nm above minima (0.65 nm)**	**Bulk (~ 1.5 nm) (1.57 nm)**
	Dop – Water	6.89 ± 1.08	6.90 ± 1.20	6.90 ± 1.22	7.44 ± 1.15
	Interfacial Water – Water	94.60 ± 18.6	97.67 ± 18.0	103.52 ± 18.53	108.04 ± 17.92
	Total Water – Water	12628.57 ± 61.52	12625.20 ± 59.23	12627.79 ± 58.38	12624.92 ± 59.80
(b)	**Groups**	**Average No. of Hydrogen Bonds: (100) O-ether-terminated diamond**			
		Minima (0.42 nm)	**~ 0.1 nm above the minima (0.53 nm)**	**~ 0.2 nm above the minima (0.63 nm)**	**Bulk (~ 1.5 nm) (1.54 nm)**
	Dop – Water	6.88 ± 1.04	7.03 ± 1.15	6.41 ± 1.14	7.41 ± 1.14
	Dia – Dop	0.00 ± 0.05	0.02 ± 0.12	0.21 ± 0.41	0.00 ± 0.00
	Water – Dia	56.12 ± 6.75	56.43 ± 6.63	56.57 ± 6.85	56.70 ± 6.44
	Interfacial Water – Water	59.92 ± 13.47	58.80 ± 13.81	60.01 ± 13.73	60.08 ± 13.69
	Total Water – Water	12689.59 ± 59.57	12685.12 ± 56.20	12687.56 ± 59.81	12690.25 ± 61.36
(c)	**Groups**	**Average No. of Hydrogen Bonds: (100) O-ketone-terminated diamond**			
		Minima (0.52 nm)	**~ 0.1 nm above the minima (0.62 nm)**	**~ 0.2 nm above the minima (0.72 nm)**	**Bulk (~ 1.5 nm) (1.55 nm)**
	Dop – Water	7.15 ± 0.99	7.12 ± 1.16	6.51 ± 1.10	7.40 ± 1.12
	Dia – Dop	0.01 ± 0.09	0.06 ± 0.23	0.55 ± 0.53	0.00 ± 0.00
	Water – Dia	94.65 ± 8.41	95.13 ± 8.43	94.55 ± 8.30	95.37 ± 8.23
	Interfacial Water – Water	43.98 ± 12.07	45.32 ± 12.01	45.36 ± 12.48	45.24 ± 12.25
	Total Water – Water	12686.45 ± 59.99	12685.39 ± 59.33	12685.52 ± 58.45	12686.05 ± 60.07
(d)	**Groups**	**Average No. of Hydrogen Bonds: (111) H-terminated diamond**			
		Minima (0.46 nm)	**~ 0.1 nm above the minima (0.56 nm)**	**~ 0.2 nm above the minima (0.74 nm)**	**Bulk (~ 1.5 nm) (1.57 nm)**
	Dop – Water	6.89 ± 1.06	7.07 ± 1.14	7.23 ± 1.17	7.39 ± 1.13
	Interfacial Water – Water	57.82 ± 13.88	52.49 ± 12.68	61.76 ± 14.89	61.34 ± 14.76
	Total Water – Water	12628.76 ± 57.74	12628.22 ± 61.57	12628.30 ± 59.23	12626.22 ± 58.90
(e)	**Groups**	**Average No. of Hydrogen Bonds: (111) OH-terminated diamond**			
		Minima (0.49 nm)	**~ 0.1 nm above the minima (0.66 nm)**	**~ 0.2 nm above the minima (0.70 nm)**	**Bulk (~ 1.5 nm) (1.52 nm)**
	Dop – Water	6.94 ± 1.01	6.49 ± 1.17	6.80 ± 1.18	7.36 ± 1.10
	Dia – Dop	0.01 ± 0.11	0.35 ± 0.53	0.18 ± 0.39	0.00 ± 0.00
	Dia – Dia	569.80 ± 17.84	568.92 ± 17.11	569.25 ± 17.57	568.35 ± 17.88
	Water – Dia	177.12 ± 9.69	178.21 ± 10.01	178.38 ± 9.78	178.28 ± 9.65
	Interfacial Water – Water	29.90 ± 9.51	30.33 ± 9.74	30.45 ± 9.97	30.52 ± 9.71
	Total Water – Water	12601.01 ± 58.68	12601.36 ± 58.16	12599.95 ± 58.91	12599.45 ± 59.28
(f)	**Groups**	**Average No. of Hydrogen Bonds: (110) H-terminated diamond**			
		Minima	**~ 0.1 nm above the minima**	**~ 0.2 nm above the minima**	**Bulk (~ 1.5 nm)**

		(0.40 nm)	(0.50 nm)	(0.59 nm)	(1.52 nm)
	Dop – Water	6.99 ± 1.04	6.95 ± 1.17	6.78 ± 1.27	7.37 ± 1.15
	Interfacial Water – Water	26.32 ± 9.87	29.23 ± 10.27	31.86 ± 10.09	33.92 ± 10.84
	Total Water – Water	12621.28 ± 56.70	12629.24 ± 58.58	12627.10 ± 57.21	12627.13 ± 59.01
(g)	**Groups**	**Average No. of Hydrogen Bonds: (110) O-ether-terminated diamond**			
		Minima (0.44 nm)	**~ 0.1 nm above the minima (0.58 nm)**	**~ 0.2 nm above the minima (0.67 nm)**	**Bulk (~ 1.5 nm) (1.59 nm)**
	Dop – Water	6.84 ± 1.09	6.74 ± 1.23	6.94 ± 1.18	7.36 ± 1.14
	Dia – Dop	0.00 ± 0.04	0.08 ± 0.27	0.00 ± 0.03	0.00 ± 0.00
	Water – Dia	103.93 ± 8.10	104.23 ± 8.09	104.65 ± 8.07	104.72 ± 8.14
	Interfacial Water – Water	35.57 ± 10.28	36.29 ± 10.14	36.11 ± 10.17	36.02 ± 10.07
	Total Water – Water	12624.18 ± 58.62	12623.65 ± 58.11	12621.72 ± 58.46	12626.98 ± 58.31

Table 5.2 shows that the average number of hydrogen bonds to the surface changes as a function of dopamine-surface separation. Interestingly, for all O-terminated systems, the greatest number of diamond-dopamine hydrogen bonds appears to form not at the absorption minima but at 0.1 – 0.2 nm above the minima *i.e.* 0.58 – 0.72 nm from the surface carbons (and dropping to zero in bulk, as expected). It is suggested that this position is the ideal distance for diamond-dopamine hydrogen bonds to occur (between the polar groups on dopamine and the surface). As the optimum adsorption position lies at 0.42 – 0.52 nm from the surface carbons, it is hypothesised that the diamond-dopamine hydrogen bonds may play a role in driving dopamine adsorption to the O-terminated surfaces, but are not the principle contributor to the optimum position. This suggests that the favourable interactions formed by desolvation of the ring outweigh the unfavourable interaction of breaking diamond-dopamine hydrogen bonds. Therefore dopamine continues to approach until the ring has reached a position to experience optimum desolvation, and the polar groups on the dopamine at this close proximity prefer to bond with the surrounding water to maximise solvation, rather than with the underlying surface.

The dopamine-water hydrogen bonds display no significant change ~ ≤ 0.2 nm of the adsorption minima *i.e.* within 0.40 – 0.74 nm from the surface carbons (**Table**

5.2). Whilst no significant change was also observed in the interfacial water-water and diamond-water hydrogen bonds in this region, it is possible the disruption by a single molecule is relatively insignificant relative to the size of these networks. To maintain the favourable dopamine-water hydrogen bonds, either interfacial water-water or surface-water hydrogen bonds will need to be broken.

It is worth noting that whilst one dopamine molecule may only cause small changes, multiple molecules will have more considerable disruption on the interfacial water structure. Multiple dopamine molecules have not been addressed in this study but are of interest for future work (see section 5.6).

5.4.6 Orientation of Dopamine Functional Groups during Adsorption

To elucidate the mechanism of dopamine adsorption on diamond surfaces, the orientations of key functional groups were analysed as a function of distance from each surface. For the dopamine, the meta OH, para OH, CN and the aromatic ring were studied, as labelled in **Figure 5.6**.

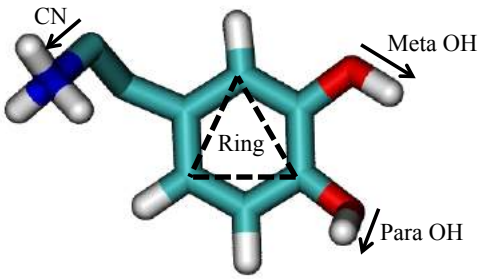

Figure 5.6*: A snapshot of dopamine used in the simulations with the key functional groups labelled. Arrows represent the para OH, meta OH and CN bonds, and the plane of the ring is denoted by the triangle that forms between three non-neighbouring ring carbons.*

The distributions of the angles, θ, that the vectors para OH, meta OH, CN and the normal to the plane of the aromatic ring make with the surface normal within each PMF constraint window are shown in **Figure 5.7**.

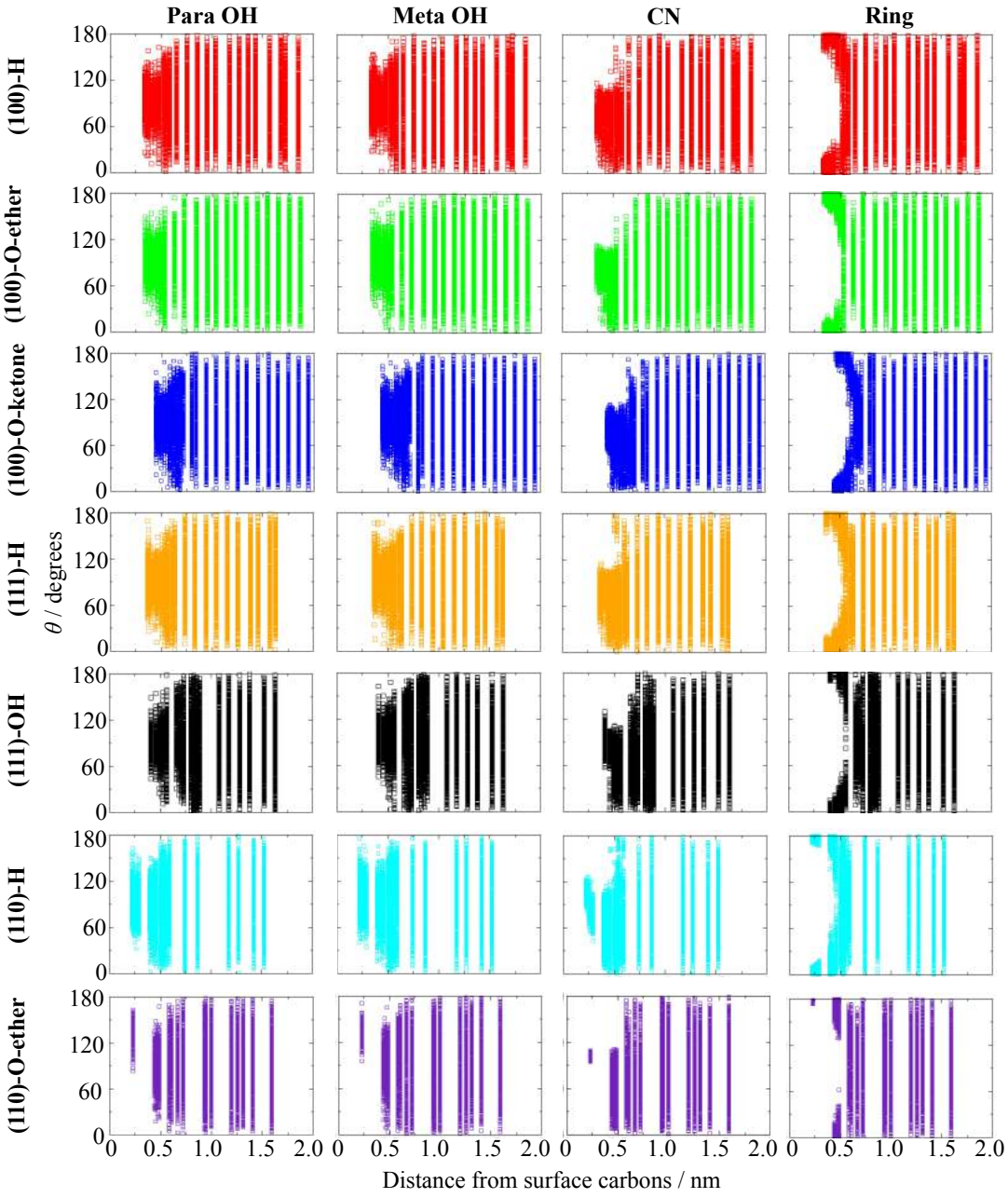

***Figure 5.7**: The distributions of bond and ring angles of dopamine at various positions away from seven different model diamond surfaces. The angle, θ, of the para OH, meta OH and CN bonds, as well as the normal to the ring plane, was calculated with respect to the surface normal (in this case, the z-axis) at each time frame (4 ps) over the last 5 ns of MD simulation for each PMF constraint window. Each plot therefore shows 20 – 30 distributions as a function of distance from the surface for each functional group. The zero point of reference is taken as the uppermost layer of carbons for each diamond surface.*

The collective shape of the distributions as a function of surface separation provides a qualitative insight into the conformational changes of each dopamine functional group during adsorption.

We observe in **Figure 5.7** that in bulk water (> 1.3 nm from the surfaces), all the functional groups are randomly orientated as the molecule is free to rotate and explore the space without inhibition from the underlying surfaces, causing wide distributions of possible orientations. As dopamine approaches the diamond surfaces, the functional groups begin to orientate into preferential configurations, thus reducing the spread of the distributions until they converge to the ideal conformation at the energy minima. All bond vectors converge to a single orientation, whereas the ring converges to two ideal orientations (**Figure 5.7**). It is noted that the starting distance (provided dopamine is in bulk) and starting orientation will not influence the orientation analysis, since dopamine is free to take any conformation within each constraint window and will always start randomly oriented in bulk (see PMF method, Chapter 2, section 2.6.5).

For a quantitative assessment of the role of each functional group of dopamine during adsorption to the diamond surfaces, the average and standard deviation of the para OH, meta OH and CN bond angles was calculated. **Tables 5.3, 5.4** and **5.5** display the bond angle for para OH, meta OH and CN, respectively, at four positions within 0.2 nm of the adsorption minima to capture the orientational changes that occur directly before the optimal adsorption position to cause dopamine to attain in the conformation observed in Figures 5.3 – 5.5. Since the dual mode of the ring would skew the statistics, the average and standard deviation of the ring plane angles were calculated in two regions > 90° and ≤ 90° at each position during adsorption (**Table**

5.6). The average and standard deviation at bulk (~ 1.5 nm) was also calculated for comparison.

Table 5.3*: Orientation of the para OH bond on dopamine during adsorption to different diamond surfaces with respect to the surface normal.*

Surface	**Orientation of para OH with respect to the surface normal (degrees)**				
	Minima (position in brackets (nm))	**~ 0.05 nm above the minima (position in brackets (nm))**	**~ 0.1 nm above minima (position in brackets (nm))**	**~ 0.2 nm above minima (position in brackets (nm))**	**Bulk (position in brackets taken at ~ 1.5 nm)**
(100)-H	89.4 ± 17.0 (0.44)	89.9 ± 20.1 (0.48)	87.2 ± 31.1 (0.54)	88.1 ± 32.3 (0.65)	86.0 ± 40.4 (1.57)
(100)-O-ether	91.5 ± 14.9 (0.42)	91.5 ± 18.4 (0.47)	83.4 ± 33.1 (0.53)	91.8 ± 25.0 (0.63)	93.1 ± 40.2 (1.54)
(100)-O-ketone	92.0 ± 13.0 (0.52)	98.7 ± 15.2 (0.58)	88.8 ± 18.8 (0.62)	102.8 ± 27.4 (0.72)	96.8 ± 43.5 (1.55)
(111)-H	89.6 ± 16.2 (0.46)	89.5 ± 20.8 (0.51)	84.5 ± 33.3 (0.56)	93.1 ± 38.0 (0.74)	91.0 ± 41.4 (1.57)
(111)-OH	90.7 ± 14.8 (0.49)	91.4 ± 19.1 (0.53)	102.3 ± 27.6 (0.66)	90.3 ± 30.8 (0.70)	91.7 ± 41.2 (1.52)
(110)-H	91.6 ± 16.7 (0.40)	92.1 ± 23.3 (0.44)	82.0 ± 33.7 (0.50)	94.1 ± 31.9 (0.59)	94.0 ± 38.6 (1.52)
(110)-O-ether	88.2 ± 15.5 (0.44)	89.5 ± 20.3 (0.49)	87.6 ± 29.8 (0.58)	86.0 ± 30.3 (0.67)	86.1 ± 41.1 (1.59)
				Overall Bulk:	91.2 ± 40.9

Table 5.4*: Orientation of the meta OH bond on dopamine during adsorption to different diamond surfaces with respect to the surface normal.*

Surface	**Orientation of meta OH with respect to the surface normal (degrees)**				
	Minima (position in brackets (nm))	**~ 0.05 nm above the minima (position in brackets (nm))**	**~ 0.1 nm above minima (position in brackets (nm))**	**~ 0.2 nm above minima (position in brackets (nm))**	**Bulk (position in brackets taken at ~1.5 nm)**
(100)-H	94.7 ± 16.5 (0.44)	94.8 ± 19.0 (0.48)	94.9 ± 27.9 (0.54)	92.7 ± 43.8 (0.65)	86.3 ± 39.1 (1.57)
(100)-O-ether	92.6 ± 15.3 (0.42)	95.0 ± 17.9 (0.47)	92.0 ± 25.6 (0.53)	119.0 ± 33.1 (0.63)	90.7 ± 38.0 (1.54)
(100)-O-ketone	94.7 ± 14.1 (0.52)	103.3 ± 17.8 (0.58)	104.9 ± 22.1 (0.62)	118.5 ± 25.8 (0.72)	101.1 ± 38.1 (1.55)
(111)-H	94.7 ± 17.0 (0.46)	94.4 ± 20.5 (0.51)	87.1 ± 26.4 (0.56)	105.0 ± 31.4 (0.74)	90.2 ± 38.2 (1.57)
(111)-OH	94.5 ± 15.1 (0.49)	95.0 ± 18.6 (0.53)	109.8 ± 33.2 (0.66)	92.8 ± 46.0 (0.70)	91.5 ± 35.7 (1.52)
(110)-H	93.2 ± 18.1 (0.40)	92.4 ± 22.1 (0.44)	92.8 ± 33.4 (0.50)	103.5 ± 38.8 (0.59)	88.0 ± 39.5 (1.52)
(110)-O-ether	92.6 ± 16.5 (0.44)	90.9 ± 22.6 (0.49)	98.7 ± 36.2 (0.58)	101.6 ± 43.4 (0.67)	94.9 ± 37.7 (1.59)
				Overall Bulk:	91.8 ± 38.0

***Table 5.5**: Orientation of the CN bond on dopamine during adsorption to different diamond surfaces with respect to the surface normal.*

Surface	Orientation of CN with respect to the surface normal (degrees)				
	Minima (position in brackets (nm))	**~ 0.05 nm above the minima (position in brackets (nm))**	**~ 0.1 nm above minima (position in brackets (nm))**	**~ 0.2 nm above minima (position in brackets (nm))**	**Bulk (position in brackets taken at ~ 1.5 nm)**
(100)-H	71.0 ± 22.0 (0.44)	67.7 ± 23.1 (0.48)	65.1 ± 21.3 (0.54)	63.5 ± 30.1 (0.65)	98.5 ± 39.1 (1.57)
(100)-O-ether	81.1 ± 14.1 (0.42)	63.7 ± 23.2 (0.47)	64.8 ± 23.9 (0.53)	54.1 ± 28.5 (0.63)	85.5 ± 36.6 (1.54)
(100)-O-ketone	61.1 ± 23.4 (0.52)	64.2 ± 21.7 (0.58)	64.9 ± 13.3 (0.62)	38.9 ± 18.4 (0.72)	72.3 ± 34.8 (1.55)
(111)-H	66.0 ± 21.5 (0.46)	69.0 ± 24.3 (0.51)	61.0 ± 23.5 (0.56)	75.2 ± 34.0 (0.74)	90.0 ± 36.8 (1.57)
(111)-OH	69.4 ± 20.0 (0.49)	61.5 ± 20.7 (0.53)	59.2 ± 24.8 (0.66)	63.2 ± 28.8 (0.70)	91.4 ± 37.2 (1.52)
(110)-H	67.1 ± 22.6 (0.40)	67.4 ± 22.9 (0.44)	61.6 ± 23.5 (0.50)	64.1 ± 35.2 (0.59)	90.8 ± 37.9 (1.52)
(110)-O-ether	68.7 ± 21.1 (0.44)	67.7 ± 22.7 (0.49)	68.7 ± 30.7 (0.58)	67.9 ± 36.1 (0.67)	85.1 ± 39.7 (1.59)
				Overall Bulk:	87.7 ± 37.4

***Table 5.6**: Orientation of the normal to the aromatic ring plane on dopamine during adsorption to different diamond surfaces with respect to the surface normal.*

Surface	Orientation of ring with respect to the surface normal (degrees)				
	Minima > 90° ≤ 90° (position in brackets (nm))	**~ 0.05 nm above the minima > 90° ≤ 90° (position in brackets (nm))**	**~ 0.1 nm above minima > 90° ≤ 90° (position in brackets (nm))**	**~ 0.2 nm above minima > 90° ≤ 90° (position in brackets (nm))**	**Bulk (position in brackets taken at ~ 1.5 nm)**
(100)-H	172.6 ± 4.2 13.6 ± 6.2 (0.44)	161.2 ± 9.4 16.2 ± 9.8 (0.48)	144.9 ± 14.2 36.3 ± 15.1 (0.54)	120.8 ± 19.6 61.1 ± 20.8 (0.65)	87.9 ± 38.2 (1.57)
(100)-O-ether	173.4 ± 4.3 5.9 ± 3.0 (0.42)	165.1 ± 6.6 16.4 ± 12.1 (0.47)	145.4 ± 14.5 32.7 ± 18.4 (0.53)	109.1 ± 13.7 60.9 ± 14.1 (0.63)	86.5 ± 41.0 (1.54)
(100)-O-ketone	171.0 ± 7.7 7.2 ± 3.5 (0.52)	169.1 ± 5.3 21.9 ± 8.9 (0.58)	146.6 ± 8.1 50.1 ± 23.0 (0.62)	103.6 ± 9.4 73.9 ± 17.6 (0.72)	80.7 ± 40.2 (1.55)
(111)-H	172.8 ± 5.5 11.2 ± 5.8 (0.46)	160.4 ± 12.8 20.8 ± 9.0 (0.51)	151.3 ± 11.4 36.6 ± 17.5 (0.56)	142.2 ± 17.9 45.9 ± 25.9 (0.74)	89.6 ± 41.0 (1.57)
(111)-OH	173.5 ± 4.1 10.4 ± 6.2 (0.49)	166.7 ± 7.3 16.7 ± 7.2 (0.53)	115.2 ±12.5 63.4 ± 13.2 (0.66)	105.7 ± 10.8 70.6 ± 20.7 (0.70)	91.4 ± 41.7 (1.52)
(110)-H	170.7 ± 3.4 13.6 ± 7.5 (0.40)	156.4 ± 14.5 19.5 ± 14.3 (0.44)	125.2 ± 19.2 42.9 ± 13.6 (0.50)	114.5 ± 10.2 59.3 ± 21.4 (0.59)	94.9 ± 40.2 (1.52)
(110)-O-ether	169.4 ± 5.5 4.8 ± 3.5 (0.44)	160.1 ± 10.5 14.7 ± 12.1 (0.49)	132.5 ± 16.8 62.5 ± 4.0 (0.58)	114.4 ± 16.7 65.9 ± 12.4 (0.67)	89.1 ± 41.1 (1.59)
				Overall Bulk:	88.6 ± 40.5

At distances of 0.44 – 0.74 nm from each of the surfaces, the para OH and meta OH groups begin to assume orientations different from random (**Figure 5.7**). By

0.2 nm away from the energy minima, both the para OH and meta OH display orientations still relatively variable, with the para OH assuming an average conformation parallel to the surface (θ = ~ 90°) (**Table 5.3**), whilst the meta OH points slightly more towards each surface on average (**Table 5.4**). Since the greatest number of dopamine-surface hydrogen bonds occurs at ~ 0.1 – 0.2 nm away from the minima, it is likely they are rotating to maximise hydrogen bonding and are potentially driving the adsorption towards forming favourable dopamine-surface hydrogen bonds. The orientations of both OH groups converge towards ~ 90° with decreasing dopamine-surface separation until both the meta and para OH groups lie parallel to each surface at the energy minima *i.e.* θ = ~ 90° with small variation.

In a similar manner, the CN bond also begins to converge at distances 0.44 – 0.74 nm towards an angle of θ = ~ 70° close to each diamond surface (**Figure 5.7**) *i.e.* pointing at an angle away from the surface towards bulk, as seen in the snapshots in Figures 5.3 – 5.5. At 0.2 nm away from the energy minima, the CN bond is already close to θ = 70° on all surfaces except the (100) O-ketone-terminated surface, where the CN bond lies at θ = ~ 39° and rotates during the final approach (within 0.1 – 0.2 nm of the minima) to reach θ = ~ 70° at the energy minima (**Table 5.5**).

At distances of 0.44 – 0.74 nm from the diamond surfaces, the ring has a preference for two different orientational modes of reflective symmetry about θ = 90°, either where the ring points away from the surface at an angle of θ = ~ 0° – 60°, or points towards the surface at an angle of θ = ~ 120° – 180° with respect to the surface normal (**Figure 5.7**). As dopamine approaches close to the energy minima, a dramatic change is observed in the ring orientation (**Table 5.6**). The ring collapses on to the surface *i.e.* from orientations of θ = 103.6 – 120.8° and θ = 45.9 – 79.3° on average at 0.2 nm away from the energy minima, to θ = 169.4 – 173.5° and θ = 4.8 – 13.6° on

average at the minima. Here, the ring lies almost flat but angled slightly to point away/towards the surface, respectively. This highlights that the ring does not remain completely flat on the diamond surfaces but rocks slightly between these two modes. This phenomenon is observed as a rocking movement on all surfaces when visualising the simulation trajectories at the PMF constraint energy minima.

5.4.7 Distribution of Dopamine O Distances during Adsorption

To further elucidate the role of the para and meta OH bonds during adsorption, the distribution of O distances for the para OH and meta OH at the adsorbed minima, 0.1 nm above the adsorbed position, 0.2 nm above the adsorbed position and bulk (~ 1.5 nm) for each of the surfaces are shown in **Figure 5.8**.

In bulk, the para O and meta O are spread over a range of distances relative to the surface as the OH groups can freely rotate relative to the ring (**Figure 5.8**). As dopamine approaches each surface, the OH groups begin to orientate into fixed positions causing the spread of the distance distributions to reduce.

At ~ 0.2 nm away from the minima *i.e.* 0.59 – 0.74 nm from the surface carbons, the para O and meta O already display a peak at a similar position to the minima on all surfaces except the (111) H-terminated, where the distribution is still similar to bulk. For para O, this peak remains consistent at all positions during the final approach to the minima in agreement with the relatively stable average orientation of ~ 90° observed for para OH in **Table 5.3**.

At ~ 0.1 nm from the minima *i.e.* 0.50 – 0.66 nm from the surface carbons, this peak drops on the O-terminated surfaces and the spread of distances increases (**Figure 5.8**). When the minimum is reached, the sharp peak is restored. This same trend is seen for the meta O, but the drop in the peak at ~ 0.1 nm away from the adsorption minima is even more distinct, covering a greater distribution. Given that

the greatest number of diamond-dopamine hydrogen bonds appear to form around this surface separation, but seem to break before the energy minima is reached (see Table 5.2), the increase in spread at ~ 0.1 nm above the adsorption minima may correlate to the broken dopamine OH – surface hydrogen bonds that cause the OH bonds to become more disordered while they rearrange to find another favourable conformation. We may expect a local energy minimum to appear in the PMF profiles around this position, however this was not captured in our profiles likely as changes in the hydrogen bonding due to a single dopamine molecule may be negligible compared to the total. Furthermore, it appears that the para OH group stays at a relatively fixed position close to the surface, whereas the meta OH iteratively rotates relative to the para OH to find the most favourable conformation, likely motivated to locate the ideal distance and angle to form a favourable hydrogen bond. Once adsorbed, the para and meta OH both settle at the approx. stable distributions about ~ 90° (**Figure 5.8**).

In addition, on the H-terminated surfaces, a drop in the peak is less distinct and the distributions also converge towards the sharpest peak at the minima relating to the relatively stable adsorption position (~ 90°). This provides further support that the drop on the O-terminated surfaces is related to the breaking of dopamine-surface hydrogen bonds. Furthermore, the adsorption peak at all positions is less distinct and spread over a wider range for both para and meta O. This indicates that the H-terminated surfaces have less influence on the dopamine OH groups, allowing them greater freedom of rotation. This is likely a consequence of their inability to hydrogen bond to the H-terminated surfaces, forcing them to bond with the solution instead, which will be less stable due to the mobility of the water molecules.

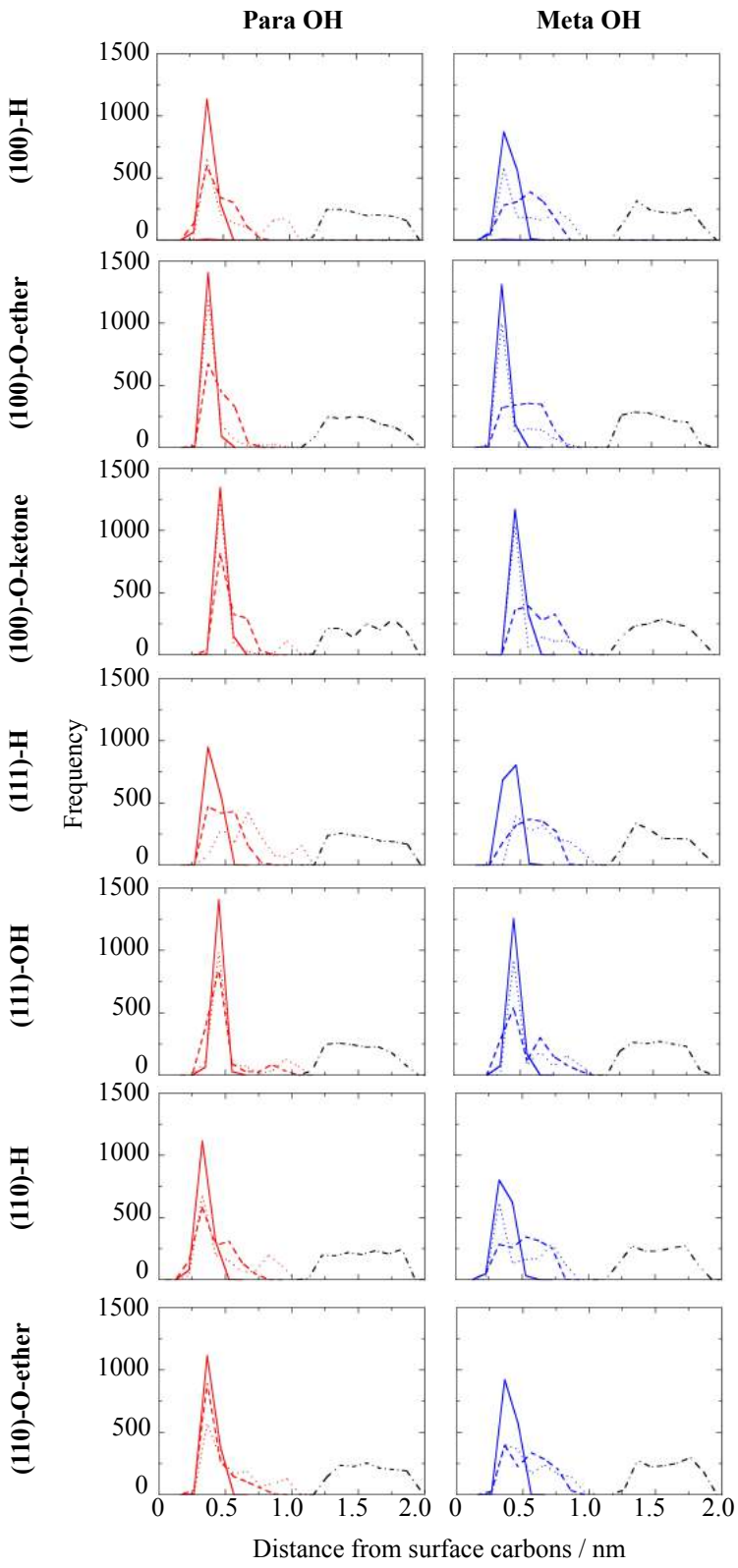

Figure 5.8: *Distribution of para O (red) and meta O (blue) z-positions at the absorption minima (solid), ~ 0.1 nm (dashed) and ~ 0.2 nm above the minima (dotted), The distribution in bulk (dotted black) is also shown for comparison.*

5.4.8 Dopamine Adsorption Pathway to Diamond

The analysis presented thus far has enabled a detailed picture to form of the structure and orientation of dopamine during the final stages of adsorption to diamond surfaces. Collating the structural results in sections 5.4.1 – 5.4.7, as well as visualising the dopamine trajectory within each PMF constraint window on each surface, enables us to map the adsorption pathway of dopamine from bulk to the optimum position on diamond, as shown in **Figure 5.9** through the use of snapshots of dopamine at different separations away from the (100) H-terminated diamond surface. The analysis in the previous sections is crucial to revealing the adsorption pathway, as the snapshots alone could not be understood without the structural analysis. Given the similarity in the structural analysis and final conformation attained close to each surface, the stages presented in **Figure 5.9** are considered representative of the general adsorption steps of dopamine to any diamond surface regardless of crystal orientation and surface termination. Furthermore, this is the first MD study of dopamine/serotonin with any solid surface, suggesting this pathway could be generalised to represent the adsorption of these molecules to other surfaces as well.

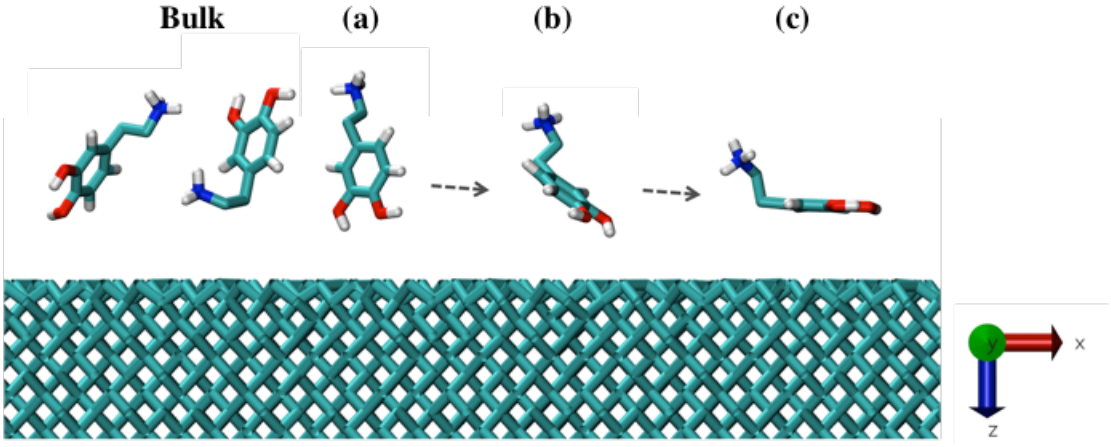

***Figure 5.9**: The proposed adsorption mechanism of dopamine on diamond (100) H-terminated surface. This mechanism is considered representative for the adsorption of dopamine on any diamond surface.*

Within bulk, dopamine adopts random orientations (**Figure 5.9**). At a distance of 0.44 – 0.74 nm from the surface carbons on the diamond surfaces, the OH groups appear to orientate to point towards the surface with the normal of the aromatic ring tilted at an angle approx. perpendicular to the surface and the NH_3^+ at the end of the ring extending into bulk water (**Figure 5.9**a). As the dopamine molecule approaches the surface, the ring begins to collapse from approx. perpendicular (~ 103 – 152° and 45 – 74°) to parallel (~ 90°) to the surface (**Figure 5.9**b) where it lies relatively flat close to the diamond at the adsorption minima (**Figure 5.9**c). Here, it sits within the first structured interfacial water layer, close enough to the surface to create a region of reduced water density and desolvate the aromatic ring. However, the ring does not remain fixed but moves in a slight rocking motion between two stable modes of orientation on the surface. This indicates that the forces on dopamine at the free energy minima (desolvation of the ring and attractive intermolecular forces) are not strong enough to keep dopamine in one conformation, and the energy barrier is small enough that it can be overcome by thermal fluctuations enabling dopamine to continually switch between the two favourable ring conformations (shown in section 5.4.6), hence creating an observable rocking motion on the surface.

During adsorption to all surfaces, the NH_3^+ group generally remains pointing away from the surface towards bulk, with the CN bond residing at an angle of ~ 70° to the *z*-axis throughout the approach (**Figure 5.9**). At the energy minima, the polar amine group is observed to remain at this conformation, sitting away from the surface in a region of higher water density, as it is more energetically favourable to keep the polar NH_3^+ group solvated. During adsorption, the OH groups rotate with the ring (**Figure 5.9**). At a distance of ~ 0.2 nm from the energy minima *i.e.* 0.59 – 0.74 nm from the surface carbons, both OH groups rotate to maximise hydrogen bonding. It is

observed at ~ 0.1 nm from the adsorption minima on O-terminated surfaces *i.e.* 0.53 – 0.66 nm away from surface carbons, the distributions of para O and meta O positions become greater than they were at ~ 0.2 nm from the adsorption minima *i.e.* 0.63 – 0.72 nm from the surface carbons, possibly correlated to the breaking of dopamine-surface hydrogen bonds. This is also observed for H-terminated surfaces but the motivation remains elusive. Ultimately, dopamine settles at the most energetically favourable conformation on all surfaces at the energy minima *i.e.* 0.40 – 0.52 nm from the surface carbons, where both OH groups sit relatively flat to the surface at an orientation of ~ 90° to the *z*-axis (**Figure 5.9**).

At ~ 0.1 – 0.2 nm from the adsorption minima *i.e.* 0.58 – 0.72 nm from the surface carbons, the greatest number of hydrogen bonds appear to form between dopamine and the O-terminated surfaces. This is likely between the OH groups and the surface, since the NH_3^+ group never penetrates close enough to bond. However, dopamine does not remain at this distance, which suggests that it prefers to break these bonds to move as close as possible to the surface to desolvate the ring instead. Desolvation of the ring (the hydrophobic effect) is therefore considered the key driving force on all surfaces, rather than the maximisation of surface-dopamine hydrogen bonds, and explains why dopamine adsorption is favourable on both hydrophobic and hydrophilic diamond surfaces. This is in agreement with Netz *et al.,* who outlined the importance of the hydrophobic effect in the desorption of a tyrosine residue from a hydrophobic diamond surface, which has structural similarity to dopamine.[38]

On the O-terminated diamond surfaces, the formation of surface-dopamine hydrogen bonds is considered to be the initial driving force for adsorption. It has been eluded to in literature that the driving force on the orientation of OH^- ions close to H-

terminated surfaces is due to the greater interaction between the electrostatic potential drop near the surface and the O– in the OH^- ions, compared to the O– in the water that has a smaller negative charge (−1.41 *vs.* −0.82 e).[54] However, the O– in the OH^- groups on dopamine has a charge of −0.70 e *i.e.* less than water O–, making this effect unlikely in our system. Consequently, the driving force for adsorption on the H-terminated surfaces is considered to be ring desolvation and maximisation of water-water hydrogen bonds.

5.4.9 Free Energy Calculations of Serotonin on Diamond Surfaces

The PMF free energy profiles of adsorption of serotonin to each diamond surface are discussed below followed by a comparison with dopamine. Similar to dopamine, the serotonin plots converged to time-independent profiles within 15 ns of MD simulation. The final PMF profiles shown below are therefore averaged over 15 ns. The PMF free energy minima for serotonin and the *z*-position at which it occurs relative to each diamond surface are outlined in **Table 5.7**. Similar to dopamine, the optimum position lies in the first structured water region for serotonin on all diamond surfaces (**Table 5.7**). This suggests that it is more favourable to break the strong interfacial water hydrogen bonds within this region. Uncertainties in the optimum position were calculated from the positions either side of the minima. It is of note that the calculated PMF free energy of adsorption is a combination of enthalpic and entropic contributions, as discussed in detail in section 5.4.14.

***Table 5.7**: Optimum PMF free energy of adsorption and the z-position at which it occurs for serotonin on different (100), (111) and (110) diamond surfaces.*

Surface	Optimal PMF Free Energy of Serotonin Adsorption (kJ mol^{-1})	Optimum Serotonin – Surface Separation (nm)	Distance away from the peak of first structured water (optimum position – peak position) (nm)
(100)-H	−22.56 ± 1.17	0.42 ± 0.01	+0.03
(100)-O-ether	−25.75 ± 1.16	0.45 ± 0.03	+0.06
(100)-O-ketone	−41.95 ± 1.07	0.52 ± 0.02	+0.11
(111)-H	−22.69 ± 1.19	0.44 ± 0.02	+0.04
(111)-OH	−30.75 ± 1.15	0.56 ± 0.14	+0.13
(110)-H	−22.09 ± 1.02	0.43 ± 0.07	+0.05
(110)-O-ether	−22.15 ± 1.47	0.44 ± 0.07	+0.02

5.4.10 Adsorption of Serotonin on (100) diamond surfaces

The PMF free energy profiles for the adsorption of serotonin to the (100) diamond surfaces are displayed in **Figure 5.10** along with a snapshot of the conformation that serotonin attains at each free energy minimum. The trend is the same as dopamine on (100) diamond surfaces with adsorption the strongest to the O-ketone-terminated surface (−41.95 ± 1.07 kJ mol^{-1}), followed by the O-ether-terminated (−25.75 ± 1.16 kJ mol^{-1}), and weakest to the H-terminated (−22.56 ± 1.17 kJ mol^{-1}) (**Figure 5.10**). Furthermore, the energy begins to deviate from bulk at a further distance from the surface on (100) O-ketone-terminated (~ 0.92 nm) compared to (100) H– and (100) O-ether-terminated diamond (~ 0.75 nm), to the same minimum position as dopamine on the O-ketone-terminated surface of 0.52 ± 0.02 nm (**Table 5.7**). The serotonin profile is likely shifted further away from the (100) O-ketone-terminated surface, compared to the other surfaces, due to both the protruding topography and intermolecular forces of the C=O groups, as discussed for dopamine (see section 5.4.2). Serotonin adopts a structural conformation at the adsorption minima similar to dopamine, where the rings lie flat to the surface with the NH_3^+ group pointing into bulk. This suggests serotonin is also driven to an ideal position

that maximises desolvation of the rings whilst ensuring solvation of the polar groups (OH, NH, NH_3^+).

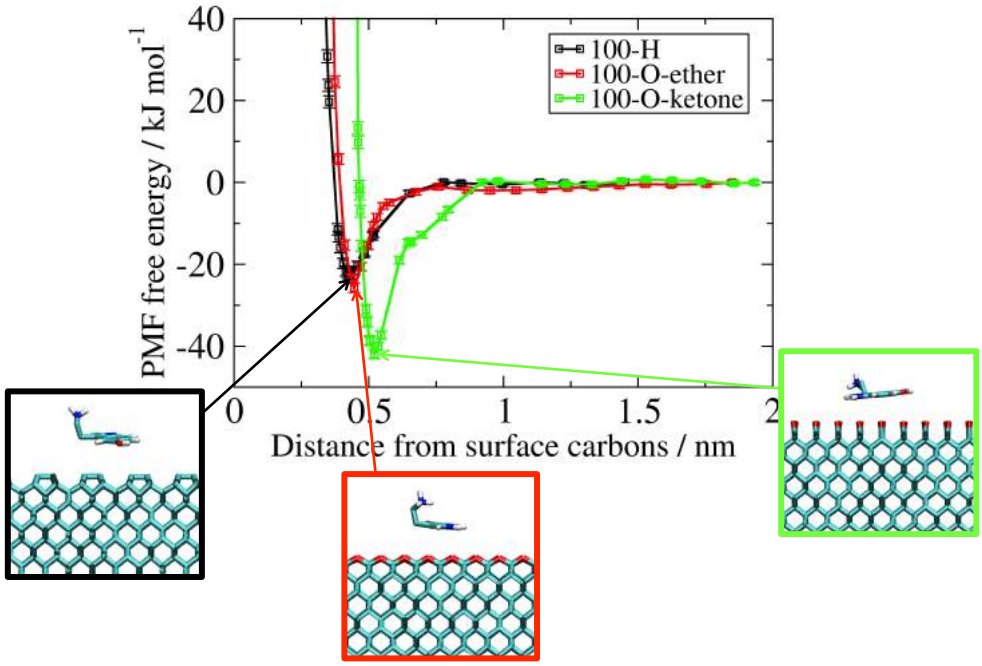

***Figure 5.10**: PMF free energy of adsorption of serotonin on (100) H-terminated, O-ether-terminated and O-ketone-terminated diamond surfaces as a function of surface separation.*

5.4.11 Adsorption of Serotonin on (111) Diamond Surfaces

The PMF free energy profiles for the adsorption of serotonin to the (111) diamond surfaces are displayed in **Figure 5.11** along with a snapshot of the conformation that serotonin attains at each free energy minimum. Similar to dopamine (section 5.4.3), serotonin adsorbs more strongly on the (111) OH-terminated diamond surface (−30.75 ± 1.15 kJ mol^{-1}) compared to the (111) H-terminated (−22.69 ± 1.19 kJ mol^{-1}) (**Figure 5.11**). In addition, the minima lies at a further distance from the OH-terminated surface (0.56 ± 0.14 nm) compared to the H-terminated (0.44 ± 0.02 nm), as expected due to spatial constraints of the additional surface O atom. The adsorption strength of serotonin is less on the (111) OH-terminated compared to the (100) O-ketone-terminated surface. This is potentially due

to unfavourable disruption of the stronger interfacial hydrogen bond network close to the (111) OH-terminated surface (as discussed for dopamine in section 5.4.3). Serotonin adopts the same conformation on the (111) diamond surfaces at the free energy minima as observed on the (100) surfaces (**Figure 5.11**).

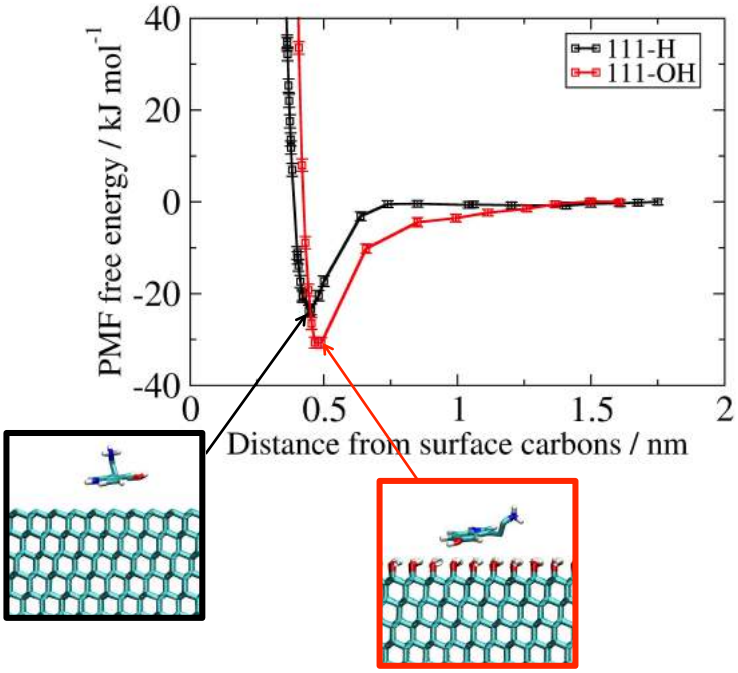

***Figure 5.11**: PMF free energy of adsorption of serotonin on (111) H-terminated, and (111) OH-terminated diamond surfaces as a function of surface separation.*

5.4.12 Adsorption of Serotonin on (110) Diamond Surfaces

The PMF free energy profiles for the adsorption of serotonin to the (110) diamond surfaces are displayed in **Figure 5.12** along with a snapshot of the conformation that serotonin attains at each free energy minimum. Similar to dopamine on (110) diamond surfaces (section 5.4.4), serotonin appears to adsorb to a similar extent on these surfaces with adsorption minima of -22.09 ± 1.02 kJ mol^{-1} on the (110) H-terminated and -22.15 ± 1.47 kJ mol^{-1} on the (110) O-ether-terminated surface (**Figure 5.12**). Thorough checking of these systems has eliminated technical errors, so the reason for the similarity remains elusive. A slight barrier to adsorption

exists on the (110) O-ether-terminated surface possibly due to unfavourable reorganisation of the interfacial hydrogen bond network at that position. Serotonin adopts the same conformation at the energy minima on the (110) diamond surfaces that was observed on the (100) and (111) surfaces (**Figure 5.12**).

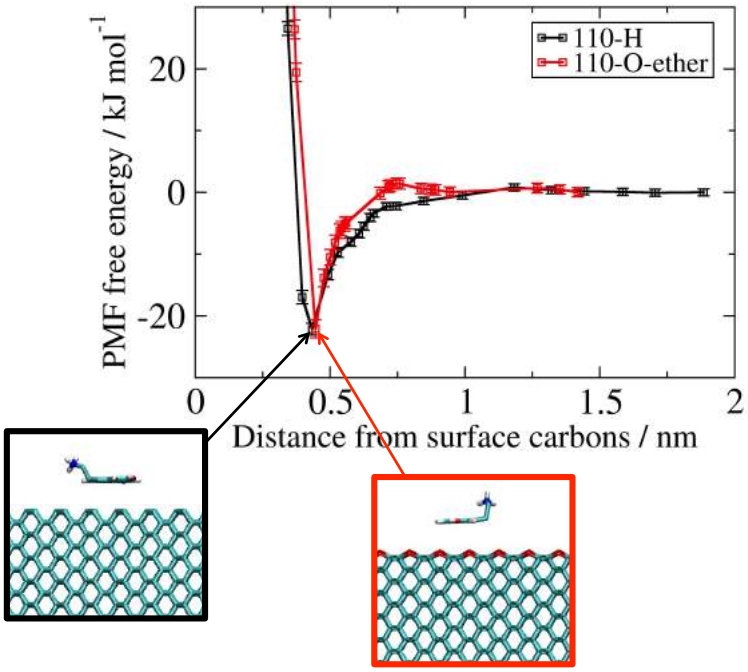

***Figure 5.12**: PMF free energy of adsorption of dopamine on (110) H-terminated, O-ether-terminated and O-ketone-terminated diamond surfaces as a function of surface separation.*

5.4.13 Serotonin Adsorption Pathway to Diamond

Serotonin displays very similar trends to dopamine for adsorption on diamond surfaces. This is likely due to the structural similarity between the molecules. Study of each PMF constraint window reveals that serotonin attains similar conformations indicating it adsorbs through a similar pathway. The proposed serotonin adsorption pathway on diamond (based on snapshots from VMD) is shown in **Figure 5.13**.

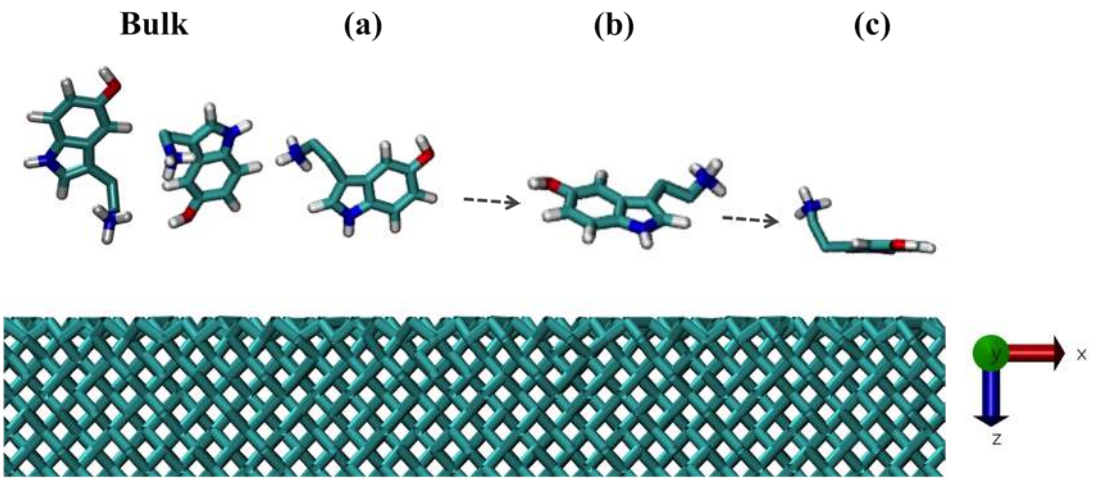

***Figure 5.13**: The proposed adsorption mechanism of serotonin on diamond (100) H-terminated surface. This mechanism is considered representative for the adsorption of dopamine on any diamond surface.*

Conclusions about the serotonin adsorption pathway on diamond can be drawn based on examination of the simulation trajectories and the qualitative similarity to the dopamine pathway. Serotonin adsorption appears to be guided by the NH group on the aromatic ring, which likely plays a similar role to the OH groups in dopamine. The similarity to dopamine strongly suggests that the formation of surface-serotonin hydrogen bonds is likely the initial driving force for NH groups pointing the O-terminated surfaces.

As serotonin approaches each surface, the aromatic ring re-orients to lie parallel to the surface at the adsorption minima. Here, it displays an observable rocking motion as it moves between two favourable conformations, similar to dopamine at the minima. The rocking motion is likely due to similar energies for both configurations, so that thermal fluctuations will overcome the energy barrier allowing serotonin to easily switch between the two conformations, hence causing the rocking motion.

At the adsorption minima, the NH_3^+ groups remain consistently pointing upwards into solution to maintain solvation. This conformation is considered ideal to maximise desolvation of the ring and solvation of the polar groups.

For all surfaces, serotonin is positioned within the first structured water region that will cause disruption in the water-water and surface-water hydrogen bond network. This suggests that, similar to the dopamine, maximising desolvation of the ring has preference over hydrogen bonding.

5.4.14 Entropic *vs.* Enthalpic Contributions to Adsorption for Dopamine and Serotonin

The free energy as a function of separation was obtained in sections 5.4.1 – 5.4.4 for dopamine and sections 5.4.9 – 5.4.12 using PMF calculations. This energy is a function of enthalpic and entropic contributions. The change in enthalpy in the system is the difference between the sum of the total interaction energies occurring in bulk, compared to at the adsorption minima. Dopamine and serotonin both attain a conformation where the aromatic ring(s) lie parallel to all diamond surfaces at the energy minima (see sections 5.4.8 and 5.4.13). This confirmation is not a consequence of the constraint method at small neurotransmitter-surface separations, as the biomolecule is free to rotate *i.e.* the ring(s) could have theoretically attained an upright geometry perpendicular to the surface if that was more energetically favourable. Instead, the ring(s) lie flat so that it shields the hydrophobic groups against the surface to minimise unfavourable interactions with the water, whilst maximising the favourable interactions of polar molecules (water-water, water-polar groups on dopamine, surface-water in the case of hydrophilic surfaces). The energy minimum for each molecule on each surface is the position where this trade-off is maximised *i.e.* where the enthalpic contribution is the greatest.

The change in entropy due to the adsorption of dopamine is complicated. At the energy minima, an entropic gain to the system exists as the water is displaced from the structured interfacial water and released into bulk solution. However, this is partially compensated by an entropic loss due to dopamine attaining a fixed conformation once adsorbed that also causes the underlying surface groups to order relative to it. Methods exist that can decompose the PMF into its respective entropic and enthalpic contributions, by calculating the separate energy contributions for the free energy of association of species-species and species-solvent.[55] This is of interest for the future, although these methods are typically done for small molecules *e.g.* methane, and will be challenging to implement for larger molecules where a greater number of interactions exist, as discussed by Wright *et al*. for the adsorption of benzene to (011) quartz.[56] It is also worth noting that GROMOS was parameterised to capture the relative free enthalpy of hydration and solvation,[45] so there is no guarantee that the entropic changes are correctly captured with this force field.

5.4.15 Comparison of Serotonin and Dopamine Adsorption on Diamond

The PMF free energy profiles of adsorption of dopamine on to all diamond surfaces (as discussed in sections 5.4.1 – 5.4.8) are plotted in **Figure 5.14**ai with a zoom-in of the minima in **Figure 5.14**aii alongside the free energy profiles for serotonin to all diamond surfaces (as discussed in sections 5.4.9 – 5.4.13) in **Figure 5.14**bi with a zoom-in of the minima in **Figure 5.14**bii.

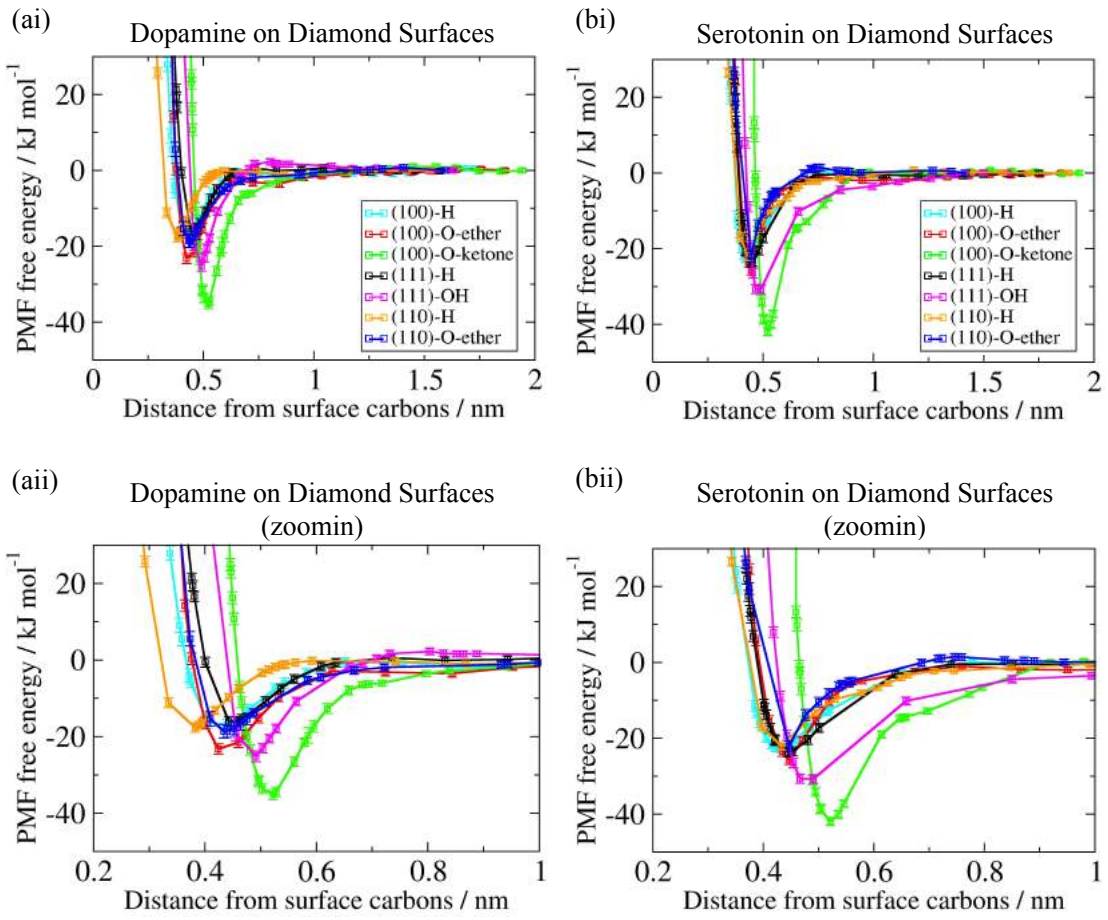

***Figure 5.14**: PMF profiles for (a) dopamine and (b) serotonin on seven different diamond surfaces with (i) the full profiles and (ii) zoom-ins of the peak region.*

Serotonin adsorbs significantly more strongly than dopamine on all surfaces *i.e.* for serotonin *vs.* dopamine: -22.56 ± 1.17 kJ mol^{-1} *vs.* -16.99 ± 1.43 kJ mol^{-1} on (100) H-terminated, -25.75 ± 1.16 kJ mol^{-1} *vs.* -23.24 ± 1.34 kJ mol^{-1} on (100) O-ether-terminated, -41.95 ± 1.07 kJ mol^{-1} *vs.* -35.15 ± 1.27 kJ mol^{-1} on (100) O-ketone-terminated, -23.69 ± 1.19 kJ mol^{-1} *vs.* -16.04 ± 1.25 kJ mol^{-1} on (111) H-terminated, -30.75 ± 1.15 kJ mol^{-1} *vs.* -25.13 ± 1.40 kJ mol^{-1} on (111) OH-terminated, -22.09 ± 1.02 kJ mol^{-1} *vs.* -17.65 ± 1.18 kJ mol^{-1} on (110) H-terminated, and -22.15 ± 1.47 kJ mol^{-1} *vs.* -18.60 ± 1.79 kJ mol^{-1} on (110) O-ether-terminated (**Figure 5.14**). The enhanced adsorption strength for serotonin further supports the important role of the hydrophobic effect through desolvation of the ring *i.e.* there is

greater adsorption energy for serotonin due to the favourable desolvation of two rings, rather than the one in dopamine. Consequently, it can be predicted that all catecholamines will follow a similar trend and adsorption mechanism. As the strength of adsorption can be directly linked to the presence of ring groups for these structures, compounds with a greater number of ring groups *e.g.* the oxidation derivatives of dopamine and serotonin including poly(dopamine) and poly(serotonin) are expected to adsorb with greater strength on diamond. This provides an explanation for the surface fouling observed on hydrophobic and hydrophilic BDD electrodes during oxidation reactions of these species (Chapter 6). Both molecules display a similar trend in adsorption with the strongest to the (100) O-ketone–, followed by (111) OH– and then (100) O-ether– terminated. The weakest adsorption was observed to the (110) O-ether– and H– terminated surfaces. As previously discussed for dopamine, the order of strength is due to favourable intermolecular (dispersion, electrostatic, hydrophobic) interactions between the surface groups and dopamine as well as optimal topographical positioning of dopamine relative to each surface, where the C=O groups are the most successful at maximising these factors to cause the greatest strength of binding.

The difference in free energy between dopamine and serotonin was similar on all diamond surfaces, with smaller differences observed on diamond surfaces containing ether groups *i.e.* 2.51 ± 2.50 kJ mol^{-1} for (100) O-ether-terminated, 3.55 ± 3.26 kJ mol^{-1} on (110) O-ether-terminated, and larger differences on surfaces containing hydrogen *i.e.* 5.57 ± 2.60 kJ mol^{-1} for (100) H-terminated, 6.65 ± 2.44 kJ mol^{-1} on (111) H-terminated, 4.44 ± 2.20 kJ mol^{-1} on (110) H-terminated, hydroxyl *i.e.* 5.62 ± 2.55 kJ mol^{-1} on (111) OH-terminated, and ketone groups *i.e.* 6.80 ± 2.34 kJ mol^{-1} on (100) O-ketone-terminated. This indicates that C–O–C groups have weak

interaction with dopamine and serotonin, due to weaker intermolecular forces and non-ideal positioning of diamond that causes unfavourable disruption to the interfacial water. The differences in general are too small to likely achieve any noticeable selectivity. Hence, it appears that none of these surfaces are suitable for selective detection between serotonin and dopamine. It is noted that the respective enthalpic and entropic contributions to the free energy of adsorption may elucidate some further differences between each molecule and the different surfaces, which is worth investigating in the future, as discussed in detail in section 5.4.14.

However, whilst the differences in free energy of dopamine and serotonin on diamond surfaces are small for a single molecule (as above), the effect may be magnified when considering realistic concentrations of serotonin and dopamine in solution. As the (100) O-ketone-terminated surface displays the greatest difference for a single molecule *i.e.* 6.80 ± 2.34 kJ mol^{-1} on (100) O-ketone-terminated, this surface is the most likely to accomplish preferential adsorption of serotonin over dopamine and is recommended to be tested experimentally. In addition, simulations of multiple and mixed dopamine/serotonin systems on this surface would be a good starting point for future work to test co-operativity and competition.

If the requirement were for a diamond surface that *strongly* binds dopamine or serotonin *e.g.* to form poly(dopamine)– or poly(serotonin)– coated diamond biosensors,[36] a ketone-terminated surface would be recommended. As ketone (C=O) surface groups are of higher abundance on (100) diamond crystal faces,[26] this single crystal surface would be ideally suited, or use of surface treatments, such as anodic polarisation, that enhance the density of C=O groups on polycrystalline diamond.[57]

As inner-sphere ET species, dopamine and serotonin are required to bind to the surface for the chemical reaction to proceed, and in systems with fast ET kinetics,

the adsorption mechanism may be the rate-limiting step (although other factors will also influence the reaction, see Chapter 3, section 3.2). DFT calculations of dopamine adsorbed on (100) O-ketone- and (100) H- terminated surfaces outlined a correlation between the stable adsorption distance and ET rate, with dopamine positioned further away from the O-ketone-terminated surface and displaying a slightly slower ET rate.[51] The findings of our work are in agreement with this literature. Hence, it is also suggested that H-terminated surfaces could enhance the dopamine ET kinetics *e.g.* the (110) H-terminated for dopamine and the (100) H-terminated for serotonin, as dopamine and serotonin appear to lie closest on average to these surfaces, respectively (see Tables 5.1 and 5.7).

If the requirement were for a diamond surface that *weakly* binds dopamine or serotonin *e.g.* that easily releases the species from the surface to reduce electrode fouling or for use in neurological medical equipment that require non-fouling surfaces,[37] a H-terminated diamond surface would be recommended. As crystallographic orientation made little difference on the adsorption strength of these species to H-terminated surfaces, any single crystal or polycrystalline diamond surface would be suitable. Weaker adsorption of dopamine and serotonin to H-terminated diamond surfaces is in agreement with experimental evidence that reports H-terminated diamond surfaces have increased resistance to neurotransmitter fouling compared to O-terminated.[58] This suggests that H-terminated diamond may be the ideal surface for diamond electrodes, as they favourably adsorb dopamine/serotonin to ensure a reaction, but weakly enough so that the reactant may not remain adsorbed on the surface, thus causing reduced fouling that may enable longer functionality. However, it is noted that the oxidation products produced during the reaction will also

cause fouling. Study of the adsorption of the oxidation products would help to further elucidate the ideal diamond surface, but was beyond the scope of this study.

5.5 Conclusions

Atomistic MD models (built in Chapter 4) were utilised to investigate the adsorption of dopamine and serotonin to seven different hydrophobic and hydrophilic model diamond surfaces using potential of mean force (PMF) constraint calculations. Significantly, the work enabled the free energy of adsorption of each molecule on to different diamond surfaces to be calculated for the first time. This led to recommendations of the ideal surfaces that will enhance/inhibit neurotransmitter binding on diamond in a range of sensor applications in healthcare and bioelectrochemisty. Through detailed structural analysis of dopamine, including the orientations and positions of key functional groups and hydrogen bonding, the first ever pathway to adsorption of dopamine and serotonin on diamond was postulated. In fact, no reports currently exist in literature on the adsorption of dopamine and serotonin to any solid surface, so the results are useful for the general field that utilise neurotransmitter-surface interfaces. The results provide information that is valuable for optimised design of diamond sensors detecting neurotransmitters (see section 5.1).

Our results show that the binding strength of dopamine and serotonin is favourable on all surfaces (−16 – −42 kJ mol^{-1}), so the species will adsorb on diamond independent of crystal orientation or surface termination. Both species followed the same trend in adsorption, with strongest binding to the (100) O-ketone-terminated surface and weakest binding to H-terminated surfaces.

In terms of selective detection of dopamine and serotonin, the similarity in adsorption indicates that none of these diamond surfaces are suitable to selectively adsorb dopamine/serotonin over the other. However, the (100) O-ketone-terminated

surface was recommended as the ideal surface for use in any device that requires *strong* adsorption of dopamine/serotonin to diamond surfaces *e.g.* in poly(dopamine)–modified diamond electrodes.[36] H-terminated surfaces were recommended for any device that requires *weaker* adsorption of dopamine/serotonin to the surface *e.g.* to potentially reduce fouling of electrodes. Based on DFT findings that correlate the stable adsorption position of dopamine to ET kinetics,[51] it is recommended that faster dopamine/serotonin ET kinetics may be observed on H-terminated diamond surfaces *i.e.* surfaces where the species have an optimum position closest to the surface. In this case, the (110) H-terminated surface for dopamine and the (100) H-terminated surface for serotonin were recommended.

The pathway to adsorption of dopamine to each diamond surface was determined to be same on all surfaces. The OH^- groups initially point towards the surface with the NH_3^+ group positioned away from the surface towards bulk water. This is followed by the ring and OH^- groups rotating until they lie approx. flat to the surface at the position of the free energy minima, and the NH_3^+ remains pointing upwards towards bulk. The final configuration is considered the ideal trade-off between desolvation of the ring and solvation of the polar groups. Interestingly, the hydrophobic effect (desolvation of the ring) is shown to be preferable over diamond-dopamine hydrogen bond formation. Serotonin and dopamine are structurally similar molecules, with serotonin containing an additional aromatic ring. The greater strength of binding to all diamond surfaces by serotonin, compared to dopamine, supports the important role of the hydrophobic effect at any neurotransmitter-surface interface.

5.6 Future Work

The work presented in this study has examined the binding strength and pathway of a single dopamine or serotonin molecule to different diamond surfaces.

Decomposing the free energy into enthalpic and entropic contributions would be useful for future work to further elucidate the role of the hydrophobic effect, which would increase the entropic contribution of each system. The introduction of multiple molecules, or mixed species systems, would be the next step to further the study to provide a closer match to dopamine/serotonin concentrations that are used experimentally and can provide a greater insight into physiological neurotransmitter systems. Investigating the species interactions would enable a fundamental understanding into cooperative or competitive binding of these species to diamond surfaces. This would reveal if the differences in adsorption strength between dopamine and serotonin observed on certain diamond surfaces *e.g.* (100) O-ketone-terminated for a single molecule is magnified with many molecules. Multiple molecule systems more akin to experimental concentrations would enable further insight into the ideal diamond surface that could be used to simultaneously and accurately detect dopamine and serotonin concentrations *in vivo*.

In order to optimise the electrochemical properties, DFT calculations of dopamine and serotonin adsorbed on each of these diamond surfaces would help to support our findings and further elucidate the difference in ET between the surfaces. Whilst the adsorption strength of serotonin and dopamine has been studied, fouling in electrochemical systems is also due to the reaction products. An investigation into the desorption force of the oxidation products (*e.g.* quinone or polymer melanin-like compounds) would help to further elucidate the ideal non-fouling diamond surface.

5.7 References

[1] a) P. Seeman, N. H. Bzowej, H. Guan, C. Bergeron, G. Reynolds, E. Bird, P. Riederer, K. Jellinger, W. Tourtellotte, *Neuropsychopharmacol.* **1987**; b) G. LaHoste, J. Swanson, S. Wigal, C. Glabe, T. Wigal, N. King, J. Kennedy, *Mol. Psychiatr.* **1996**, *1*, 121-124.

[2] a) K.-P. Lesch, R. Mössner, *Biol. Psychiatr.* **1998**, *44*, 179-192; b) T. R. Insel, E. A. Mueller, I. Alterman, M. Linnoila, D. L. Murphy, *Biol. Psychiatr.* **1985**, *20*, 1174-1188.
[3] G. Di Giovanni, V. Di Matteo, M. Pierucci, E. Esposito, *Prog. Brain Res.* **2008**, *172*, 45-71.
[4] S. Kapur, G. Remington, *Am. J. Psychiatr.* **1996**, *153*, 466-476.
[5] R. D. Oades, *Prog. Brain Res.* **2008**, *172*, 543-565.
[6] D. M. Sasaki-Adams, A. E. Kelley, *Neuropsychopharmacol.* **2001**, *25*, 440-452.
[7] C. Damsa, A. Bumb, F. Bianchi-Demicheli, P. Vidailhet, R. Sterck, A. Andreoli, S. Beyenburg, *J. Clin. Psychiatr.* **2004**, *65*, 1064-1068.
[8] E. Esposito, *Curr. Drug Targets* **2006**, *7*, 177-185.
[9] R. T. Kachoosangi, R. G. Compton, *Anal. Bioanal. Chem.* **2007**, *387*, 2793-2800.
[10] K. Wu, J. Fei, S. Hu, *Anal. Biochem.* **2003**, *318*, 100-106.
[11] E. Rand, A. Periyakaruppan, Z. Tanaka, D. A. Zhang, M. P. Marsh, R. J. Andrews, K. H. Lee, B. Chen, M. Meyyappan, J. E. Koehne, *Biosens. Bioelectron.* **2013**, *42*, 434-438.
[12] a) J. Li, X. Lin, *Sensors Actuat. B Chem.* **2007**, *124*, 486-493; b) T. Selvaraju, R. Ramaraj, *Electrochem. Commun.* **2003**, *5*, 667-672.
[13] G.-P. Jin, X.-Q. Lin, J.-m. Gong, *J. Electroanal. Chem.* **2004**, *569*, 135-142.
[14] B. K. Swamy, B. J. Venton, *Analyst* **2007**, *132*, 876-884.
[15] a) B. A. Patel, X. Bian, V. Quaiserová-Mocko, J. J. Galligan, G. M. Swain, *Analyst* **2006**, *132*, 41-47; b) L. Hutton, M. E. Newton, P. R. Unwin, J. V. Macpherson, *Anal. Chem.* **2008**, *81*, 1023-1032; c) A. Moore, V. Celorrio, M. M. de Oca, D. Plana, W. Hongthani, M. J. Lázaro, D. J. Fermín, *Chem. Comm.* **2011**, *47*, 7656-7658; d) G. R. Salazar-Banda, H. B. Suffredini, L. A. Avaca, S. A. Machado, *Mater. Chem. Phys.* **2009**, *117*, 434-442.
[16] T. Kondo, Y. Niwano, A. Tamura, J. Imai, K. Honda, Y. Einaga, D. A. Tryk, A. Fujishima, T. Kawai, *Electrochim. Acta* **2009**, *54*, 2312-2319.
[17] A. Fujishima, T. N. Rao, E. Popa, B. Sarada, I. Yagi, D. Tryk, *J. Electroanal. Chem.* **1999**, *473*, 179-185.
[18] A. Suzuki, T. A. Ivandini, K. Yoshimi, A. Fujishima, G. Oyama, T. Nakazato, N. Hattori, S. Kitazawa, Y. Einaga, *Anal. Chem.* **2007**, *79*, 8608-8615.
[19] B. Sarada, T. N. Rao, D. Tryk, A. Fujishima, *Anal. Chem.* **2000**, *72*, 1632-1638.
[20] E. Popa, H. Notsu, T. Miwa, D. Tryk, A. Fujishima, *Electrochem. Solid-State Lett.* **1999**, *2*, 49-51.
[21] G. M. Swain, A. B. Anderson, J. C. Angus, *MRS bulletin* **1998**, *23*, 56-60.
[22] J. V. Macpherson, *Phys. Chem. Chem. Phys.* **2015**, *17*, 2935-2949.
[23] a) P. Roach, D. Farrar, C. C. Perry, *J. Am. Chem. Soc.* **2006**, *128*, 3939-3945; b) M. S. Lord, M. Foss, F. Besenbacher, *Nano Today* **2010**, *5*, 66-78.
[24] T. Teraji, S. Mitani, C. Wang, T. Ito, *J. Cryst. Growth* **2002**, *235*, 287-292.
[25] T. Kondo, K. Honda, D. A. Tryk, A. Fujishima, *J. Electrochem. Soc.* **2005**, *152*, E18-E23.
[26] L. A. Hutton, J. G. Iacobini, E. Bitziou, R. B. Channon, M. E. Newton, J. V. Macpherson, *Anal. Chem.* **2013**, *85*, 7230-7240.
[27] R. Trouillon, Y. Einaga, M. A. Gijs, *Electrochem. Commun.* **2014**, *47*, 92-95.
[28] A. R. Leach, *Molecular Modelling: Principles and Applications*, Pearson Education, **2001**.

[29] R. A. Latour Jr, *Curr. Opin. Solid St. M.* **1999**, *4*, 413-417.
[30] L. B. Wright, T. R. Walsh, *J. Phys. Chem. C* **2012**, *116*, 2933-2945.
[31] L. M. Ghiringhelli, B. Hess, N. F. van der Vegt, L. Delle Site, *J. Am. Chem. Soc.* **2008**, *130*, 13460-13464.
[32] W. Qin, X. Li, W.-W. Bian, X.-J. Fan, J.-Y. Qi, *Biomaterials* **2010**, *31*, 1007-1016.
[33] M. Hoefling, F. Iori, S. Corni, K.-E. Gottschalk, *Langmuir* **2010**, *26*, 8347-8351.
[34] C. Sanchez, P. Belleville, M. Popall, L. Nicole, *Chem. Soc. Rev.* **2011**, *40*, 696-753.
[35] a) T. Secker, R. Hervé, Q. Zhao, K. Borisenko, E. Abel, C. Keevil, *Biofouling* **2012**, *28*, 563-569; b) H. J. Mathieu, *Surf. Interface Anal.* **2001**, *32*, 3-9; c) A. E. Hadjinicolaou, R. T. Leung, D. J. Garrett, K. Ganesan, K. Fox, D. A. Nayagam, M. N. Shivdasani, H. Meffin, M. R. Ibbotson, S. Prawer, *Biomaterials* **2012**, *33*, 5812-5820.
[36] O. Pop-Georgievski, N. Neykova, V. Proks, J. Houdkova, E. Ukraintsev, J. Zemek, A. Kromka, F. Rypaček, *Thin Solid Films* **2013**, *543*, 180-186.
[37] a) M. Roham, J. M. Halpern, H. B. Martin, H. J. Chiel, P. Mohseni, *IEEE T. Bio-Med. Eng.* **2008**, *55*, 2628-2634; b) A. Thalhammer, R. J. Edgington, L. A. Cingolani, R. Schoepfer, R. B. Jackman, *Biomaterials* **2010**, *31*, 2097-2104.
[38] D. Horinek, A. Serr, M. Geisler, T. Pirzer, U. Slotta, S. Lud, J. Garrido, T. Scheibel, T. Hugel, R. Netz, *Proc. Natl. Acad. Sci.* **2008**, *105*, 2842-2847.
[39] K. B. Borisenko, H. J. Reavy, Q. Zhao, E. W. Abel, *J. Biomed. Mater. Res. Part A* **2008**, *86*, 1113-1121.
[40] C. Nebel, J. Ristein, *Thin-Film Diamond II (Semiconductors and Semimetals), Vol. 77*, Elsevier B. V., Amsterdam, Netherlands., **2004**.
[41] A. W. Schuettelkopf, D. M. Van Aalten, *Acta Crystallogr. D Biol. Crystallogr.* **2004**, *60*, 1355-1363.
[42] T. A. Ostomel, Q. Shi, P. K. Stoimenov, G. D. Stucky, *Langmuir* **2007**, *23*, 11233-11238.
[43] J. Armstrong, R. Barlow, *Br. J. Pharmacol.* **1976**, *57*, 501-516.
[44] A. Chattopadhyay, R. Rukmini, S. Mukherjee, *Biophys. J.* **1996**, *71*, 1952-1960.
[45] C. Oostenbrink, A. Villa, A. E. Mark, W. F. Van Gunsteren, *J. Comput. Chem.* **2004**, *25*, 1656-1676.
[46] avogadro.openmolecules.net, *Avogadro: an open-source molecular builder and visualization tool. Version 1.1.1*, **2012**.
[47] S. Pronk, S. Páll, R. Schulz, P. Larsson, P. Bjelkmar, R. Apostolov, M. R. Shirts, J. C. Smith, P. M. Kasson, D. van der Spoel, *Bioinformatics* **2013**, *29*, 845-854.
[48] a) H. J. Berendsen, D. van der Spoel, R. van Drunen, *Comput. Phys. Commun.* **1995**, *91*, 43-56; b) B. Hess, C. Kutzner, D. Van Der Spoel, E. Lindahl, *J. Chem. Theory Comput.* **2008**, *4*, 435-447; c) D. Van Der Spoel, E. Lindahl, B. Hess, G. Groenhof, A. E. Mark, H. J. Berendsen, *J. Comput. Chem.* **2005**, *26*, 1701-1718.
[49] W. Humphrey, A. Dalke, K. Schulten, *J. Mol. Graphics* **1996**, *14*, 33-38.
[50] P. Jedlovszky, J. Brodholt, F. Bruni, M. Ricci, A. Soper, R. Vallauri, *J. Chem. Phys.* **1998**, *108*, 8528-8540.

[51] D. Tryk, H. Tachibana, H. Inoue, A. Fujishima, *Diamond Relat. Mater.* **2007**, *16*, 881-887.
[52] C. Janiak, *J. Chem. Soc.* **2000**, 3885-3896.
[53] a) K. A. Melzak, C. S. Sherwood, R. F. Turner, C. A. Haynes, *J. Colloid Interface Sci.* **1996**, *181*, 635-644; b) B. D. Kay, K. R. Lykke, J. R. Creighton, S. J. Ward, *J. Chem. Phys.* **1989**, *91*, 5120-5121.
[54] P. Koelsch, P. Viswanath, H. Motschmann, V. Shapovalov, G. Brezesinski, H. Möhwald, D. Horinek, R. R. Netz, K. Giewekemeyer, T. Salditt, *Colloid Surf. A* **2007**, *303*, 110-136.
[55] a) N. Choudhury, B. M. Pettitt, *J. Phys. Chem. B* **2006**, *110*, 8459-8463; b) D. E. Smith, L. Zhang, A. Haymet, *J. Am. Chem. Soc.* **1992**, *114*, 5875-5876.
[56] L. B. Wright, C. L. Freeman, T. R. Walsh, *Mol. Simul.* **2013**, *39*, 1093-1102.
[57] C. H. Goeting, F. Marken, A. Gutiérrez-Sosa, R. G. Compton, J. S. Foord, *Diamond Relat. Mater.* **2000**, *9*, 390-396.
[58] J. Xu, Q. Chen, G. M. Swain, *Anal. Chem.* **1998**, *70*, 3146-3154.

Chapter 6

Electrochemical Comparison of Hydrogen- vs. Oxygen- Terminated Boron Doped Diamond Electrodes

6.1 Overview and Key Advances to Knowledge in this Chapter

Electrochemical biosensors are an essential tool for detection and quantification of biological molecules in a wide range of fields including healthcare, security, and environmental monitoring. A key challenge in biosensor fabrication is finding a robust electrode material that produces a distinct, accurate and reproducible signal for the species of interest. Boron-doped diamond (BDD) has exceptional electrochemical properties including an extremely wide solvent window, low background currents, and reduced chemical fouling making it an attractive choice in electrochemical biosensing devices.

In this chapter, the electrochemical responses *e.g.* CV shape, oxidation/reduction peak position, peak-to-peak separation for a range of electroactive inner-sphere (surface sensitive) species on H- (hydrogen plasma) and O- (alumina polished) terminated BDD were reported. Previous electrochemical BDD studies comparing inner-sphere species on H- and O- terminated BDD are typically missing essential characterisation of factors that will influence the response in addition to the termination *e.g.* the boron dopant density, diamond quality (sp^2 carbon content) and

surface characterisation, thus rendering the results inconclusive. This is the first study using well-defined H- and O- terminated surfaces and high quality conducting BDD material so that any differences in electrochemical response are entirely prescribed to the different surface terminations. The results of this chapter extend the work by Hutton *et al.,* who previously reported comparison of the electrochemical response of $Fe(CN)_6^{4-}$ on alumina polished and hydrogen plasma terminated surfaces, and, to the best of our knowledge, no further CV studies comparing species on alumina polished and hydrogen plasma treated BDD exist in the scientific community.

The electrochemical responses of a range of biologically relevant inner-sphere species ($Fe(CN)_6^{4-/3-}$, NADH, riboflavin, dopamine, ascorbic acid, serotonin, $Fe^{2+/3+}$) on conducting BDD were recorded. These were compared against each other, as well as with responses reported for carbon electrodes in literature, enabling the reason for the CV responses to be postulated based on chemical information. In addition, the electrochemical response of the outer-sphere (non-surface sensitive) species, $Ru(NH_3)_6$, on semi-conducting BDD was reported and a novel microscale 'read-write' surface patterning technique was introduced. This technique is useful for future creation of microarrays on electrodes facilitating multiple simultaneous experiments.

The results of this chapter can now be input alongside the voltammetric responses for these species on other electrode materials, enabling the scientific community to make an informed choice on the electrode material used to detect that species in future experiments. They can also be used as a guide in future experiments to map electrochemical data on BDD to the species, dopant density and type of surface termination reported. Hence, the results of this chapter significantly contribute to knowledge in the diamond and electrochemical fields providing information that is essential for choice and rational design of biosensor material in the future.

6.2 Introduction

Controlling the surface chemistry of electrodes is of great importance for the fabrication of sensors in order to improve electrocatalytic performance and enable an assessment of the impact of surface chemistry on the fundamentals of electrochemical phenomena.[1] Understanding the influence of surface treatments on the electron transfer (ET) kinetics of redox active species can also help to improve the sensitivity, stability and accuracy of detection. Species that are categorised as 'inner-sphere' require chemisorption or bridging to the electrode for the reaction to occur, whereas 'outer-sphere' mediators can transfer electrons without the need for surface interactions (see Chapter 3, section 3.5). Manipulating surface groups on electrodes can encourage favourable adsorption to improve the reaction kinetics for the inner-sphere couple, but may also cause increased fouling if the reactant, intermediate or product is prone to remain on the surface after electron transfer (ET). .

In the electrochemistry field, conducting boron doped diamond (BDD) electrodes are proving popular due to their biocompatibility, larger solvent windows (compared to a metal electrode), low background currents, processability and high resistance to fouling.[2] Chemical functionalisation of BDD is particularly attractive due to the considerable stability of the surface chemical bonds.[3] At the simplest level, diamond can be either –H or –O terminated. For example, diamond materials grown under a hydrogen atmosphere are hydrogen (–H) terminated, rendering the surface hydrophobic. Alternatively, oxygen (–O) termination is possible using a variety of methods including, for example, boiling in acid, exposure to an O_2 plasma or anodic polarisation.[4] O-terminated surfaces are hydrophilic. Other methods also exist for terminating the surface with a wide variety of more complex molecular species.[3] On insulating diamond, H-termination results in a measurable surface

conductivity, due to surface transfer doping and an increase in available charge carriers (see Chapter 1, section 1.2.5).[5] Hence, for diamond, changing surface termination not only influences the surface chemistry but can also affect the electrical characteristics.

Different electrode kinetics give rise to different CV responses.[6] **Figure 6.1** demonstrates the effect of varying the intrinsic rate of electron transfer (k^0) on the cyclic voltammetry (CV) response for a model diffusion-limited system. Each CV was calculated using a finite-element (FEM) simulation with Bulter-Volmer kinetics to describe the flux at the electrode surface.[6] The simulations were run by Sze-yin Tan, University of Warwick (see Declaration). The model assumes entirely planar diffusion and all other parameters except k^0 are kept constant (electrode size = 1 mm, temperature (T) = 298 K, number of electrons (n) = 1, transfer coefficient (α) = 0.5, diffusion coefficient (D) = 5×10^{-6} cm s^{-1}, concentration (c) = 1 mM, and scan rate (v) = 0.1 V s^{-1}). Since the rate of mass transport (k^t) remains constant *i.e.* v, D, A and n are fixed (see Chapter 3, equation 3.9) the trend is purely due to changes in k^0. **Figure 6.1**a depicts a 'reversible' wave shape, where the value of k^0 is considerably fast compared to mass transport (*i.e.* $k^0 \sim > 10^{-3}$ cm s^{-1}) so that the system maintains a Nernstian equilibrium (59 mV peak-to-peak separation, ΔE_p, for n = 1 and T = 298 K). Experimentally, the system is considered kinetically limited if there is a greater than 10 mV increase in ΔE_p from reversible *i.e.* > 69 mV.[7] As k^0 decreases, ΔE_p increases and the wave shape becomes more elongated. Greater overpotentials are therefore required to drive the reaction. The response no longer obeys Nernstian conditions and is described as 'quasi-reversible' (**Figure 6.1**b) *i.e.* $\sim 10^{-3} > k^0 > 10^{-8}$ cm s^{-1}. The system eventually becomes 'irreversible' (**Figure 6.1**c) for extremely sluggish electron transfer kinetics (*i.e.* $k^0 \sim < 10^{-8}$ cm s^{-1}), where only the half-

reaction is observed in the potential window. Importantly for this study, we see that the shape of the CVs can provide significant comparison of the ET kinetics of our species at different H- and O- terminated BDD electrodes.

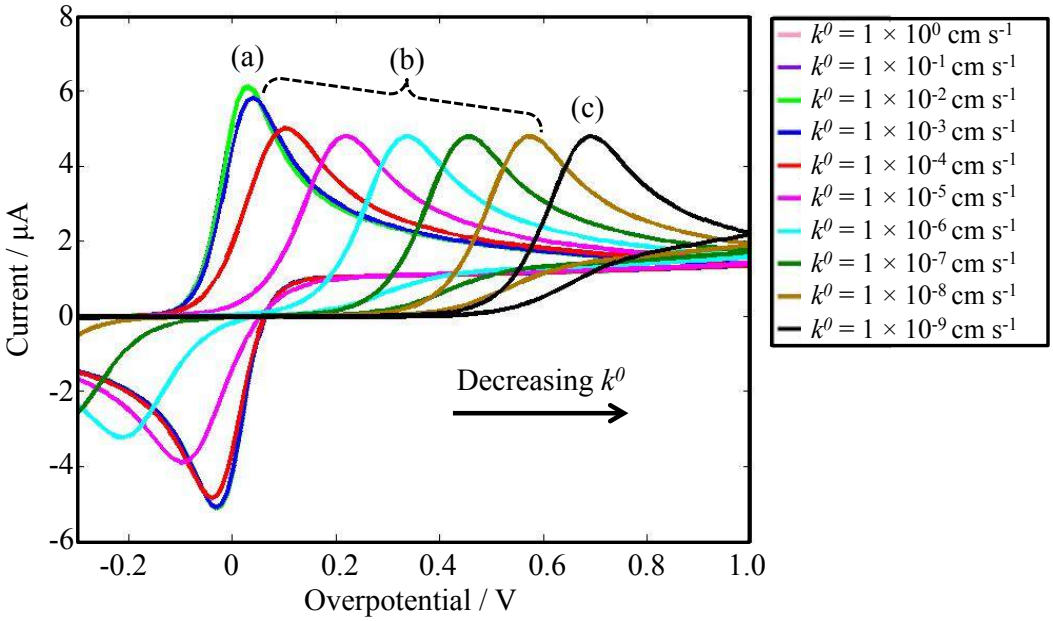

***Figure 6.1**: Schematic of CVs for a model planar diffusion-limited system calculated using finite-element simulations on a 1 mm diameter disc macroelectrode as k^0 is varied from 10 to 10^{-8} cm s^{-1}. The CVs display (a) reversible, (b) quasi-reversible and (c) irreversible wave shapes with decreasing k^0. All other parameters are constant: T = 298 K, n = 1, α = 0.5, D = 5×10^{-6} cm s^{-1}, c = 1 mM, and v = 0.1 V s^{-1}.*

The amount of boron doping in diamond controls the electrical properties. For metal-like behaviour, the diamond must be doped with > 10^{20} B atoms cm^{-3}.[8] Boron levels less than this result in p-type semi-conducting behaviour (see Chapter 1, Figure 1.6). Furthermore, the removal of local charge carriers as the surface termination changes from H- to O- termination is expected to have a significant effect on the ET kinetics of any inner/outer-sphere redox couple for semi-conducting BDD electrodes. As a conducting (metal-like) BDD electrode contains a sufficiently high density of charge carriers, removal of the H-termination layer is unlikely to have a significant effect on the electrochemical response towards an outer-sphere species. However,

inner-sphere species are surface sensitive and will behave differently on different chemical functionalisations.

Notable studies by Fujishima,[9] McCreery[10] and Swain[11] investigated the effect of surface termination on diamond and carbon electrodes for a range of inner-sphere mediators. These studies focus on as-grown or hydrogen plasma treated BDD rendering the surface H-terminated, and anodically or oxygen plasma treated BDD rendering the surface O-terminated. Considerably fewer reports exist comparing the effect of hydrogen plasma (–H) and alumina polishing (–O) treatments on the electrochemical response.[12]

Different oxygen surface treatments have been found to result in different chemical groups on the electrode surface, as determined by X-ray photoelectron spectroscopy (XPS) measurements *i.e.* XPS comparison of alumina and anodically treated BDD surfaces showed that anodically treated BDD surfaces contain a high proportion of C=O groups in the form of highly oxidised carbon functional groups *i.e.* COOH and carbonate groups, whereas alumina polished displayed a mix of C–OH, C–O–C and C=O groups (**Figure 6.2**).[12-13] XPS spectra and high-resolution electron energy spectroscopy (HREELS) of oxygen plasma treated BDD revealed a high proportion of C–O–C groups on the surface.[4b, 14]

Cathodic electrochemical treatment of the BDD electrode surface is thought to result in H functionalisation, although reports suggest the chemical environment may be different from that obtained by exposure to a hydrogen environment.[15] We also note that as-grown (H-terminated) diamond surfaces will slowly convert to O-termination over an unspecified amount of time, once exposed to air.

Many surface functionalisation studies employ low-quality, nanocrystalline thin film diamond, which contains a high abundance of sp^2 carbon impurities at the

grain boundaries. Sp^2 carbon will present different functionalities to the surrounding BDD surface when oxygen terminated,[16] thus influencing ET.[17] In this study, we use high quality (minimal sp^2 carbon content), well-characterised microcrystalline freestanding BDD electrodes to elucidate changes specifically due to the surface termination.

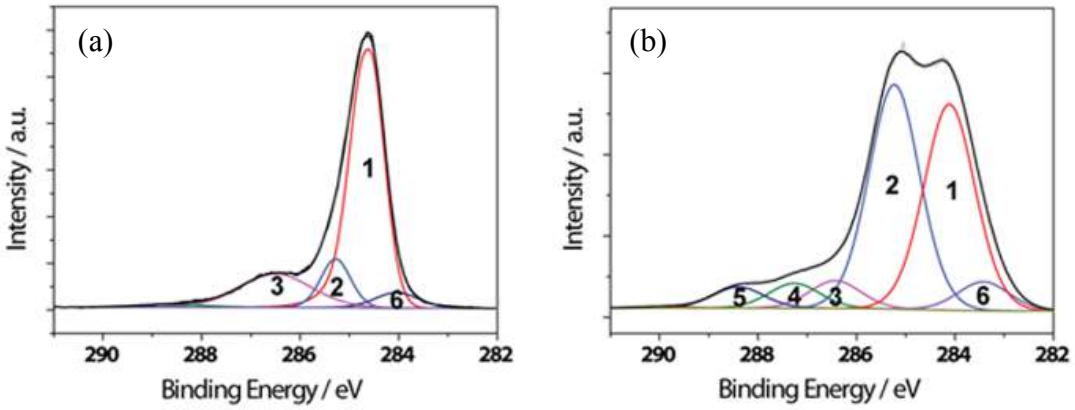

Figure 6.2*: C1s XPS spectra at room temperature for an (a) alumina polished and (b) anodically polarised BDD electrode.*[12] *Peaks are labelled as: (1) sp^3 carbon, (2) C–OH and C–O–C, (3) C=O, (4) COOH (5) polycarbonate groups (6) sp^2 carbon.*

One application of diamond surface manipulation is controlled microscale patterning. Patterning of an electrode can lead to higher detection sensitivities, the ability to sense multiple analytes and to make many measurements on one device. Various approaches to patterning have been proposed,[18] the most popular being lithography, where a mask is used to define regions of the surface for subsequent chemical modification.[19] For conventional metal electrodes, self-assembled monolayers, or physisorbed molecules are typically attached to the localised region of interest in order to tailor the molecular surface chemistry.[20] Microscale chemical patterning of diamond surfaces has been achieved using several techniques including lithographic chemical/molecular functionalization,[21] and scanning probe modification.[22] However, these are write-only processes and other techniques must

then be utilised to "read" the resulting chemical functionalization. Methodologies that operate dual "read-write" chemical analysis of electrodes on the micron scale are desirable to facilitate fast and accurate read-outs.

The aim of this study was to investigate the effect of surface chemistry, in particular, hydrogen plasma and alumina polishing treatments, on the electrochemical response of conducting polycrystalline BDD electrodes for a range of inner-sphere redox couples: $Fe(CN)_6^{4-/3-}$, NADH, riboflavin, dopamine, ascorbic acid, serotonin, and $Fe^{2+/3+}$. This provides a fundamental insight into the surface sensitivity of these electrochemical mediators. The influence of surface termination on the electrochemical response of semi-conducting BDD for the outer-sphere mediator $Ru(NH_3)_6^{3+}$ was also investigated. In this case, the semi-conducting surface was initially hydrogen plasma treated and then gradually oxidised using anodic polarisation. Using this redox system, a new electrochemical approach to the microscale "read-write" chemical patterning of semi-conducting diamond electrodes using scanning electrochemical cell microscopy (SECCM)[23] is presented.

6.3 Experimental Methods

6.3.1 Solutions

All solutions were prepared using MilliQ water (Millipore Corp., resistivity 18.2 MΩ cm at 25 °C). For electrochemical measurements 1 mM potassium ferrocyanide ($Fe(CN)_6^{4-}$, 99.99%, Sigma Aldrich), iron (II) sulphate $FeSO_4.7H_2O$ (Fe^{2+}, ≥ 99.0%, Sigma-Aldrich), dopamine hydrochloride (≥ 98%, Sigma Aldrich), serotonin hydrochloride (99%, Acros Organics), riboflavin (≥ 98%, Sigma Aldrich), β-Nicotinamide adenine dinucleotide (NADH, 95%, Sigma Aldrich), europium (III) nitrate pentahydrate (99.9%, Sigma Aldrich), L-ascorbic acid (≥ 99.0%, Sigma

Aldrich) and hexaammineruthenium (III) chloride ($Ru(NH_3)_6^{3+}$, 99%, Sigma Aldrich) were employed, either in 0.1 M potassium chloride (KCl, 99%, Fisher Scientific, analytical grade), 0.1 M potassium nitrate (KNO_3, 99%, Fisher Scientific), 0.1 M perchloric acid ($HClO_4$, Acros organics, reagent grade, 70%) or 0.1 M phosphate buffered saline (PBS, pH 6.96). All solutions were deaerated prior to use by purging with N_2 gas for 1 hour.

6.3.2 Materials Preparation

The voltammetric response of H- and O- terminated BDD was tested using two polycrystalline diamond electrodes – (1) chemical vapour deposited, conducting (metal-like) freestanding polycrystalline BDD in wafer form (> 3×10^{20} boron atoms cm^{-3}), and (2) freestanding, semi-conducting polycrystalline BDD (*ca*. 2×10^{18} boron atoms cm^{-3}), both grown by Element Six, Harwell, UK. All samples were polished to an ~ nm finish using a diamond lapping technique.[12] The conducting (metal-like) BDD electrodes were cut from the wafer using a laser micromachiner (E-355H-3-ATHI-O system, Oxford Lasers) into either (1) ~ 4 × 4 mm squares (for H-termination studies), or (2) ~ 1 mm diameter discs (for O-terminated studies). The semi-conducting BDD electrode was of dimensions 5.1 × 3.9 mm.

6.3.3 Fabrication of O-terminated BDD Electrodes

For the O-terminated electrochemical studies, the 1 mm diameter BDD discs were mounted as macroelectrodes. A schematic of the set-up is shown in **Figure 6.3**a. The discs were acid cleaned by boiling in concentrated H_2SO_4 (95%, Fisher Scientific) supersaturated with KNO_3.[24] This served to both remove any loose sp^2 carbon produced during the laser cutting,[25] and to oxygen-terminate the BDD surfaces.[26] A reliable ohmic connection was established by sputtering (Edwards

E606 sputter/evaporator) Ti (20 nm) | Au (1 μm) to the back of the conducting BDD and then annealing in a tube furnace for 4 hours at 475 °C to form titanium carbide to ensure the contact.[27] The discs were each positioned (diamond side facing outwards) into a pulled borosilicate glass capillary (O.D. 2 mm, I.D. 1.16 mm, Harvard Apparatus, UK) and heat-sealed into place under vacuum (Narishige, PB-7). To form an electrical connection, the capillary was filled with silver epoxy (RS Components Ltd, UK) and a copper wire inserted (O.D. 0.5 mm). The wire was glued into place using epoxy resin (Araldite, Bostik Ltd., UK) glue. The disc was then polished back using carbimet abrasive polishing discs (Buehler Ltd, Germany) to expose the top surface. Aerial and side views of a final glass-sealed macroelectrode are shown in **Figure 6.3**b.

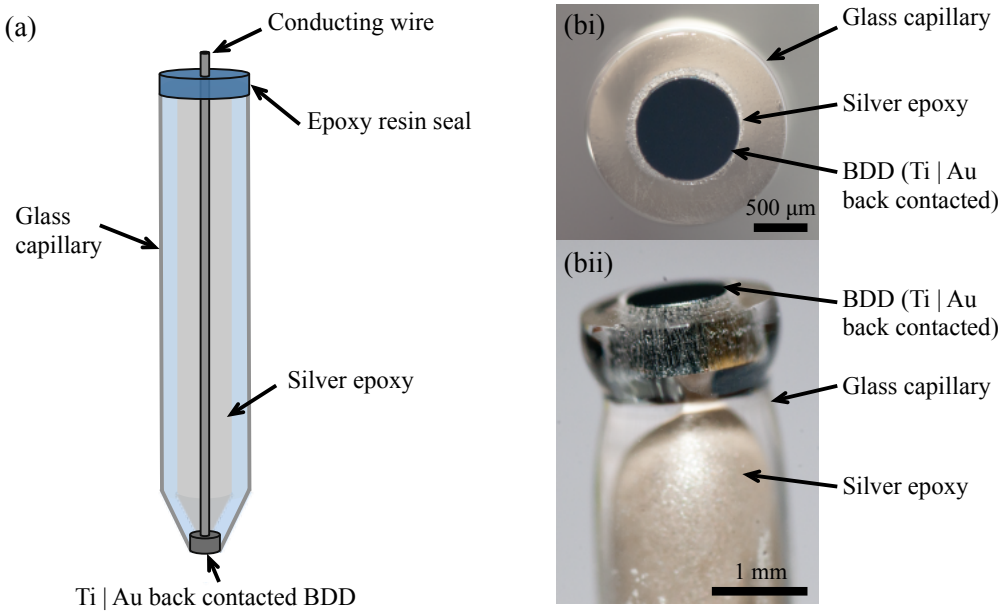

***Figure 6.3**: (a) Schematic and (b) images of a glass-sealed 1 mm diameter BDD disc macroelectrode from (i) aerial and (ii) side views.*

Optical images (Olympus BH-2-HLSH) of the BDD macroelectrode surface were taken to confirm the removal of all glass and determine the electrode size and grain structure. The growth and nucleation faces of 1 mm BDD discs are shown in

Figure 6.4a and b respectively. The growth face (distinguished by larger grain sizes) was used in all experiments. Prior to each use, the electrodes were alumina polished (0.05 μm sized particles, micropolish, Buehler Ltd, Germany) on a microcloth polishing pad saturated with distilled water (Buehler Ltd), cleaned using a dry, clean polishing pad and rinsed with distilled water to ensure a clean, O-terminated surface.

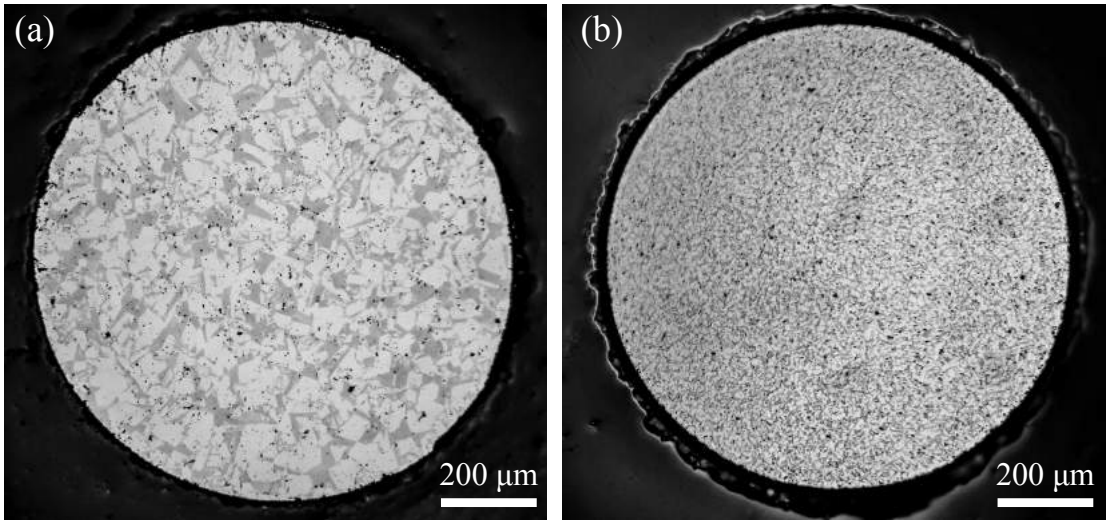

Figure 6.4*: Optical images of the 1 mm BDD disc surfaces from the (a) growth and (b) nucleation face. Larger grains, or fewer grain boundaries, are observed on the growth face. The growth face was used in all experiments.*

6.3.4 Fabrication of H-terminated BDD Electrodes

The highly doped BDD samples were acid cleaned and back contacted prior to hydrogenation, as the annealing temperature (500 °C) required to form the carbide electrical contact will likely destroy the hydrogen functionalisation. A Ti (20 nm) | Pt (200 nm) back contact was sputtered, followed by 4 hours annealing at 475°C to form the titanium-carbide bonds, for all samples that undergo hydrogenation. Ti | Au contact is unsuitable for H-termination as it is destroyed in the hydrogen plasma by the extreme temperatures (600 – 800°C). Hence, Pt was chosen due to its availability, ability to form a high conductivity contact that will not tarnish with time and high melting temperature, although it noted that other metals could also be an option if

available. For the hydrogen termination, the electrodes were placed in a 1 kW hydrogen plasma CVD reactor operating at 500 Torr using H_2 gas for 10 mins (Department of Chemistry, University of Bristol, UK). The samples were then left to cool for a further 10 mins under a constant hydrogen flow at a rate of 500 sccm (standard cubic centimetres per minute). Contact angle measurements (Krüss DSA100 Drop Shape Analyser), as discussed in Chapter 3, section 3.11.3, were performed prior to use to confirm successful H-termination *i.e.* a hydrophobic surface displaying a water contact angle as high as ~ 90°.[28] The samples were stored in ultra-pure water and displayed a high degree of surface stability, with the same degree of hydrophobicity lasting for up to 2 months post-hydrogenation. Besides the gradual surface oxidation over time, the hydrogen-termination layer is highly sensitive and can be destroyed by most standard diamond chemical cleaning treatments. For example acid cleaning, alumina polishing and sonicating in acetone will all remove the H-termination layer. The electrodes were therefore only cleaned by rinsing in ultra-pure water and remained covered when possible to avoid build-up of dust and dirt residue on the surface.

H-terminated BDD samples cannot be glass-sealed as the fabrication procedure destroys the H-termination, and the hydrogenation cannot be performed post-fabrication due to the comparable plasma temperature that would likely melt the glass casing (borosilicate glass capillary melting temperature 815 °C, Harvard Apparatus, UK). In the future, all-diamond devices will help to overcome this problem.[29] The back-contacted BDD electrodes were therefore mounted on a Ti | Pt sputter-annealed (using the same conditions as mentioned previously) quartz slide using silver epoxy, and left to dry for an hour. To form an electrical connection, a Cu wire was attached to the slide also with silver epoxy. The sample and wire were then

sealed into place using epoxy resin and left to dry overnight. The final set-up for H-terminated conducting BDD electrodes is shown in **Figure 6.5**a – b.

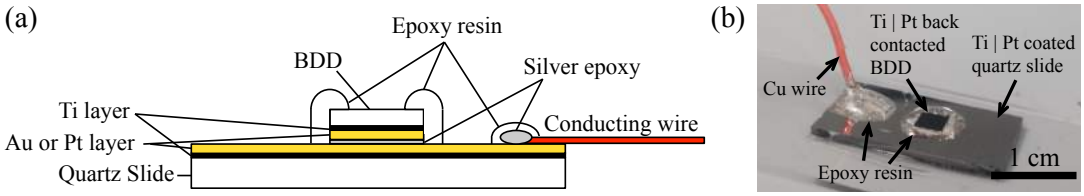

Figure 6.5*: (a) Schematic of the in-house built back-contacted diamond electrode. (b) Image of back-contacted H-terminated BDD used in experiments.*

The H-terminated semi-conducting BDD electrode required a top contact directly on to the conducting surface, as there are limited charge carriers within the material for a back contact to be established (**Figure 6.6**a). The electrode was acid cleaned, H-terminated (without contacts) and then masked off with a glass slide to protect the H-termination layer, leaving a ~ 1 mm thick strip exposed at one end. Other conventional masking methods such as photoresist or Kapton taping will likely remove the H-termination layer. Au (210 nm) was sputtered onto the exposed region (**Figure 6.6**b). The Ti layer was not necessary, as Au on a H-terminated diamond surface forms a direct ohmic contact.[30] A copper wire was then attached to the Au using silver epoxy and left to dry for an hour. The electrode was attached to a quartz slide by painting a layer of epoxy resin around the edges and over the Au contact and left to dry overnight. This ensured that the BDD and wire remained in place and helped to protect the contact from the solutions. The final set-up for the H-terminated semi-conducting BDD electrode is shown in **Figure 6.6**a – b.

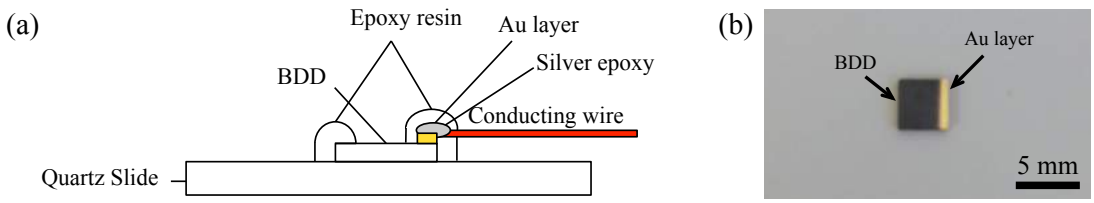

***Figure 6.6**: (a) Schematic of the in-house built top-contacted diamond electrode. This set-up is necessary for semi-conducting BDD samples, where a back contact is not sufficient due to fewer charge carriers in the material. (b) Image of Au top-contacted ~ 4 × 4 mm H-terminated BDD.*

6.3.5 Electrochemical Measurements

Electrochemical measurements on the O-terminated macroelectrodes were made in a three-electrode set-up using an Ag/AgCl reference electrode and platinum wire counter (**Figure 6.7**a). Experiments on the voltammetric response of H-terminated (conducting and semi-conducting) BDD electrodes were performed using a large-scale microcapillary technique (**Figure 6.7**b).[31]

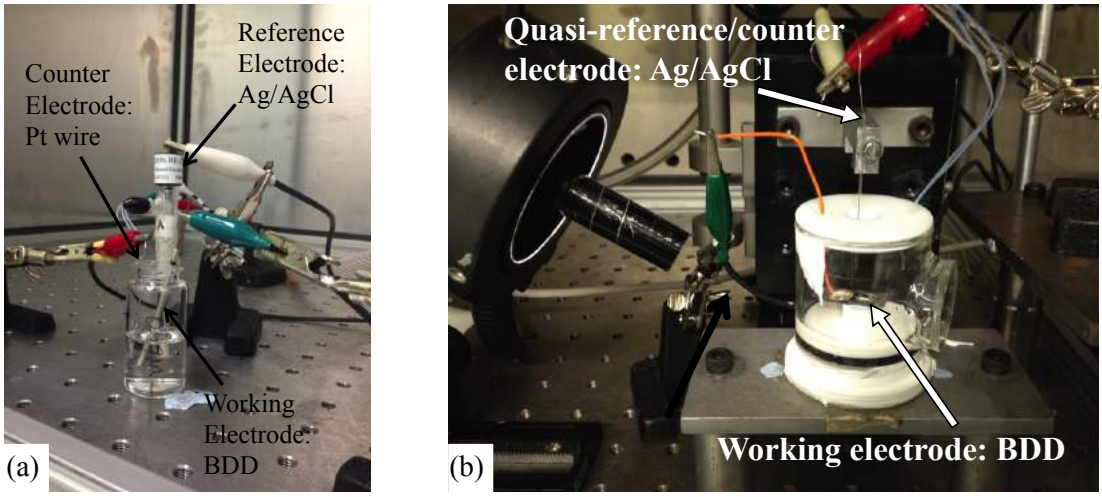

***Figure 6.7**: (a) Three-electrode macroelectrode set-up for electrochemical studies of alumina polished O-terminated BDD. (b) Large-scale microcapillary set-up for experiments on hydrogen plasma treated H-terminated BDD. The BDD is mounted on a conducting glass slide and connected through a copper wire. A glass capillary containing the solution of interest and the Ag/AgCl quasi-reference/counter electrode (QRCE) is lowered so that the meniscus contacts the electrode. The entire set-up is contained within a humidity cell to reduce evaporation.*

The large-scale microcapillary set-up employed a glass borosilicate capillary (O.D. 1.2 mm, I.D. 0.69 mm, Harvard Apparatus, UK) pulled and polished to an inner diameter of 48 – 60 μm (**Figure 6.8**). The capillary was immersed in dichlorodimethylsilane (Fisher Scientific, UK) solution for 2 minutes to make the outer walls hydrophobic, and Ar gas was flown through the capillary during and for 1 minute post-immersion to prevent internal coating. The hydrophobicity enabled confinement of the meniscus at the end of the capillary. The capillary was then filled with the solution of interest (defined below) and an Ag/AgCl (AgCl-coated Ag wire) quasi-reference/counter electrode (QRCE) was inserted. The meniscus from the tip was positioned on a localised region of the surface using *x*-*y*-*z* micropositioners, aided by visualisation from a high magnification camera (Pixelink PL-B776U). Once the meniscus was close (~ one capillary radius) to the surface, a gentle tap on the *z*-micropositioner enabled contact to be formed between the capillary meniscus and the surface. This technique facilitated multiple measurements through the ease of movement to clean, fresh locations on the H-terminated electrode surface using the *x*-*y*-*z*- micropositioners, as shown in **Figure 6.8**. All microcapillary experiments were performed in a humidity cell deaerated with N_2 gas to reduce evaporation at the meniscus.

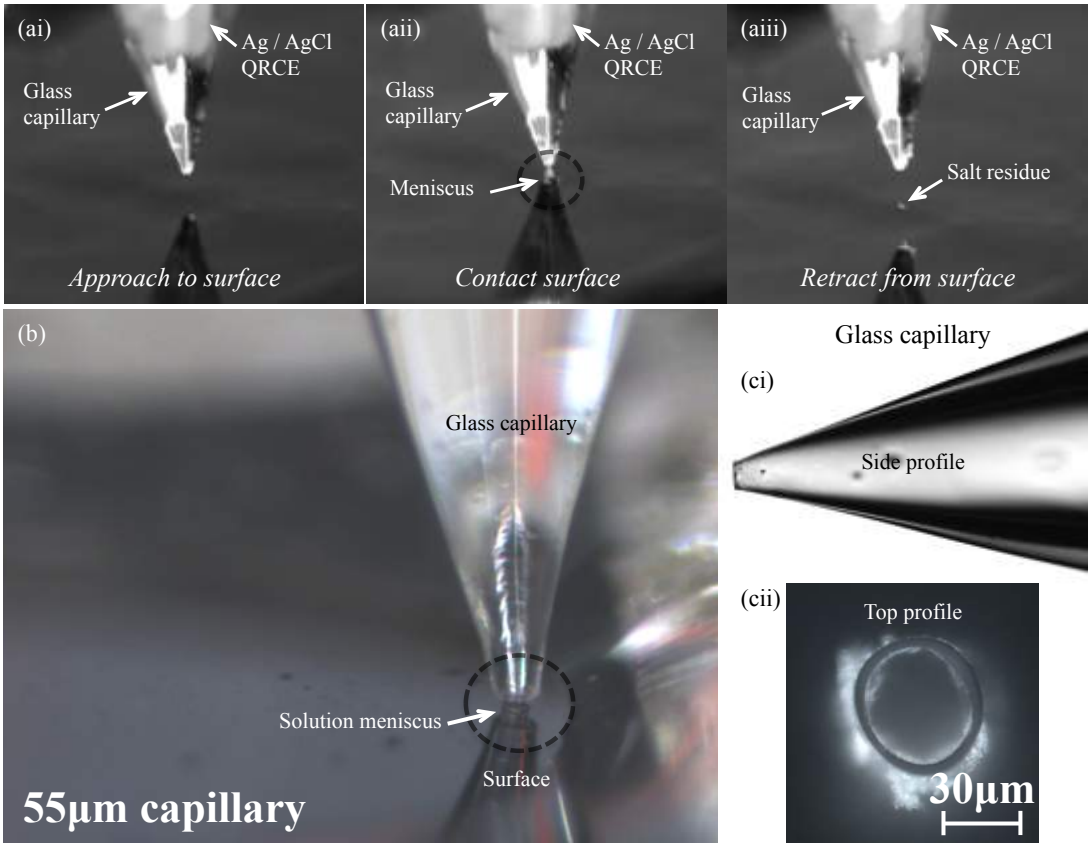

***Figure 6.8**: (a) The process of landing to form contact between the capillary meniscus and surface (in this case, HOPG). The capillary is (i) approached to the surface, (ii) gently tapped to form contact, and (iii) retracted to move to a new location, leaving behind a salt residue to mark the area. This enables multiple experiments to be run on the same surface. (b) The meniscus (highlighted with a circle) formed on a H-terminated BDD electrode prior to the experiment, and (c) side (i) and top (ii) views of the capillary. The dimensions of the tip are approx. the same as the dimensions of the meniscus at the start of the experiment.*

The premise that the local semi-conducting BDD surface termination could be both modified (write) and detected electrochemically (read) was investigated using SECCM. The SECCM imaging in this thesis was carried out by Dr. Hollie Patten and Dr. Laura Hutton, University of Warwick (see Declaration). A schematic of the set-up is shown in **Figure 6.9**. A borosilicate theta capillary of inner diameter of *ca.* 1 – 2 μm, filled with solution (2 mM $Ru(NH_3)_6^{3+}$ in 50 mM KNO_3) was used as the read-write probe. A potential, V_{bias}, of 200 mV was applied between the QRCEs in each barrel. During approach to the surface, a small oscillation (60 nm) in the *z*-position of

the probe was applied. When the meniscus came into contact with the surface, an alternating current component, i_{AC}, in the current between the barrels was established; which was very sensitive to the tip-substrate separation. In SECCM, i_{AC} is used as a set point for electrochemical imaging, in this case to maintain contact between the meniscus and diamond surface. For the studies herein, the i_{AC} values were in the range 80 – 120 pA, about 1 % of the mean conductance current, i_{barrel}, and about two orders of magnitude above the background (residual) value of i_{AC} when the probe was away from the surface. The BDD electrode was grounded and the effective potential controlled by floating the conductimetric cell at a potential, V_{float}, so that the potential of the diamond substrate was $-(V_{float} + V_{bias}/2)$ with respect to the QRCE potential.[32]

All experiments were performed in an air-conditioned laboratory of temperature 25 ± 2 °C using a potentiostat (CHI730A, CHI Instruments, US) connected to a desktop computer.

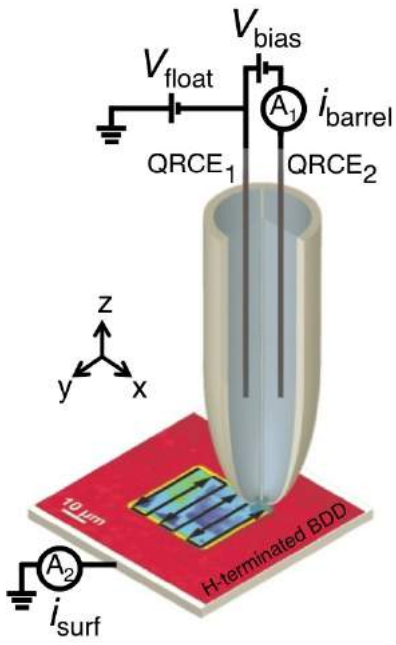

Figure 6.9*: Illustration of the SECCM set-up, showing the use of a theta capillary of ~ µm diameter to both locally modify the BDD surface (write) and then subsequently read the resulting surface change.*

6.4 Results and Discussion

6.4.1 BDD Characterisation

6.4.1.1 Contact Angles

Prior to use, the surface termination of O- and H- terminated diamond samples were assessed using water contact angles. Images of the water drop shape profiles obtained on freshly H- and O- terminated highly doped BDD, and freshly H-terminated semi-conducting BDD samples are shown in **Figure 6.10**. The samples were considered H-terminated if the contact angle obtained was > 60° and O-terminated if < 40°.[28] It is noted that the H-termination remained for 2 – 3 months post-treatment, with a gradual decline in the contact angle observed from approx. 1 month onwards.

(a) H-terminated conducting BDD (b) O-terminated conducting BDD

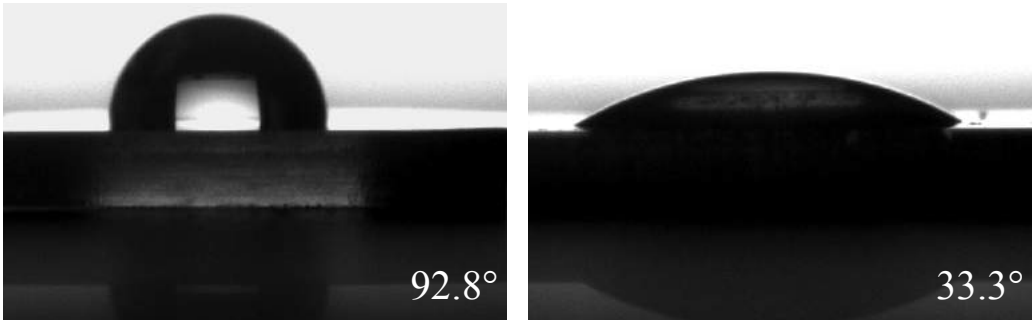

(c) H-terminated semiconducting BDD

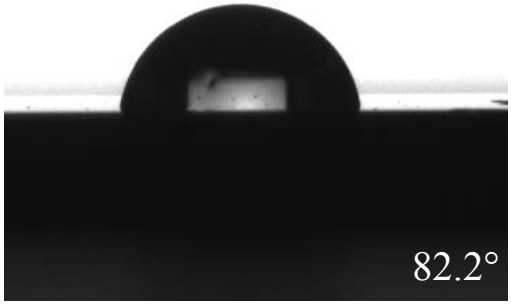

***Figure 6.10**: Typical contact angles for (a) H-terminated and (b) O-terminated conducting (metal-like) BDD of [B] = 3 × 10^{20} boron atoms cm^{-3} and (c) H-terminated semi-conducting BDD of [B] = 2 × 10^{18} boron atoms cm^{-3} at laser wavelength = 514 nm.*

6.4.1.2 Raman Spectroscopy

Micro-Raman spectroscopy was used to assess the sp^3 and sp^2 content of the conducting and semi-conducting BDD electrodes (see Chapter 3, section 3.11.2). A single peak was observed at 1332 cm^{-1} characteristic of sp^3 carbon (σ bonds). The asymmetry of the peak in **Figure 6.11**a is due to Fano-type interference and can be attributed to a high boron concentration ~ ≥ 10^{20} boron atoms cm^{-3}.[33] No peak asymmetry is observed in the semi-conducting BDD electrode (**Figure 6.11**b). This provides further evidence that the conducting BDD is sufficiently doped to be metal-like. No other distinctive features were observed in the spectra, which is indicative of the absence of sp^2 carbon. However, Raman was only surveyed in three different regions of the heterogeneous BDD surface, indicating sp^2 sites may still be present that have not been detected by Raman. Electrochemical analysis will provide the most accurate assessment of overall surface sp^2 carbon presence.

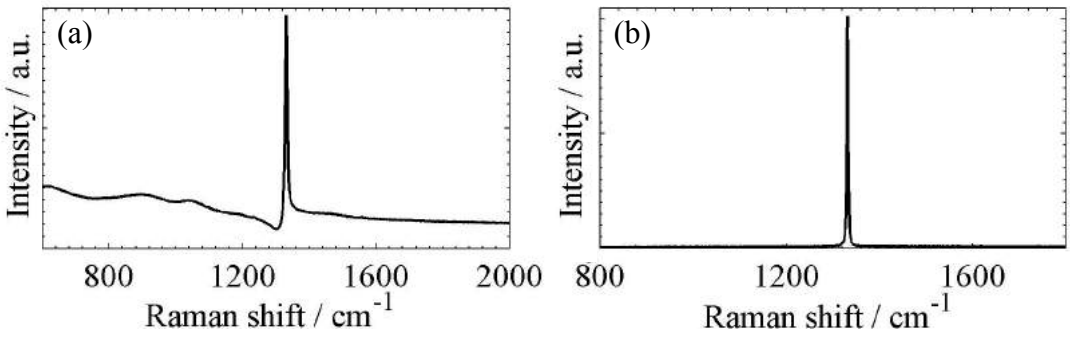

***Figure 6.11**: Typical Raman spectra for (a) conducting (metal-like) BDD of [B] = 3 × 10^{20} boron atoms cm^{-3} and (b) semi-conducting BDD of [B] = 2 × 10^{18} boron atoms cm^{-3} at laser wavelength = 514.5 nm.*

6.4.1.3 Solvent Windows

The material and electrochemical properties of the electrodes are presented in **Table 6.1**. The alumina polished O-terminated semi-conducting BDD sample used in this study has been previously characterised by Hutton *et al*. (**Table 6.1**).[12]

***Table 6.1**: Material and electrochemical properties of conducting (metal-like) and semi-conducting BDD electrodes used in this study. The semi-conducting electrode was characterised by Hutton et al.[12]*

Electrode	Surface Treatment	[B] (atoms cm^{-3})	Thickness (µm)	Grain Size (µm)	Resistivity (Ω cm)	sp^2 signature at ~ −1 V	Solvent window (V)
Conducting BDD	Alumina polished	3×10^{20}	635	2 – 25	0.05	yes	3.64
Semi-conducting BDD	Alumina polished	2×10^{18}	880	7 – 100	88	yes	3.89

Solvent windows were recorded in 0.1 M KNO_3 at a scan rate of 0.1 V s^{-1} to investigate the potential range over which the electrode can perform ET before oxidation/reduction of the solvent occurs. **Figure 6.12**a displays the solvent window for the alumina polished O-terminated conducting BDD used in this study, along with a comparison to the solvent windows produced by the 'highest grade' (negligible sp^2 content) conducting BDD and sp^2 containing conducting BDD (**Figure 6.12**b). Sp^2 carbon contributions are normally seen in the solvent window by an oxygen reduction (ORR) signature > −1 V *vs.* SCE[34] and surface sp^2 oxidation processes occurring just before the anodic solvent window.[35] The alumina polished O-terminated conducting BDD electrode used in this study does not show evidence of a small ORR signature in the solvent window, hence surface sp^2 sites are not present (**Figure 6.12**b).

The solvent window displays an increase in current at the cathodic and anodic potential extremes due to solvent hydrogen and oxygen evolution, respectively. The solvent window on BDD is quantified by measuring the voltage between the current density limits ± 0.4 mA cm^{-2} (**Table 6.1**).[12] Both electrodes display wider solvent windows in comparison to other electrode materials, as expected for BDD.[36]

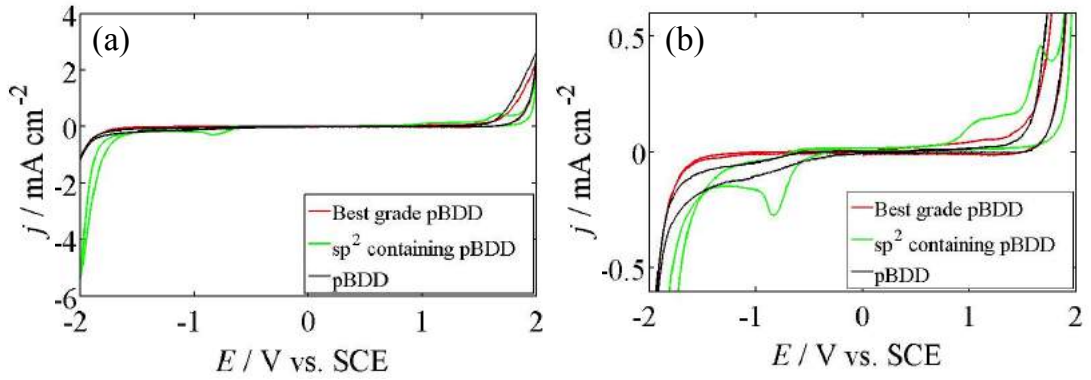

***Figure 6.12**: Solvent windows recorded in 0.1 M KNO_3 at 0.1 V s^{-1} for (a) alumina polished O-terminated BDD (black) compared to best grade i.e. negligible sp^2 (red) and sp^2 containing BDD (green). The scale in (b) has been reduced to a ±0.6 mA cm^{-2} window to display the background currents.*

There was considerable difficulty in running a solvent window on H-terminated diamond in the microcapillary set-up, as sweeping to extreme potentials (~ 2 V) served to oxidise the surface causing the meniscus of the capillary to wet and irreversibly increase the electrode area. However, from the literature, Fujishima *et al.,* showed a wider solvent window on an oxygen plasma treated O-terminated conducting electrode compared to an as-grown H-terminated one *i.e.* water electrolysis begins at ~ −0.8 V *vs.* Ag/AgCl on O- compared to ~ −0.5 V *vs.* Ag/AgCl on H- terminated diamond.[37] Our solvent windows are considerably wider than observed by Fujishima *et al.*, indicative of the very high quality sp^3 BDD diamond that we are employing.

6.4.1.4 $Ru(NH_3)_6^{3+/2+}$

$Ru(NH_3)_6^{3+}$ is an important species for testing if the BDD is non-degenerately doped and for checking the macroelectrode is working correctly, based on its well-characterised CV response.[28] In particular, $Ru(NH_3)_6^{3+}$ is an outer-sphere species that is highly sensitive to the number of charge carriers in the material at the applied potential. The E^0 of $Ru(NH_3)_6^{3+}$, corrected for Ag/AgCl, is −0.12 V,[6] which lies in

the band gap of O- and H- terminated BDD (see Chapter 1, Figure 1.7). As this potential range is strongly depleted of charge carriers, the ET kinetics of $Ru(NH_3)_6^{3+/2+}$ are highly dependent on the dopant level of the diamond material.[38] The CV of $Ru(NH_3)_6^{3+}$ will not be reversible if the BDD is not sufficiently doped to be metal-like. CVs for the reduction of 1 mM $Ru(NH_3)_6^{3+/2+}$ in 0.1 M KCl on O- (alumina polished) and H- (hydrogen plasma) terminated conducting BDD are shown in **Figure 6.13**.

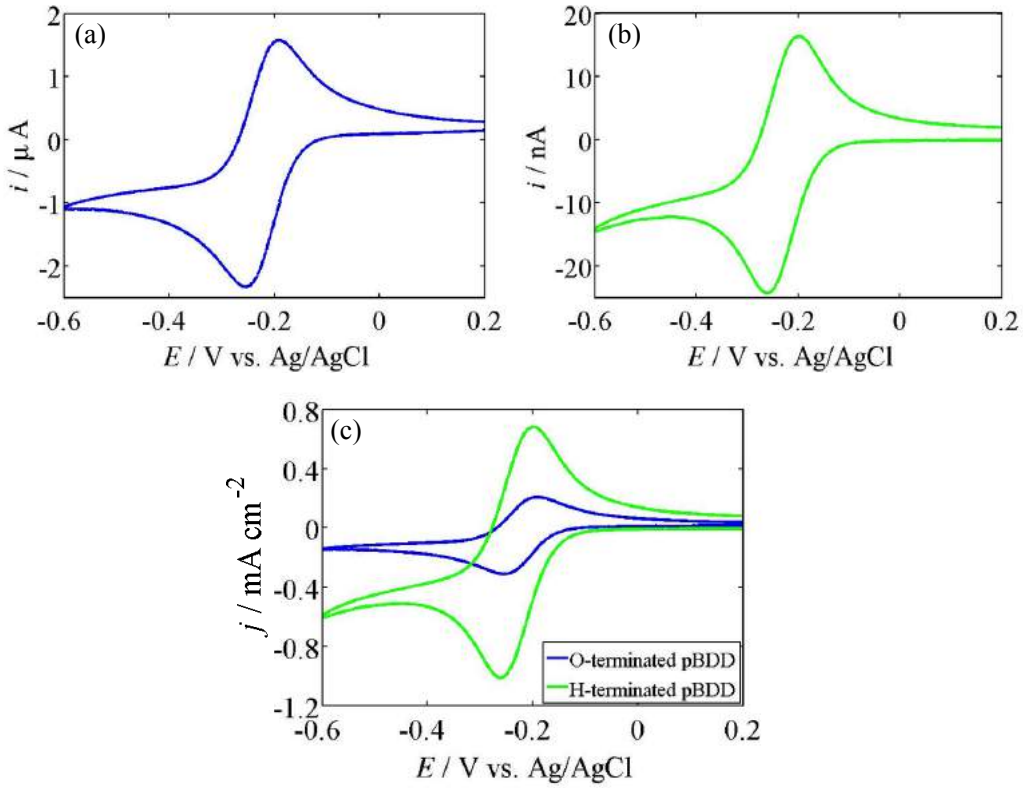

***Figure 6.13**: CVs of the first sweeps for the reduction of 1 mM $Ru(NH_3)_6^{3+/2+}$ in 0.1 M KCl using (a) 980 μm diameter alumina polished O-terminated conducting BDD macroelectrode (blue) with ΔE_p = 61 mV, (b) 55 μm diameter microcapillary on hydrogen plasma treated H-terminated conducting BDD (green) with ΔE_p = 62 mV, and (c) current density, j, plots of (a) and (b) to enable comparison between the different methodologies. Scan rate 0.1 V s^{-1}.*

As described in the experimental (section 6.3) for O-terminated electrodes all measurements are carried out on a ~ 1 mm diameter electrode, whilst for H-terminated electrodes a microcapillary electrochemical cell of diameter ~ 55 μm was

employed. The currents have been normalised with respect to electrode area. Note that the mass transport rates for both electrode geometries will be different, with the microcapillary delivering higher mass transport due to the smaller geometry. As discussed in Chapter 3, section 3.6.1, the rate constant of mass transport, k^t, is inversely proportional to electrode surface area (Chapter 3, equation 3.5). Assuming linear diffusion dominates in both set-ups and all other terms are constant, the increase in mass transport in the microcapillary set-up with respect to the macroelectrode can be calculated as:

$$\frac{k^t_{microcapillary}}{k^t_{macro}} = \left(\frac{A_{macro}}{A_{microcapillary}} \right) \tag{6.1}$$

Hence, for our systems, at the simplest level mass transport in the microcapillary set-up is at least 3.2×10^2 times higher than in the macroelectrode.

Both the O- and H-terminated BDD CVs in **Figure 6.13**, with the fast outer-sphere ET species, $Ru(NH_3)_6^{3+/2+}$,[39] display reversible ET kinetics with a ΔE_p response of 63 ± 2 mV and 67 ± 5 mV, respectively. This indicates that the material is suitably doped to be conducting (metal-like) for electroanalysis and a reliable ohmic contact has been achieved. The influence of different dopant levels on the ΔE_p of $Ru(NH_3)_6^{3+/2+}$ is discussed in detail later (see section 6.4.3).

As a reversible system, the $E_{1/2}$ value can be estimated as the mean of the peak potentials:

$$E_{1/2} = \frac{(E_{pa} + E_{pc})}{2} \tag{6.2}$$

Equation 6.2 can be used to estimate $E_{1/2}$ for any reversible diffusion-limited redox reaction. For non-reversible reactions (quasi- and irreversible), $E_{1/2}$ can be estimated as the potential at half the faradaic peak current (i_p). Similar $E_{1/2}$ (*vs.* Ag/AgCl) values were observed for alumina polished O- (−0.22 ± 0.01 V), and

hydrogen plasma H- (−0.23 ± 0.01 V) terminated surfaces indicating that the electrode kinetics of $Ru(NH_3)_6^{3+/2+}$ are insensitive to the surface termination. This is in agreement with previous studies of $Ru(NH_3)_6^{3+/2+}$ on carbon-based electrode materials[9a, 10b, 39a, 40] and is characteristic of an outer-sphere species.[10a, 41]

It was considered that the Ag/AgCl QRCE utilised in the microcapillary set-up may cause potential reference electrode drifts from solution to solution (see Chapter 3, section 3.7). To mitigate against drift due to degradation of the AgCl layer, CVs of $Ru(NH_3)_6^{3+/2+}$ were run before every experiment to check that the CV is reproducible (*i.e.* $E_{1/2}$ = ~ 0.22 V, E_{pc} = ~ 0.25 V, and ΔE_p = 59 – 69 mV).[28] This check also served to help minimise resistance within the microcapillary set-up, as any resistive components would cause E_{pc} to shift to higher overpotentials and the overall ΔE_p to increase. For the macroelectrode set-up a conventional fritted glass-sealed Ag/AgCl reference electrode was employed (Chapter 3, section 3.7).

The i_p for $Ru(NH_3)_6^{3+/2+}$ at 298 K can be predicted using the Randles-Sevcik equation which describes an ET process limited by linear (planar) diffusion, as described in Chapter 3, equation 3.8. The i_p on O-terminated BDD is in close agreement with theory *i.e.* 1.86 ± 0.39 μA *vs.* 1.90 μA, experiment *vs.* theory. The i_p on H-terminated BDD is larger than predicted *i.e.* 14.71 ± 6.44 nA *vs.* 6.0 nA, experiment *vs.* theory, showing that Randles-Sevcik cannot be truly applied to the microcapillary set-up most likely due to wetting effects *i.e.* the diameter of the droplet not equaling the size of the inner diameter of the capillary (~ 55 μm diameter circular region), and possible contributions from radial diffusion.

Having characterised the BDD material, investigations were conducted into: (1) the influence of O- (alumina polished) and H- (hydrogen plasma) termination on the response of different inner-sphere redox mediators on conducting (metal-like)

BDD electrodes, and (2) the effect of changing the surface termination from H- (hydrogen plasma) to O- (anodically polarised) on the response of the outer-sphere redox couple $Ru(NH_3)_6^{3+/2+}$ on a semi-conducting BDD electrode. Analysis focused on comparison of the ΔE_p and $E_{1/2}$ positions for each redox species on the two differently functionalised surfaces.

6.4.2 Electrochemical Response of Inner-Sphere Mediators on H- and O-terminated Conducting BDD

6.4.2.1 $Fe(CN)_6^{4-/3-}$

$Fe(CN)_6^{4-/3-}$ is an essential precursor for Prussian blue dye that is employed in paints, blueprints and as a remedy for certain heavy metal poisons.[42] Hence, accurate electrochemical detection of $Fe(CN)_6^{4-/3-}$ is important in the decoration, forensics and healthcare industries. It is also frequently used in electrochemical studies as a redox probe for characterisation of new electrodes, such as electrodes functionalised with biomolecules, due to its well-defined voltammetric behaviour.[28] CVs for the oxidation of 1 mM $Fe(CN)_6^{4-/3-}$ in 0.1 M KCl on O- (alumina polished) and H- (hydrogen plasma) terminated conducting BDD are shown in **Figure 6.14.**

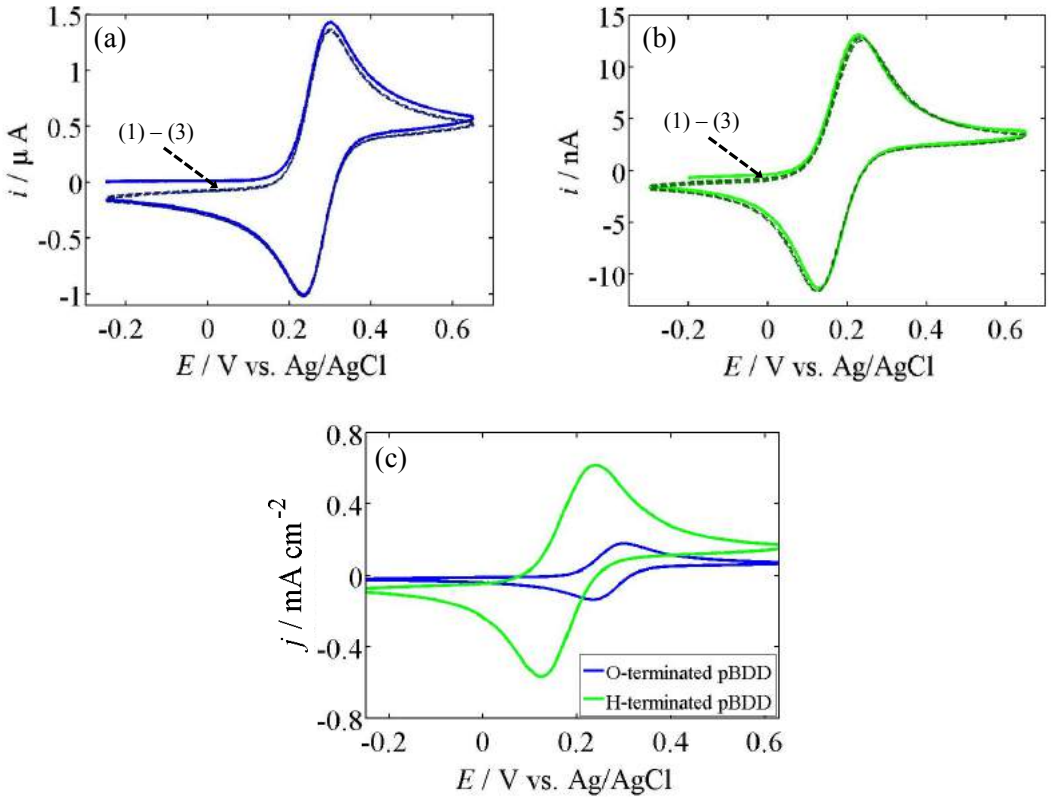

***Figure 6.14**: CVs for the oxidation of 1mM $Fe(CN)_6^{4-/3-}$ in 0.1 M KCl using (a) 980 μm diameter alumina polished O-terminated conducting BDD macroelectrode (blue) with ΔE_p = 69 ± 11 mV, (b) 55 μm diameter microcapillary on hydrogen plasma treated H-terminated conducting BDD (green) with ΔE_p = 96 ± 12 mV, and (c) current density, j, plots of (a) and (b) to enable comparison between the different methodologies. First sweep (solid) is followed by subsequent sweeps (1) – (3) (dashed). Scan rate: 0.1 V s^{-1}.*

A clear difference was observed in the electrochemical response. On the O-terminated surface, $Fe(CN)_6^{4-/3-}$ displayed close to reversible ET kinetics (ΔE_p = 69 ± 11 mV) and $E_{1/2}$ value of +0.27 ± 0.02 V. This finding is in agreement with literature which has reported reversible ET of $Fe(CN)_6^{4-/3-}$ on alumina polished conducting BDD, of a similar quality to that used herein and recorded under the same mass transport conditions.[12] Interestingly, slower ET kinetics were observed on the H-terminated BDD surface, with an observed ΔE_p = 96 ± 12 mV and a negative shift in $E_{1/2}$ to +0.16 ± 0.01 V (**Figure 6.14**). However, it is important to note that as diffusional mass transport is at least 3.2 × 10^2 times greater in the microcapillary than

the macroelectrode set-up, ET kinetics which appeared reversible for the macroelectrode can be more readily revealed for the microcapillary set-up. To ascertain the ET kinetics, finite element modelling would need to be carried out.[23c, 43]

The shift in $E_{1/2}$ is also worthy of comment, with ET for $Fe(CN)_6^{4-/3-}$ occurring at more positive potentials on the O-terminated surface, than for H-terminated BDD. Given E^0 for $Fe(CN)_6^{4-/3-}$ corrected to the Ag/AgCl electrode is +0.14 V,[6] this could point at ET for $Fe(CN)_6^{4-/3-}$ being more kinetically facile on the H-terminated surface. The oxidation of $Fe(CN)_6^{4-}$ proceeds by a one-electron transfer process:

$$[Fe(CN)_6]^{4-} \rightleftharpoons [Fe(CN)_6]^{3-} + e^-$$

The inner-sphere mechanism for $Fe(CN)_6^{4-/3-}$ ET at electrodes is not well understood.[44] Reports have shown that the rate of reaction increases with an increasing proportion of exposed sp^2 carbon sites on GC surfaces.[11a] The reaction is also dependent on the concentration of supporting electrolyte, or more specifically the concentration and type of cations, which are believed to bind to $Fe(CN)_6^{4-/3-}$ to form a precursor complex that interacts with the surface.[45] Evidence suggests that this complex binds favourably to a particular non-oxide surface site, such as H- on diamond or sp^2 groups on GC, but cannot interact strongly with oxygen groups.[10b] As higher potentials are required to drive ET transfer on the alumina polished O-terminated BDD surface, it is suggested that energetic barriers to adsorption due to electrostatic repulsion exist that hinder binding of the complex to the surface. Calculations of the free energy of adsorption using molecular models could further elucidate this theory.

It is also noted that all subsequent CV sweeps overlay the first sweep for both alumina polished and hydrogen plasma treated surfaces (**Figure 6.14)**, indicating that

the redox process does not foul the electrode within the timescale of the experiment. Hence, the oxidation/reduction products of the reaction must not adsorb strongly to BDD surfaces. Electrode fouling has been observed on GC surfaces during $Fe(CN)_6^{4-}$ oxidation.[46] Studies have reported that $Fe(CN)_6^{4-/3-}$ can form poorly soluble oxidation products.[47] This phenomenon was not observed on BDD, due to the lack of sp^2 binding sites on the BDD surface.

6.4.2.2 β-Nicotinamide adenine dinucleotide (NADH)

NADH is a coenzyme essential for metabolism reactions within cells. Accurate electrochemical detection of this redox species is essential in the study of mitochondrial health linked to aging and numerous health conditions, and for the design of new targeted drugs in the healthcare and pharmaceutical industries.[48] CVs for the oxidation of 1 mM NADH in 0.1 M PBS on O- (alumina polished) and H- (hydrogen plasma) terminated conducting BDD are shown in **Figure 6.15.**

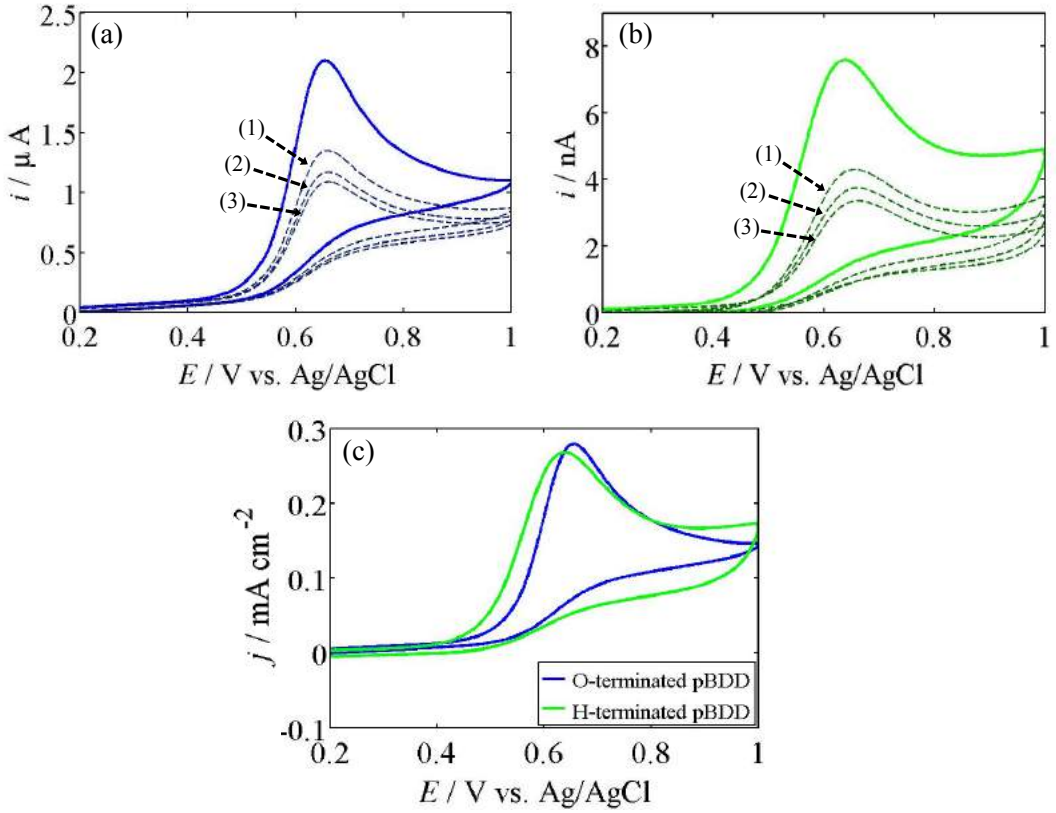

***Figure 6.15**: CVs for the oxidation of 1 mM NADH in 0.1 M PBS using (a) 980 μm diameter alumina polished O-terminated conducting BDD macroelectrode (blue), (b) 60 μm diameter microcapillary on hydrogen plasma treated H-terminated conducting BDD (green), and (c) current density, j, plots of (a) and (b) to enable comparison between the different methodologies. First sweep (solid) is followed by subsequent sweeps (1) – (3) (dashed). Scan rate: 0.1 V s^{-1}.*

The oxidation reaction of NADH occurs as an inner-sphere two-electron one-proton process to form NAD^+ as shown in **Figure 6.16**.

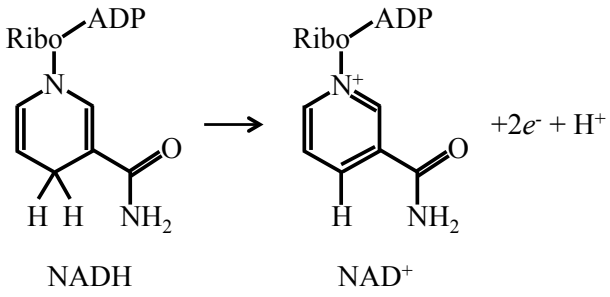

***Figure 6.16**: Oxidation reaction of NADH to NAD^+.*[49]

Both O- and H- terminated BDD surfaces displayed irreversible ET kinetics for NADH oxidation. On the H-terminated BDD surface, an $E_{1/2}$ of +0.55 ± 0.03 V was observed. On the O-terminated surface, $E_{1/2}$ shifts in the positive direction to +0.59 ± 0.03 V, suggesting a less kinetically facile ET process especially when qualitative differences in mass transport are taken into account. A previous study by Fujishima *et al.* interestingly showed no difference in the response of NADH to conducting BDD after either a short-term, moderate anodic oxidative treatment (+1.5 V for 10 mins in KH_2PO_4/K_2HPO_4 buffer) or long-term exposure to air (for up to several weeks) to the as-grown, H-terminated surface. However no information was provided on sp^2 carbon content or how long the H-terminated electrode had been exposed to air before use.[50]

The E^0 for $NADH/NAD^+$, corrected to the Ag/AgCl electrode, is −0.54 V.[51] Both O- and H- terminated BDD surfaces display a large anodic shift in $E_{1/2}$ relative to E^0. This indicates that NADH oxidation is sluggish on BDD electrodes, irrespective of surface termination. No reduction peak was obtained on either BDD surface within the range of the solvent window *i.e.* sweeping to cathodic potentials up to −1.5 V. It has been reported that unmodified GC electrodes undergo rapid deactivation when oxidising NADH, causing an anodic shift by approximately 300 mV.[52] This is attributed to strong adsorption of the polar oxidation product NAD^+ to the polar surface carbon-oxygen functional groups. Swain *et al.* reported similar results for the polar species anthraquinone-2,6-disulfonate (ADS) on as-grown, H-terminated conducting BDD and hydrogenated GC.[11a] Whilst ADS did not bind to the hydrogenated surfaces, it readily adsorbed by strong dipole-dipole interactions to GC and HOPG surfaces that contained a high proportion of carbon-oxygen functional groups (predominately C=O and COOH groups at edge plane defect sites). Hence, the

slower ET kinetics observed in **Figure 6.15** on alumina polished O-terminated BDD may be tentatively attributed to adsorption of NAD^+ to the surface carbon-oxygen groups.

Fouling is observed on both hydrogen plasma and alumina polished conducting BDD surfaces, shown by the gradual decrease in the current over subsequent sweeps (**Figure 6.15**). Fujishima *et al.* reported reproducible CVs on as-grown, H-terminated conducting BDD only when implementing a wait period of ~ 2 mins between CVs which was believed to provide sufficient time for NAD^+ to desorb from the surface.[50]

6.4.2.3 Riboflavin (Vitamin B2)

Riboflavin (vitamin B_2) is an essential vitamin in the human body.[53] A deficiency of riboflavin is linked to various conditions including stomatitis, anaemia, and birth defects.[54] Hence, accurate electrochemical detection of riboflavin is important for early medical diagnosis and treatment in the healthcare industry. CVs for the reduction of 1 mM riboflavin in 0.1 M PBS on O- (alumina polished) and H- (hydrogen plasma) terminated conducting BDD are shown in **Figure 6.17.**

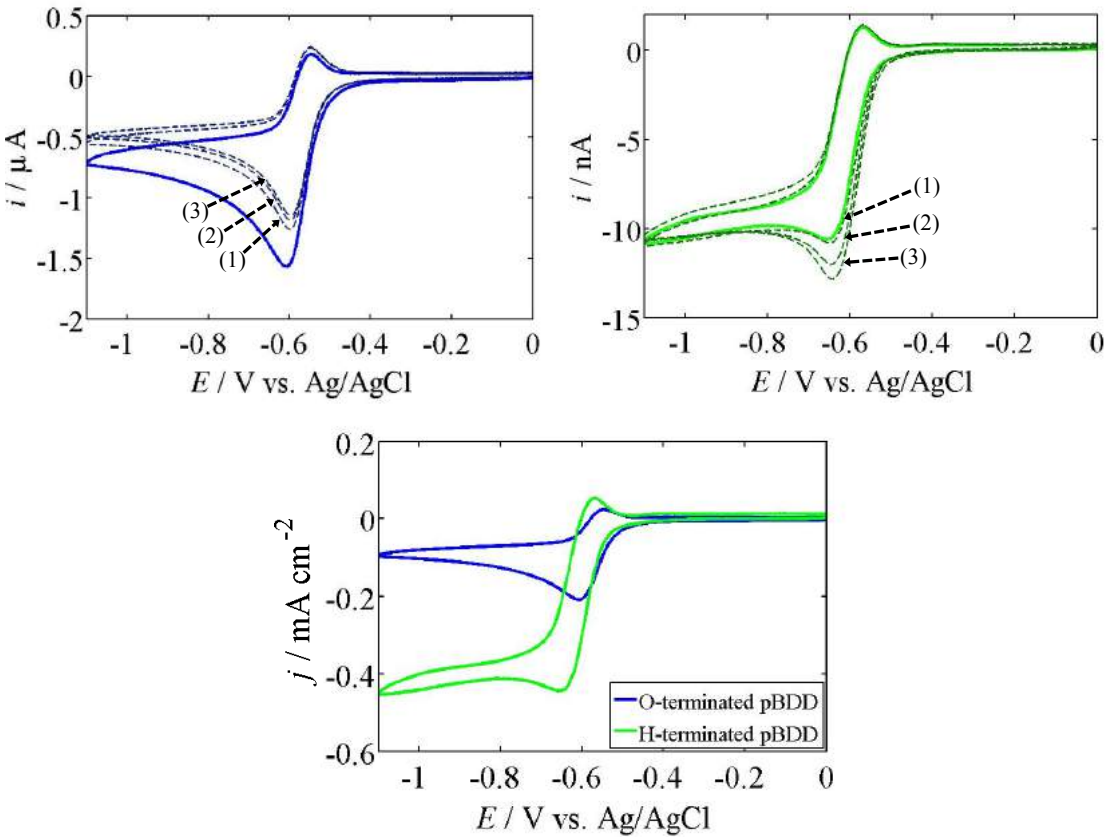

***Figure 6.17**: CVs for the reduction of 1 mM riboflavin in 0.1 M PBS using (a) 980 μm diameter alumina polished O-terminated conducting BDD macroelectrode (blue) with ΔE_p = 70 ± 21 mV, (b) 55 μm diameter microcapillary on hydrogen plasma treated H-terminated conducting BDD (green) with ΔE_p = 84 ± 6 mV, and (c) current density, j, plots of (a) and (b) to enable comparison between the different methodologies. First sweep (solid) is followed by subsequent sweeps (1) – (3) (dashed). Scan rate: 0.1 V s^{-1}*

The reduction of riboflavin is a two-electron two-proton process converting from a quinone to hydroquinone species.[55] The form of the reactant and product is highly dependent on pH,[56] as shown in **Figure 6.18**. Importantly, at the relevant pH of this study (pH 7), riboflavin exists in an electrically neutral form (pKa = 10), whereas the reduced hydroquinone species deprotonates (pKa = 6.2) to carry a negative charge.

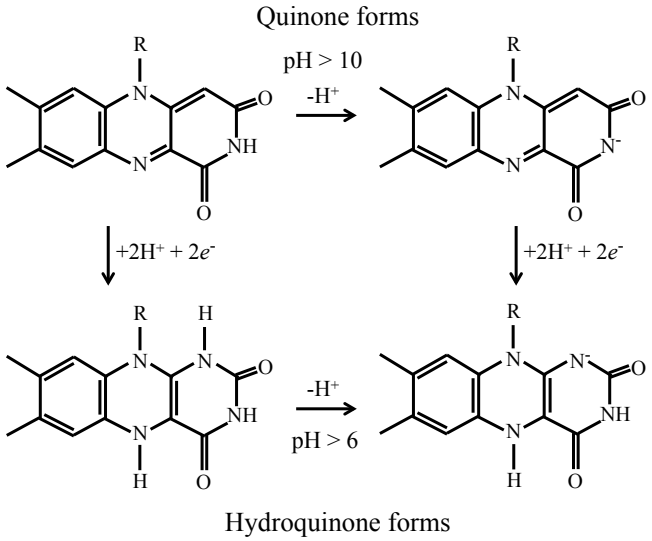

***Figure 6.18**: Reduction of riboflavin from a quinone to hydroquinone species, dependent on the pH of the solution*.[56]

Quasi-reversible ET kinetics are observed on both surfaces (**Figure 6.17**) with ΔE_p values of 70 ± 21 mV on the alumina polished O- and ΔE_p of 84 ± 6 mV on the hydrogen plasma H- terminated conducting BDD electrodes. The $E_{1/2}$ values for reduction are −0.65 ± 0.01 V on H- and −0.55 ± 0.02 V on O-, compared to the E^0 for riboflavin of −0.42 V *vs.* Ag/AgCl.[57] Both the ΔE_p and $E_{1/2}$ data suggest that for both surfaces ET is nowhere near as sluggish as for example NADH, above.

Whilst the O-terminated diamond produces a wave shape typical of a diffusion-limited system, the CV on H-terminated displays an almost steady-state response, similar to that typically observed on ultramicroelectrodes. This phenomenon has also been reported by Foord *et al.,* where interestingly he attributed the response to partial blockage of the hydrogenated electrode by riboflavin, leaving 'microscopic islands' where the reaction occurs.[56]

Reports have demonstrated enhanced ET kinetics for riboflavin (in pH 6) on anodically treated (+1.8 V for 300 s in 0.2 M PBS) GC surfaces that can be ascribed to an increase of C=O sites.[58] Alumina polished surfaces do not have as many C=O

sites as anodically polarised BDD, hence the increase in ET on an alumina polished surface would not be expected to be as significant.[12]

Repeat CVs showed that the O-terminated surface was more prone to surface fouling than the H-terminated; in fact the current at the H-terminated surface increases slightly with subsequent sweeps. This observation questions the interpretation by Foord *et al*,[56] of the H-termination behaviour. As the reduction product (**Figure 6.18**d) is charged it is likely, that it can adsorb to polar surface carbon-oxygen groups with time. Increased fouling was also observed on an unmodified GC electrode containing carbon-oxygen groups, compared to when modified by a surface monolayer.[59]

6.4.2.4 $Fe^{2+/3+}$

Iron is essential in the human body for the synthesis of haemoglobin. Iron deficiency anaemia is caused by numerous health problems such as Crohn's disease,[60] chronic kidney disease,[61] and gastrointestinal cancers.[62] Iron (II) sulphate, studied herein, is commonly used in healthcare for the treatment of iron deficiency,[63] as well as for various industrial applications such as steel manufacture,[64] wastewater treatment,[65] and agriculture.[66] Hence, accurate electrochemical detection of iron (such as iron (II) sulphate) is important to monitor and improve medical care and industrial technologies in these fields. CVs for the oxidation of 1 mM iron (II) sulphate in 0.1 M $HClO_4$ on O- (alumina polished) and H- (hydrogen plasma) terminated conducting BDD are shown in **Figure 6.19.**

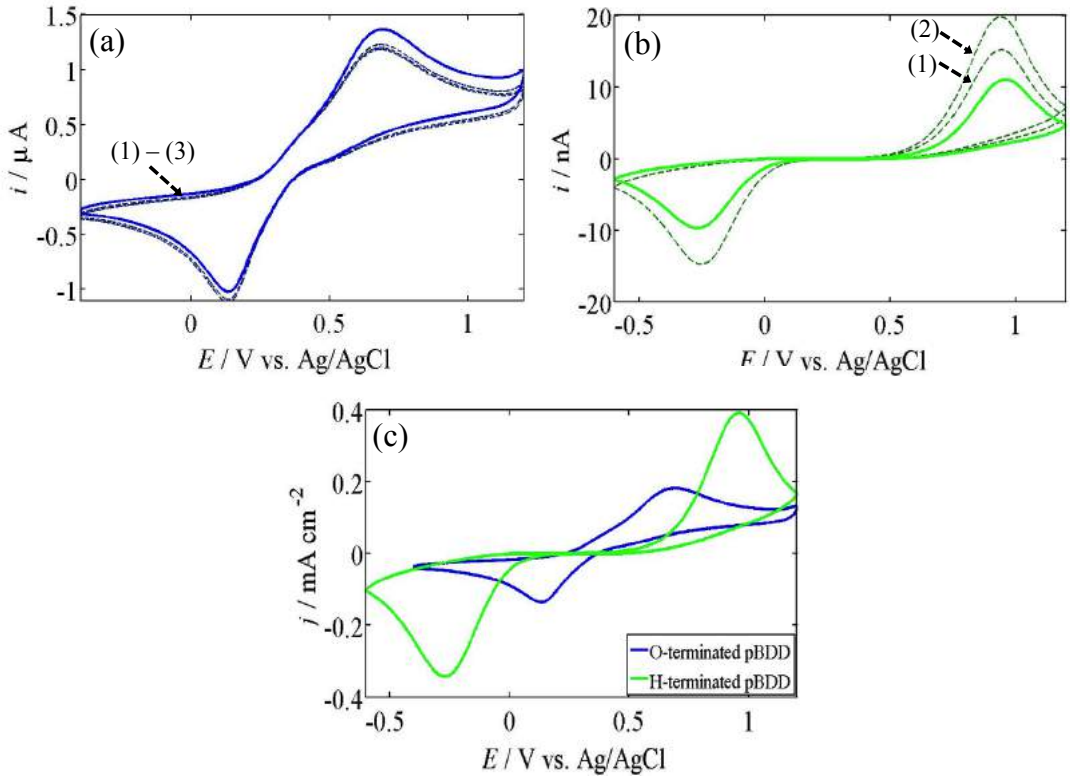

***Figure 6.19**: CVs for the oxidation of 1 mM iron (II) sulphate in 0.1 M $HClO_4$ using (a) 980 μm diameter alumina polished O-terminated conducting BDD macroelectrode (blue) with ΔE_p = 0.58 ± 0.03 V, (b) 60 μm diameter microcapillary on hydrogen plasma treated H-terminated conducting BDD (green) with ΔE_p = 1.21 ± 0.06 V, and (c) current density, j, plots of (a) and (b) to enable comparison between the different methodologies. First sweep (solid) is followed by subsequent sweeps (1) – (3) (dashed). Scan rate: 0.1 V s^{-1}.*

The redox reaction of $Fe^{2+/3+}$ (in $FeSO_4.7H_2O$, see section 6.3.1) follows a one-electron transfer mechanism:

$$Fe^{2+} \rightleftharpoons Fe^{3+} + e^-$$

Sluggish quasi-reversible ET kinetics are exhibited on both O- and H-terminated surfaces (**Figure 6.19**). However, there is a clear difference in how the $Fe^{2+/3+}$ species interacts with the different surfaces, with the alumina polished O-terminated exhibiting a much smaller ΔE_p value (0.58 ± 0.03 V) than the hydrogen plasma H-terminated conducting BDD surface (1.21 ± 0.06 V). The $E_{1/2}$ for the oxidation of $Fe^{2+/3+}$ on H-terminated is +0.80 ± 0.06 V compared to +0.48 ± 0.03 V

on the O-terminated. Qualitative accounting for mass transport differences, this data suggests ET is faster on the O-terminated surface.

The findings support several studies found in literature, suggesting that the ET kinetics are enhanced on electrode surfaces that contain carbon-oxygen functionalities.[10b, 39a, 67] It has been shown that C=O groups are of particular importance, acting to catalyse the reaction of $Fe^{2+/3+}$ and therefore increase ET.[10a] Work by Fujishima *et al.,* confirmed this experimentally by adding dinitrophenylhydrazine (DNPH) to solution which binds covalently to C=O groups rendering them inactive, showing that the $Fe^{2+/3+}$ reaction is retarded when DNPH is present.[4b] It has also been shown that the supporting electrolyte used may have an effect on the ET kinetics observed. Work by Nagy *et al.,* concluded that on Au electrodes chemisorbed Cl^- provided a bridging group for inner-sphere catalysis, resulting in a larger rate enhancement.

Whilst the CVs are relatively reproducible on the O-terminated, the current appears to enhance over subsequent sweeps on the H-terminated surface (**Figure 6.19**). The potential is swept out to high anodic values (+1.2 V) in order to drive Fe^{2+} oxidation on the H-terminated surface. This will likely begin to oxidise the surface, causing an increase in the meniscus wetting *i.e.* the electrode area, that enhances the current values with each successive sweep.

6.4.2.5 Dopamine

Dopamine is a neurotransmitter that plays a key role in brain function where a deficiency has been linked to various neurodegenerative conditions such as Parkinson's disease, Alzheimer's disease, and depression (see Chapter 5, section 5.2). Accurate electrochemical detection of dopamine is important for greater understanding, early medical diagnosis and improved treatment of these conditions.

CVs for the oxidation of 1 mM dopamine hydrochloride in 0.1 M PBS on O- (alumina polished) and H- (hydrogen plasma) terminated conducting BDD are shown in **Figure 6.20.**

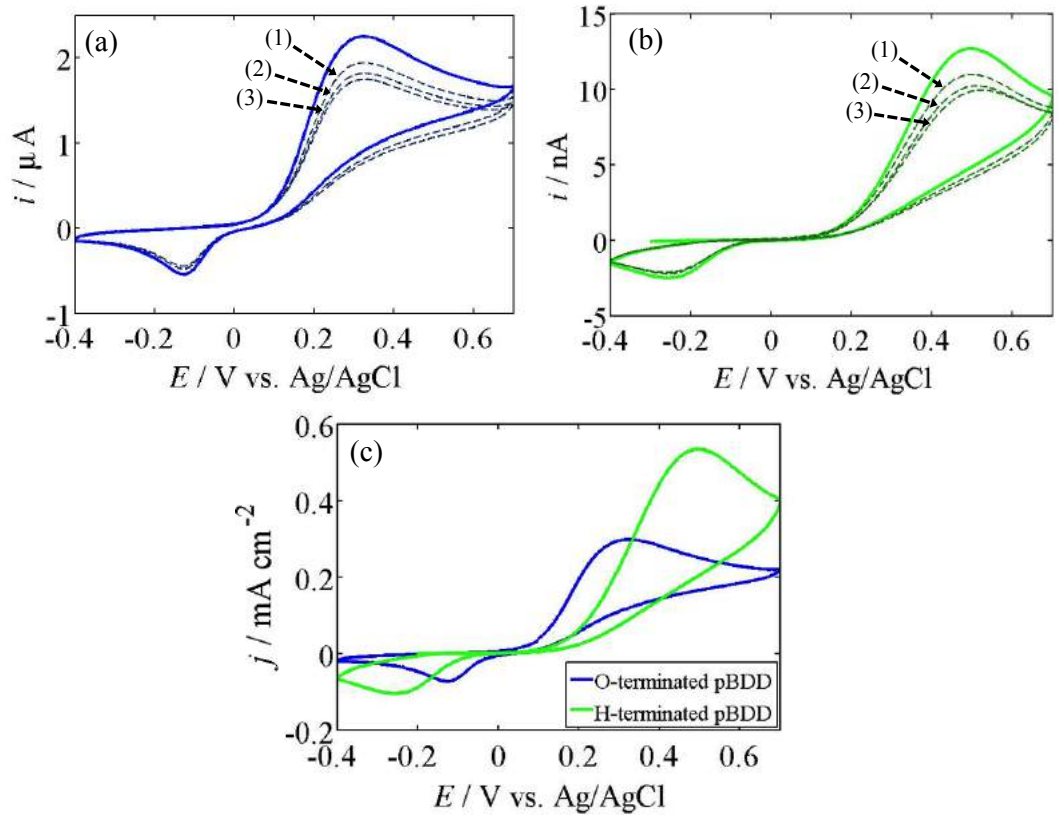

***Figure 6.20**: CVs for the oxidation of 1 mM dopamine hydrochloride in 0.1 M PBS using (a) 980 μm diameter alumina polished O-terminated conducting BDD macroelectrode (blue) with ΔE_p = 450 mV, (b) 55 μm diameter micro capillary on hydrogen plasma H-terminated conducting BDD (green) with ΔE_p = 750 mV, and (c) current density, j, plots of (a) and (b) to enable comparison between the different methodologies. First sweep (solid) is followed by subsequent sweeps (1) – (3) (dashed). Scan rate: 0.1 V s^{-1}.*

Gradual fouling over successive sweeps was observed on both BDD surfaces. Dopamine oxidation occurs through a two-electron two-proton transfer mechanism, as shown in **Figure 6.21**. The reaction initally forms dopaminequinone but also undergoes a series of side reactions to form a melanin-like compound (similar to the glue secreted by mussels), which can bond strongly to any type of surface.[68]

Consequently, electrode fouling will be a problem regardless of the electrode material used.

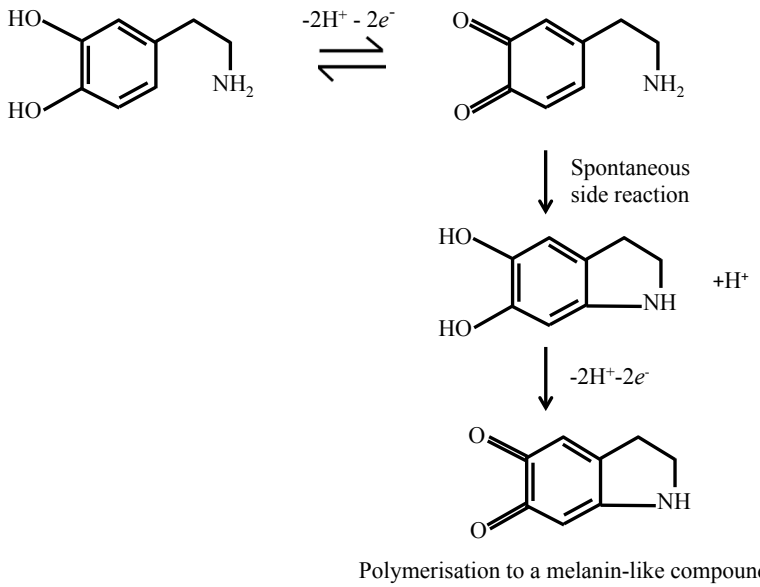

***Figure 6.21**: Redox mechanism for dopamine in neutral pH.*[69]

Very sluggish electrode kinetics were observed on both conducting BDD electrodes. Dopamine on BDD has been found to have the slowest rate of electrooxidation, but minimal deteroriation in the voltammeteric response over time compared to other carbon electrodes.[69] This supports the idea that dopamine adsorbs weakly to sp^3 carbon thus inhibiting ET, but its oxidation products also bind weakly to cause reduced fouling. In contrast, it has been shown that dopamine binds strongly to sp^2 carbon sites on surfaces.[41b] As minimal sp^2 sites exist in our BDD diamond, differences in the ET kinetics are solely due to the surface termination.

Dopamine displayed quasi-reversible ET behaviour on alumina polished O-terminated conducting BDD with ΔE_p of 452 ± 7 mV and $E_{1/2}$ for oxidation of +0.18 ± 0.01 V (**Figure 6.20**). On the hydrogen plasma H-terminated conducting BDD surface, the ΔE_p was much larger, 691 ± 43 mV, and there was a positive shift of $E_{1/2}$ to +0.32 ± 0.03 V.[70] Even though mass transport is higher in the capillary the

significant difference in ΔE_p suggests that ET is likely to be faster on the O-terminated BDD surface.

One previous study reported ET to be relatively unaffected when comparing as-grown (H-terminated) to anodically-polarised conducting BDD.[71] However, a contrasting study showed ET to be faster on cathodically (–H) treated (−3 V for 5 mins in 0.5 M H_2SO_4) compared to anodically (–O) treated (+3 V for 5 mins in 0.5 M H_2SO_4) conducting BDD.[72] DFT calculations showed a correlation between the stable adsorption distance and ET rate, with dopamine sitting slightly further away from a (100) carbonyl functionalised diamond surface (4.1 Å) compared to the (100) fully H-terminated surface (2.9 Å),[73] which matches to the slightly slower ET rate observed on anodically polarised conducting BDD.[74]

Interestingly, our results show that dopamine is likely to be kinetically more facile on alumina polished O-terminated compared to hydrogen plasma H-terminated conducting BDD. It is important to consider that different chemical groups are formed on the surface of BDD after alumina polishing compared to anodic treatment. For example, a higher proportion of C–O–C and C–OH groups exist on the alumina polished surface, whereas the anodically treated surface has an abundance of highly oxidised groups *e.g.* C=O and COOH (see **Figure 6.2**).[12] It is also noted that as-grown and cathodically polarised H-terminated BDD surfaces are not well characterised unlike hydrogen plasma surfaces, so results from these surfaces should be analysed with caution.

As presented in Chapter 5, protonated dopamine adsorbs favourably to any diamond surface, but has the greatest binding strengths to oxygen-terminated surfaces, particularly those containing carbonyl groups. Strong adsorption of dopamine and the subsequent oxidation products to the C=O groups may block the

reaction causing slower kinetics on an anodically treated compared to alumina polished surface. The oxidation reaction may also proceed more quickly on C–OH and C–O–C groups, however quantum mechanical calculations probing the ET transfer process of dopamine on the different surface groups may be required to prove this.

It is also of note that our molecular models always depicted the stable position of dopamine to be when the ring is flattened against each diamond surface and the ammonium group pointing out towards the bulk solution, to balance the trade-off of desolvation/solvation of nonpolar/polar groups (Chapter 5). This conformation has also been reported by the adsorption of a tyrosine containing peptide on diamond, which is structurally similar to dopamine.[75] It follows that the conformation chosen by Tryk *et al.*, where the polar ammonium group points towards both hydrophobic and hydrophilic surfaces, may not be structurally favourable.[73] DFT studies of dopamine in the proposed orientation on model alumina, anodic and hydrogen-treated surfaces could assist to further understanding.

6.4.2.6 Ascorbic Acid (Vitamin C)

Ascorbic acid (Vitamin C) is an essential nutrient in the human body to maintain a healthy immune system, fight infections and prevent scurvy.[76] Accurate electrochemical detection of ascorbic acid is therefore important for early medical diagnosis and treatment in the healthcare industry. CVs for the oxidation of 1 mM ascorbic acid in 0.1 M PBS on O- (alumina polished) and H- (hydrogen plasma) terminated conducting BDD are shown in **Figure 6.22.**

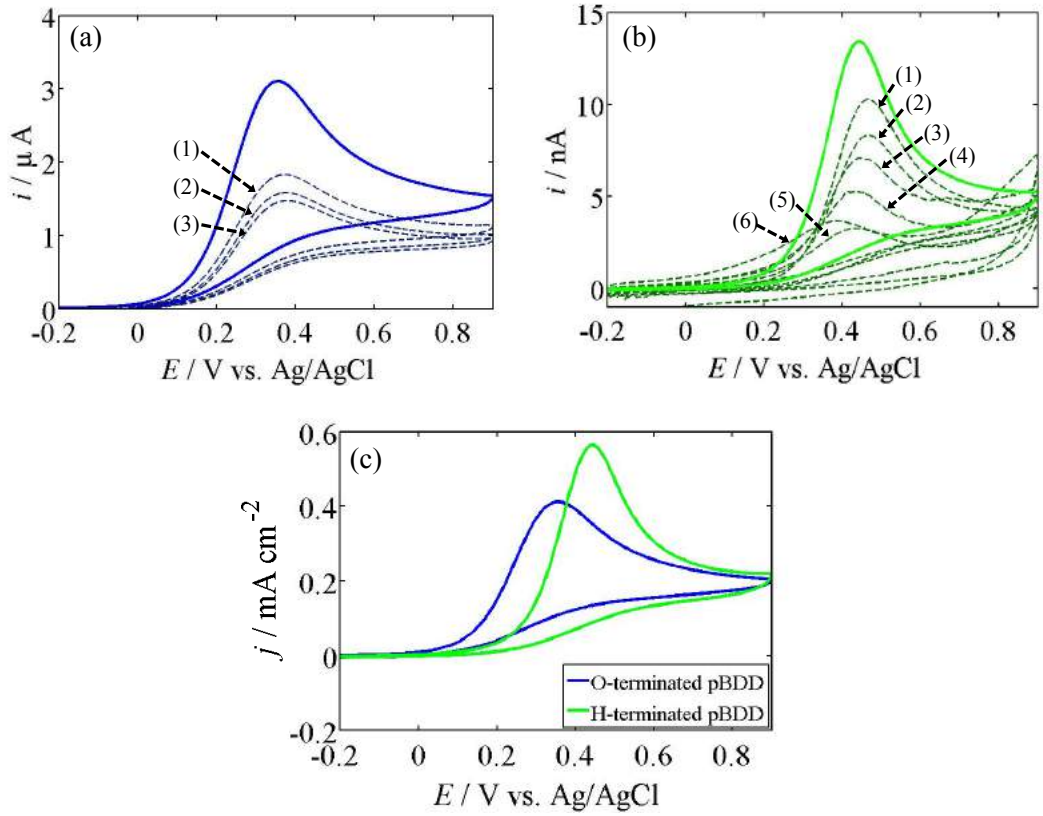

***Figure 6.22**: CVs for the oxidation of 1mM L-ascorbic acid in 0.1 M PBS using (a) 980 μm diameter alumina polished O-terminated conducting BDD macroelectrode (blue), (b) 55 μm diameter microcapillary on hydrogen plasma treated H-terminated conducting BDD (green), and (c) current density, j, plots of (a) and (b) to enable comparison between the different methodologies. First sweep (solid) is followed by subsequent sweeps (1) – (6) (dashed). Scan rate 0.1 V s^{-1}.*

Oxidation of ascorbic acid exhibits irreversible ET kinetics on both surfaces (**Figure 6.22)**. The O-terminated BDD electrode displays $E_{1/2}$ = +0.21 ± 0.02 V compared with $E_{1/2}$ = +0.35 ± 0.03 V on the H-terminated surface (E^0 = −0.16 V *vs.* Ag/AgCl)[51] If mass transport were the same for both electrodes, then the O-terminated surface would be exhibiting fast ET kinetics, however, when accounting for higher mass transport in the microcapillary these differences may not be that significant. The oxidation of L-ascorbic acid follows a two-electron two-proton inner-sphere ET mechanism to form dehydro-L-ascorbic acid:[77] The oxidised species then

undergoes a rapid hydration reaction to form an inactive compound,[78] as shown in **Figure 6.23**.

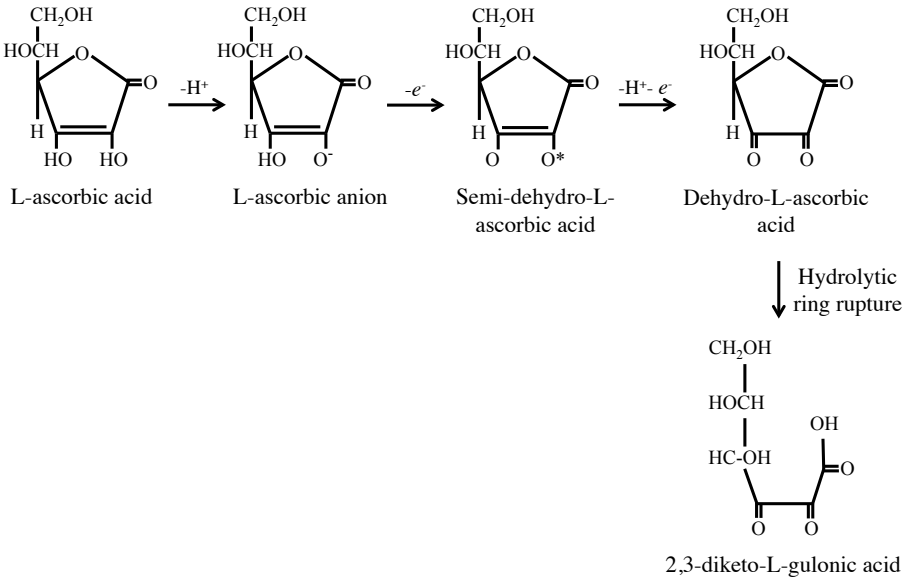

***Figure 6.23**: Oxidation reaction of L-ascorbic acid, followed by a rapid, irreversible hydration reaction.*[79]

McCreery *et al.*, reported that ascorbic acid is insensitive to surface oxides on GC and HOPG, but ET is inhibited by coverage of an adsorbed monolayer (methylene blue) on the surface that blocks sp^2 sites.[10b] This suggests that on GC and HOPG electrodes, ascorbic acid interacts via a non-oxide surface process. As minimal sp^2 sites were observed in our BDD electrodes, any differences must be due to the surface treatments. On BDD, Fujishima *et al.* have reported a reduction in the ET rate on an anodically treated (+2.6 V for 75 mins in 0.1 M KOH) O-terminated BDD, with the E_p shifting positively from +0.81 V on as-grown (–H), to +1.33 V on anodically-treated (–O) BDD (*vs.* SCE).[71] The sluggish kinetics were attributed to weak adsorption to the O-terminated surface.[71] More specifically, the C=O and COOH groups introduced by anodic treatment were thought to form a dipolar field that repels the ascorbic acid. DFT calculations were employed to confirm this observation, with

weaker attraction observed between ascorbic acid and a (100) C=O terminated (1.2 kcal mol^{-1}) compared to a (100) C–H terminated (7.7 kcal mol^{-1}) model diamond surface.[73]

Our data, in contrast, suggests that the differences may not be that great. This could be because there are fewer C=O and COOH groups on the alumina polished surface, ascorbic acid no longer experiences strong surface repulsion and can favourably bind, enabling faster ET kinetics than observed on anodically polarised BDD surfaces. Again, DFT calculations of the ET kinetics of ascorbic acid on the different surface groups would help to further elucidate this.

Fouling was observed on both surfaces, but a faster decline in the current response over subsequent sweeps was observed on the alumina polished O-, compared to the H-, terminated BDD surfaces (**Figure 6.22**). The C–O–C and C–OH groups could be enhancing surface adsorption, that accelerates fouling, compared to the H-termination. Fouling on O-terminated BDD was highly reproducible. In particular, the electrode displayed a near linear drop in i_p over subsequent sweeps, and was restored back to the original i_p after alumina polishing to reproduce a clean O-terminated surface. It follows that ascorbic acid, and the resulting oxidation products, adsorb to the alumina polished surface and gradually build a surface layer over time that blocks the electrode, which can be easily removed through alumina polishing. On the H-terminated surface, a drop was also observed in i_p over subsequent sweeps, but to a lesser extent suggesting that the reaction products adsorb less favourably to this surface. There is also a clear negative shift in $E_{1/2}$ on the final sweep due to local surface oxidation.

6.4.2.7 Serotonin

Serotonin is an essential neurotransmitter similar to dopamine, and is connected to various neurodegenerative diseases such as OCD, anxiety and depression (see Chapter 5, section 5.2). Accurate electrochemical detection of serotonin is important for improved understanding, early detection and rapid treatment of these diseases. CVs for the oxidation of 1 mM serotonin hydrochloride in 0.1 M PBS on O- (alumina polished) and H- (hydrogen plasma) terminated conducting BDD are shown in **Figure 6.24.**

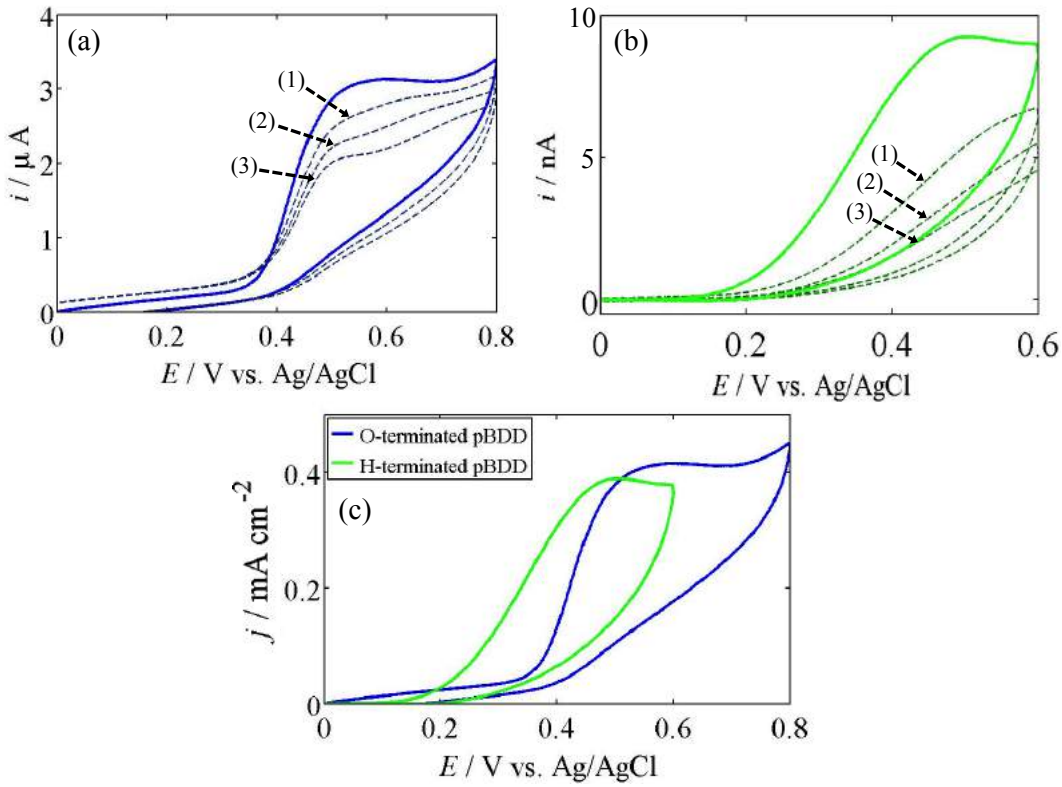

Figure 6.24*: CVs for the oxidation of 1 mM serotonin hydrochloride in 0.1 M PBS using (a) 980 μm diameter alumina polished O-terminated conducting BDD macroelectrode (blue), (b) 55 μm diameter microcapillary on hydrogen plasma H-terminated conducting BDD (green), and (c) current density, j, plots of (a) and (b) to enable comparison between the different methodologies. First sweep (solid) is followed by subsequent sweeps (1) – (3) (dashed). Scan rate: 0.1 V* s^{-1}.

Serotonin oxidation proceeds by a two-electron two-proton transfer mechanism,[80] shown in **Figure 6.25**. The oxidation of serotonin is a two-electrode,

two-proton process that follows a complex reaction pathway to form a quinone-imine compound along with a range of different species formed in side reactions.[81]

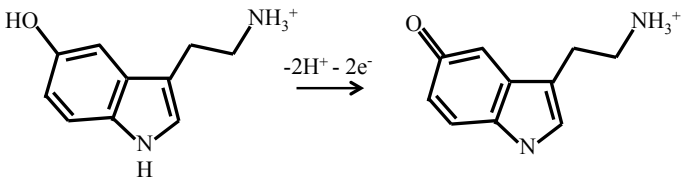

***Figure 6.25**: Oxidation reaction of serotonin*.[82]

Both the alumina polished O- and hydrogen plasma H- terminated conducting BDD electrodes exhibit irreversible kinetics (**Figure 6.24**). The reduction reaction was observed but required driving to high cathodic potentials (~ −1.0 V) that would affect the surface chemistry. Whilst the CVs display similar peak positions, the $E_{1/2}$ on the H-terminated (+0.34 ± 0.10 V) is shifted to the left of the O-terminated (+0.43 ± 0.03 V), compared to E^0 of +0.21 V corrected for the Ag/AgCl electrode[83] (**Figure 6.24**). This indicates that serotonin is more kinetically facile on the H-terminated BDD surface, especially when taking into account the faster mass transport in the microcapillary set-up.

The O-terminated peak position in **Figure 6.24** is comparable to that reported by Unwin *et al,* on a similar alumina polished O-terminated conducting BDD electrode (E_p = +0.53 V *vs.* SCE).[84] Fujishima *et al.*, in contrast reported negligible difference in serotonin oxidation between as-grown and anodically treated (+1.8 V for 10 mins in PBS) conducting BDD electrodes.[85] This suggests that the higher abundance of C–O–C and C–OH groups introduced by alumina polishing of BDD may be inhibiting the ET kinetics. However, caution must be taken to results on as-grown BDD surfaces, as the surface may have oxidised over time and no longer be fully hydrogenated.

Similar to dopamine, serotonin was found to display the slowest ET kinetics but greatest resistance to fouling on alumina polished O-terminated BDD, compared to other carbon electrodes (namely, GC and carbon nanotube networks).[84] This relates to strong adsorption of the oxidation products to the sp^2 sites on carbon electrode surfaces, as shown in the case of fouling of carbon-fibre electrodes during serotonin oxidation.[86] Whilst the surface fouling is so far considered relatively irreversible on GC, carbon-fibre and as-grown H-terminated BDD electrodes,[85] it has been reported that cycling to cathodic potentials (between +0.8 and −0.6 V in 0.1 M NaCl/5 mM HEPES buffer) can serve to remove the adsorbed quinone species and refresh an alumina polished O-terminated BDD electrode surface.[84] **Figure 6.24** shows a decline in the current response over subsequent sweeps due to electrode fouling on both surfaces, although the current drops at a faster rate on the H-terminated surface. It follows that whilst favourable interactions of serotonin to hydrogen plasma H-terminated BDD electrodes enhances the ET kinetics, it also accelerates the surface fouling. Serotonin oxidation produces a range of oxidation products that have been shown to adsorb on alumina polished O-terminated BDD surfaces to form a film that grows with successive potential sweeps.[82] Our results suggest that the film formation occurs more rapidly on H-terminated surfaces compared to O-. Employment of molecular models to study the film formation, and DFT studies to investigate the ET kinetics, on the different BDD surface groups may help to further elucidate why this occurs. It is noted that the rate of film growth on alumina polished BDD during serotonin oxidation has been related to the boron content of the grain.[82] It follows that the variability observed between repeats in this study may be due to the capillary landing on different BDD grains that contain different surface groups and boron dopant levels.

6.4.2.8 Summary of Inner-Sphere ET Kinetics on Conducting BDD

The ΔE_p, E_p, i_p from the CVs and expected i_p assuming Randles-Sevcik, (Chapter 3, equation 3.8) of inner-sphere redox couples on O- (alumina polished) and H- (hydrogen plasma) terminated conducting BDD are summarised in **Tables 6.2** and **6.3**, respectively. Discrepenices between the actual i_p and Randles-Sevcik approximations are due to the assumptions that: the electrode area is the same as the microcapillary menisus, which is generally not the case due to variable surface wetting, constant temperature (298 K), and diffusion coefficients are the same as literature (below). The $E_{1/2}$ values quoted in the text were estimates based on (E_{pa} + E_{pc})/2 for reversible reactions (section 6.4.1.4, equation 6.2), and the potential at i_p/2 for non-reversible reactions. The diffusion coefficients for each species were taken as: 8.8×10^{-6} cm s^{-1} for $Ru(NH_3)_6^{3+/2+}$,[39b] 6.3×10^{-6} cm s^{-1} for $Fe(CN)_6^{4-/3-}$,[87] 6.0×10^{-6} cm s^{-1} for dopamine,[88] 5.4×10^{-6} cm s^{-1} for serotonin,[88] 3.2×10^{-6} cm s^{-1} for NADH,[89] 7.2×10^{-6} cm s^{-1} for riboflavin,[90] 5.3×10^{-6} cm s^{-1} for ascorbic acid,[88] 9.0×10^{-6} cm s^{-1} for $Fe^{2+/3+}$,[91] and 7.9×10^{-6} cm s^{-1} for $Eu^{3+/2+}$.[92]

***Table 6.2**: Summary of CV data for species on O- (alumina polished) terminated conducting BDD.*

Species	**CVs on O-terminated (alumina polished) BDD / *E vs.* Ag/AgCl**					
	E_{pc} **/ V**	E_{pa} **/ V**	ΔE_p **/ mV**	i_{pc} **/ µA**	i_{pa} **/ µA**	**Expected** i_p **/ µA**
$Ru(NH_3)_6^{3+/2+}$	−0.25 ± 0.01	−0.19 ± 0.01	63 ± 2	−2.31 ± 0.04	1.86 ± 0.39	1.90
$Fe(CN)_6^{4-/3-}$	0.23 ± 0.01	0.30 ± 0.01	69 ± 11	−1.44 ± 0.11	1.48 ± 0.12	1.61
NADH	–	0.66 ± 0.03	–	–	2.23 ± 0.30	1.15
Riboflavin	−0.62 ± 0.02	−0.55 ± 0.01	70 ± 21	−1.58 ± 0.14	0.63 ± 0.02	1.73
$Fe^{2+/3+}$	0.13 ± 0.01	0.71 ± 0.03	578 ± 30	−0.94 ± 0.26	1.20 ± 0.23	1.93
Dopamine	−0.13 ± 0.01	0.33 ± 0.01	452 ± 7	−0.47 ± 0.06	2.34 ± 0.45	1.57
Ascorbic Acid	–	0.37 ± 0.02	–	–	1.91 ± 0.30	1.48
Serotonin	–	0.60 ± 0.03	–	–	2.28 ± 0.22	1.49

***Table 6.3**: Summary of CV data for species on H- (hydrogen plasma) terminated conducting BDD.*

Species	CVs on H-terminated (hydrogen plasma) BDD / *E vs.* Ag/AgCl					
	E_{pc} / V	E_{pa} / V	ΔE_p / mV	i_{pc} / nA	i_{pa} / nA	Expected i_p / nA
$Ru(NH_3)_6^{3+/2+}$	−0.26 ± 0.01	−0.19 ± 0.01	67 ± 5	−16.61 ± 6.51	14.71 ± 6.44	6.00
$Fe(CN)_6^{4-/3-}$	0.13 ± 0.02	0.23 ± 0.02	107 ± 12	−10.75 ± 3.02	11.28 ± 3.22	4.36
NADH	–	0.59 ± 0.03	–	–	4.42 ± 1.48	4.30
Riboflavin	−0.65 ± 0.01	−0.57 ± 0.01	84 ± 6	−10.83 ± 1.18	8.50 ± 0.62	5.44
$Fe^{2+/3+}$	−0.31 ± 0.06	0.91 ± 0.04	1214 ± 65	−4.26 ±6.21	10.00 ± 5.02	7.21
Dopamine	−0.13 ± 0.02	0.56 ± 0.03	691 ± 43	−1.02 ± 0.48	9.71 ± 2.06	4.95
Ascorbic Acid	–	0.41 ± 0.03	–	–	5.48 ± 3.50	4.65
Serotonin	–	0.55 ± 0.10	–	–	10.35 ± 0.85	4.70

6.4.3 Electrochemical Response of an Outer-Sphere Mediator to the Surface Termination on Semi-conducting BDD

6.4.3.1 $Ru(NH_3)_6^{3+/2+}$

Experiments explored the effect of applied anodic potential on the electrochemical response of $Ru(NH_3)_6^{3+/2+}$ on freestanding H- (hydrogen plasma) terminated moderately doped semi-conducting polycrystalline BDD with the large-scale microcapillary technique (**Figure 6.26**a). **Figure 6.26**b shows CVs recorded at a scan rate of 0.1 V s^{-1} for reduction of 1 mM $Ru(NH_3)_6^{3+}$ in 0.1 M KNO_3 on a hydrogen plasma treated H-terminated semi-conducting BDD electrode,[12, 93] functionalised before use and confirmed to be hydrophobic by contact angle analysis.[94] A typical initial CV, shown in **Figure 6.26**b (red), with a start and end potential of 0.2 V, and a reverse potential of −0.7 V, was recorded on the freshly H-terminated surface. With the capillary held in the same position, the electrode was then subject to anodic polarisation at +1.5 V *vs.* Ag/AgCl QRCE for 1 s, followed by a wait period of 5 s at the start potential and a CV was recorded again. This procedure was repeated 30 times. The resulting CVs are shown in **Figure 6.26**b after (i) 5; (ii)

10; (iii) 15; (iv) 20; (v) 25 and (vi) 30, 1 s pulses. The initial (blue) and final (dashed black) CVs are shown separately in **Figure 6.26**c for clarity.

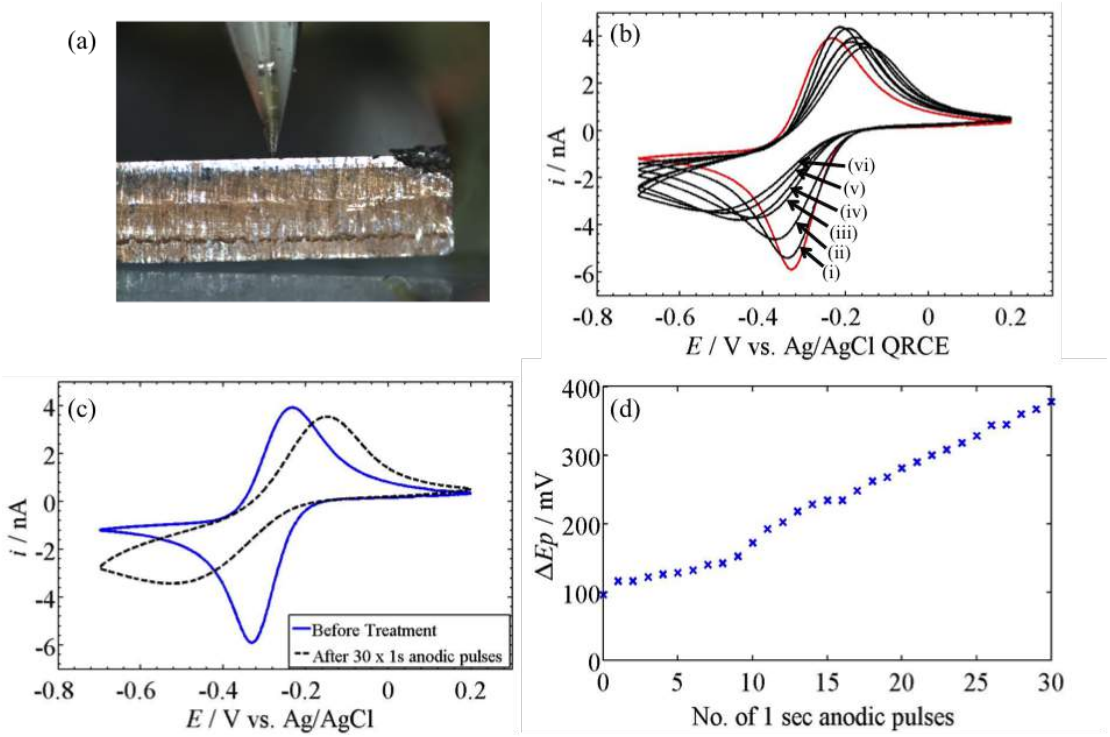

Figure 6.26*: (a) Image of the microcapillary set-up on the semi-conducting BDD electrode. (b) Successive CVs recorded at 0.1 V* s^{-1} *after [×5], 1 sec anodic pulses at +1.5 V, recorded successively for a total of 30 pulses, for the reduction of 1 mM* $Ru(NH_3)_6^{3+}$ *in 0.1 M* KNO_3 *on hydrogen plasma treated H-terminated semi-conducting BDD, using a microcapillary of diameter ~ 52 μm.* (c) CVs before and after [×30] 1 sec anodic pulses. (d) Peak-to-peak separation (ΔE_p) after each 1 sec anodic pulse.

The CVs in **Figure 6.26**b – c indicate that anodic oxidation of the surface results in decreasing ET kinetics**.** It is well documented that anodic polarisation of the BDD surface leads to a change in surface termination;[4c],[12] the relative contributions of different –O groups formed on the surface dependent on the polycrystallinity of the material and the extent of the treatment. However, besides changing the surface chemistry, oxidation of the electrode surface using the microcapillary set-up will also change the wetting of the droplet on the surface. On O-terminated semi-conducting BDD, ET has been shown to be sluggish for $Ru(NH_3)_6^{3+/2+}$.[12] However, as shown

here, surface transfer doping due to H-termination (see Chapter 1, section 1.2.5),[95] results in a peak-to-peak separation, ΔE_p, for the redox couple $Ru(NH_3)_6^{3+/2+}$ of ~ 96 mV, indicative of significantly faster ET kinetics than would be expected for the O-terminated surface. The ΔE_p of the CV after each anodic pulse is shown in **Figure 6.26**d.

Notably, after just 1 s of anodic treatment, on the freshly H-terminated surface, ΔE_p is observed to increase from ~ 96 mV to 116 mV. As shown in **Figure 6.26**d, repeated anodic polarisation leads to a significant increase in ΔE_p due to the removal of local charge carriers as the surface termination changes from H- to O-termination. After 30 s of anodic treatment ΔE_p is ~ 378 mV. Note that such effects would be unlikely if the material was doped to be metal-like as the number of available charge carriers would be sufficiently high to ensure fast ET irrespective of surface termination.[12] For example, H- and O-terminated conducting (metal-like) BDD macroelectrodes show very similar CV responses towards the reduction of $Ru(NH_3)_6^{3+}$.[12]

6.4.3.2 Application of Diamond Surface Treatments: Electrode Patterning

Given the results above, the premise that the local BDD surface termination could be both modified (write) and detected electrochemically (read) was investigated using SECCM (see section 6.3.5, Figure 6.9). The SECCM imaging was carried out by Dr. Hollie Patten and Dr. Laura Hutton, University of Warwick (see Declaration). The SECCM probe (~ 1 – 2 μm diameter) was used to anodically oxidise a small scan area of 10 μm × 10 μm (scanning bottom to top) of a H-terminated semi-conducting electrode by scanning the SECCM meniscus over the surface a total of three times using an effective anodic oxidation potential of +1.5 V (1 μm s^{-1} tip scan speed). To

view the resulting surface modification, SECCM imaging was carried out over a larger scan area of 20 μm × 20 μm after each oxidative scan at an effective potential of −0.3 V, which is only sufficient to reduce $Ru(NH)_6^{3+}$ on the H-terminated surface. **Figure 6.27** shows (i) the BDD electrochemical current response and (ii) the conductance current response between the two channels of the theta pipette for the reduction of 2 mM $Ru(NH)_6^{3+}$ after the (a) first; (b) second and (c) third oxidative (modification) scans.

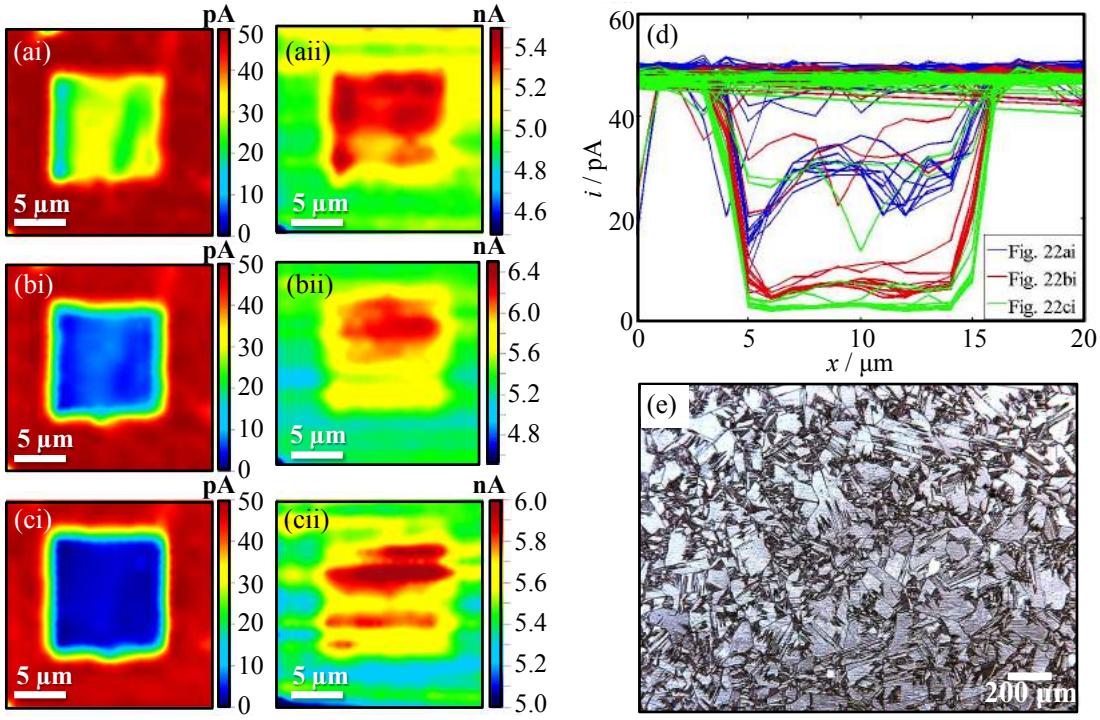

***Figure 6.27**: SECCM read-write (i) electrochemical current maps and (ii) tip dc conductance maps recorded simultaneously, after three consecutive oxidative scans (a) to (c), recorded with (i) the BDD electrode biased at −0.3 V (read), after writing took place at +1.5 V and (ii) +200 mV applied between the two QRCEs in each barrel, in a theta capillary of ~ 1 – 2 μm diameter, filled with 2 mM $Ru(NH_3)_6^{3+}$ and 50 mM KNO_3 on H-terminated BDD. (d) Overlay of the line scans in ai – ci showing a drop in the current in the anodic region after each oxidative scan. (e) Optical image of the grain structure of the BDD polycrystalline electrode employed.*

Anodic treatment results in a measurably smaller current for reduction of $Ru(NH)_6^{3+}$ due to partial anodic removal of the H-termination layer, qualitatively

consistent with the data in **Figure 6.26**. The residence time of the meniscus in the vicinity of the electrode surface was ~ 1 s during local modification (writing) and subsequent activity imaging (reading), and this is clearly sufficient to modify the surface termination. **Figures 6.27**ai to ci, show that there is a gradual decrease in $Ru(NH_3)_6^{3+}$ reductive currents in the square region with consecutive scans, indicating the gradual removal of the H-termination layer with subsequent oxidative scans. After three scans the currents in the central region of the O-terminated area of the surface have dropped by over 90%, compared to the surrounding H-terminated regions. The drop in current after each successive scan is demonstrated clearly by the plot of each line scan in **Figure 6.27**d.

Figures 6.27aii – cii are further illuminating on the effect of surface termination. These show the dc conductance current between the QRCEs in the barrels of the theta pipette, highlighting that in the modified region increases by about 20% which can be attributed to a change in the meniscus contact[32] due to increased wetting of the surface in the O-terminated regions. Interestingly, the area of the activity scan modified by anodic polarisation displays a heterogeneously varying current, reminiscent of earlier work on metallic O-terminated polycrystalline BDD which showed that differently doped grains (facet) have different electroactivity.[96],[97] These current zones most likely represent the different crystal facets of the polycrystalline material, as shown optically in **Figure 6.27**d, which contain differing amounts of boron, and may also be subject to different degrees of oxygen termination (or depletion of charge carriers), during the 'write' process.

6.5 Conclusions

Electrochemical analysis was used to detect a range of biologically important species. The work revolutionises understanding of these species by advancing

knowledge of how different conducting BDD electrode surfaces *i.e*. alumina polished (–O) and hydrogen plasma (–H) treated, influence the detection of a range of inner-sphere redox mediators. This was the first study to-date that definitively investigates the effect of surface termination on the electrochemical response of species, where all other factors are carefully controlled to not influence the response. Furthermore, it was the first study in literature that probes the effect of alumina polishing diamond on the electrochemical response of a range of species, with prior knowledge focused on anodic polarisation treatments. Significantly, the results can now be added alongside the literature for these molecules on other electrode surfaces to enable the field to make informed decisions on the choice of electrode material when developing sensors in the future (see section 6.1).

Tests were performed in order to ensure the electrochemical response was due solely to surface termination *i.e.* the BDD electrodes were shown to be sufficiently boron doped to be conducting (3×10^{20} B atoms cm^{-3}) and displayed minimal sp^2 content. In order to facilitate measurements on the surfaces, two different set-ups were employed: a macroelectrode (~ 1 mm diameter) for the O-terminated and a microcapillary (~ 55 μm diameter) for the H-terminated electrode. The microcapillary enabled access to multiple regions of the H-terminated surface to prevent damaging the surface treatment in one-use. However, increased mass transport in the microcapillary set-up (estimated at ~ 3.2×10^2 times greater than the macroelectrode) will enhance the observed ET kinetic response compared to the macroelectrode set-up *i.e.* for the same k^0 value, the CV will appear more spread out, (greater ΔE_p) in the microcapillary set-up than with the macroelectrode. Hence in this work we can only make qualitative interpretations about the differences in k^0 for the same species on O-

and H-terminated electrodes. Finite element models would need to be applied to quantitatively determine kinetic differences.

Analysis of the $\Delta E_{p,}$ and $E_{1/2}$ values from the CVs highlighted possible surface trends *i.e.* qualitatively $Fe(CN)_6^{4-/3-}$, $Fe^{2+/3+}$, dopamine and ascorbic acid appeared to display faster ET on alumina polished O-terminated BDD, whereas serotonin appeared to be inhibited on this surface. This suggests that the ET has potential to be enhanced on a particular surface, however, without accounting for mass transport these trends are only speculative. Furthermore, due to the complexity of the inner-sphere mechanisms for each species, the ET process can be complicated with no general rule for all species. Molecular models (MD and quantum) could be employed to help elucidate the favourable interactions of each species to different surface groups *e.g.* C=O, C–O–C, C–H, C–OH.

Electrochemical biosensors require a surface that can accurately and selectively detect a species with minimal fouling to prevent electrode deactivation.[69] The oxidation products of the biological species (dopamine, serotonin, ascorbic acid, riboflavin and NADH) fouled the BDD electrode, but to a lesser extent than has been observed on other carbon electrodes. Of the species tested, $Fe^{2+/3+}$ was found to be the most surface sensitive displaying well-defined peaks and markedly different kinetics on the different BDD surfaces.

An interesting application that utilises the different electrochemical responses of a mediator to H- and O- terminations is patterning. The use of SECCM imaging to electrochemically pattern ~ micron sized areas on the diamond surface was presented. To do so, the surface properties of a diamond electrode were altered such that electrochemistry was inhibited in some regions, while being relatively facile in others. This concept was illustrated with the outer-sphere mediator $Ru(NH)_6^{3+}$, on a semi-

conducting BDD electrode. The SECCM tip (~ 1 – 2 μm diameter) was used to convert regions of the H-terminated surface to O-terminated, which could be read using the electrochemical response towards $Ru(NH)_6^{3+}$; smaller currents were indicative of the O-terminated regions of the surface.

6.6 Future Work

The most important next step for this study would be to extract out k^0 values for each system using finite-element simulations in order to quantify differences solely due to the kinetics. This would enable the surface sensitivity of the species to be revealed. Similar CV experiments on the influence of other surface treatments, *e.g.* anodic/cathodic polarisation or oxygen plasma, to the electrochemical response of each species on BDD could be performed in order to extensively screen for the ideal surface that enhances ET for a species.

The SECCM patterning technique opens up the prospect for creation of specialised surface patterned electrochemical (and electronic) devices *e.g.* as a microarray device.[98] The next big challenge would be to pattern conducting BDD. On these surfaces we envisage inner-sphere redox probes *e.g.* $Fe^{2+/3+}$ could be employed to read the modification process.

6.7 References

[1] M. Shen, A. J. Bard, *J Am Chem Soc* **2011**, *133*, 15737-15742.
[2] a) Y. V. Pleskov, *Russ J Electrochem* **2002**, *38*, 1275-1291; b) J. Xu, M. C. Granger, Q. Chen, J. W. Strojek, T. E. Lister, G. M. Swain, *Anal. Chem.* **1997**, *69*, 591A-597A; c) R. G. Compton, J. S. Foord, F. Marken, *Electroanalysis* **2003**, *15*, 1349-1363.
[3] S. Szunerits, C. E. Nebel, R. J. Hamers, *MRS Bulletin* **2014**, *39*, 517-524.
[4] a) D. Ballutaud, N. Simon, H. Girard, E. Rzepka, B. Bouchet-Fabre, *Diamond Relat. Mater.* **2006**, *15*, 716-719; b) H. Notsu, I. Yagi, T. Tatsuma, D. A. Tryk, A. Fujishima, *J. Electroanal. Chem.* **2000**, *492*, 31-37; c) H. A. Girard, N. Simon, D. Ballutaud, E. de La Rochefoucauld, A. Etcheberry, *Diamond Relat. Mater.* **2007**, *16*, 888-891.
[5] P. Strobel, M. Riedel, J. Ristein, L. Ley, *Nature* **2004**, *430*, 439-441.

[6] A. J. Bard, L. R. Faulkner, *Electrochemical Methods: Fundamentals and Applications, Vol. 2*, Wiley New York, **1980**.
[7] A. N. Simonov, G. P. Morris, E. A. Mashkina, B. Bethwaite, K. Gillow, R. E. Baker, D. J. Gavaghan, A. M. Bond, *Anal. Chem.* **2014**, *86*, 8408-8417.
[8] J. P. Lagrange, A. Deneuville, E. Gheeraert, *Diamond Relat. Mater.* **1998**, *7*, 1390-1393.
[9] a) I. Yagi, H. Notsu, T. Kondo, D. A. Tryk, A. Fujishima, *J. Electroanal. Chem.* **1999**, *473*, 173-178; b) I. Duo, C. Levy-Clement, A. Fujishima, C. Comninellis, *J. Appl. Electrochem.* **2004**, *34*, 935-943.
[10] a) P. Chen, M. A. Fryling, R. L. McCreery, *Anal. Chem.* **1995**, *67*, 3115-3122; b) P. Chen, R. L. McCreery, *Anal. Chem.* **1996**, *68*, 3958-3965.
[11] a) J. Xu, Q. Chen, G. M. Swain, *Anal. Chem.* **1998**, *70*, 3146-3154; b) G. M. Swain, A. B. Anderson, J. C. Angus, *MRS bulletin* **1998**, *23*, 56-60.
[12] L. A. Hutton, J. G. Iacobini, E. Bitziou, R. B. Channon, M. E. Newton, J. V. Macpherson, *Anal. Chem.* **2013**, *85*, 7230-7240.
[13] H. B. Suffredini, V. A. Pedrosa, L. Codognoto, S. A. Machado, R. C. Rocha-Filho, L. A. Avaca, *Electrochim. Acta* **2004**, *49*, 4021-4026.
[14] P. E. Pehrsson, T. W. Mercer, *Surf. Sci.* **2000**, *460*, 49-66.
[15] G. R. Salazar-Banda, L. S. Andrade, P. A. Nascente, P. S. Pizani, R. C. Rocha-Filho, L. A. Avaca, *Electrochim. Acta* **2006**, *51*, 4612-4619.
[16] a) B. Williams, J. Glass, *J. Mater. Res.* **1989**, *4*, 373-384; b) J. Philip, P. Hess, T. Feygelson, J. Butler, S. Chattopadhyay, K. Chen, L. Chen, *J. Appl. Phys.* **2003**, *93*, 2164-2171.
[17] J. Xu, M. C. Granger, Q. Chen, J. W. Strojek, T. E. Lister, G. M. Swain, *Anal. Chem.* **1997**, *69*, 591A-597A.
[18] a) A. A. Tseng, A. Notargiacomo, T. Chen, *J. Vac. Sci. Technol. B* **2005**, *23*, 877-894; b) Z. Nie, E. Kumacheva, *Nat. Mater.* **2008**, *7*, 277-290; c) J. V. Barth, G. Costantini, K. Kern, *Nature* **2005**, *437*, 671-679.
[19] Y. Xia, G. M. Whitesides, *Annu. Rev. Mater. Sci.* **1998**, *28*, 153-184.
[20] J. C. Love, L. A. Estroff, J. K. Kriebel, R. G. Nuzzo, G. M. Whitesides, *Chem. Rev.* **2005**, *105*, 1103-1169.
[21] a) A. Hartl, E. Schmich, J. A. Garrido, J. Hernando, S. C. R. Catharino, S. Walter, P. Feulner, A. Kromka, D. Steinmuller, M. Stutzmann, *Nat. Mater.* **2004**, *3*, 736-742; b) B. Rezek, L. Michalíková, E. Ukraintsev, A. Kromka, M. Kalbacova, *Sensors* **2009**, *9*, 3549-3562; c) G.-J. Zhang, K.-S. Song, Y. Nakamura, T. Ueno, T. Funatsu, I. Ohdomari, H. Kawarada, *Langmuir* **2006**, *22*, 3728-3734; d) L. Marcon, M. Wang, Y. Coffinier, F. Le Normand, O. Melnyk, R. Boukherroub, S. Szunerits, *Langmuir* **2009**, *26*, 1075-1080; e) L. Marcon, C. Spriet, Y. Coffinier, E. Galopin, C. Rosnoblet, S. Szunerits, L. Héliot, P.-O. Angrand, R. Boukherroub, *Langmuir* **2010**, *26*, 15065-15069.
[22] a) Y. Kaibara, K. Sugata, M. Tachiki, H. Umezawa, H. Kawarada, *Diamond Relat. Mater.* **2003**, *12*, 560-564; b) M. Tachiki, T. Fukuda, K. Sugata, H. Seo, H. Umezawa, H. Kawarada, *Appl. Surf. Sci.* **2000**, *159*, 578-582; c) S. E. Pust, S. Szunerits, R. Boukherroub, G. Wittstock, *Nanotechnology* **2009**, *20*, 075302.
[23] a) N. Ebejer, M. Schnippering, A. W. Colburn, M. A. Edwards, P. R. Unwin, *Anal. Chem.* **2010**, *82*, 9141-9145; b) S. C. Lai, P. V. Dudin, J. V. Macpherson, P. R. Unwin, *J. Am. Chem. Soc.* **2011**, *133*, 10744-10747; c) N. Ebejer, A. G. Güell, S. C. Lai, K. McKelvey, M. E. Snowden, P. R. Unwin,

Ann. Rev. Anal. Chem. **2013**, *6*, 329-351; d) K. McKelvey, M. A. O'Connell, P. R. Unwin, *Chem. Comm.* **2013**, *49*, 2986-2988.
[24] T. Watanabe, T. K. Shimizu, Y. Tateyama, Y. Kim, M. Kawai, Y. Einaga, *Diamond Relat. Mater.* **2010**, *19*, 772-777.
[25] C. Prado, S. J. Wilkins, P. Gründler, F. Marken, R. G. Compton, *Electroanalysis* **2003**, *15*, 1011-1016.
[26] P. K. Bachmann, D. Leers, H. Lydtin, *Diamond Relat. Mater.* **1991**, *1*, 1-12.
[27] L. Hutton, M. E. Newton, P. R. Unwin, J. V. Macpherson, *Anal. Chem.* **2008**, *81*, 1023-1032.
[28] J. V. Macpherson, *Phys. Chem. Chem. Phys.* **2015**, *17*, 2935-2949.
[29] M. B. Joseph, E. Bitziou, T. L. Read, L. Meng, N. L. Palmer, T. P. Mollart, M. E. Newton, J. V. Macpherson, *Anal. Chem.* **2014**, *86*, 5238-5244.
[30] B. Rezek, C. Sauerer, C. Nebel, M. Stutzmann, J. Ristein, L. Ley, E. Snidero, P. Bergonzo, *Appl. Phys. Lett.* **2003**, *82*, 2266-2268.
[31] T. M. Day, P. R. Unwin, J. V. Macpherson, *Nano. Lett.* **2006**, *7*, 51-57.
[32] M. E. Snowden, A. G. Güell, S. C. S. Lai, K. McKelvey, N. Ebejer, M. A. O'Connell, A. W. Colburn, P. R. Unwin, *Anal. Chem.* **2012**, *84*, 2483-2491.
[33] J. W. Ager III, W. Walukiewicz, M. McCluskey, M. A. Plano, M. I. Landstrass, *App. Phys. Lett.* **1995**, *66*, 616-618.
[34] S. Koizumi, C. Nebel, M. Nesladek, *Physics and Applications of CVD Diamond*, John Wiley & Sons, **2008**.
[35] H. B. Martin, A. Argoitia, U. Landau, A. B. Anderson, J. C. Angus, *J. Electrochem. Soc.* **1996**, *143*, L133-L136.
[36] C. Nebel, J. Ristein, *Thin-Film Diamond II (Semiconductors and Semimetals), Vol. 77*, Elsevier B. V., Amsterdam, Netherlands., **2004**.
[37] D. Tryk, K. Tsunozaki, T. N. Rao, A. Fujishima, *Diamond Relat. Mater.* **2001**, *10*, 1804-1809.
[38] a) N. Vinokur, B. Miller, Y. Avyigal, R. Kalish, *J. Electrochem. Soc.* **1996**, *143*, L238-L240; b) C. Levy-Clement, F. Zenia, N. Ndao, A. Deneuville, *New Diamond Front. Carbon Technol.* **1999**, *9*, 189-206.
[39] a) M. C. Granger, M. Witek, J. Xu, J. Wang, M. Hupert, A. Hanks, M. D. Koppang, J. E. Butler, G. Lucazeau, M. Mermoux, *Anal. Chem.* **2000**, *72*, 3793-3804; b) J. V. Macpherson, D. O'Hare, P. R. Unwin, C. P. Winlove, *Biophys. J.* **1997**, *73*, 2771.
[40] K. R. Kneten, R. L. McCreery, *Anal. Chem.* **1992**, *64*, 2518-2524.
[41] a) H.-H. Yang, R. McCreery, *Anal. Chem.* **1999**, *71*, 4081-4087; b) S. H. DuVall, R. L. McCreery, *Anal. Chem.* **1999**, *71*, 4594-4602.
[42] K. Dunbar, R. A. Heintz, *Prog. Inorg. Chem.* **1997**, *45*, 283-392.
[43] a) A. G. Güell, N. Ebejer, M. E. Snowden, K. McKelvey, J. V. Macpherson, P. R. Unwin, *Proc. Natl. Acad. Sci.* **2012**, *109*, 11487-11492; b) M. E. Snowden, A. G. Güell, S. C. Lai, K. McKelvey, N. Ebejer, M. A. O'Connell, A. W. Colburn, P. R. Unwin, *Anal. Chem.* **2012**, *84*, 2483-2491.
[44] K. K. Cline, M. T. McDermott, R. L. McCreery, *J. Phys. Chem.* **1994**, *98*, 5314-5319.
[45] L. Peter, W. Dürr, P. Bindra, H. Gerischer, *J. Electroanal. Chem. Interfacial Electrochem.* **1976**, *71*, 31-50.
[46] R. Trouillon, D. O'Hare, *Electrochim. Acta* **2010**, *55*, 6586-6595.
[47] J. Kawiak, T. Jędral, Z. Galus, *J. Electroanal. Chem. Interfacial Electrochem.* **1983**, *145*, 163-171.
[48] A. Radoi, D. Compagnone, *Bioelectrochemistry* **2009**, *76*, 126-134.

[49] P. Belenky, K. L. Bogan, C. Brenner, *Trends Biochem. Sci.* **2007**, *32*, 12-19.
[50] T. N. Rao, I. Yagi, T. Miwa, D. Tryk, A. Fujishima, *Anal. Chem.* **1999**, *71*, 2506-2511.
[51] J. Stenesh, in *Biochemistry*, Springer, **1998**, pp. 293-315.
[52] F. Pariente, E. Lorenzo, F. Tobalina, H. Abruna, *Anal. Chem.* **1995**, *67*, 3936-3944.
[53] H. J. Powers, *Am. J. Clin. Nutr.* **2003**, *77*, 1352-1360.
[54] H. P. Smedts, M. Rakhshandehroo, A. C. Verkleij-Hagoort, J. H. de Vries, J. Ottenkamp, E. A. Steegers, R. P. Steegers-Theunissen, *Eur. J. Clin. Nutr.* **2008**, *47*, 357-365.
[55] B. Janik, P. J. Elving, *Chem. Rev.* **1968**, *68*, 295-319.
[56] A. Chatterjee, J. Foord, *Diamond Relat. Mater.* **2009**, *18*, 899-903.
[57] M. I. Page, *Chemistry of Enzyme Action*, Elsevier, **1984**.
[58] H.-Y. Gu, A.-M. Yu, H.-Y. Chen, *Anal. Lett.* **2001**, *34*, 2361-2374.
[59] S. B. Revin, S. A. John, *Electrochim. Acta* **2012**, *75*, 35-41.
[60] C. Gasche, A. Berstad, R. Befrits, C. Beglinger, A. Dignass, K. Erichsen, F. Gomollon, H. Hjortswang, I. Koutroubakis, S. Kulnigg, *Inflamm. Bowel Dis.* **2007**, *13*, 1545-1553.
[61] T. B. Drüeke, F. Locatelli, N. Clyne, K.-U. Eckardt, I. C. Macdougall, D. Tsakiris, H.-U. Burger, A. Scherhag, *New Eng. J. Med.* **2006**, *355*, 2071-2084.
[62] D. C. Rockey, J. P. Cello, *New Eng. J. Med.* **1993**, *329*, 1691-1695.
[63] M. Alleyne, M. K. Horne, J. L. Miller, *Am. J. Med.* **2008**, *121*, 943-948.
[64] R. King, J. Miller, D. Wakerley, *Brit. Corros. J.* **1973**, *8*, 89-93.
[65] D. Georgiou, A. Aivazidis, J. Hatiras, K. Gimouhopoulos, *Water Res.* **2003**, *37*, 2248-2250.
[66] R. Amarowicz, R. Pegg, P. Rahimi-Moghaddam, B. Barl, J. Weil, *Food Chem.* **2004**, *84*, 551-562.
[67] T.-C. Kuo, R. L. McCreery, *Anal. Chem.* **1999**, *71*, 1553-1560.
[68] M. Hawley, S. Tatawawadi, S. Piekarski, R. Adams, *J. Am. Chem. Soc.* **1967**, *89*, 447-450.
[69] A. N. Patel, S.-y. Tan, T. S. Miller, J. V. Macpherson, P. R. Unwin, *Anal. Chem.* **2013**, *85*, 11755-11764.
[70] H. Mohammad-Shiri, M. Ghaemi, S. Riahi, A. Akbari-Sehat, *Int. J. Electrochem. Sci.* **2011**, 317-336.
[71] E. Popa, H. Notsu, T. Miwa, D. Tryk, A. Fujishima, *Electrochem. Solid-State Lett.* **1999**, *2*, 49-51.
[72] R. Trouillon, Y. Einaga, M. A. Gijs, *Electrochem. Commun.* **2014**, *47*, 92-95.
[73] D. Tryk, H. Tachibana, H. Inoue, A. Fujishima, *Diamond Relat. Mater.* **2007**, *16*, 881-887.
[74] A. Fujishima, T. N. Rao, E. Popa, B. Sarada, I. Yagi, D. Tryk, *J. Electroanal. Chem.* **1999**, *473*, 179-185.
[75] D. Horinek, A. Serr, M. Geisler, T. Pirzer, U. Slotta, S. Lud, J. Garrido, T. Scheibel, T. Hugel, R. Netz, *Proc. Natl. Acad. Sci.* **2008**, *105*, 2842-2847.
[76] J. S. Flier, L. H. Underhill, M. Levine, *New Eng. J. Med.* **1986**, *314*, 892-902.
[77] a) G. Dryhurst, *Biological Electrochemistry, Vol. 1*, Elsevier, **2012**; b) M. R. Deakin, P. M. Kovach, K. Stutts, R. M. Wightman, *Anal. Chem.* **1986**, *58*, 1474-1480.
[78] S. Ono, M. Takagi, T. Wasa, *Bull. Chem. Soc. Jpn.* **1958**, *31*, 356-364.
[79] P. W. Washko, R. W. Welch, K. R. Dhariwal, Y. Wang, M. Levine, *Anal. Biochem.* **1992**, *204*, 1-14.

[80] M. Z. Wrona, G. Dryhurst, *Bioorg. Chem.* **1990**, *18*, 291-317.
[81] M. Z. Wrona, G. Dryhurst, *J. Org. Chem.* **1987**, *52*, 2817-2825.
[82] A. N. Patel, P. R. Unwin, J. V. Macpherson, *Phys. Chem. Chem. Phys.* **2013**, *15*, 18085-18092.
[83] S. A. Mozaffari, T. Chang, S.-M. Park, *Biosens. Bioelectron.* **2010**, *26*, 74-79.
[84] A. G. Güell, K. E. Meadows, P. R. Unwin, J. V. Macpherson, *Phys. Chem. Chem. Phys.* **2010**, *12*, 10108-10114.
[85] B. Sarada, T. N. Rao, D. Tryk, A. Fujishima, *Anal. Chem.* **2000**, *72*, 1632-1638.
[86] B. P. Jackson, S. M. Dietz, R. M. Wightman, *Anal. Chem.* **1995**, *67*, 1115-1120.
[87] P. Bertoncello, I. Ciani, F. Li, P. R. Unwin, *Langmuir* **2006**, *22*, 10380-10388.
[88] G. Gerhardt, R. N. Adams, *Anal. Chem.* **1982**, *54*, 2618-2620.
[89] H. Zare, S. Golabi, *J. Solid State Electrochem.* **2000**, *4*, 87-94.
[90] K.-i. Yamamoto, M. Hiwatari, F. Kohori, K. Sakai, M. Fukuda, T. Hiyoshi, *J. Artif. Organs* **2005**, *8*, 198-205.
[91] A. E. Fischer, Y. Show, G. M. Swain, *Anal. Chem.* **2004**, *76*, 2553-2560.
[92] T. Matusinovic, D. E. Smith, *Inorg. Chem.* **1981**, *20*, 3121-3122.
[93] L. Hutton, M. E. Newton, P. R. Unwin, J. V. Macpherson, *Anal. Chem.* **2009**, *81*, 1023-1032.
[94] R. Boukherroub, X. Wallart, S. Szunerits, B. Marcus, P. Bouvier, M. Mermoux, *Electrochem. Commun.* **2005**, *7*, 937-940.
[95] F. Maier, M. Riedel, B. Mantel, J. Ristein, L. Ley, *Phys. Rev. Lett.* **2000**, *85*, 3472.
[96] H. V. Patten, K. E. Meadows, L. A. Hutton, J. G. Iacobini, D. Battistel, K. McKelvey, A. W. Colburn, M. E. Newton, J. V. Macpherson, P. R. Unwin, *Angew. Chem. Int. Edit.* **2012**, *51*, 7002-7006.
[97] H. V. Patten, S. C. S. Lai, J. V. Macpherson, P. R. Unwin, *Anal. Chem.* **2012**, *84*, 5427-5432.
[98] C. A. Gunawan, M. Ge, C. Zhao, *Nat. Commun.* **2014**, *5*.

Chapter 7

Particle Translocation through a Single Crystal Diamond Pore Fabricated by Electron Beam Induced Chemical Etching

7.1 Overview and Key Advances to Knowledge in this Chapter

Pore-based sensing devices are currently a hot topic in the scientific community. Solid-state pore devices facilitate single molecule/particle sensing by monitoring the change in conductance current as an analyte is electrophoretically driven through a pore fabricated in an insulating material. The simplicity and versatility of the technique offers enormous potential for a wide range of biosensor applications in numerous fields, such as healthcare, biosecurity, and environmental monitoring. A fundamental challenge for pore-based biosensors is reaching sufficiently high signal-to-noise ratios in order to resolve the spatial and temporal dimensions required to detect small molecule *e.g.* DNA sequencing. Single crystal diamond is an ideal platform material for pore technologies as it is robust, amenable to microfabrication, chemically inert, and has a high resistivity and low dielectric constant that would enable extremely fast, low noise measurements. There are currently no single crystal diamond pore devices in existence, so the development of a diamond pore device in this chapter is wholly new and original to the field.

In this work, individual sub-micron pores were fabricated, for the first time, in single crystal diamond, and proof-of-concept experiments were performed to demonstrate the capability of the diamond pores to sense particle events. The diamond pores were fabricated using a novel two-step protocol employing laser micromachining and electron beam induced chemical etching (EBIE) to expose the pore. The pores were observed to be conical, high aspect ratio and produces expected electrochemical *i-V* responses. Each pore was accessed through a large-scale microcapillary setup and polystyrene (PS) particle blockade events were captured through a single diamond pore. Analysis of the events revealed different type of pore-particle interactions *e.g.* instantaneous, direct translocation, inhibited translocation.

The results of this chapter are fundamental in revealing the potential of single crystal diamond in pore devices to the scientific community, and it is hoped that they encourage the community to consider using diamond in pore devices in the future. The detection of PS particles through diamond pores demonstrates to the scientific community that single crystal diamond can feasibility sense molecules, and with low noise due to its exceptional electronic properties, it has enormous potential to advance the field. The different pore-particle events observed advance knowledge of diamond-PS particle interactions. This is the first time individual high aspect ratio pores in single crystal diamond have been fabricated, providing a new structure to the diamond community. The novel EBIE etching technique used to fabricate the diamond pores is an entirely new methodology to the field and has potential in the future for controlled etching of the diamond surface in various applications. The development of single crystal diamond pores paves the way for a wide range of future diamond sensing applications, and has enormous potential in the future to reach pore-based DNA sequencing.

7.2 Introduction

Detecting events at the single particle (and ultimately molecule) level, on very short time scales is a fundamental challenge in the scientific community. One approach to the problem is the use of solid-state micro-pores, as employed in traditional Coulter counters (sub-micron to millimeter sized pores),[1] or, as employed more recently, nanopores.[2] These sensors operate in real-time and rely on the measurement of changes in conduction current as the analyte (particle or molecule) passes through the pore. The amplitude, shape, duration and frequency of each translocation event can provide unique information about an individual analyte such as size, speed and relative population.[3] The dimension of the smallest constriction of the pore controls the maximum size of molecules/particles that can pass through for detection. Highly sensitive electronics allows detection of very small changes in the conduction current, facilitating high-resolution size discrimination. The simplicity of the concept linked with the versatility of the method had led to the use of solid-state pores for a wide range of applications involving micro- and nano- sized particles,[4] polymers,[5] and proteins.[6] The capability of the technology to facilitate rapid and direct evaluation of individual DNA bases has made it particularly attractive for next-generation DNA sequencing.[7]

The choice of substrate material in which the pore is placed is critical for the stability and sensing capability of the device. In order to facilitate low noise and fast data acquisition experiments over the widest range of analytes the material should ideally have: (i) a high electrical resistivity and low dielectric constant; (ii) chemical stability in a wide range of solvents and; (iii) must be amenable to processing such that single pores of a known geometry can be reproducibly fabricated at the single pore level. It is for the latter reason why lipid bilayers containing a single biological

protein such as α-hemolysin[8] or MspA[9] of a fixed and known geometrical dimension are often used in combination with solid-state micro-pores. However, identifying short (μs) events remains technically challenging (due to bandwidth constraints) and biological devices suffer from poor stability[10] and complex manufacturability.[11]

To-date various materials have been employed to produce micro- and nano-pores, including silicon nitride,[12] glass,[13] aluminum oxide,[14] graphene,[15] and track etched polymer foils,[16] using a range of fabrication methodologies, typically involving electron beam or focused ion beam (FIB) milling.[17] The thickness of the pore is often an important consideration, for example for sequencing of long chain molecules such as DNA, single-base discrimination requires high spatial resolution that is provided by low aspect ratio pores,[2] such as atomically thin graphene.[15] In contrast, investigation of pore-particle translocation dynamics is suited to pores where the length of the pore is greater than that of the analyte to facilitate enhanced time resolution and longer event signals.[18] Consideration of the platform material and fabrication methodology is therefore crucial to fabricate pores of appropriate dimensions for analyte detection.

One material that has received little attention to-date but has properties which make it ideal for micro- and nano- pore particle translocation measurements is diamond. Diamond is chemically stable and durable offering extremely high resistance to chemical attack in strong acid and alkali solutions,[19] allowing treatments to be applied to clean the pore without changing the geometry or degrading the structure. This is highly advantageous as the pores get smaller in size, as devices often fail due to analytes irreversibly blocking the pore.[20] Moreover, diamond surfaces are not prone to hydration “swelling” phenomenon, as found with silicate-

based structures, *e.g.* glass and quartz,[21] changing the geometrical properties of the pore. Diamond is also robust, amenable to microfabrication techniques, and can be easily modified between hydrophilic (O-terminated) and hydrophobic (H-terminated) surface functionalization for enhanced chemical selectivity.[22] Furthermore, the optical transparency of diamond offers the potential for dual optical-conductance sensing.[23] In single crystal form, diamond has a very high resistivity in the insulating state (10^{13} – 10^{16} Ωcm), a very low dielectric constant (5.7) and a low dielectric loss tangent (< 1 x 10^{-5} at 30 – 150 GHz),[24] making it near ideal for fast, low noise current-time measurements, compared to other materials. This means diamond should not require further surface modification to reduce overall dielectric noise, unlike materials such as silicon nitride, which often require coating with materials such as polydimethylsiloxane (PDMS).[25]

There are no reports in the literature for the formation of individual micro- or nano- pores which span a single crystal diamond substrate.[26] The main method involves the use of annealing nickel (or carbon soluble metal) nanoparticles on a diamond surface to locally remove carbon and produce etch pits into the upper surface of diamond as shown in **Figure 7.1**. Pore density is very high (**Figure 7.1**) and no pores are produced which span the entirety of the diamond film, thus making the pores unsuitable for particle translocation measurements.[26] Masuda and coworkers reported a method for fabrication of sub-micron through-hole diamond pores using oxygen plasma etching through a porous alumina mask.[27] However, the dense array renders the material microporous making it unsuitable for particle translocation studies. Furthermore, these studies focus primarily on the use of polycrystalline diamond which is far from optimal due to its inferior electrical properties, reduced physical properties due to grain boundaries and lack of optical defects that can be

leveraged for sensing,[28] compared to single crystal diamond. Moreover, contamination from amorphous and sp^2 carbon, often inherent in polycrystalline diamond unless growth conditions are carefully controlled, will increase the capacitance of the diamond causing increased dielectric noise in particle transduction measurements.[29]

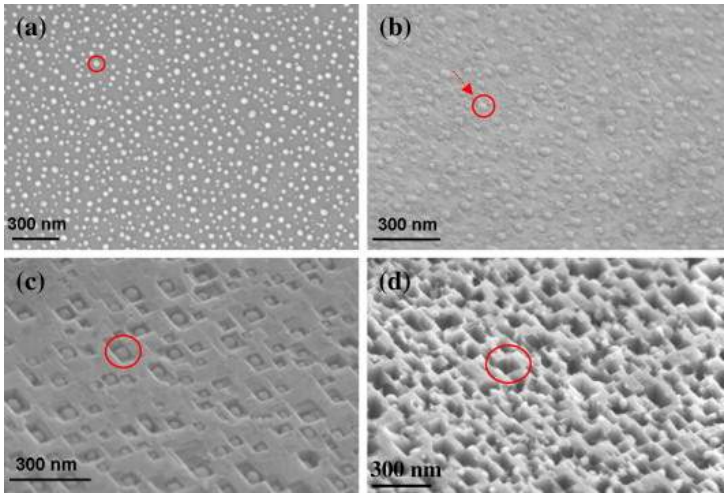

Figure 7.1*: SEM images of a porous polycrystalline diamond surface created by etching with Ni nanoparticles after (a) 30 s, (b) 3 min, (c) 10 min, and (d) 6 hr of annealing at 800 °C.*[26a]

In this work, we demonstrate a new methodology for the fabrication of single sub-micron pore structures in freestanding single crystal diamond, and show how such structures can be employed to investigate polymeric particle translocation.

7.3 Experimental Methods

7.3.1 Solutions

All solutions were prepared using Milli-Q water (Millipore Corp., UK) with a resistivity of 18.2 MΩ at 25 °C that was filtered through a 0.22 μm syringe filter (Millex® filter units, Millipore Corp). 0.1 M KCl (Sigma-Aldrich, USA) solutions were prepared for electrochemical characterization of the diamond pores. For the

particle translocation experiments, PS particles of mean 800 nm diameter (Sigma-Aldrich, USA) were dispersed in filtered 0.01 M KCl solution (pH 6.9) containing 0.1 % Triton X-100 (Sigma-Aldrich, US) at a concentration of 10^7 particles ml^{-1}. The diamond substrate was cleaned prior to use in concentrated sulphuric acid (98% H_2SO_4; Sigma Aldrich, US) supersaturated with KNO_3 (Fischer Scientific, UK)[30] and individual pores were cleaned *in situ* by cycling a potential across the pore between −2 and +2 V in 0.5 M $HClO_4$ (Sigma-Aldrich, MO, USA).

7.3.2 Diamond Pore Fabrication

Diamond samples (Element Six, Ascot, UK) were thinned using a laser micromachiner (see Chapter 3, section 3.12.1). The laser micromachining was carried out by Dr. Max Joseph, University of Warwick (see Declaration). Due to the high transparency of the insulating diamond surface, black glass pen was applied evenly to the upper diamond surface to ensure the laser pulse energy was maximally absorbed. This enabled the diamond to be ablated evenly rather than fracturing or being otherwise uncontrollably damaged. A higher laser power (15% attenuation) was required for the initial cut of the diamond surface, while a lower power was sufficient to cut a surface that had already been partially ablated. Hence, the laser power was reduced to 5% attenuation after the first pass and for all subsequent passes to maximize the *z*-resolution of the thinning technique. To maximize the regularity of ablation, the pitch between pulses and lines of pulses were the same (3 μm or ½ of the laser spot size) and the stage speed was kept slow enough (0.3 mm s^{-1}) so that no significant acceleration/deceleration artefacts were observed. A laser frequency of 100 Hz was employed to ensure that the pitch between pulses was 3 μm. To keep the laser spot in focus, for ideal laser ablation, the focal position was moved downwards in line with the depth of material removed with each pass. This depth was monitored

by WLI profiling of the ablated structures after several passes (see Chapter 3, section 3.12.2). This laser process was repeated in sixteen isolated regions per substrate and the final diamond substrate post-trench insertion was imaged using a polarized optical microscope (see Chapter 3, section 3.11.1).

Pores were fabricated by electron-beam induced etching (EBIE, see Chapter 3, section 3.12.4). The fabrication was performed, and EBIE entrance side imaged, using an FEI Nova NanoSEM variable pressure[31] scanning electron microscope (FE-SEM) equipped with a magnetic field-assisted GSED.[32] The diamond pores were fabricated by Dr. Aiden Martin, University of Technology, Sydney (see Declaration). The FE-SEM chamber was filled with water (Milli-Q) vapour to a pressure of 13 Pa to mediate EBIE and suppress charging of the electrically insulating diamond surface. Prior to EBIE, the diamond substrate was coated *ex situ* with a ~ 30 nm graphitic carbon coating to further suppress surface charging during electron irradiation. For the diamond substrate used in this study, eight of the pores were fabricated using a stationary 15 keV, 24 nA electron beam, including pores (1) – (4) described later (see Table 7.2). The diameter of each pore was varied by changing the focal distance of the electron beam relative to the surface, thus controlling the electron irradiation area on the diamond. Two of the pores were fabricated using the same stationary beam method (5 keV, 34 nA electron beam), and one pore using a 10 keV, 33 nA electron beam. Two further pores were fabricated using a focused electron beam rastered across a 500 × 500 nm area using electron beam energies of 15 and 5 keV, respectively.

7.3.3 Diamond Pore Characterisation

Pore cross-sectioning was achieved using focused ion beam (FIB) milling (see Chapter 3, section 3.12.5). The pore was slowly exposed by progressive vertical

slicing using a 5 kV, 10 nC μm^{-2} focused beam of positively charged Ga^+ ions, and monitored *in situ* by backscattered electron (BSE) imaging using a 20 keV electron beam positioned at an angle of 53° relative to the FIB beam. High-resolution images of the EBIE exit side and diamond pore cross-section were acquired using FE-SEM (see Chapter 3, section 3.12.3). For both systems, an in-lens detector was used at electron beam energy between 10 and 20 keV with a working distance of 4 mm. The average depth of each trench was determined using white light interferometry (WLI, Contour GT, Bruker, UK) and the pore entrance-exit areas were measured using thresholding with ImageJ software (US National Institutes of Health). Raman spectroscopy of the diamond substrate was performed using a Renishaw Raman microscope system with 514.5 nm excitation wavelength (see Chapter 3, section 3.11.2).

7.3.4 Particle Characterisation

The hydrodynamic diameters of the PS particles were determined by dynamic light scattering (DLS) (see Chapter 3, section 3.12.6) using Malvern Zetasizer NanoS, and captured by FE-SEM (Zeiss Supra 55 VP) using a 2 keV electron beam and a type II secondary electron (SE2) detector.

7.3.5 Electrochemical Measurements

The custom-built holder was designed in SolidWorks (Dassault Systémes, FR) and fabricated by micro-stereolithography (MSL) by photo cross-linking commercial R11 resin using a Perfactory Mini Multi-Lens system (Envisiontec, DE). Current-voltage (*i*-*E*) responses were made using a potentiostat (CHI730A, CH Instruments Inc., US) connected to a desktop computer. Current-time (*i*-*t*) responses were recorded at a sampling frequency of 100 kHz using a data acquisition (DAQ) card (NI

PCIe-6259, National Instruments, UK) attached to a laptop running custom-built LabVIEW code (LabVIEW 2014, National Instruments, UK). Data was not filtered as the use of the above in combination with a grounded Faraday cage isolated the system from external sources of noise.

7.3.6 Signal Processing

The *i-t* traces were analysed using specially developed MATLAB R2014b (MathWorks Inc., UK) scripts. A schematic of the event analysis protocol is shown in **Figure 7.2** for a section of particle event data. Event minima were identified where the first derivative of the running average (i_{avg}), calculated every 20 ms, was zero. Events were filtered so that those with a prominent height greater than 0.2 nA *i.e.* greater than ~ one standard deviation from the local baseline were considered in the analysis. The start and end points of each event were identified as the first inflection points either side of the peak minima. The local baseline (i_{base}) was defined around each event by averaging ±500 data points either side of the start and end. This method eliminates long-time drift and prevents low frequency noise affecting the data analysis. The blockade height (Δi) was then defined as the difference between the current at the peak minima (i_{min}) and i_{base} for each event. The midpoint of each event was identified as (i_{base} + i_{min})/2 and the duration (τ) calculated by the full-width half maximum method.

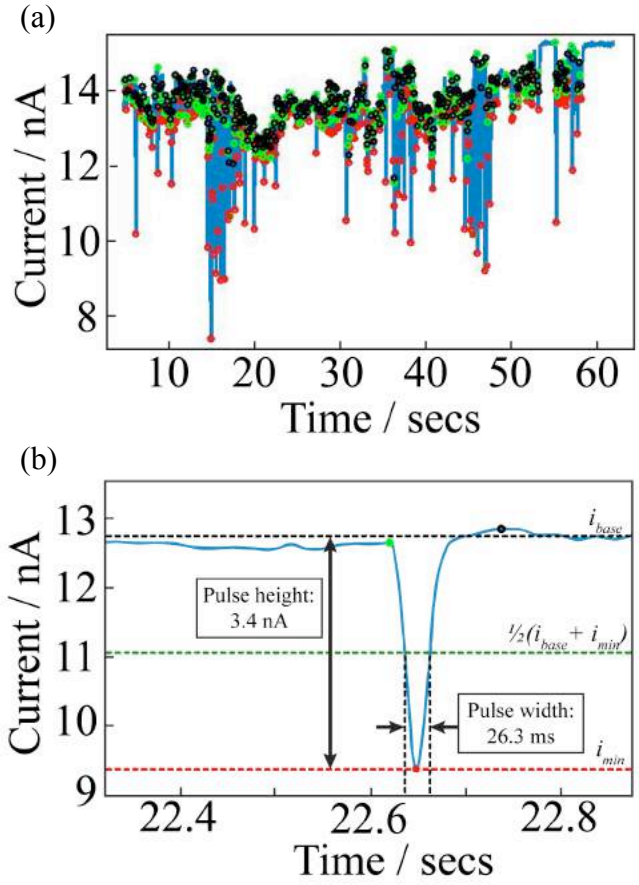

***Figure 7.2**: Schematic of the data analysis protocol to analyse particle-pore blockade events. (a) displays a section of experimental data where the minima of prominent peaks (i_{min}) were identified (red dots) along with their local start (green dots) and end (black dots) values, and (b) displays the analysis of a single particle-pore blockade event. The local baseline i_{base} was identified for each event so that the height and duration could be calculated.*

7.3.7 Finite Element Model (FEM) Simulations

Finite element model (FEM) simulations were employed to estimate the ionic flow through the diamond pore prior to blockade events *i.e.* in absence of particles in the pore, and during blockade events *i.e.* in the presence of a single particle in the pore. This model enabled the open-pore current to be predicted based on the experimental pore geometry. It also enabled the size of the particle within the pore to be predicted for different blockade events by varying the particle geometry to reproduce the experimental blockade current.

The geometry of the pore is shown in **Figure 7.3**a with an illustration of the resulting two-dimensional (2D) axisymmetric model (**Figure 7.3**b). The model consisted of three principle domains, with coordinates *r* and *z*, respectively. The pore was modelled as a truncated cone centered at (*z, r*) = (0,0) μm and assuming circular geometry of the entrance and exit apertures. For the PS particle experiments, a semicircle of varying radii was placed on the axial boundary centered at (0,0) to model a spherical particle within the pore. The specific dimensions of the pore (and particle) are outlined where used in the results (section 7.4). Two external rectangular domains either side of the pore were extended to z_d = 30 μm and r_d = 4.8 μm, to represent the surrounding solutions. The size of the domain was chosen to achieve bulk characteristics at the furthest domain boundaries whilst maintaining a small enough model to minimise computational time to < 10 minutes.

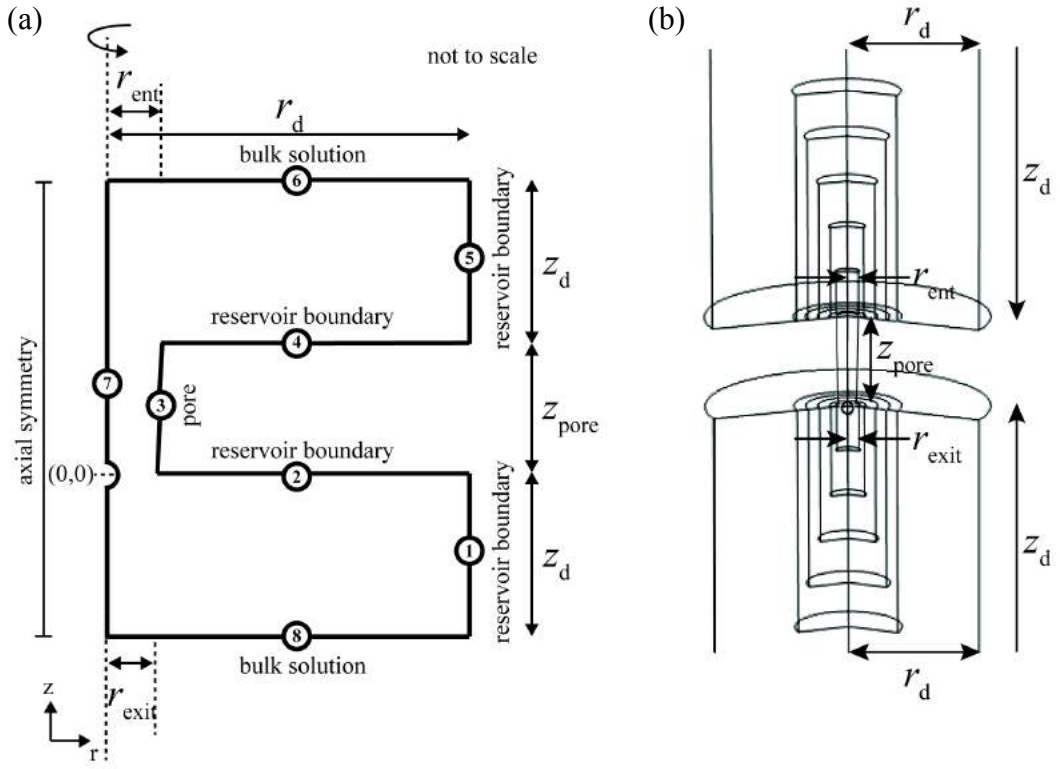

***Figure 7.3**: Schematic of (a) the 2D simulation domain and (b) the 3D axial symmetric system displaying a central pore of lengths z_{pore} and entrance/exit radii r_{ent} and r_{exit} surrounded either side by two domains of the lengths z_d and r_d with subdomains to facilitate meshing.*

Triangular mesh elements were used with the greatest mesh resolution within the pore. Additional rectangular domains of incrementing size were placed either side of the pore to enable a gradual increase in the mesh element size using a growth rate of 1.1 × per element away from each sub-boundary towards a maximum element size of 0.2 μm in bulk. The total mesh consisted of 497,976 elements and the simulation was solved to obtain a stationary solution using the PARDISO solver in COMSOL. The ionic flux through the pore was calculated using the Nernst-Planck equation that describes the motion of a charged species in solution when an electric potential difference is applied across the solution:[33]

$$\mathbf{J}_i = -D_i \nabla c_i - \frac{z_i F}{RT} D_i c_i \nabla \phi + c_i \mathbf{v} \tag{7.2}$$

where $\mathbf{J}_i$, D_i, c_i, z_i and u_i represent the ionic flux vector, diffusion coefficient, concentration, charge and mobility of species i (K^+, Cl^-), F is Faraday's constant (96485 C mol^{-1}), R is the gas constant (8.314 J K^{-1} mol^{-1}), T is the temperature (293.15 K) and Φ is the local electric potential (−1 – +1 V for *i-E* measurements, 0 – 200 mV for pore-particle measurements). The three terms on the right hand side of Equation 7.2 represent contributions from diffusion (Fick's first law, see Chapter 3, equation 3.3), migration due to the influence of the applied electric field and convection, respectively (see Chapter 3, section 3.6). In this system, convection was assumed absent so the velocity field was set to zero ($\mathbf{v}$ = 0) leaving the remaining diffusion and migration contributions.

The particle and pore surfaces were assumed to be uncharged insulating boundaries ($\mathbf{J}_i = 0$). The solution parameters were chosen to represent 0.01 M KCl for pore-particle measurements at 298 K (or scaled accordingly for 0.1 M used in *i-E* measurements) using D_{K+} = 1.957 × 10^{-9} m^2 s^{-1},[34] c_{K+} = 0.01 M, z_{K+} = +1, u_{K+} =

7.89 s mol kg^{-1},[35] $D_{Cl-} = 2.032 \times 10^{-9}$ m^2 s^{-1},[34] $c_{Cl-} = 0.01$ M, $z_{Cl-} = -1$ and $u_{Cl-} = 8.20$ s mol kg^{-1}.[35] The model was used to obtain a stationary solution for the ionic flux through the pore by solving equation 7.2 subject to the boundary conditions outlined in **Table 7.1**. The ionic fluxes $\mathbf{J}_{K+}$, $\mathbf{J}_{Cl-}$ were calculated along the horizontal line through (0,0). The ionic current, i_p, due to the presence of a particle in the pore was then calculated using the equation:

$$i_p = (\mathbf{J}_{K+} - \mathbf{J}_{Cl-})F \tag{7.3}$$

where i_p relates to the current due to the flow of K^+ and Cl^- species. All FEM simulations were performed using COMSOL Multiphysics 4.4 (COMSOL AB, SE).

***Table 7.1**: Summary of the boundary conditions used for the simulation of ionic flux through a pore, where r_d is the domain width of 30 μm, z_d is the domain height of 4.8 μm, r_{exit} is the radius of the pore exit, r_{ent} is the radius of the pore entrance, z_{pore} is the thickness of the pore, c_b is the bulk concentration (0.1 M or 0.01M) of species i in solution, and* **n** *the unit normal vector. The pore and particle dimensions are described where used in the results (section 7.4).*

Boundary	Boundary Type	Coordinates (r,z) / μm	Equation
1	Reservoir Boundary	$(r_d, -(z_d + ½ \times z_{pore})) - (r_d, -½ \times z_{pore})$	$0 = \nabla c \cdot \mathbf{n}$
2	Reservoir Boundary	$(r_d, -½ \times z_{pore}) - (r_{exit}, -½ \times z_{pore})$	
3	Pore	$(r_{exit}, -½ \times z_{pore}) - (r_{ent}, ½ \times z_{pore})$	
4	Reservoir Boundary	$(r_{ent}, ½ \times z_{pore}) - (r_d, ½ \times z_{pore})$	
5	Reservoir Boundary	$(r_d, ½ \times z_{pore}) - (r_d, (z_d + ½ \times z_{pore}))$	
6	Bulk solution	$(r_d, (z_d + ½ \times z_{pore})) - (0, (z_d + ½ \times z_{pore}))$	$c_i = c_b$
7	Axis of symmetry	$(0, (z_d + ½ \times z_{pore})) - (0, -(z_d + ½ \times z_{pore}))$	$0 = \nabla c \cdot \mathbf{n}$
8	Bulk solution	$(0, -(z_d + ½ \times z_{pore})) - (r_d, -(z_d + ½ \times z_{pore}))$	$c_i = c_b$

7.4 Results and Discussion

7.4.1 Diamond Trench Formation

Prior to pore formation, it was necessary to fabricate thin (< 5 μm thick) trenches in the starting single crystal diamond substrate, as outlined in **Figure 7.4**a.

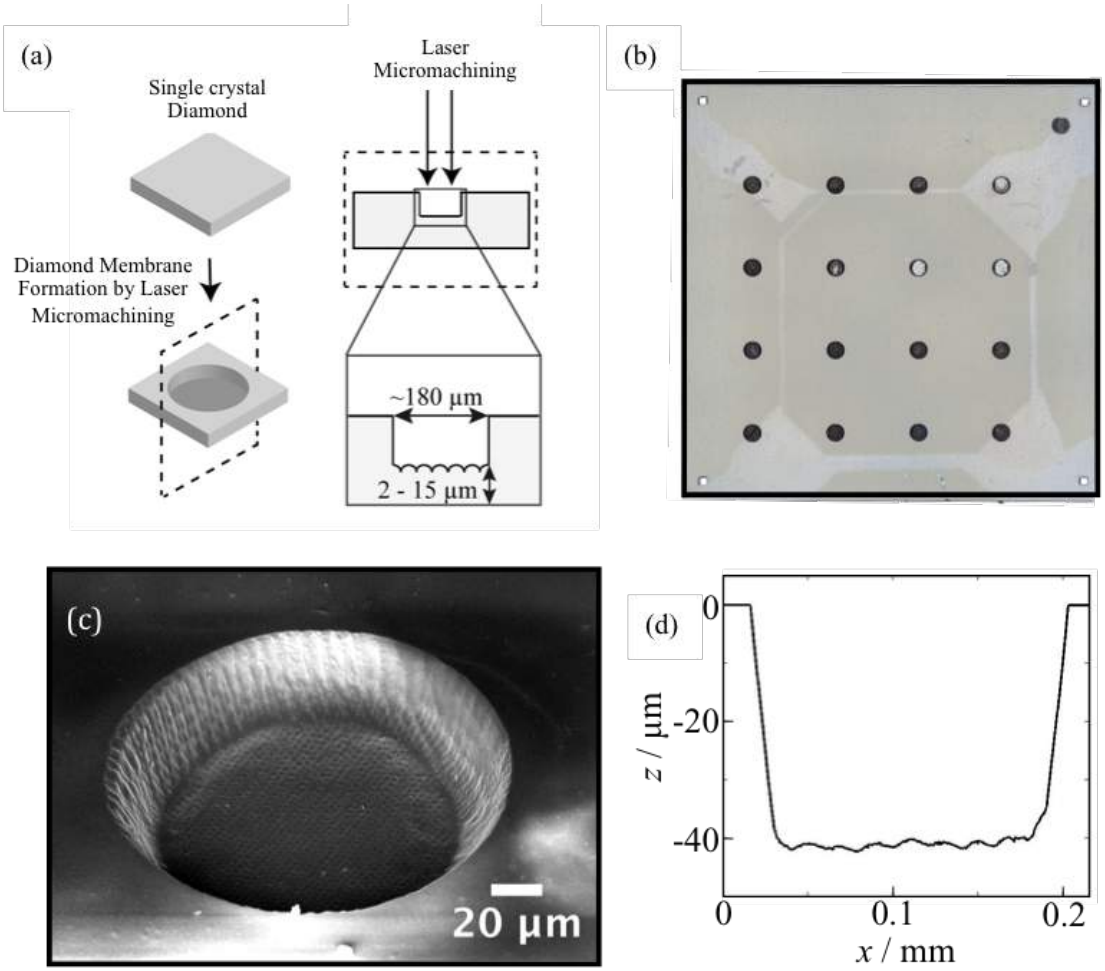

***Figure 7.4**: Fabrication of an array of circular trenches supported in a single crystal diamond substrate using laser micromachining. (a) Illustration of the laser micromachining procedure for trench formation. (b) Optical image of a single crystal diamond substrate post-insertion of sixteen lasered trenches. Characterisation of a single lasered trench by (c) FE-SEM displaying the rastered cross-hatch laser path and (d) WLI cross-sectioning to assess surface roughness.*

The starting material, thin (50 ± 3 µm laser cut to size ~ 4 × 4 mm) plates of high pressure, high temperature (HPHT) single crystal (100) insulating diamond, polished to < 5 nm roughness on both sides (Element 6, UK) were first laser micromachined (E-355H-3-ATHI-O, Oxford Lasers, UK) to create isolated circular trenches of diameter ~ 180 µm and depth 35 – 48 µm, as illustrated in **Figure 7.4**a. The laser micromachining was performed by Dr. Max Joseph, University of Warwick (see Declaration). Depth control during the thinning procedure was achieved by

modulating the frequency, stage speed, attenuator percentage and the pitch between the lines and laser pulses, as described in more detail in the experimental (section 7.3.2). **Figure 7.4**b displays an optical image of a typical diamond substrate post-trench insertion. In total on the substrate (of size 4.38 × 4.48 mm), sixteen isolated circular trenches were fabricated of diameter ~ 180 μm and average thickness of 1.9 – 4.4 μm with roughness 1 – 2 μm, (inner face) and < 5 nm (polished outer face), measured by WLI. A typical FE-SEM image of a lasered trench is shown in **Figure 7.4**c. Here, the rastered cross-hatch pattern formed by several laser passes can be clearly observed. **Figure 7.4**d displays a WLI cross-section of an ablated trench, with clear undulations on the inner surface of ~ 1 μm roughness produced by the laser path.

Figure 7.5 shows Raman spectra for a non-lasered region of the diamond substrate and a region of a laser ablated trench fabricated in the same substrate.

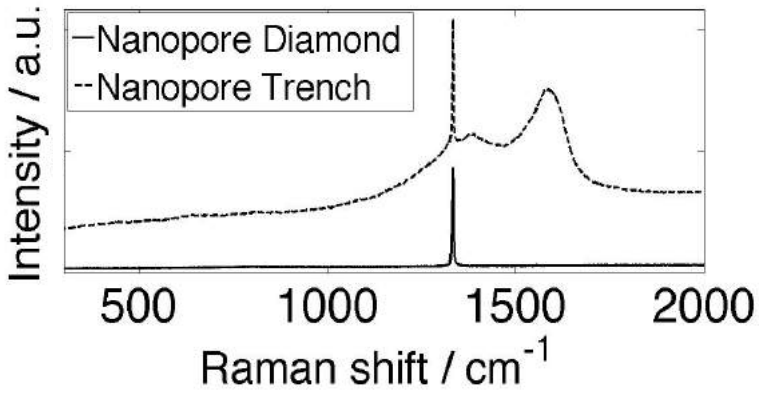

Figure 7.5*: Raman spectra of a non-lasered region of the diamond substrate (-) and a region of a laser ablated trench fabricated in the same diamond substrate (--).*

A single, sharp peak at 1332 cm^{-1} was observed in both spectra that is characteristic of single crystal diamond (**Figure 7.5**). In addition, the diamond laser ablated trench (dashed black line) displayed an additional "G" peak at 1575 cm^{-1} characteristic of the presence of sp^2 carbon within the trench. This suggests that graphitic carbon residue is left within the pore from laser treatment that cannot be

removed by the standard acid cleaning protocol. As diamond can withstand harsh chemical treatments and it is suggested that future devices should look towards better cleaning strategies, for example etching the surface post fabrication of the pore.

7.4.2 Diamond Pore Formation

A single pore was inserted into each trench using gas-mediated electron beam induced etching (EBIE),[36] as illustrated in **Figure 7.6**a. The EBIE etching was carried out by Dr. Aiden Martin, University of Technology, Sydney (see Declaration).

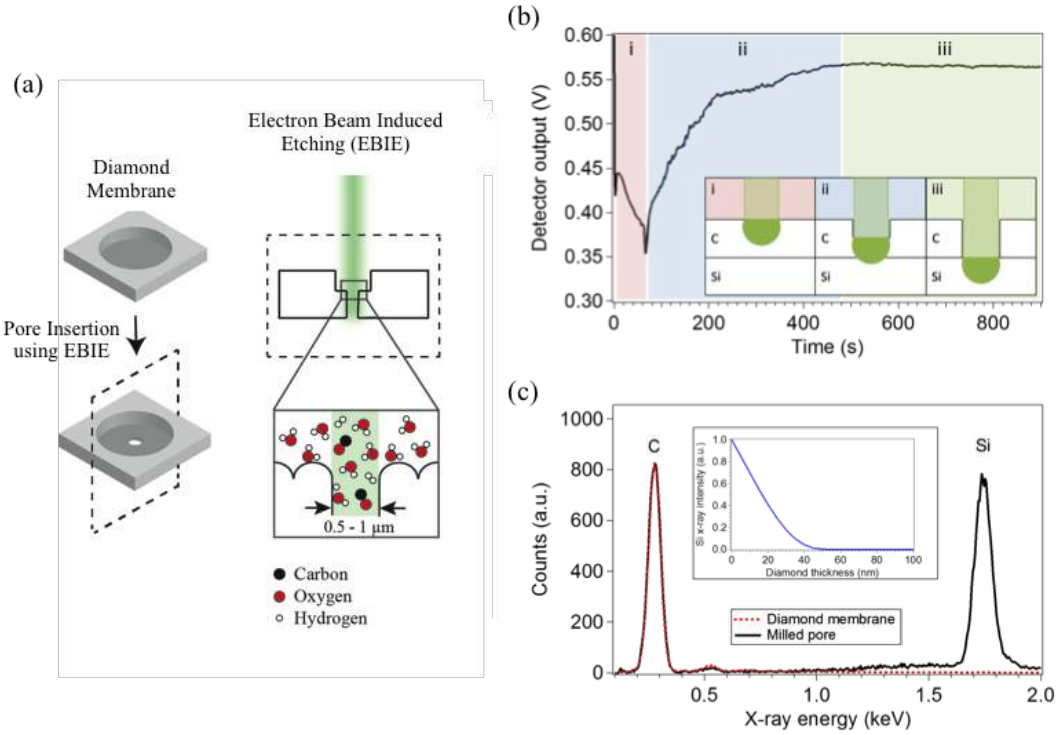

***Figure 7.6**: Single crystal diamond pore fabrication using water-mediated electron beam induced etching (EBIE). (a) Illustration of the EBIE fabrication procedure. (b) In situ endpoint monitoring of pore formation during EBIE pore fabrication. (c) EDS spectra acquired using a 3 keV electron beam. The diamond substrate is mounted on silicon. When the electron beam irradiates a pore-free diamond trench (-) no signal from the underlying silicon is detected, however when a trench containing a pore is irradiated (-), silicon X-rays are detected confirming complete penetration through the diamond. Inset: Intensity of X-rays generated in the underlying silicon as a function of diamond over layer thickness simulated for a 3 keV electron beam using the Monte Carlo package CASINO.*

EBIE is a nanoscale, direct-write technique. The main advantage of EBIE over conventional electron-beam or FIB milling is the elimination of sputtering, material graphitization and ion implantation during processing, as well as greater material selectivity.[37] The method proceeds through a dry-chemical process where gaseous precursor molecules (here, H_2O) decompose on the diamond surface leading to oxygen termination. Simultaneously, the surface is irradiated by an electron beam which breaks C–C bonds resulting in desorption of a surface carbon and oxygen atom as CO, leaving a void in the substrate.[38] This procedure is simpler than current methodologies that typically involve several preparatory stages and post-fabrication modifications.[11] The diamond substrate was mounted on silicon for stability. Pore formation was monitored using *in situ* endpoint detection[39] by measuring the gaseous secondary electron detector (GSED) output voltage during etching, as shown in **Figure 7.6**b. The GSED voltage initially drops as etch pit formation initiates, and electrons are contained wholly within the diamond substrate (**Figure 7.6**bi). As the electron beam penetrates into the underlying silicon, the GSED output voltage increases (**Figure 7.6**bii), until diamond material is completely etched in the region irradiated by the electron beam, and the GSED output voltage saturates (**Figure 7.6**biii).

After etching, the pores were characterized *in situ* in the FE-SEM by energy-dispersive X-ray spectroscopy (EDS) to confirm pore formation (**Figure 7.6**c). At low electron beam energies, the depth at which X-rays are generated in the material is very shallow. For diamond on silicon, when the thickness of diamond is less than the electron penetration range and the electron beam energy is greater than the critical ionization energy (Si K 1s = 1.84 keV),[40] X-rays will be generated in the underlying silicon. The intensity of the X-rays generated was determined as a function of

diamond thickness at an electron beam energy of 3 keV, using the Monte Carlo simulation package CASINO.[41] The simulations show X-rays are generated in the underlying silicon when the diamond thickness is less than ~ 50 nm (**Figure 7.6**c inset). Hence, X-ray spectra measured using a 3 keV electron beam can be used to show with confidence that etch pits in diamond have been milled down to at least 50 nm from the underlying silicon. When the fabricated pores were examined by EDS (using a 3 keV electron beam), all pores exhibited a detectable silicon X-ray signal. EDS examination of both a non-lasered region of the diamond substrate and a pore-free trench did not reveal any detectable silicon X-ray signal.

Further confirmation was made using conventional FE-SEM to image both surfaces of the trench containing a single pore. **Figure 7.7**a – di and ii show FE-SEM images of the entrance (inner surface) and exit (outer surface) apertures of four EBIE single crystal diamond pores, respectively. The entrance-exit FE-SEM images (of 42 pores in total) were all in the range of 0.5 – 1 μm diameter (for trench thicknesses in the range 2 – 15 μm) with the entrance side of similar shape to the exit. This highlights that the EBIE method can produce individual sub-micron sized pores of ~ 3 μm thickness in single crystal diamond with fairly reproducible entrance-exit size characteristics.

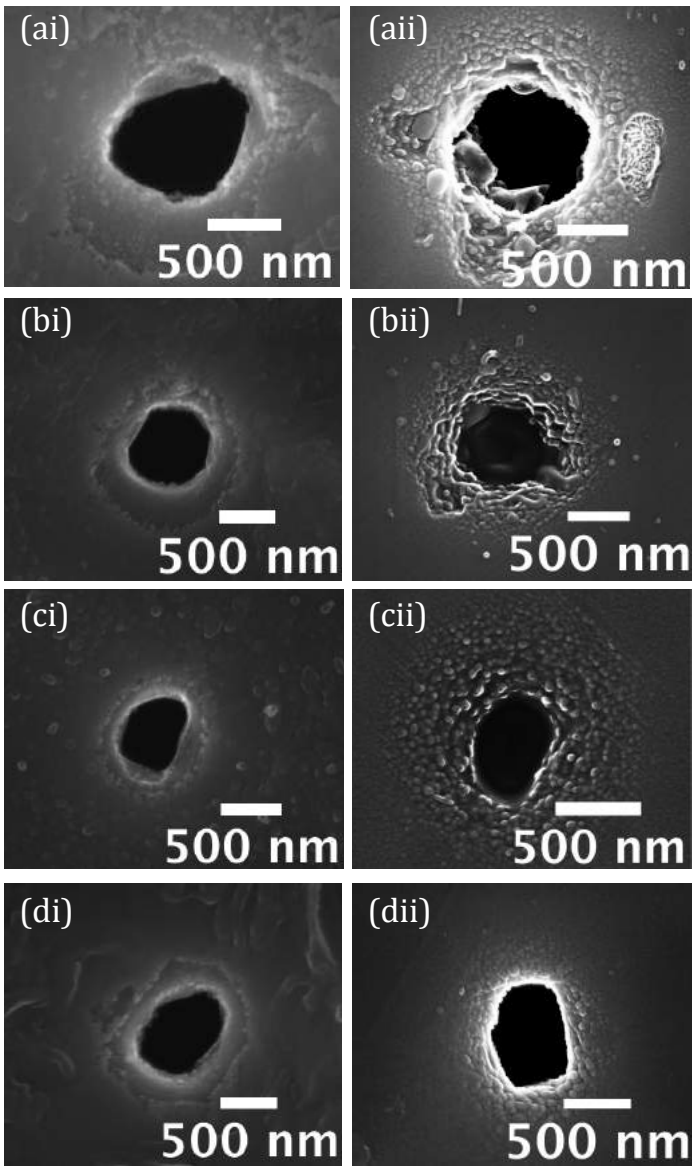

***Figure 7.7**: (a) – (d) FE-SEM images of single crystal diamond pores fabricated by EBIE with (i) entrance and (ii) exit apertures. (a) corresponds to pore (1) used for particle experiments. Each pore displays similar size and shape characteristics.*

The dimensions of four EBIE pores are detailed in **Table 7.2**, of which pores (1) – (2) correspond to images (a) – (b) in **Figure 7.7**, respectively. Typically, the area of the entrance is only slightly larger than the area of the corresponding exit aperture, as measured using pixel thresholding (ImageJ, US National Institutes of Health).

***Table 7.2**: Dimensions of four diamond EBIE pores calculated from microscopy and electrochemical (i-V) data. Pores 1 – 2 correspond to images a – b in Figure 7.7. The exit side for pore 4 could not be imaged, although the predicted area based on the pore conductance suggests it is of similar dimensions to the entrance. [a)]Measured by interferometry; [b)]Measured from SEM images; [c)]Calculated form i-E response (see Figure 7.10), [d)]Calculated from FEM simulation (see section 7.4.3.1 for details).*

Pore	Trench Thickness (*L*) [μm][a)]	Trench surface roughness (Root mean squared) [μm][a)]	Diameter of pore entrance [nm][b)]	Diameter of pore exit [nm][b)]	Experimental Current @ + 1 V [μA][c)]	Theoretical Current @ + 1 V [μA][d)]
1.	3.0 ± 0.50	0.50	789.7 ± 15.5	777.6 ± 10.0	0.17	0.17 ± 0.05
2	3.5 ± 0.64	0.64	729.6 ± 17.9	714.5 ± 19.7	0.15	0.13 ± 0.04
3.	2.0 ± 0.82	0.82	450.5 ± 9.1	440.2 ± 16.4	0.09	0.08 ± 0.04
4.	7.2 ± 0.62	3.94	454.2 ± 10.9	–	0.03	0.03 ± 0.01

To elucidate the sub-surface pore geometry, a cross-section of a typical diamond pore within an isolated trench was created using FIB milling, as shown in **Figure 7.8**a. The sensing capability of the device is dependent on the smallest constriction within the pore. The cross-section in **Figure 7.8**b displays a conical geometry through a representative diamond pore.

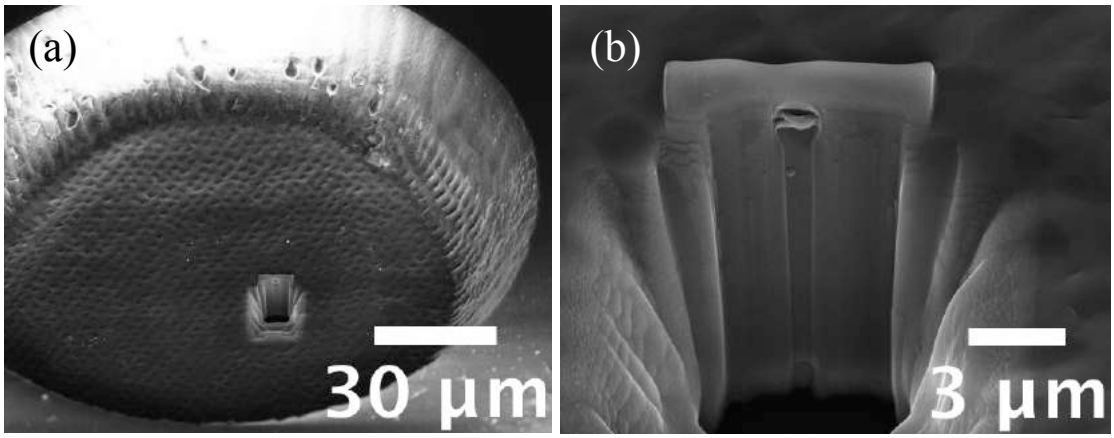

***Figure 7.8**: FE-SEM images of (a) the lasered trench from which an individual pore was accessed by focused ion beam (FIB) milling and (b) the resulting pore cross-section obtained that displays the conical geometry.*

The pore that was cross-sectioned is of dimensions 1.40 μm (diameter of entrance side) × 0.48 μm (diameter of exit side) × 12.48 μm (thickness). The thickness of the pore renders it to be very high aspect ratio *i.e.* of thickness-to-diameter aspect ratio of 26, where low aspect ratios are defined as less than 0.1.[42] The EBIE entrance side displays larger dimensions to the exit, and a decreasing conical channel is observed through the pore (in this case, of conic angle 2.1° relative to the axis through the center of the pore). This geometry can be justified by consideration of the EBIE etching mechanism. As EBIE proceeds into the substrate, electrons scattered from the primary irradiation area give rise to broadening of the pore entrance. This broadening continues until the pore reaches a depth where electron penetration at the substrate surface is dampened, eliminating lateral etching. The conical shape within the pore is caused by a change in the focal point of the electron beam in relation to the surface during EBIE. The electron beam is initially under focused and approaches the focal point as etching proceeds. Slight broadening may occur at the EBIE exit side due to scattered electrons penetrating through the exit giving rise to material removal outside the primary irradiation area. However, this was not observed in the pore cross-sectioning (**Figure 7.8**b) suggesting the effect is minimal leaving the pore to attain an overall conical shape. Understanding sub-surface pore geometries is critical in analysing particle translocation events, as it is the smallest constriction in the structure that controls the maximum size of particle that can translocate through the pore.

7.4.3 Conductance Measurements using Diamond Pores

7.4.3.1 Open Pores

Individual pore solution conductance was measured using a large-scale micro-capillary setup,[43] as shown in **Figure 7.9**. This is the first time that the conventional large-scale micro-capillary setup for accessing microscale regions of surfaces has been extended to facilitate flow through pores. The technique involved fabrication of a novel holder that submerged one side of the substrate in electrolyte solution, whilst the other side is wet by the micro-capillary (**Figure 7.9**a).

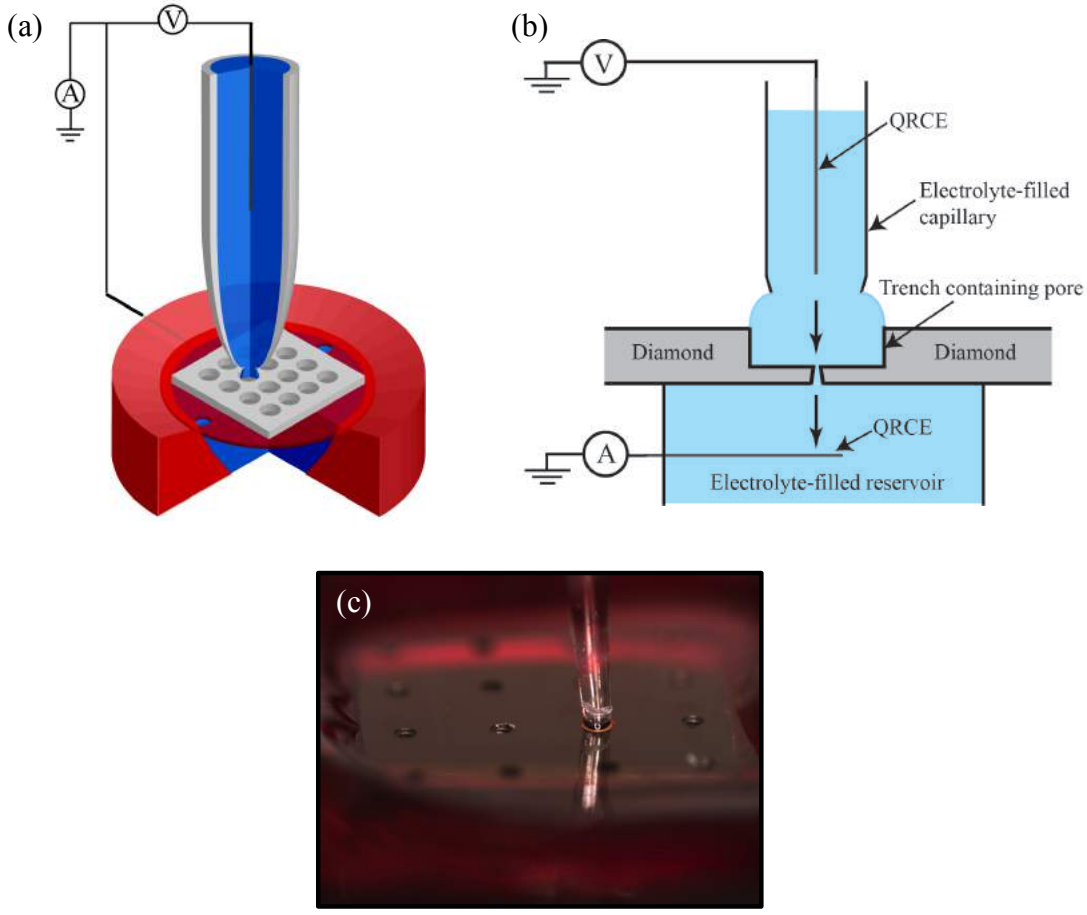

***Figure 7.9**: (a) Schematic of the electrochemical setup for diamond pore experiments. The diamond substrate was mounted in a specialised holder and a ~ 200 μm glass micro-capillary, filled with the solution of interest, positioned so that the meniscus wets an individual trench containing a single pore. (b) Illustration of the large-scale micro-capillary method for single pore investigation. A potential is applied between two Ag/AgCl quasi-reference counter electrodes (QRCEs) positioned above and below the substrate to facilitate electrochemical studies through an individual pore. (c) Snapshot from a camera of the micro-capillary positioned to contact the solution meniscus with an individual trench in the diamond substrate.*

The diamond substrate was mounted in a custom-built flow cell fabricated by micro-stereolithography (MSL) by photo cross-linking commercial R11 resin,[44] shown in **Figure 7.9**a. The cell was designed with three essential features; (i) a central hole fabricated to the exact dimensions of the diamond substrate with a thin 100 μm lip for the substrate to slot into; (ii) a circular reservoir with inlet/outlet channels to allow back-filling with solution and removal of any air bubbles beneath the substrate; and (iii) a side channel for insertion of a AgCl-coated Ag wire (Ag/AgCl) serving as a quasi-reference counter electrode (QRCE) into the reservoir solution. The base of the MSL cell was sealed with optically clear quartz to allow visual monitoring of air bubble formation within the reservoir. All components were sealed into place using epoxy adhesive to ensure a leak-free device and the reservoir filled with solution so that all sixteen pores in the diamond single crystal substrate were wetted and filled with solution from the pore exit facing side. Note that this arrangement enabled solution to be confined to individual pores.

In order to electrochemically interrogate an individual pore the microcapillary electrochemical method,[45] as illustrated in **Figure 7.9**b, was used to deliver solution to an individual trench (and hence pore structure) and electrically connect the circuit by providing a second QRCE. Briefly, a glass borosilicate capillary was pulled and polished to an inner diameter of 200 μm. The microcapillary and holder reservoir were filled initially with a 0.1 M KCl solution and an Ag/AgCl QRCE was inserted into the microcapillary channel. The microcapillary was positioned using *x-y-z* micropositioners and a high magnification camera so that the meniscus wetted an entire circular trench, as shown in **Figure 7.9**c. All measurements were made in a two-electrode setup (see Chapter 3, section 3.7) where a potential difference was applied between the Ag/AgCl QRCEs placed either side of the diamond substrate to

facilitate ionic conductance current through the pore. By simply repositioning the microcapillary over individual trenches it was possible to make ion conductance measurements on a pore-by-pore basis.

The current-voltage (*i-E*) characteristics in the ±1 V range for four independent diamond pores, fabricated by EBIE are shown in **Figure 7.10**.

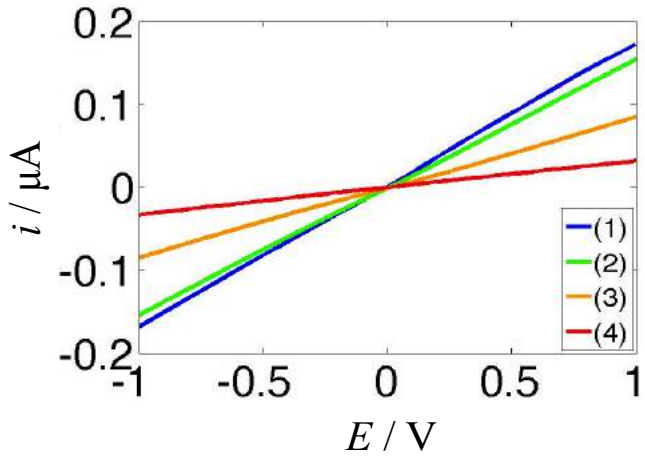

***Figure 7.10**: i-E curves from four single crystal diamond pores fabricated by EBIE. The dimensions and predicted i-E response for each pore are displayed in Table 7.2.*

All pores displayed linear *i-E* responses with no evidence of ionic current rectification[46] or electrostatic gating[47], which is as expected for pores of this (~ μm) size. The dimensions of the four representative pores that produce the *i-E* curves in **Figure 7.10** are outlined in Table 7.2, labelled 1 – 4 accordingly. FEM simulations were employed to match the pore geometry to the theoretical *i-E* response (details of the model can be found in section 7.3.7). The four pores used in **Figure 7.10** were modelled based on the measured dimensions in Table 7.2. The expected conductance current at an applied potential of +1 V was determined and compared to the corresponding experimental *i-E* response at that potential (**Figure 7.10**). Close agreement was observed between the predicted and experimental current through the

different sized diamond pores (see Table 7.2) confirming that the observable pore dimensions and conical sub-surface geometry is representative.

7.4.3.2 Polystyrene (PS) Particle Translocation

To assess the detection capability of the diamond pores, PS particles were electrophoretically driven through an individual pore. The PS particles, imaged by FE-SEM in **Figure 7.11**, had a size distribution of 800 ± 471 nm as measured by dynamic light scattering (DLS, **Figure 7.11**) and were negatively charged, displaying a negative zeta potential at the electrolyte pH (pH = 6.9)[4b, 48] due to the presence of sulphate groups bound to the polymer chain.

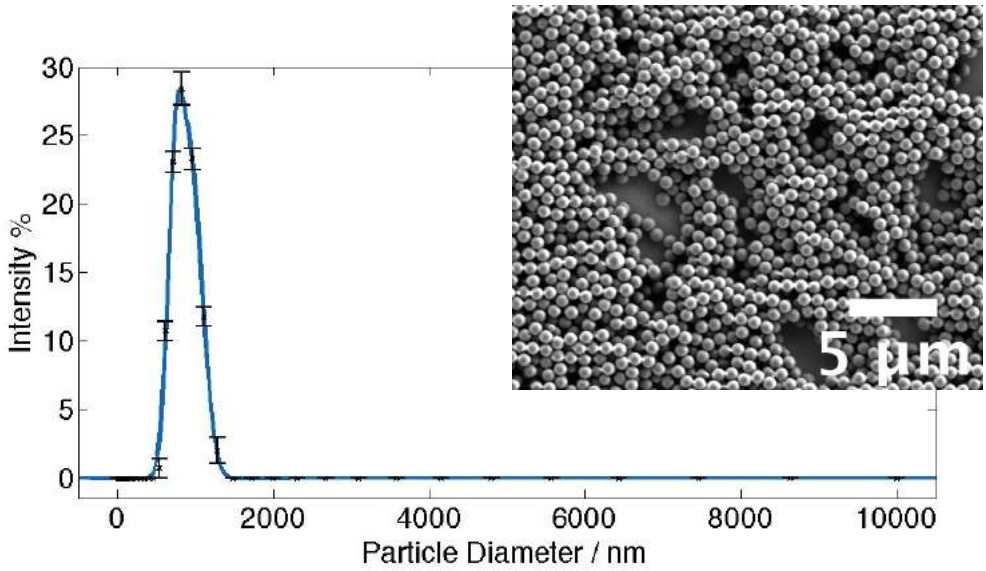

***Figure 7.11**: PS particles used in experiments: FE-SEM image of PS particles along with a plot of the size distribution measured by DLS.*

To facilitate pore-particle interactions, a voltage of +200 mV was applied across the diamond pore of exit diameter 777.6 nm (measured by FE-SEM, labelled 1 in Figure 7.7 and Table 7.2). Individual peaks were observed in the *i-t* responses that were not observed in the conductance trace in the absence of particles, shown in **Figure 7.12**a, associated with pore-particle translocation/blockade events. **Figure**

7.12b shows the resulting current-time (*i-t*) trace of PS particles as they translocate through a diamond pore.

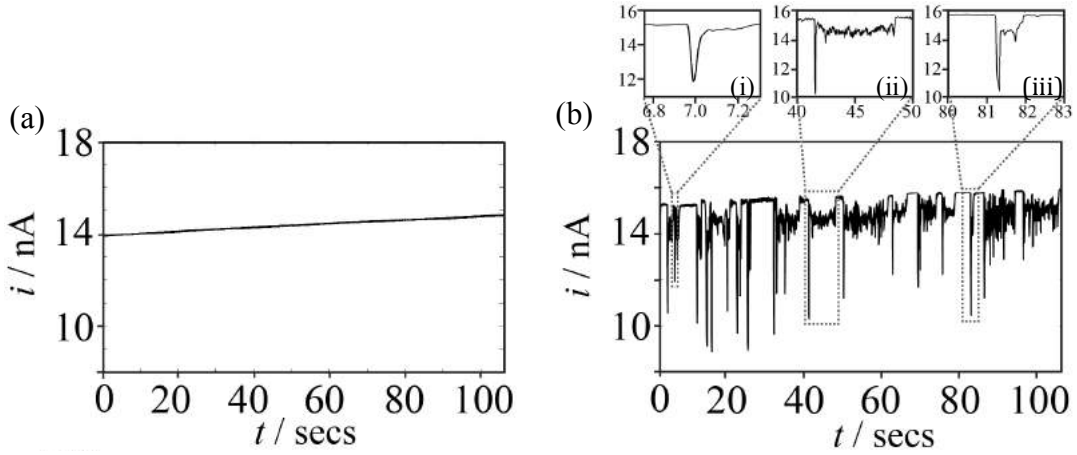

***Figure 7.12**: Blockade event analysis of negatively charged PS particles interacting with a diamond pore. Current-time (i-t) traces (a) in the absence of particles displaying no blockade events, and (b) on addition of PS particles are displayed, with three frequently occurring particle blockade events highlighted in (i) – (iii).*

The high aspect ratio of the diamond pore used in the experiments in **Figure 7.12** (length of ~ 3 μm and diameter of ~ 778 nm *i.e.* thickness-to-diameter aspect ratio of ~ 3.9) facilitates enhanced time resolution and longer event signals, allowing the observation of greater detail within events that can elucidate different particle dynamics. **Figure 7.12**bi – iii shows zoom-ins of three particle events. All events displayed a characteristic pulse on entry, often followed by a tail relating to the pore-particle interactions. The initial current pulse (where the current drops quickly in magnitude from ~ 15 – 9 nA) can be attributed to a single particle (or aggregation of particles) entering the pore. Upon entry, the particle displaces the largest proportion of electrolyte solution at the smallest constriction *i.e.* the EBIE exit side of the diamond pore. Variability in the initial current drop is due to displacement at the constriction by different particle sizes in solution. The events display a transient tail off as the particle travels through the channel until it eventually exits through the

larger (entrance) side, restoring current back to the baseline value associated with an open pore. A distinctive asymmetry in current either side of the peak is observed for all events, which is indicative of translocation through a conical-shaped pore.[4b] This is in agreement with the observed internal conical geometry of EBIE fabricated diamond pores (see Figure 7.8b).

The difference in the length and shape of events in the *i-t* trace is indicative of different particle dynamics within the pore. For clarity, the different pore-particle interaction types observed for our system have been categorized, as shown in **Figure 7.13**.

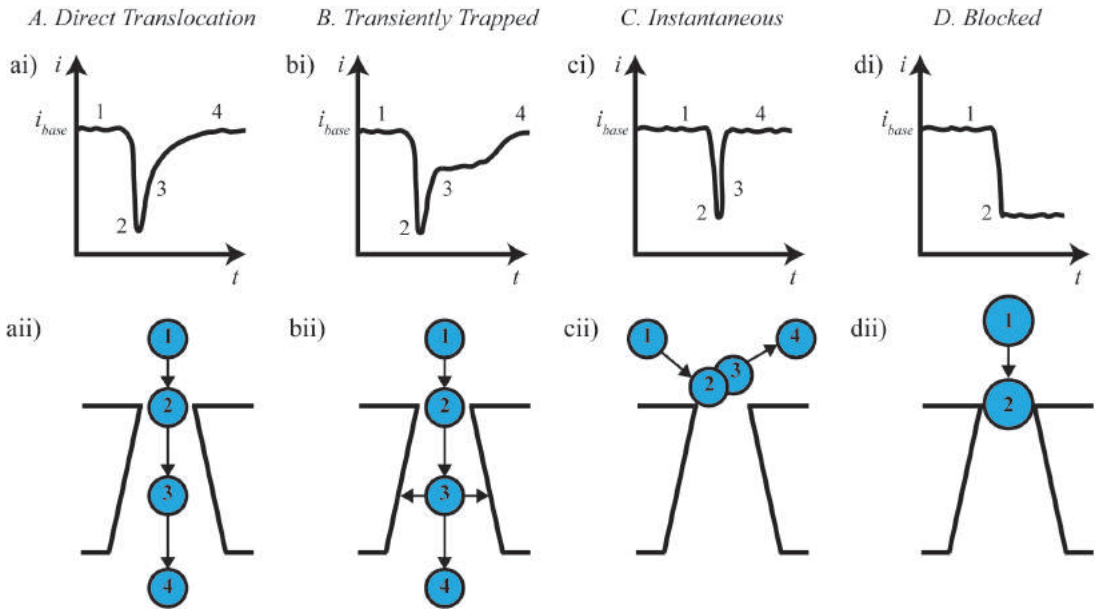

Figure 7.13: *Different particle blockade events A – D through a conical pore where (i) displays the representative i-t trace and (ii) is an illustration of the corresponding pore-particle interaction. Four main event categories exist: (a) Direct translocation of a single (or aggregated) particle; (b) Translocation of a single (or aggregated) particle which becomes transiently trapped within the channel during travel; (c) Instantaneous pore-particle interactions; (d) Complete pore blockage by a particle of comparable size to the pore. Events consists of (1) baseline pore current prior to an event, (2) decrease in current due to particle blocking the pore opening, (3) increase in pore current as the particle moves away from the pore opening, and (4) pore current returning back to baseline post-event. Not to scale.*

Four main categories of blockade event exist (**Figure 7.13**): (A) Direct translocation, where the particle travels through the diamond pore without interacting with the walls thus causing a steady increase in the pore current beyond the initial pulse back to the baseline; (B) Hindered translocation, where the particle interacts with the walls of the diamond pore during translocation causing it to become transiently trapped within the channel. This produces fluctuating tails beyond the peak with current oscillations that relate to binding and detachment of the particle with the diamond channel. Pevarnik and coworkers reported similar *i-t* traces with distinctive current fluctuations due to a PS particle temporarily sticking to a cylindrical polyethyleneterephthalate (PET) pore during translocation.[49] This pattern maps the internal structure of the pore, especially with smaller particles that can achieve higher spatial resolution and more distinctive tail fluctuations; (C) Instantaneous blockage, where the particle interacts with or near to the pore aperture but rebounds back into the bulk solution instead of entering; (D) Complete blockage, where the particle becomes permanently stuck in the pore causing the current to drop indefinitely. This event type was not observed during the course of our experiments.

The categorizations in **Figure 7.13** enable qualitative interpretation of the different observed blockade event types. For example, it is noted that Figure 7.12bi displays a category A event, whereas Figure 7.12bii – iii are category B, due to the appearance of tail fluctuations. Furthermore, Figure 7.12bii displays distinct tail fluctuations mapped by the particle that are considered to be features on the pore wall introduced by the EBIE sub-surface etching.

Finite-element method (FEM) simulations were employed to estimate the expected change in current during particle blockade events (for details of the model see section 7.3.7). The pore was modelled as a truncated cone of height z_{pore} = 3 μm,

entrance radii r_{ent} = 0.395 μm and exit radii r_{exit} = 0.389 μm (assuming circular geometry of both apertures), based on the dimensions of the experimental diamond pore used in the particle experiments (labelled 1 in Table 7.2). Prior to particle insertion, the open-pore current in absence of the particle (i_{base}) was calculated at the applied potential of +200 mV. The model successfully reproduced the average experimental open-pore baseline (15.0 nA).

A single particle was then added to the model by placing it at the apparent smallest constriction (exit side) of the pore that will cause the greatest observed change in blockade current, with the center of the particle aligning with the edge of the pore (see Figure 7.3). The resulting blockade current was calculated as discussed in section 7.3.7. Particles of varying diameters of 100 – 800 nm were investigated to calculate the range of expected peak blockade currents due to a single particle entering the pore. **Figure 7.14** displays the expected blockade currents for three different pore geometries – the maximum and minimum cylindrical geometries based on the entrance and exit pore areas, respectively, and the predicted conical geometry (see Table 7.2).

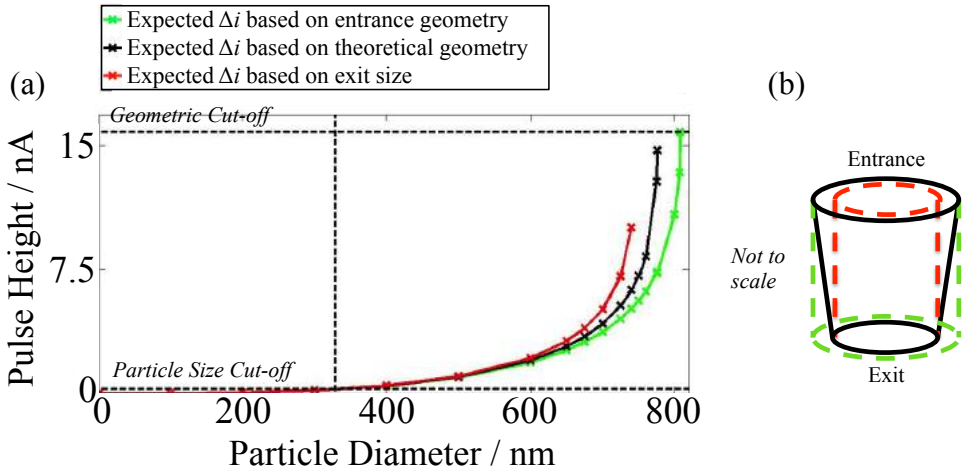

***Figure 7.14**: (a) The expected change in current (pulse height, Δi) as a function of particle size, as the particle translocates through the maximum (dotted green), minimum (dotted red) and predicted (solid black) pore geometries as illustrated in (b). The lower boundary is due to the lower limit of available particle sizes in solution, and upper boundary due to geometrical constraints based on the EBIE entrance and exit dimensions. The pore is modelled on the experimental dimensions (pore 1, Table 7.2).*

In general, larger particles caused greater values of Δ*i* due to larger displacement of electrolyte at the aperture (**Figure 7.14**). An upper limit of 15.0 nA was considered to be the largest possible change in current based on a particle completely blocking the smallest constriction (diameter 778 nm, Table 7.2). A lower limit of 0.1 nA was considered the smallest possible change in current based on the smallest particle size in solution blocking the pore constriction *i.e.* of diameter 329 nm based on the particle distribution (800 ± 471 nm diameter based on DLS particle distribution, see Figure 7.11). However, the mean particle size in solution (of diameter 800 nm) is larger than the size of the smallest constriction (of diameter 778 nm). Hence, all particles of diameter ≥ 778 nm in the solution will not translocate the pore, limiting the range of particle sizes that can enter the pore to be less than the mean of the particle distribution (diameters of 329 – 778 nm).

Closer analysis of the events in the *i-t* trace (Figure 7.12b) was performed in order to examine how the different categories relate to the different particle sizes in solution. Histograms of the change in current due to blockade events (Δi) and the pulse durations (τ) (n = 1068 events) are shown in **Figures 7.15**a – b, respectively. Both plots display a spread in the current and time responses indicative of the different sized PS particle traversing the diamond pore.

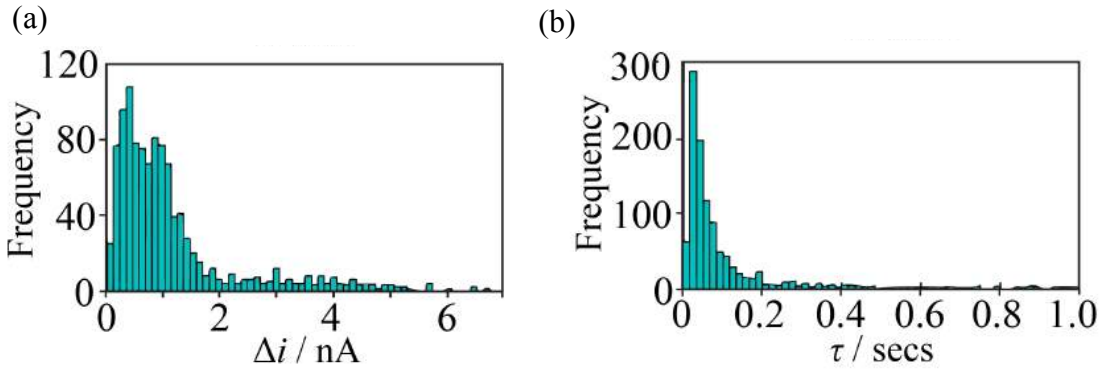

Figure 7.15: *Histograms (a) and (b) display the change in current (Δi) and pulse duration (τ) due to particle blockade, respectively (1068 blockade events).*

We observe in **Figure 7.15**a that 84% of events have Δi < 1.7 nA corresponding to blockade events by a single particle of diameter < 570 nm, with the most frequent Δi = 0.3 – 0.5 nA due to a single particle of diameter 322 – 401 nm. This corresponds to an optimum pore : particle ratio of ~ 1.9 : 1. The proportions of < 570 nm and < 401 nm diameter particles in solution are approx. 5% and 0.1% respectively, however, the high particle concentration (3.57×10^7 particles ml^{-1}) enables a higher probability of particle events. All events were considerably below complete blockage (< 7 nA compared to < 15 nA) with the interaction of particles of diameter > 600 nm with the pore observed to be rare, recording < 10 events within the timescale of the experiment and no particles of diameter > 749 nm were observed to interact with the pore within the timescale of the experiment. It is noted that the

observed Δi responses are a combination of category A – C event types (translocation and instantaneous). Inspection of the blockade *i-t* event traces in Figure 7.12b showed a high frequency of category A – B type events, so it is considered that translocation dominates the Δi responses.

Figure 7.15b displays the pulse durations as the particle interacts with the pore aperture. The pulse durations denote the period of time before the response flattens out (see experimental, section 7.3), considered either when the blockade current returns to baseline as the particle moves away from the aperture (category A and C events), or when the particle becoming transiently stuck within the pore (category B). This captures the period of time in which the particle blocks the pore constriction and eliminates processes due to sticking that are considered stocastic. The most frequent pulse durations were observed between 20 – 40 ms with 75% having a duration of less than 100 ms. The distribution is observed to be a first order statistic exponential, with the long tail relating to longer pulse durations likely caused by larger single particles or aggregates. The relatively long ~ ms durations are indicative of the high aspect ratio (~ 3 μm length) of the diamond pore for translocation events. The different pulse durations are due to either translocation or instantaneous blockade events. It is generally difficult to distinguish the event type from duration alone, however, the longest durations (~ > 100 ms) are most likely due to the larger sized particles stuck either at or near the aperture (category C) or translocating at a slower rate within the pore relative to smaller particles (category A – B).

The relationship between the pulse durations and blockade currents will ultimately help to map the different event types based on particle size. **Figure 7.16** displays the correlation plot relating Δi and τ.

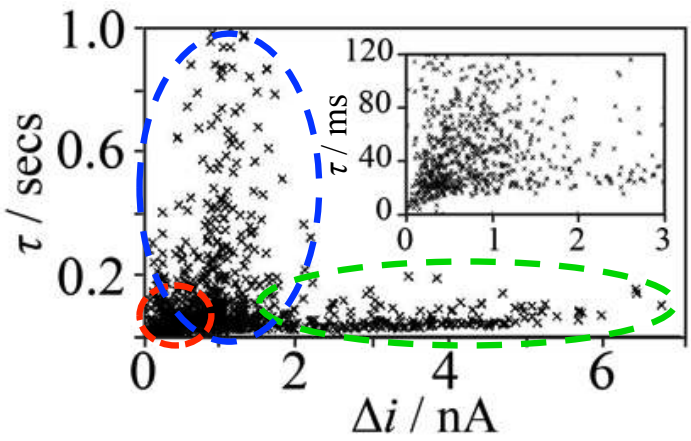

Figure 7.16: *Scatter plot displaying the range and most frequent (inset) Δi-τ responses (1068 events) indicative of the different pore-particle interactions. Regions 1 – 3 are highlighted as containing predominantly different category blockade events, with a high proportion of instantaneous blockade events in region 1, inhibited translocation in region 2, and direct translocation in region 3 (see main text).*

Figure 7.16 can be summarized into three key regions based on Δi, τ and the predicted particle size relative to the pore from FEM simulations. Region 1 is low magnitude, fast events that display a near linear correlation between blockade current and pulse duration (**Figure 7.16**) *i.e.* $\Delta i \sim < 0.7$ nA, $\tau \sim < 40$ ms for a single particle of diameter ~ 329 – 440 nm, where 329 nm is the smallest particle in solution), which can be attributed to direct translocation of small particles through the pore (category A). This means that the particles are sufficiently small to enter and translocate through the pore without hitting the walls. The most frequent Δi of 0.3 – 0.5 nA (Figure 7.15a) and τ of 20 – 40 ms (Figure 7.15b) reside within this region. Whilst some instantaneous blockades also fall in this region, as Δi is proportional to τ (**Figure 7.16**c inset) it suggests that a higher proportion of these events are direct translocation. Furthermore, inspection of the different particle events in Figure 7.12b showed a high proportion of category A *i-t* traces (Figure 7.13a) in further support of direct translocation of small particles.

Region 2 is mid-range blockade events for larger particles (**Figure 7.16**) *i.e.* ~ $0.7 < \Delta i < 1.7$ nA for a single particle of diameter ~ 440 – 570 nm) where a single particle (or aggregation of small particles) becomes stuck either during translocation (category B) or from random collisions with or near the pore aperture before bouncing back into bulk solution (category C, Figure 7.13c). This causes a wide spread of pulse duration times dependent on the variable particle dynamics. Blockade events of magnitude ~ 1 nA appear to have the broadest range of pulse durations, compared to other event magnitudes. The wide range of τ in this region suggests particles of this size (~ 500 nm diameter) are more prone to becoming stuck in the pore constriction.

Finally, region 3 displays larger magnitude events (**Figure 7.16**) *i.e.* Δi ~ > 1.7 nA for a single particle of diameter ~ 570 – 749 nm, where 749 nm is the largest particle event observed). This region has a near linear increase of Δi proportional to τ suggesting translocation by a single particle (or aggregation of small particles) (category A – B) dominates, with larger particles causing the greater Δi and τ. Fewer blockade events are observed in this region with the lowest frequency Δi of > 1.7 nA (Figure 7.15a) and τ of > 100 ms (Figure 7.15b) residing here. Examination of the less frequent blockade event types in Figure 7.12b displays pulses followed by long fluctuating tails (*e.g.* Figure 7.12bii), suggesting that this region is dominated by a particle that is large enough to interact with the diamond pore walls during translocation, causing it to become transiently stuck within the pore (category B events, Figure 7.13b) but never fully stuck to cause complete blockage.

Further pore-particle experiments were conducted using the same diamond pore and range of PS particle sizes. **Figure 7.17** shows the resulting *i-t* trace and data analysis of the blockade events. Fewer blockade events were observed in the *i-t* trace (**Figure 7.17**a), with a higher proportion of inhibited translocation events. This

suggests that particles may be residing in the pore from previous experiments that hinders particle translocation. The distribution of Δi (**Figure 7.17**b) matches to the previous experiment (Figure 7.15a) with the most frequent events occurring at $\Delta i < 1$ nA. A Gaussian distribution of τ is observed (**Figure 7.17**d) with the most frequent events occurring at $\tau < 40$ ms. Whilst this distribution of τ does not match to previous experiments (Figure 7.15b), fewer events were analysed in this experiment (128 compared to 1068 events previously) so the events were considered not sufficiently sampled. The Δi- τ plot in **Figure 7.17**c displays similar event regions to Figure 7.16 *i.e.* a dominance of instantaneous events at $\tau < 40$ ms and $\Delta i < 0.1$ nA, followed by a region of inhibited translocation at $\Delta i \sim 0.4$ nA, and direct translocation for $\Delta i > 1$ nA due to the linear Δi- τ response. The similarity in event trends observed in this experiment compared to the previous experiment (Figure 7.15 – 7.16) demonstrates the reproducibility of the diamond pore device.

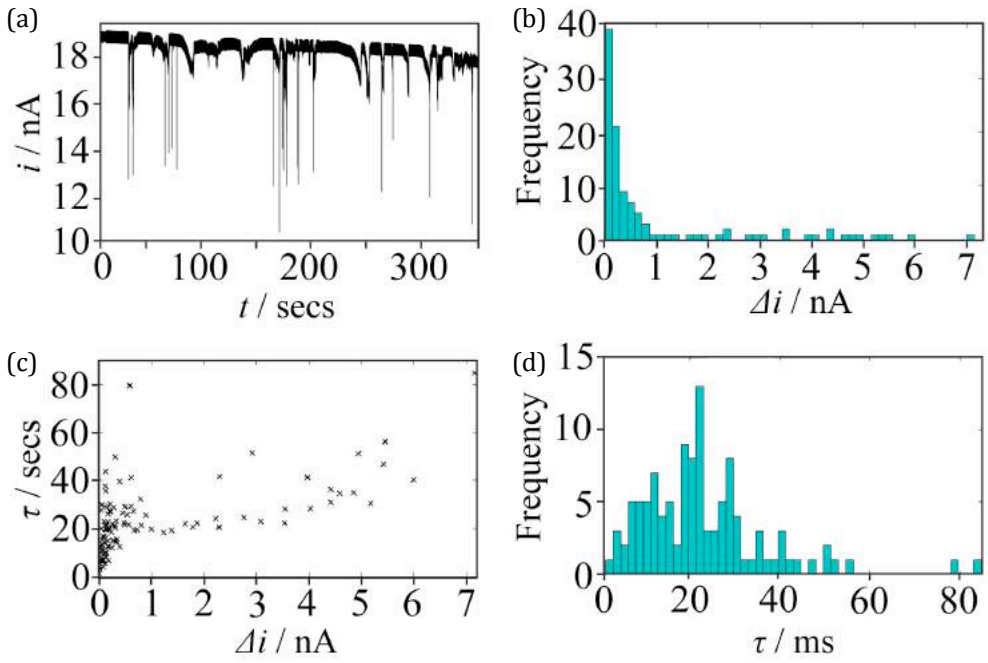

***Figure 7.17**: (a) Current-time (i-t) trace and the corresponding data analysis including histograms of (b) the change in current due a blockade event and (d) the event duration; and (c) a scatter plot of the blockade current-duration correlation (128 events).*

This work in this chapter has focused on investigating single particle dynamics within a pore. It is important to discuss other factors that will also influence the Δi and τ of the different pore-particle events, which should be considered in future experiments. Pore geometry is highly influential to the particle dynamics.[50] Size limitations and geometrical incompatibility between the pore and spherical particles, namely geometrical constrictions on entry and sub-surface features due to the EBIE etching mechanism can inhibit entry of larger particles. The position and orientation of the particle is also considered to have an effect on the observed blockade events, with the off-axis positioning of spherical particles causing a significant increase in the resistance compared to a particle residing on the channel axis.[51] The particle positioning will also influence whether it will directly translocate (category A) or interact with the walls (category B).

The trade-off between competition and co-operation is also a crucial feature in particle dynamics.[52] Due to the high proportion of particles larger than the pore (diameters of $\geq$ 778 nm), competition is believed to dominate in solution with a higher proportion of particle collisions near the pore inhibiting the frequency of blockade events. In addition, for smaller particles, co-operation can play a key role, causing longer blockade durations than expected as the particles aggregate into non-spherical structures. This is believed to be the reason for the wide range of pulse durations in the region of $\sim 0.7 < \Delta i < 1.7$ nA, where translocation can be hindered by different shaped particle aggregates that have reduced compatibility with the pore geometry.

7.5 Conclusions

In conclusion we have shown, for the first time, the fabrication of single crystal diamond pores and their capability in sensing applications. The work is highly significant as it demonstrates that diamond is a viable material in pore technology and

encourages the field to consider using single crystal diamond as the platform material in future pore-based sensors (see section 7.1).

Single crystal diamond pores were successfully fabricated using a novel two-step laser thinning process to first produce trenches of ~ 1.9 – 4.4 μm thickness and then EBIE to expose a pore in each trench. The pores were characterised using both microscopy and electrochemical techniques and shown to exhibit reproducible characteristics. The experimental *i-E* response displayed good agreement to the predicted *i-E* response at +1 V, calculated from FEM simulations modelled on the observed dimensions and predicted conical geometry of the pore. The sensing capability of a diamond pore was investigated using PS particles. FEM simulations of a particle within the pore enabled the predicted size of the particle responsible for each blockade event to be revealed (assuming a single particle blocks the pore). Low noise *i-t* traces were achievable without the requirement for noise filtering or surface modification *e.g.* with a high dielectric constant material,[53] that is often employed for other materials. Furthermore, the high aspect ratio of the pores allowed for high enough time resolution to observe detailed particle dynamics based on the interactions of the PS particles with the diamond pore. We have therefore shown that single crystal diamond has the ideal electrical and mechanical properties for use in micro and nanopore devices. The variety of apparent types or categories of blockade events observed, in terms of duration, magnitude and shape, hint at providing a fundamental insight into the interactions between the particles and pores.

7.6 Future Work

Single crystal diamond has huge potential to advance micro- and nanopore technologies by utilising dual optical-conductance capabilities[23] and in-built doped diamond microelectrodes[54] that, through electric-field enhancement,[55] could

facilitate analyte detection into the single-nucleotide base resolution. The next step from this work is to calibrate the device for detection of single particles of one size only. Future work should also focus on variation of the surface chemistries of diamond *i.e.* through atomistic modelling, in combination with refinement of the EBIE etching process, or biological functionalisation of the solid-state pore, can enable the optimisation of the micro- and nano- pore properties for biomolecule specificity in the future.

7.7 References

[1] a) R. DeBlois, C. Bean, *Rev. Sci. Instrum.* **1970**, *41*, 909-916; b) H. Bayley, C. R. Martin, *Chem. Rev.* **2000**, *100*, 2575-2594.

[2] C. Dekker, *Nat. Nanotechnol.* **2007**, *2*, 209-215.

[3] S. Howorka, Z. Siwy, *Chem. Soc. Rev.* **2009**, *38*, 2360-2384.

[4] a) J. Kong, H. Wu, L. Liu, X. Xie, L. Wu, X. Ye, Q. Liu, *J. Nanosci. Nanotechnol.* **2013**, *13*, 4010-4016; b) W.-J. Lan, D. A. Holden, B. Zhang, H. S. White, *Anal. Chem.* **2011**, *83*, 3840-3847; c) K. Venta, M. Wanunu, M. Drndić, *Nano Lett.* **2013**, *13*, 423-429; d) Y. Astier, L. Datas, R. Carney, F. Stellacci, F. Gentile, E. DiFabrizio, *Small* **2011**, *7*, 455-459; e) R. Vogel, G. Willmott, D. Kozak, G. S. Roberts, W. Anderson, L. Groenewegen, B. Glossop, A. Barnett, A. Turner, M. Trau, *Anal. Chem.* **2011**, *83*, 3499-3506.

[5] P. Rowghanian, A. Y. Grosberg, *J. Phys. Chem. B* **2011**, *115*, 14127-14135.

[6] a) E. C. Yusko, J. M. Johnson, S. Majd, P. Prangkio, R. C. Rollings, J. Li, J. Yang, M. Mayer, *Nat. Nanotechnol.* **2011**, *6*, 253-260; b) D. S. Talaga, J. Li, *J. Am. Chem. Soc.* **2009**, *131*, 9287-9297; c) C. Plesa, J. W. Ruitenberg, M. J. Witteveen, C. Dekker, *Nano Lett.* **2015**; d) D. Japrung, J. Dogan, K. J. Freedman, A. Nadzeyka, S. Bauerdick, T. Albrecht, M. J. Kim, P. Jemth, J. B. Edel, *Anal. Chem.* **2013**, *85*, 2449-2456.

[7] a) A. J. Storm, C. Storm, J. Chen, H. Zandbergen, J.-F. Joanny, C. Dekker, *Nano Lett.* **2005**, *5*, 1193-1197; b) S. W. Kowalczyk, M. W. Tuijtel, S. P. Donkers, C. Dekker, *Nano Lett.* **2010**, *10*, 1414-1420; c) D. Fologea, J. Uplinger, B. Thomas, D. S. McNabb, J. Li, *Nano Lett.* **2005**, *5*, 1734-1737; d) U. F. Keyser, B. N. Koeleman, S. Van Dorp, D. Krapf, R. M. Smeets, S. G. Lemay, N. H. Dekker, C. Dekker, *Nat. Phys.* **2006**, *2*, 473-477.

[8] a) J. J. Kasianowicz, E. Brandin, D. Branton, D. W. Deamer, *PNAS* **1996**, *93*, 13770-13773; b) H. Bayley, P. S. Cremer, *Nature* **2001**, *413*, 226-230; c) J. Clarke, H.-C. Wu, L. Jayasinghe, A. Patel, S. Reid, H. Bayley, *Nat. Nanotechnol.* **2009**, *4*, 265-270.

[9] I. M. Derrington, T. Z. Butler, M. D. Collins, E. Manrao, M. Pavlenok, M. Niederweis, J. H. Gundlach, *Proc. Natl. Acad. Sci.* **2010**, *107*, 16060-16065.

[10] M. Montal, P. Mueller, *Proc. Natl. Acad. Sci.* **1972**, *69*, 3561-3566.

[11] B. N. Miles, A. P. Ivanov, K. A. Wilson, F. Doğan, D. Japrung, J. B. Edel, *Chem. Soc. Rev.* **2013**, *42*, 15-28.

[12] a) A. Storm, J. Chen, X. Ling, H. Zandbergen, C. Dekker, *Nat. Mater.* **2003**, *2*, 537-540; b) K. Briggs, H. Kwok, V. Tabard‐Cossa, *Small* **2014**, *10*, 2077-2086.
[13] B. Zhang, J. Galusha, P. G. Shiozawa, G. Wang, A. J. Bergren, R. M. Jones, R. J. White, E. N. Ervin, C. C. Cauley, H. S. White, *Anal. Chem.* **2007**, *79*, 4778-4787.
[14] M. D. Fischbein, M. Drndić, *Appl. Phys. Lett.* **2008**, *93*, 113107.
[15] a) C. A. Merchant, K. Healy, M. Wanunu, V. Ray, N. Peterman, J. Bartel, M. D. Fischbein, K. Venta, Z. Luo, A. C. Johnson, *Nano Lett.* **2010**, *10*, 2915-2921; b) G. F. Schneider, S. W. Kowalczyk, V. E. Calado, G. Pandraud, H. W. Zandbergen, L. M. Vandersypen, C. Dekker, *Nano Lett.* **2010**, *10*, 3163-3167.
[16] a) A. Mara, Z. Siwy, C. Trautmann, J. Wan, F. Kamme, *Nano Lett.* **2004**, *4*, 497-501; b) P. Y. Apel, I. V. Blonskaya, S. N. Dmitriev, O. L. Orelovitch, A. Presz, B. A. Sartowska, *Nanotechnol.* **2007**, *18*, 305302.
[17] K. Healy, B. Schiedt, A. P. Morrison, *Nanomedicine* **2007**, *2*, 875-897.
[18] a) M. Pevarnik, K. Healy, M. E. Toimil-Molares, A. Morrison, S. E. Létant, Z. S. Siwy, *ACS Nano.* **2012**, *6*, 7295-7302; b) D. Kozak, W. Anderson, R. Vogel, S. Chen, F. Antaw, M. Trau, *ACS Nano* **2012**, *6*, 6990-6997.
[19] R. Ramesham, M. Rose, *Diam. Relat. Mater.* **1997**, *6*, 17-26.
[20] M. Wanunu, *Phys. Life Rev.* **2012**, *9*, 125-158.
[21] R. K. Iler, *The Chemistry of Silica*, Wiley, New York, **1979**.
[22] a) H. V. Patten, L. A. Hutton, J. R. Webb, M. E. Newton, P. R. Unwin, J. V. Macpherson, *Chem. Comm.* **2015**, *51*, 164-167; b) L. A. Hutton, J. G. Iacobini, E. Bitziou, R. B. Channon, M. E. Newton, J. V. Macpherson, *Anal. Chem.* **2013**, *85*, 7230-7240.
[23] W. H. Pitchford, H.-J. Kim, A. P. Ivanov, H.-M. Kim, J.-S. Yu, R. J. Leatherbarrow, T. Albrecht, K.-B. Kim, J. B. Edel, *ACS Nano* **2015**, *9*, 1740-1748.
[24] a) S. Coe, R. Sussmann, *Diam. Relat. Mater.* **2000**, *9*, 1726-1729; b) J. von Windheim, V. Venkatesan, D. Malta, K. Das, *Diam. Relat. Mater.* **1993**, *2*, 841-846.
[25] V. Tabard-Cossa, D. Trivedi, M. Wiggin, N. N. Jetha, A. Marziali, *Nanotechnol.* **2007**, *18*, 305505.
[26] a) H.-a. Mehedi, J.-C. Arnault, D. Eon, C. Hébert, D. Carole, F. Omnes, E. Gheeraert, *Carbon* **2013**, *59*, 448-456; b) W. Smirnov, J. Hees, D. Brink, W. Müller-Sebert, A. Kriele, O. A. Williams, C. Nebel, *Appl. Phys. Lett.* **2010**, *97*, 073117; c) Y. Takasu, S. Konishi, W. Sugimoto, Y. Murakami, *Electrochem. Solid St.* **2006**, *9*, C114-C117; d) H.-A. Mehedi, C. Hébert, S. Ruffinatto, D. Eon, F. Omnès, E. Gheeraert, *Nanotechnol.* **2012**, *23*, 455302.
[27] H. Masuda, K. Yasui, M. Watanabe, K. Nishio, M. Nakao, T. Tamamura, T. N. Rao, A. Fujishima, *Electrochem. Solid St.* **2001**, *4*, G101-G103.
[28] I. Aharonovich, A. D. Greentree, S. Prawer, *Nat. Photonics* **2011**, *5*, 397-405.
[29] E. Mahé, D. Devilliers, C. Comninellis, *Electrochim. Acta* **2005**, *50*, 2263-2277.
[30] T. Watanabe, T. K. Shimizu, Y. Tateyama, Y. Kim, M. Kawai, Y. Einaga, *Diam. Relat. Mater.* **2010**, *19*, 772-777.
[31] G. Danilatos, *Adv. Electron. Electron Phys.* **1988**, *71*, 109-250.
[32] B. Thiel, M. Toth, R. Schroemges, J. Scholtz, G. van Veen, W. Knowles, *Rev. Sci. Instrum.* **2006**, *77*, 033705.
[33] W. Nernst, *Z. Phys. Chem. Leipzig* **1888**, 613.

[34] D. R. Lide, *Handbook of organic solvents*, CRC Press, **1994**.
[35] R. A. Robinson, presented, Butterworths, London, Month, **1959**.
[36] a) I. Utke, S. Moshkalev, P. Russell, *Nanofabrication using Focused Ion and Electron Beams: Principles and Applications*, Oxford University Press, New York, U.S.A, **2012**; b) J. Taniguchi, I. Miyamoto, N. Ohno, S. Honda, *Jpn. J. App. Phys.* **1996**, *35*, 6574-6578; c) J.-i. Niitsuma, X.-l. Yuan, S. Koizumi, T. Sekiguchi, *Jpn. J. Appl. Phys.* **2006**, *45*, L71.
[37] M. Toth, C. J. Lobo, W. R. Knowles, M. R. Phillips, M. T. Postek, A. E. Vladár, *Nano Lett.* **2007**, *7*, 525-530.
[38] a) A. A. Martin, M. Toth, I. Aharonovich, *Sci. Rep.* **2014**, *4*; b) A. A. Martin, A. Bahm, J. Bishop, I. Aharonovich, M. Toth, *Phys. Rev. Lett.* **2015**, *115*, 255501.
[39] I. Utke, P. Hoffmann, J. Melngailis, *J. Vac. Sci. Tech. B* **2008**, *26*, 1197-1276.
[40] J. B. Kortright, A. C. Thompson, *X-ray Data Booklet* **2001**.
[41] D. Drouin, A. R. Couture, D. Joly, X. Tastet, V. Aimez, R. Gauvin, *Scanning* **2007**, *29*, 92-101.
[42] M. Tsutsui, S. Hongo, Y. He, M. Taniguchi, N. Gemma, T. Kawai, *ACS nano* **2012**, *6*, 3499-3505.
[43] T. S. Miller, J. V. Macpherson, P. R. Unwin, *Phys. Chem. Chem. Phys.* **2014**, *16*, 9966-9973.
[44] a) R. D. Fisher, M. M. Mbogoro, M. E. Snowden, M. B. Joseph, J. A. Covington, P. R. Unwin, R. I. Walton, *ACS Appl. Mater. Inter.* **2011**, *3*, 3528-3537; b) S. Sansuk, E. Bitziou, M. B. Joseph, J. A. Covington, M. G. Boutelle, P. R. Unwin, J. V. Macpherson, *Anal. Chem.* **2012**, *85*, 163-169; c) E. Bitziou, M. E. Snowden, M. B. Joseph, S. J. Leigh, J. A. Covington, J. V. Macpherson, P. R. Unwin, *J. Electroanal. Chem.* **2013**, *692*, 72-79; d) T. M. Day, P. R. Unwin, J. V. Macpherson, *Nano Lett.* **2007**, *7*, 51-57.
[45] P. V. Dudin, P. R. Unwin, J. V. Macpherson, *J. Phys. Chem. C* **2010**, *114*, 13241-13248.
[46] a) H. S. White, A. Bund, *Langmuir* **2008**, *24*, 2212-2218; b) R. Karnik, C. Duan, K. Castelino, H. Daiguji, A. Majumdar, *Nano Lett.* **2007**, *7*, 547-551.
[47] H. S. White, A. Bund, *Langmuir* **2008**, *24*, 12062-12067.
[48] D. Breite, M. Went, A. Prager, A. Schulze, *Polymers* **2015**, *7*, 2017-2030.
[49] M. Pevarnik, K. Healy, M. E. Toimil-Molares, A. Morrison, S. E. Létant, Z. S. Siwy, *ACS Nano* **2012**, *6*, 7295-7302.
[50] M. Davenport, K. Healy, M. Pevarnik, N. Teslich, S. Cabrini, A. P. Morrison, Z. S. Siwy, S. E. Létant, *ACS Nano* **2012**, *6*, 8366-8380.
[51] Z. Qin, J. Zhe, G.-X. Wang, *Meas. Sci. Technol.* **2011**, *22*, 045804.
[52] M. Grzelczak, J. Vermant, E. M. Furst, L. M. Liz-Marzán, *ACS Nano* **2010**, *4*, 3591-3605.
[53] B. N. Miles, A. P. Ivanov, K. A. Wilson, F. Doğan, D. Japrung, J. B. Edel, *Chem. Soc. Rev.* **2013**, *42*, 15-28.
[54] M. B. Joseph, E. Bitziou, T. L. Read, L. Meng, N. L. Palmer, T. P. Mollart, M. E. Newton, J. V. Macpherson, *Anal. Chem.* **2014**, *86*, 5238-5244.
[55] G. A. Chansin, R. Mulero, J. Hong, M. J. Kim, A. J. Demello, J. B. Edel, *Nano Lett.* **2007**, *7*, 2901-2906.

Chapter 8

Building Coarse-Grained Models: Towards Larger Scale Diamond-Biomolecule Systems

8.1 Overview and Key Advances to Knowledge in this Chapter

The work in Chapters 4 – 7 has brought us to the point where the development of larger-scale molecular dynamics (MD) models would be highly beneficial in order to interpret our experimental results. In particular, understanding interfacial processes that occur at the surface of diamond electrodes (Chapter 6) and pores (Chapter 7) is fundamental for optimising the detection capability of these biosensors. Coarse-grained (CG) MD is an essential tool to model systems that occur on time and length scales inaccessible for all-atom systems and have proven successful in the study of surface-biomolecule systems. Hence, development of new CG models of diamond and polystyrene nanoparticle (PSNP) would enable simulations in the future that match more closely to the realistic experimental systems in Chapters 6 – 7, facilitating key molecular insights of the results achieved *i.e.* addressing questions such as how PSNPs interact with the diamond pores and how multiple (reactant and product) molecules interact with different diamond electrode surfaces.

These models are the first coarse-grained representations to be built of diamond surfaces and PSNPs with cross-links. Hence, they have huge potential to advance numerous avenues of scientific knowledge in the future, as they can be used

in the molecular dynamics community by anyone interested in simulating a system related to diamond or PSNPs. The CG representations of diamond were built based on our atomistic models (Chapters 4 and 5) that provide target data. The CG models retain the different diamond surface topographies but the parameters have not yet been validated for diamond making them 'diamond-like'. The self-assembly of DPPC lipids on different diamond-like surfaces was preliminarily investigated and differences *e.g.* lipid monolayer/bilayer formation were discussed. This is the first study of lipid self-assembly on diamond surfaces, with no prior knowledge in the field. The diamond-lipid results will be beneficial to advise experiments on the ideal diamond surface for functionalisation of the diamond pores developed in Chapter 7 to create a novel biological diamond pore device that will improve spatial resolution.

In general, the CG diamond models will be of use to the diamond community, as they enable simulations of a wide range of diamond-biomolecule systems, where the biologically relevant length and timescales are beyond the scope of our atomistic models. Hence, they have the potential to facilitate key scientific advances in the future by assisting in understanding of experimental data, as well as guiding experimental setup, in numerous future studies of diamond-biomolecule systems.

Our coarse-grained PSNP model is the most realistic to-date, as it was developed to mimic the experimental NP cross-linking procedure. This model can be used in the molecular dynamics community, as well as any biological and chemical fields that use PSNPs systems, where the models can assist in advancing understanding of their systems.

8.2 Introduction

The computational cost of atomistic molecular dynamics (MD) simulations limits studies to time scales of < 100 ns and length scales of < 10 nm.[1] In order to probe interesting biological phenomenon that occur on greater scales than feasibly accessible through atomistic modelling, coarse-grained (CG) MD is employed.[2] CG MD is a technique that compromises the accuracy of all-atom simulations to significantly speed up computations. To do so, the atoms are mapped to CG bead sites in order to reduce the number of degrees of freedom in the system. CG MD can simulate larger systems and longer time steps by using fewer interaction sites, softer interaction potentials and increased time steps (see Chapter 2, section 2.5). Hence, dynamical processes that were unfeasible using all-atom MD, such as protein folding,[3] lipid bilayer self-assembly[4] and membrane-protein interactions[5] can now be addressed.

This chapter outlines the model building protocols for two CG systems that may be of use to the MD community. These are: (1) CG cross-linked polystyrene nanoparticles (PSNPs), and (2) CG diamond-like substrates.

8.2.1 Polystyrene Nanoparticles (PSNPs)

In recent years NPs, such as quantum dots, fullerenes, polymeric and metal nanoparticles, have attracted a great deal of attention because their properties (e.g. chemical, optical, electronic and mechanical) are often very different from the bulk material. By manipulating NP size, shape and surface chemistry, it is possible to tailor these properties for specific applications. As a result, NPs are now widely used in consumer products such as coatings, sunscreens, and pharmaceuticals. In addition, porous, or branched NPs have the innate ability to encapsulate and transport molecules and have thus shown considerable potential as delivery vehicles for anti-

cancer agents[6] and DNA[7] (gene therapy). It is also possible to functionalise NPs with targeting moieties and imaging agents, meaning that they can also be used as sophisticated diagnostic tools and biosensors.[8] PSNPs are a popular test-case for experiments as they are readily available, easy to functionalise and can be produced with a narrow size distribution. Hence, CG models of PSNP systems can be of use to understand processes on the molecular-level for a wide range of applications.

8.2.2 Diamond-like Surfaces

The second model presented is CG diamond-like surfaces based on the previous atomistic diamond models (Chapter 4). These models were built in collaboration with Dr. Syma Khalid, University of Southampton (see Declaration). The CG MD models are described as 'diamond-like' as whilst the surface is patterned to reproduce the structure of the different atomistic diamond faces, the force field interactions have not yet been validated for diamond. The models are still useful without validation in order to study the adsorption of biological macromolecules onto general patterned carbon-based hydrophobic and hydrophilic surfaces, given that interesting results can be still be obtained, such as self-assembly of phospholipids on to model hydrophobic and hydrophilic surfaces, which has not been previously investigated. Model validation will be needed in the future to match the surfaces more closely to diamond. These models may be of use for studies of biological processes on diamond surfaces that are too large to capture atomistically, such as NP interactions in pore sensing devices (Chapter 7) or electrode fouling due to large/multiple molecule aggregation and assembly on diamond surfaces (Chapter 6). Preliminary work aims to capture lipid self-assembly on diamond-like surfaces. This is of relevance to developing the diamond pore-based sensor in Chapter 7 into a biological pore device, where the synthetic pore is functionalised with lipids

containing a well-characterised protein for sensing, typically *staphylococcal* α-hemolysin as it has a well-defined pore channel that enables the responses from each biomolecule to be well-understood and reproducible.[9] Dependent on the surface nature, lipids will assemble as a monolayer (suspended device) or bilayer (supported device) on the surface, as shown in Chapter 1, Figure 1.12. Phospholipid functionalised surfaces are of particular interest for molecular recognition and to study the binding to biomimetic membranes that can improve understanding of biomolecule-membrane interactions. Furthermore, solid-state pores, such as the diamond pores fabricated in Chapter 7, can be functionalised with lipids to create a platform for biological pore devices (see Chapter 1, Figure 1.12). Yusko *et al.*,[10] demonstrated how SiN pores coated with lipids can be used to reduce the translocation speed and enhance molecular selectivity. Suspended devices have been reported to remain stable for several months, in comparison to supported devices that only last a few hours due to bilayer degradation (Chapter 1, Figure 1.12).[11] Through the use of MD simulations, the diamond surface that should produce the most stable lipid structure in pore devices could be predicted.

CG MD models of support lipid bilayers are a relatively new field to the community with only a few studies currently in existence. This is due to the challenging nature of capturing the large-scale behaviour of both the lipids and solid support. A recent review by Bennun *et al.* outlined the CG MD models that have been developed so far to capture supported lipid monolayer/bilayer systems.[12] These studies focused on elucidating the structural and thermodynamic behaviour of pre-formed dipalmitoylphosphatidylcholine (DPPC) lipid bilayers[13] and monolayers[14] on hydrophobic and hydrophilic substrates, typically consisting of a hexagonal or quadratic lattice of beads. Xing and Faller also investigated the influence of roughness

by the addition of 'dips' to the surface.[13a] In this study, substrates were built with varying surface patterns that mimic the geometry of the different diamond faces. Preliminary simulations to capture DPPC lipid self-assembly on to these different surfaces were presented in order to demonstrate the potential for these models. This prevents any pre-assumption about the lipid structure, and captures how lipid structures form on surfaces in experiments such as vesicle adsorption,[15] Langmuir-Blodgett,[16] and biological nanopores.[17]

8.3 Building Coarse-Grained Polystyrene Nanoparticles

Different sized uncharged hydrophobic PSNPs were built using a CG model for polystyrene[18] combined with an approach that mimics the experimental cross-linking of a polystyrene chain to form an nanoparticle.[19] The CG model was chosen as it had been developed to be compatible with the popular MARTINI biomolecular force field[20] that is used for MD simulation of lipids and numerous biological molecules.[21] By treating the NP at the CG-level we were also able to retain some of its amorphous character.

Each polystyrene monomer was mapped onto four interaction sites, one corresponding to the position of the backbone atoms and three that represented the aromatic ring (**Figure 8.1**). This mapping corresponds to the "A-mapping" scheme developed by Rossi *et al.*,[18] that reproduces best the structural properties of polystyrene.

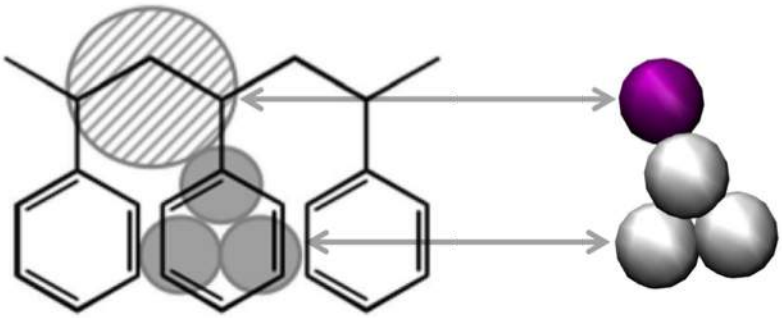

***Figure 8.1**: CG mapping scheme for polystyrene.[18] The atomic structure of polystyrene is drawn in black and the corresponding CG particles are drawn in grey. Each monomer is represented by a backbone particle (diagonal grey lines) and three particles that make up the aromatic ring (solid grey).*

The two outermost aromatic CG beads of polystyrene were designated cross-linking particles. To construct a PSNP, a linear, extended polystyrene chain of 40, 200, 500 or 1000 monomers was built. A 20 ns MD simulation in vacuum was then carried out to collapse the chain (all the chains collapsed within 1 ns). The collapsed chain was placed in a cubic box and solvated with CG water molecules. To generate cross-links, 10000 steps (200 ps) of MD simulation were carried out, after which a bond was introduced between any cross-linking particles that were within 0.533 nm of each other (0.533 nm is equivalent to the distance of 1.3σ, as outlined for general NP formation by Liu *et al.*,[22] where σ = 0.41 nm is the non-bonded LJ parameter that represents the effective radius of the polystyrene ring particle).[18] This was followed by a further 10 000 steps of MD and any new cross-links were identified. The entire procedure was repeated until no further cross-links were found.

The radii, r, of the resultant PSNPs were estimated from their radii of gyration r_g over an additional 50 ns simulation with the cross-links in place. The r_g of the PSNPs were found to be 1.0, 2.0, 2.2 and 2.9 nm for the 40-, 200-, 500- and 1000-monomer chains respectively, as shown in **Figure 8.2**.

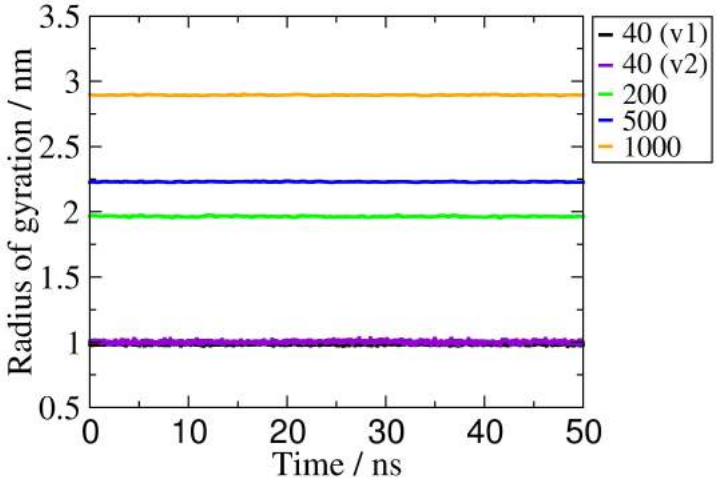

***Figure 8.2**: Radius of gyration of the PSNPs following the cross-linking procedure. The numbering in the legend refers to the number of monomers in the polystyrene chain. The two different PSNPs with chain length of 40 are labelled v1 and v2.*

Assuming a spherical shape for the PSNPs, their radii were estimated according to the relation $r = \sqrt{5/3}\, r_g$ and were found to be 1.3, 2.6, 2.8 and 3.7 nm for the 40-, 200-, 500- and 1000-monomer chains respectively. To test the effect of the cross-linking procedure on the size of the resultant PSNPs, the procedure for the 40-monomer chain was repeated starting from the extended chain, but where different velocities were assigned to the particles at the start of the simulation. r_g of this second 40-monomer PSNP was also 1.0 nm (**Figure 8.2**). Snapshots of three final cross-linked PSNPs models built from 40-, 200- and 500- monomers chains with 76, 360 and 835 monomers added, respectively, are shown in **Figure 8.3**.

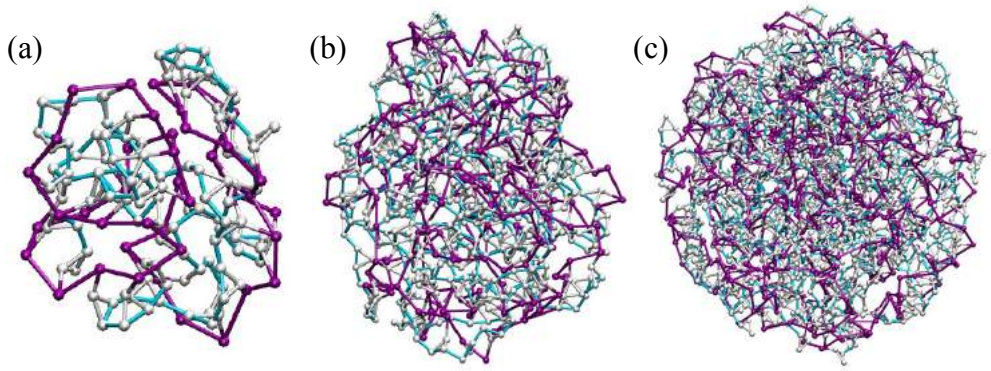

Figure 8.3*: CG models of different sized PSNPs built by cross-linking of radii (a) 1.3 nm (40 monomers), (b) 2.6 nm (200 monomers), and (c) 2.8 nm (500 monomers). Pink = polystyrene backbone beads; White = polystyrene aromatic ring beads; Blue = cross-links.*

The outlined methodology produced the first CG MD model of cross-linked PSNPs of varying size. This model has already been successfully utilised by Thake *et al.*, to study the permeation of different sized PSNPs through model lipid bilayers.[23]

8.4 Building Coarse-Grained Diamond-like Surfaces

Four diamond-like CG models were built based on the atomistic (111) H-terminated, (111) OH-terminated, 2 × 1 (100) H-terminated and 2 × 1 (100) O-ether-terminated surfaces (Chapter 4). The CG mapping was developed to retain the structural pattern of each diamond surface. Other mappings were also attempted, however the 3:1 *i.e.* three atoms combining as one CG bead was found to best reproduce the underlying crystal structure. The atomistic to CG bead mapping for the (111) surface is shown in **Figure 8.4**a. The coordinates from the atomistic slab (Chapter 4) were grouped by averaging the centre of mass of three neighbouring beads along the *xy*- direction within the same plane (**Figure 8.4**b). This mapping was projected throughout the slab to create stacks of beads forming the final CG slab

shown in **Figure 8.4**c. This reduced the (111) slab from 28800 atoms to 9600 CG beads.

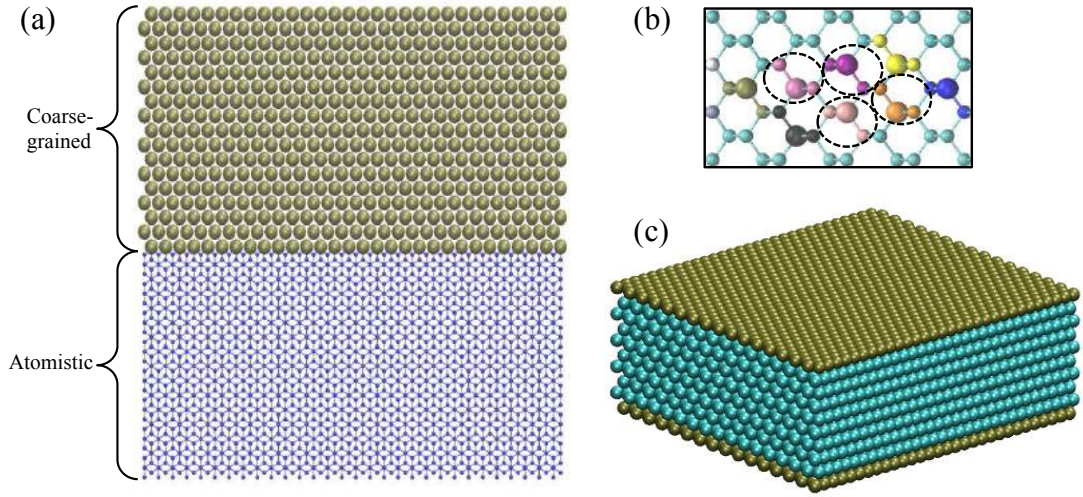

Figure 8.4*: (a) 3:1 CG mapping of (111) diamond surface, (b) illustration of the mapping process i.e. each colour represents one CG bead, (c) model CG (111) diamond-like hydrophilic slab. Gold = hydrophilic CG bead, Cyan = hydrophobic CG bead.*

The final CG (100)-O-ether- and (100) H- terminated CG slabs are shown in **Figure 8.5**. The (100) surfaces followed the same 3:1 mapping for bulk diamond with extra beads added to account for the surface bridging of the ether oxygens (**Figure 8.5**a)[24] and reproduce the surface reconstruction pattern of the carbons on (100) H-terminated (**Figure 8.5**b). The (100) surfaces reduced from 27200 atoms to 9066 CG beads. All CG slabs retained the same *xy*- dimensions as the atomistic models.

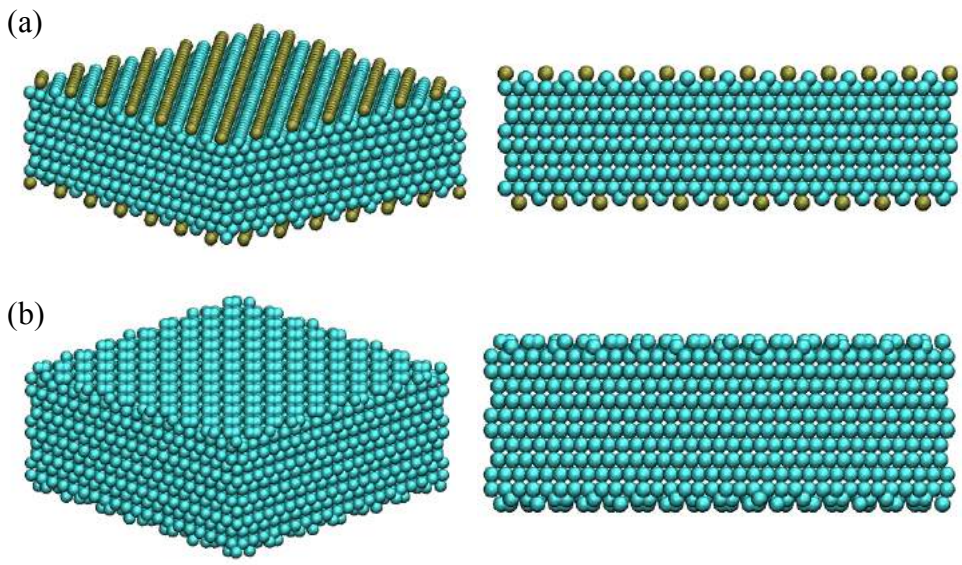

Figure 8.5*: Model CG (100) diamond-like slabs: (a) hydrophilic i.e. to mimic the 2 × 1 (100)-O-ether model surface and (b) hydrophobic i.e. to mimic the 2 × 1 (100)-H model surface. Gold = hydrophilic bead, Cyan = hydrophobic bead.*

8.5 Preliminary Work: Self-Assembly of Lipids on Surfaces

In this section, we outline the system setup for preliminary simulations into lipid self-assembly on model diamond-like surfaces. Hence, the model captures lipids interacting with hydrophobic and hydrophilic surfaces that have structural similarity to diamond.

Preliminary systems were setup for the hydrophobic and hydrophilic (100) diamond-like surfaces. The simulation box consisted of a mixed system of 512 lipids, 6351 waters (~ 12 waters per lipid) and diamond. Enough lipids were placed into the box to allow either a monolayer or bilayer to form on the surface. The final system dimensions were (100)-H: 7.133 × 7.133 × 25.089 nm^3 and (100)-O-ether: 7.133 × 7.133 × 25.432 nm^3. The CG parameters for DPPC lipids and water were as described in the MARTINI force field.[20]. The diamond beads were described by apolar (type C) interaction sites in the MARTINI model,[20] except for the hydrophilic surface beads that were described by the polar (P5) interaction sites. 'Repulsive' beads were

placed on the opposite side of the slab to force lipids to self-assemble only on one surface. These were described by the apolar (type C) interaction site, which was modified so that the LJ potential was purely repulsive to the lipid beads. This was achieved by setting the C6 part ($4\varepsilon\sigma^6$) of the LJ interaction (see Chapter 2, section 2.3.4) between lipid and diamond beads to zero. The diamond beads were fixed in position by an elastic network (harmonic restraints) in which all atoms within a distance cut-off (0.7 nm) were connected via harmonic potentials with spring constants of 15000 kJ mol^{-1} nm^{-2}.

All simulations were carried out using the GROMACS software package.[25] Three-dimensional periodic boundary conditions were used so that each slab appeared as infinite in the *xy*- plane. The system was coupled to a Berendsen thermostat and barostat[26] with coupling constants τ_T = 2.0 ps and τ_P = 5.0 ps to maintain the temperature at 300 K and pressure at 1 bar. LJ interactions were cut-off at 1 nm, and electrostatics were treated using the simple cut-off with a real-space cut-off of 1 nm.[27] The system was energy minimised and equilibrated for 1 ns in the *NVT* ensemble followed by 1 ns in the NAP_zT ensemble with position restraints on the lipids. MD simulations were run for 200 ns in the NAP_zT ensemble using a time step of 10 fs with coordinates saved every 1000 ps.

Preliminary simulations displayed the lipids collapsing directly on to the hydrophobic (100) diamond-like surface to form a lipid monolayer (**Figure 8.6**).

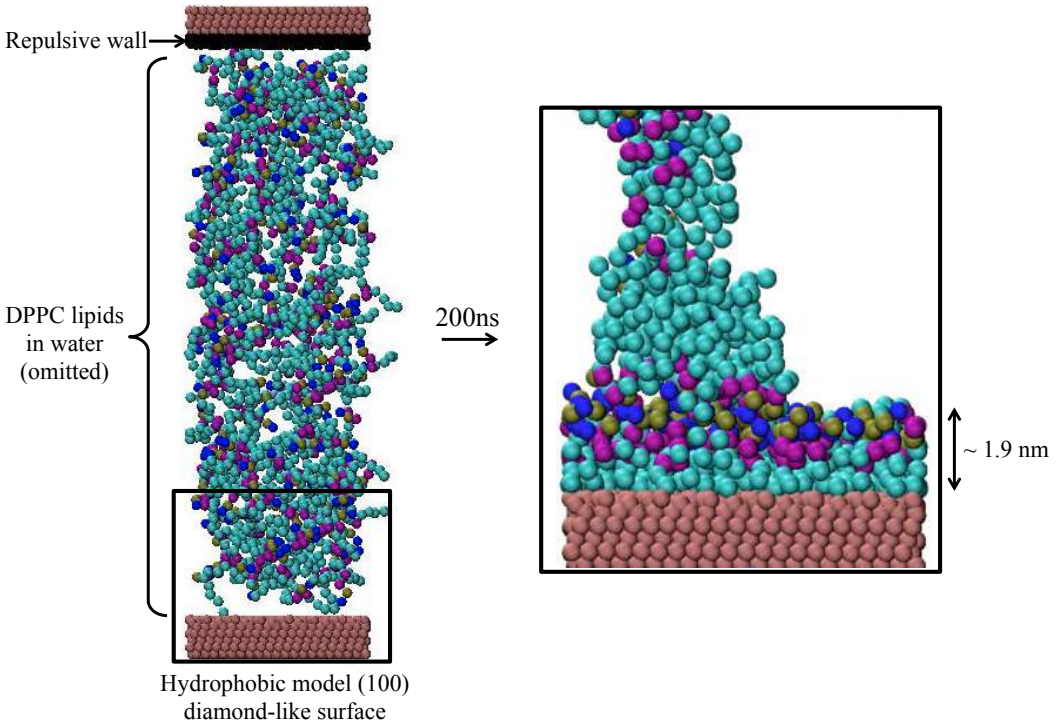

***Figure 8.6**: Self-assembly of DPPC lipids into a monolayer formation on a model hydrophobic (100) diamond-like surface.*

Whilst this indicates that monolayer assembly can be captured, the lipid head group – surface bead distance was measured as ~ 1.9 nm after 200 ns simulation time, which was thinner than expected for a DPPC monolayer (2.49 nm).[28] This suggests that the lipids may not have packed closely enough to produce a fully formed monolayer. Closer inspection (using VMD) of the surface observed that the lipids were wetting the surface in agreement with this hypothesis (**Figure 8.7**). Running the system for longer may produce the desired monolayer structure, however the results may also be a consequence of the choice of bead type causing strong hydrophobic interactions, which would need to be investigated further in the future. In addition, optimisation of the concentration of lipid to water is deemed necessary to prevent extra features due to the excess lipids.

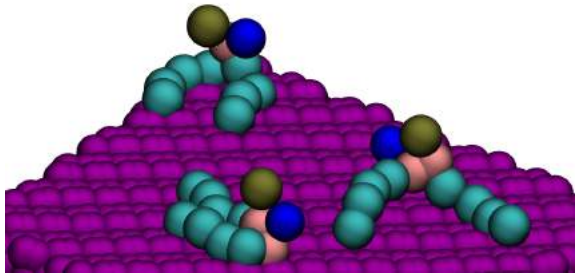

***Figure 8.7**: DPPC lipids wetting a model hydrophobic (100) diamond-like surface.*

Preliminary results were similar for the (100) hydrophobic diamond-like surface, with the lipids formed into a bilayer structure above a trapped water layer on the surface (**Figure 8.8**). This water layer was thicker (~ 5.9 nm) than expected (~ 1 nm) and displayed gradual reduction over time e.g. from ~ 9.8 nm at 100 ns to ~ 5.9 nm at 200 ns. This suggests that longer run times are needed to reach the final equilibrated state. However, it is clear that our system can capture self-assembly on surfaces, which displays great promise for future investigations.

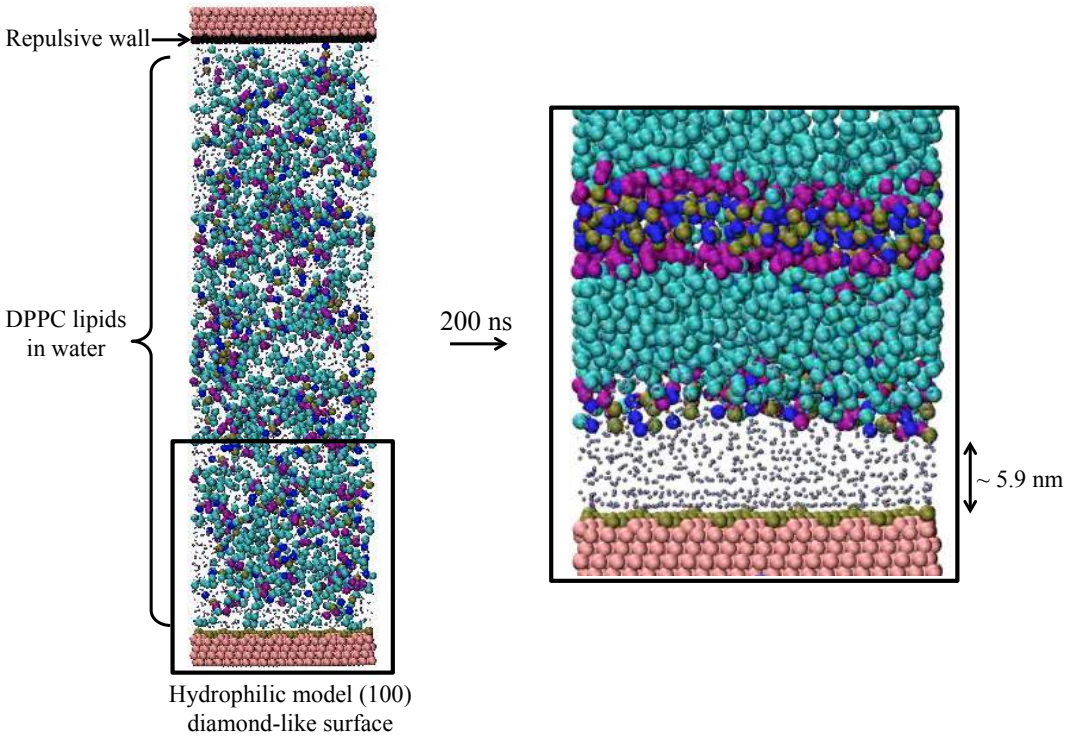

***Figure 8.8**: Self-assembly of DPPC lipids into a bilayer (multilayer) formation on hydrophilic (100) diamond-like surface.*

8.6 Conclusions

Coarse-grained MD was utilised to develop two new models of PSNPs and diamond-like surfaces that are essential for understanding a numerous biomedical and technological systems involving these species. Lipid bilayers/monolayers supported on solid surfaces are essential biomimetic platforms to understand interactions of biomolecules with cell membranes. Significantly, this work built the first diamond-lipid MD model systems and captured lipid self-assembly on these surfaces. Understanding how supported bilayer systems behave on the atomic level can help to optimise diamond devices to match more closely to, or improve the design of, experiments that utilise these systems (see section 8.1). The diamond-like models were built to mimic the surface pattern of the atomistic diamond surfaces, but not to capture the interactions of diamond. This is the first time CG diamond-like surfaces have been built. Initial studies provide an insight into lipid structuring on the different surfaces. In order for the interactions to match more closely to diamond, the force field should be fine tuned to reproduce experimental measurements for water contact angles and lipid-diamond interactions e.g. confocal and AFM measurements of lipid monolayer/bilayers.[29]

Preliminary investigations have observed self-assembly of DPPC lipids on to different diamond surfaces. This is the first time self-assembly of lipids on surfaces has been investigated using CG MD. These models have enormous potential, however, further work is needed to optimise the systems and longer runs are required to ensure the final equilibrated lipid bilayer/monolayer structures have been reached. Once run on all surfaces, differences in the lipid bilayer structure and dynamics can be elucidated. Simulations of a pre-formed bilayer and monolayer on these surfaces could also enable visualisation of the most stable structure.

Polystyrene NPs are frequently used in various biomedical and technological applications. Understanding how PSNPs interact on the atomic scale in these systems can enable rational design of experiments that can improve or advance technologies involving PSNPs (see section 8.1). In this chapter, the first cross-linked CG PSNP model was built for MD. This was done by collapsing a PS chain into a ball and then adding cross-links to neighbouring beads to maintain its structure, similar to the fabrication procedure used in experiments. This model has already been successfully utilised in permeation studies of lipid membranes[23] and it is hoped it will be used to probe numerous systems comprising PSNPs in the future.

8.7 Future Work

The two models that were built in this chapter have potential for use in a wide range of PSNP and diamond-based biological systems in the future. The next step is to parameterise the diamond-like models so that the interactions mimic experimental diamond. This would enable the models to be used to investigate how PSNPs interact with diamond surfaces and within confined channels in order to achieve a molecular-level understanding of different particle events within pores, as discussed in Chapter 7. In addition, the interaction of PSNPs with different terminated surfaces would enable optimisation of diamond pores for PSNP detection.

8.8 References

[1] R. Bradley, R. Radhakrishnan, *Polymers* **2013**, *5*, 890-936.
[2] R. E. Rudd, J. Q. Broughton, *Phys. Rev. B* **1998**, *58*, R5893.
[3] C. Clementi, *Curr. Opin. Struct. Biol.* **2008**, *18*, 10-15.
[4] S. J. Marrink, A. H. De Vries, A. E. Mark, *J. Phys. Chem. B* **2004**, *108*, 750-760.
[5] P. J. Bond, J. Holyoake, A. Ivetac, S. Khalid, M. S. Sansom, *J. Struct. Biol.* **2007**, *157*, 593-605.
[6] K. K. Cotí, M. E. Belowich, M. Liong, M. W. Ambrogio, Y. A. Lau, H. A. Khatib, J. I. Zink, N. M. Khashab, J. F. Stoddart, *Nanoscale* **2009**, *1*, 16-39.

[7] T. Xia, M. Kovochich, M. Liong, H. Meng, S. Kabehie, S. George, J. I. Zink, A. E. Nel, *ACS nano* **2009**, *3*, 3273-3286.
[8] M. Liong, S. Angelos, E. Choi, K. Patel, J. F. Stoddart, J. I. Zink, *J. Mater. Chem.* **2009**, *19*, 6251-6257.
[9] H. Bayley, O. Braha, L. Q. Gu, *Adv. Mat.* **2000**, *12*, 139-142.
[10] E. C. Yusko, J. M. Johnson, S. Majd, P. Prangkio, R. C. Rollings, J. Li, J. Yang, M. Mayer, *Nat. Nanotechnol.* **2011**, *6*, 253-260.
[11] R. J. White, E. N. Ervin, T. Yang, X. Chen, S. Daniel, P. S. Cremer, H. S. White, *J. Am. Chem. Soc.* **2007**, *129*, 11766-11775.
[12] S. V. Bennun, M. I. Hoopes, C. Xing, R. Faller, *Chemistry and physics of lipids* **2009**, *159*, 59-66.
[13] a) C. Xing, R. Faller, *J. Phys. Chem. B* **2008**, *112*, 7086-7094; b) M. Skepö, *J. Chem. Phys.* **2008**, *129*, 185101; c) S. V. Bennun, A. N. Dickey, C. Xing, R. Faller, *Fluid phase equilibria* **2007**, *261*, 18-25; d) M. I. Hoopes, M. Deserno, M. L. Longo, R. Faller, *J. Chem. Phys.* **2008**, *129*, 175102.
[14] C. Xing, R. Faller, *Soft Matter* **2009**, *5*, 4526-4530.
[15] P. Nollert, H. Kiefer, F. Jähnig, *Biophysical journal* **1995**, *69*, 1447.
[16] A. Ulman, *An Introduction to Ultrathin Organic Films: From Langmuir--Blodgett to Self--Assembly*, Academic press, **2013**.
[17] R. J. White, B. Zhang, S. Daniel, J. M. Tang, E. N. Ervin, P. S. Cremer, H. S. White, *Langmuir* **2006**, *22*, 10777-10783.
[18] G. Rossi, L. Monticelli, S. R. Puisto, I. Vattulainen, T. Ala-Nissila, *Soft Matter* **2011**, *7*, 698-708.
[19] J. Liu, M. Mackay, P. Duxbury, *EPL* **2008**, *84*, 46001.
[20] S. J. Marrink, H. J. Risselada, S. Yefimov, D. P. Tieleman, A. H. De Vries, *J. Phys. Chem. B* **2007**, *111*, 7812-7824.
[21] a) C. A. López, A. J. Rzepiela, A. H. De Vries, L. Dijkhuizen, P. H. Hünenberger, S. J. Marrink, *Journal of Chemical Theory and Computation* **2009**, *5*, 3195-3210; b) L. Monticelli, S. K. Kandasamy, X. Periole, R. G. Larson, D. P. Tieleman, S.-J. Marrink, *Journal of chemical theory and computation* **2008**, *4*, 819-834.
[22] J. Prates Ramalho, P. Gkeka, L. Sarkisov, *Langmuir* **2011**, *27*, 3723-3730.
[23] T. H. Thake, J. R. Webb, A. Nash, J. Z. Rappoport, R. Notman, *Soft Matter* **2013**, *9*, 10265-10274.
[24] C. Nebel, J. Ristein, *Thin-Film Diamond II (Semiconductors and Semimetals), Vol. 77*, Elsevier B. V., Amsterdam, Netherlands., **2004**.
[25] a) H. J. Berendsen, D. van der Spoel, R. van Drunen, *Comput. Phys. Commun.* **1995**, *91*, 43-56; b) B. Hess, C. Kutzner, D. Van Der Spoel, E. Lindahl, *J. Chem. Theory Comput.* **2008**, *4*, 435-447; c) E. Lindahl, B. Hess, D. Van Der Spoel, *J. Mol. Model.* **2001**, *7*, 306-317; d) D. Van Der Spoel, E. Lindahl, B. Hess, G. Groenhof, A. E. Mark, H. J. Berendsen, *J. Comput. Chem.* **2005**, *26*, 1701-1718.
[26] H. J. Berendsen, J. P. M. Postma, W. F. van Gunsteren, A. DiNola, J. Haak, *J. Chem. Phys.* **1984**, *81*, 3684-3690.
[27] T. Darden, D. York, L. Pedersen, *J. Chem. Phys.* **1993**, *98*, 10089-10092.
[28] P. Balgavý, M. Dubničková, N. Kučerka, M. A. Kiselev, S. P. Yaradaikin, D. Uhríková, *BBA Bio.* **2001**, *1512*, 40-52.
[29] P. K. Ang, K. P. Loh, T. Wohland, M. Nesladek, E. Van Hove, *Adv. Funct. Mater.* **2009**, *19*, 109-116.

Chapter 9

Conclusions

Advances in synthetic growth techniques in the last 10 years have established diamond as a viable material for industrial applications. Diamond also has exceptional properties that make it highly attractive for use in biosensing technologies. As a relatively new material in this field, there is currently a significant lack of understanding of how diamond can be exploited for biosensing. This work aimed to advance understanding of diamond in two popular biosensor technologies: electrochemical and pore-based. There are gaps in the literature of how the different crystal orientations and surface termination of diamond can influence the detection capability, and this work aimed to significantly advance knowledge in this area. Our work also aimed to develop diamond in pore-based technologies, with no diamond pore-based sensor devices currently in existence.

The first approach taken to advance the field in this work was to develop atomistic models of the different diamond-water interfaces. Seven biocompatible diamond surface models were built of varying crystal orientation i.e. (100), (111) and (110), and surface termination i.e. –H (hydrogen), C–O–C (ether), C=O (ketone) and OH (hydroxyl) (Chapter 4). The structural and dynamical properties of interfacial water close to these surfaces were investigated using molecular dynamics (MD) simulations. The studies revealed differences in the density, lateral arrangement, orientation, hydrogen bonding, mobility and lateral diffusion coefficient of surface

water, which was linked to the topography and chemistry of the underlying substrate (Chapter 4). All diamond surfaces displayed distinct structured water layers with properties that deviate from bulk. Analysis of the first structured water layer (closest to the surface) showed clear differences in the interfacial water properties for hydrophobic and hydrophilic diamond. The lateral diffusion coefficient was significantly smaller for water close to O-terminated surfaces, whereas H-terminated surfaces retained bulk-like water behaviour. This key result demonstrates that O-terminated surfaces have greater ordering effect on the water, which in turn will influence how biomolecules adsorb to these surfaces. The O-ketone-terminated surface displayed the largest difference in water ordering, with the highest water density in the structured regions, water orientation that deviates most significantly from bulk, and slowest lateral diffusion coefficient of interfacial water compared to all other surfaces. Disruption of this highly structured water by biomolecules will be more challenging compared to other surfaces, and will have a significant influence on the energetics of the system. Understanding the behaviour of the interfacial water is an essential prerequisite for investigating biomolecule adsorption on the different diamond surfaces, as the biomolecules must cross from bulk into these interfacial water regions in order to adsorb. In the future, the behaviour of the interfacial water due to the presence of an adsorbed biomolecule can be directly compared to our results of the water in absence of any biomolecules.

The models were also used to investigate the diamond-water-ion interfaces by the addition of different KCl concentrations to the solution and revealed that ions cannot penetrate the first structured water layer at experimentally relevant concentrations (Chapter 4). The electrical double layer (an interfacial structure that

plays a significant role in electrochemical sensors) was not captured by our models and will be addressed in future work.

The second approach to advance knowledge in the field was to utilise the atomistic diamond MD models (from Chapter 4) to probe biomolecule adsorption on different diamond surfaces. A thorough understanding of the diamond-solution-biomolecule interface is key to enabling rational design of biosensors to optimise the detection capability of diamond. These models are essential tools for probing the interface on the atomic scale and the results help to guide diamond biosensor design in the future. The models investigated how two neurotransmitters essential in brain function, dopamine and serotonin, adsorbed on to different diamond surfaces (Chapter 5), building on the models developed in the Chapter 4. Potential of mean force (PMF) free energy calculations were performed to produce profiles of the free energy landscape to adsorption for each biomolecule. Adsorption characteristics were similar for dopamine and serotonin, with both adsorbing most favourably to C=O terminated surfaces and least favourably to H-terminated surfaces due to favourable intermolecular forces between the molecule and O-terminated surfaces. This enables us to advise diamond sensor design by reporting that the presence of C=O and C-H terminated surfaces will increase or decrease the strength of adsorption, respectively. Only the adsorption step was captured which is not necessarily the slowest step in an electrochemical reaction. This makes it challenging to directly compare these results to electrochemical experiments. Density functional theory (DFT) would be useful to implement in the future in conjunction to these models to probe the electrode reaction step at the adsorption minima.

The structural changes of key functional groups on dopamine and serotonin during adsorption was revealed using the constraint MD simulations at different

separations and the pathway to adsorption of dopamine and serotonin on diamond was proposed (Chapter 5). The aromatic ring was observed to collapse from perpendicular to parallel to the surface at the adsorption minima, with the NH_3^+ group pointing into bulk. The ideal conformation was a trade-off between maximising desolvation of the ring and solvation of the polar groups on dopamine/serotonin. This work is limited as the electrical double layer, that frequently plays a key role in biomolecule adsorption, was not included in our models and would need to be addressed in future studies. The models only capture adsorption of one molecule, with only small differences in free energy observed for adsorption on the different diamond surfaces. It is anticipated that running multiple or mixed dopamine/serotonin systems more akin to experimentally relevant solutions will magnify any differences observed between the surfaces. Multiple molecules will also elucidate the role of species cooperation and competition that is experimentally observed in these systems. These are essential limitations of the current models that will be addressed in future work.

The third approach to advance knowledge was to experimentally investigate how changing the diamond surface termination and boron concentration can influence the electrochemical response of different biomolecules on diamond. The electrochemical response of a range of inner-sphere species on H- (hydrogen plasma) and O- (alumina polished) terminated conducting BDD was investigated experimentally using cyclic voltammetry (CVs) (Chapter 6). These studies were performed in different setups i.e. macroelectrode for O-terminated and microcapillary for H-terminated with different mass transport rates. This meant it was only possible to qualitatively determine differences in k^0 for the different terminated surfaces and in the absence of finite element modelling. For the seven different inner-sphere species ($Fe(CN)_6^{4-/3-}$, NADH, riboflavin, $Fe^{2+/3+}$, dopamine, ascorbic acid, serotonin), the CVs

revealed qualitative differences in the electrochemical response on the O- and H-surfaces. In particular, the species $Fe(CN)_6^{4-/3-}$, $Fe^{2+/3+}$, dopamine and ascorbic acid were qualitatively observed to have faster ET on the O-terminated surface, whereas serotonin was faster on the H-terminated surface. These results guide experimental design of electrochemical sensing of these biomolecules, by advising on the ideal diamond surface to improve detection. Our approach is limited by differences in the setups that introduce different mass transport rates. Finite element models will need to be utilised in the future to account for this problem.

The electrochemical response when gradually oxidising H-terminated semi-conducting BDD (Chapter 6) was also reported in this work, of which no prior knowledge exists in the field. The outer-sphere mediator, $Ru(NH)_6^{3+}$, displayed increasingly sluggish kinetics with enhanced surface oxidation. This enabled the development of a new electrochemical 'read-write' technique using SECCM, where localised (micron sized) regions of the H-terminated surface were oxidised and then mapped based on the different electrochemical responses of the mediator on H- and O-terminated surfaces. This patterning technique will be used in the future for the creation of specialised electrochemical devices. The next challenge is to extend the technique to conducting BDD electrodes using an inner-sphere species that displays sufficiently different electrochemistry on H- and O- terminated diamond *e.g.* $Fe^{2+/3+}$.

The fourth approach to advance knowledge in the field was in the fabrication of the first single-crystal diamond pores, and demonstration of their sensing capability using polystyrene particles (Chapter 7). The fabrication involved a two-step protocol of laser thinning the membrane and then insertion of a micropore by EBIE. The pores were characterised using microscopy and open pore conductance measurements; with the experimental data matching FEM simulations based on the measured dimensions.

The sensing capability of a single pore was tested using polystyrene particles in a large-scale microcapillary setup. The particles displayed characteristic spikes in the conductance trace as particles were electrically driven through the pore that could be related to the predicted particle size. The low noise and high aspect ratio of the diamond pores enabled different particle dynamics such as instantaneous, translocation and inhibited translocation to be elucidated. This work is hugely significant to the field as it successfully demonstrates that diamond is a feasible material in pore-based sensing devices, and opens up new avenues for a wide range of future experiments with these structures. The experiments were only proof-of-concept and are limited by the multiple particles that create complex blockade event signals. Future work with single sized particles is required to clear up the signals and truly appreciate the sensing capability of the device. The next challenge is to reduce the dimensions of the pore down to the nanoscale in order to achieve single-nucleotide detection for the development of a next-generation diamond DNA sequencing device. This can be achieved through optimisation of the pore fabrication strategy, or by adapting the pore into a biological sensing device in which the orifice is functionalised with phospholipids containing a well-characterised protein such as α-hemolysin. MD modelling of the system would also be highly beneficial in order to interpret the particle dynamics on the molecular scale and to elucidate the ideal diamond surface termination in order to specialise the device for a particular analyte. Single crystal diamond pores also have the potential as dual optical-conductance devices, or for the growth of embedded electrodes using boron-doped diamond to enable electric field control during translocation (Chapter 7).

The final approach to advance the field was in the development of new coarse-grained (CG) MD models of polystyrene nanoparticles and diamond surfaces

(Chapter 8). These models are important tools to assist in elucidating larger scale processes at diamond sensor interfaces that cannot be feasibly accessed using the atomistic models. CG polystyrene nanoparticles of varying size were built by mimicking a cross-linking methodology that is used to fabricate nanoparticles experimentally. The CG diamond-like surface models were fabricated to reproduce the carbon pattern of the different diamond surfaces. Preliminary work into the self-assembly of DPPC phospholipids on to hydrophobic and hydrophilic diamond-like surfaces has been presented. Initial systems demonstrated the early stages of self-assembly of a monolayer on to the hydrophobic surface, and bilayer close to the hydrophilic surface. These simulations are in their early stages but have huge potential for a range of future applications to complement experiments and guide future sensor design. The diamond-like models are not parameterised to mimic the behaviour of the different diamond surfaces, and this will be addressed in the future so that the models can be used to complement sensor experiments.

Appendix

A. Tables of Parameters

The following tables outline the force field parameters for the atomistic diamond models used in Chapters 4 and 5 of this study.

SURFACE	PARAMETERS							
(110)-H	Atom type[1] (1 = LJ)[2]	Partial Charge (e)	Mass in a.m.u.[1]	Mass atom type code[1]	Description[1]	C6[1] [kJ mol^{-1} nm^{6}]	C12[1] [kJmol^{-1} nm^{12}]	Notes
	CH0 (bulk)[1]	0	12.011[1]	6 (16.043 a.m.u.)[1]	Bare sp3 carbon, 4 bound heavy atoms[1]	0.0023970816[1]	0.0002053489[1]	Partial charges were previously calculated as ~0.073 – 0.083 e based on estimated C-H dipole moments[4,5] and bond lengths.[6,7]
	CH1[1]	0	13.019[1]	6[1]	Aliphatic or sugar CH-group[1]	0.00606841[1]	9.70225E-5[1]	CH1 (united atoms): carbon (CH0) and surface hydrogen (HC) combined into a single atom.[1]
	Bond Stretching (Type 2 = G96 bond)[2]		**Ideal Bond Length (nm)**	**Force constant (10^6 kJ mol^{-1} nm^{-4})**	**Example Usage[1]**	**Nonbonded Parameters C6**	**Nonbonded Parameters C12**	**Notes**
	CH0 – CH0[1]		0.1545[3]	7.1500E+6[1]	C, CHn - C, CHn[1]	0.0023970816[1]	0.0002053489[1]	GROMOS code: gb_27[1] Bond length modified from 0.153 to 0.1545 nm for a better representation of diamond.[3]
	CH0 – CH1[1]		0.1545[3]	7.1500E+6[1]	C, CHn – C, CHn[1]	0.003813984[1]	0.0001411505[1]	
	Bond-Angle Bending (2 = G96 angle)[2]		**Ideal bond angle (degree)**	**Force constant (kJ mol^{-1})**	**Example Usage[1]**			**Notes**
	CH0 – CH0 – CH0[1]		109.5[1]	520[1]	CHn, C – CHn – C, CHn, OA, OM, N, NE[1]			GROMOS code: ga_13[1] Tetrahedral => sp3 hybridization
	CH0 – CH0 – CH1[1]		109.5[1]	520[1]	CHn, C – CHn – C, CHn, OA, OM, N, NE[1]			
	Torsional Dihedral-Angle (Type 1 = proper dih.)[2]	**Phase Shift (deg)**	**Force constant (kJ mol^{-1})**	**Multiplicity (m)**	**Example Usage[1]**			**Notes**
	CH0 – CH0 – CH0 – CH0[1]	0[1]	5.92[1]	3[1]	- CHn, SI – CHn -[1]			GROMOS code: gd_34[1]
	CH0 – CH0 – CH0 – CH1[1]	0[1]	5.92[1]	3[1]	- CHn, SI – CHn -[1]			GROMOS code: gd_34[1]

***Table A1**: Parameters for the H-terminated (110) diamond model.*

SURFACE	PARAMETERS							
(110)-O-ether	Atom type[1] (1 = LJ)[2]	Partial Charge (e) (*ab initio* calculation using Compound 1)	Mass in a.m.u.[1]	Mass atom type code[1]	Description[1]	C6[1] [kJ mol^{-1} nm^{6}]	C12[1] [kJmol^{-1} nm^{12}]	Notes
	CH0 (bulk)[1]	0	12.011[1]	6[1]	Bare sp3 carbon, 4 bound heavy atoms[1]	0.0023970816[1]	0.0002053489[1]	C-OA dipole moment is ~0.17 eÅ.[8]
	CH0[1]	+0.345	12.011[1]	6[1]	Bare sp3 carbon, 4 bound heavy atoms[1]	0.0023970816[1]	0.0002053489[1]	
	OE[1]	-0.690	15.999[1]	8[1]	Ether or ester oxygen[1]	0.0022619536[1]	1.21E-6[1]	
	Bond Stretching (Type 2 = G96 bond)[2]		**Ideal Bond Length (nm)**	**Force constant (10^6 kJ mol^{-1} nm^{-4})**	**Example Usage[1]**	**Nonbonded Parameters C6**	**Nonbonded Parameters C12**	**Notes**
	CH0 – CH0[1]		0.1545[3]	7.1500E+6[1]	C, CHn - C, CHn[1]	0.0023970816[1]	0.0002053489[1]	GROMOS code: gb_27[1] Bond length modified from 0.153 to 0.1545 nm for a better representation of diamond.[3]
	CH0 – OE[1]		0.1430[3]	8.1800E+6[1]	CHn – OE[1]	0.0023285376[1]	1.5763E-5[1]	GROMOS code: gb_18[1]
	Bond-Angle Bending (2 = G96 angle)[2]		**Ideal bond angle (degree)**	**Force constant (kJ mol^{-1})**	**Example Usage[1]**			**Notes**
	CH0 – CH0 – CH0[1]		109.5[1]	520[1]	CHn, C – CHn – C, CHn, OA, OM, N, NE[1]			GROMOS code: ga_13[1] Tetrahedral => sp3 hybridization
	CH0 – CH0 – OE[1]		109.5[1]	520[1]	CHn, C – CHn – C, CHn, OA, OM, N, NE[1]			
	CH0 – OE – CH0[1]		109.5[1]	450[1]	X – OA, SI – X[1]			GROMOS code: ga_12[1]
	Torsional Dihedral-Angle (Type 1 = proper dih.)[2]	**Phase Shift (deg)**	**Force constant (kJ mol^{-1})**	**Multiplicity (m)**	**Example Usage[1]**			**Notes**
	CH0 – CH0 – CH0 – CH0[1]	0[1]	5.92[1]	3[1]	- CHn, SI – CHn -[1]			GROMOS code: gd_34[1]
	CH0 – CH0 – CH0 – OE[1]	0[1]	5.92[1]	3[1]	- CHn, SI – CHn -[1]			
	CH0 – OE – CH0 – CH0[1]	0[1]	1.26[1]	3[1]	- CHn – OA - (no sugar)[1]			GROMOS code: gd_23[1]
	CH0 – OE – CH0 – OE[1]	0[1]	1.26[1]	3[1]	- CHn – OA - (no sugar)[1]			

***Table A2**: Parameters for the O-ether-terminated (110) diamond model.*

SURFACE	PARAMETERS							
(111)-H	**Atom type[1] (1 = LJ)[2]**	**Partial Charge (e)**	**Mass in a.m.u.[1]**	**Mass atom type code[1]**	**Description[1]**	**C6[1] [kJ mol^{-1} nm^{6}]**	**C12[1] [kJmol^{-1} nm^{12}]**	**Notes**
	CH0 (bulk)[1]	0	12.011[1]	6 (16.043 a.m.u.)[1]	Bare sp3 carbon, 4 bound heavy atoms[1]	0.0023970816[1]	0.0002053489[1]	Partial charges were previously calculated as ~0.073 – 0.083 e based on estimated C-H dipole moments[4,5] and bond lengths.[6,7]
	CH1[1]	0	13.019[1]	6[1]	Aliphatic or sugar CH-group[1]	0.00606841[1]	9.70225E-5[1]	CH1 (united atoms): carbon (CH0) and surface hydrogen (HC) combined into a single atom.[1]
	Bond Stretching (Type 2 = G96 bond)[2]		**Ideal Bond Length (nm)**	**Force constant (10^{6} kJ mol^{-1} nm^{-4})**	**Example Usage[1]**	**Nonbonded Parameters C6**	**Nonbonded Parameters C12**	**Notes**
	CH0 – CH0[1]		0.1545[3]	7.1500E+6[1]	C, CHn - C, CHn[1]	0.0023970816[1]	0.0002053489[1]	GROMOS code: gb_27[1] Bond length modified from 0.153 to 0.1545 nm for a better representation of diamond.[3]
	CH0 – CH1[1]		0.1545[3]	7.1500E+6[1]	C, CHn – C, CHn[1]	0.003813984[1]	0.0001411505[1]	
	Bond-Angle Bending (2 = G96 angle)[2]		**Ideal bond angle (degree)**	**Force constant (kJ mol^{-1})**	**Example Usage[1]**			**Notes**
	CH0 – CH0 – CH0[1]		109.5[1]	520[1]	CHn, C – CHn – C, CHn, OA, OM, N, NE[1]			GROMOS code: ga_13[1] Tetrahedral => sp3 hybridization
	CH0 – CH0 – CH1[1]		109.5[1]	520[1]	CHn, C – CHn – C, CHn, OA, OM, N, NE[1]			
	Torsional Dihedral-Angle (Type 1 = proper dih.)[2]	**Phase Shift (deg)**	**Force constant (kJ mol^{-1})**	**Multiplicity (m)**	**Example Usage[1]**			**Notes**
	CH0 – CH0 – CH0 – CH0[1]	0[1]	5.92[1]	3[1]	- CHn, SI – CHn -[1]			GROMOS code: gd_34[1]
	CH0 – CH0 – CH0 – CH1[1]	0[1]	5.92[1]	3[1]	- CHn, SI – CHn -[1]			

***Table A3**: Parameters for the H-terminated (111) diamond model.*

SURFACE	PARAMETERS							
(111)-OH	Atom type[1] (1 = LJ)[2]	Partial Charge (e) (*ab initio* calculation using Compound 2)	Mass in a.m.u.[1]	Mass atom type code[1]	Description[1]	C6[1] [kJ mol^{-1} nm^{6}]	C12[1] [kJmol^{-1} nm^{12}]	Notes
	CH0[1] (bulk)	0	12.011[1]	6[1]	Bare sp3 carbon, 4 bound heavy atoms[1]	0.0023970816[1]	0.0002053489[1]	Serine charges used by Horinek *et al.*,2008 for diamond were (C: +0.266, O: -0.674, H: +0.408).[9]
	CH0[1]	+0.34	12.011[1]	6[1]	Bare sp3 carbon, 4 bound heavy atoms[1]	0.0023970816[1]	0.0002053489[1]	
	OA[1]	-0.76	15.999[1]	8[1]	Hydroxyl or sugar oxygen[1]	0.0022619536[1]	1.505529E-6[1]	
	H[1]	+0.42	1.008[1]	1[1]	Hydrogen not bound to carbon[1]	0.0[1]	0.0[1]	
	Bond Stretching (Type 2 = G96 bond)[2]		**Ideal Bond Length (nm)**	**Force constant (10^{6} kJ mol^{-1} nm^{-4})**	**Example Usage[1]**	**Nonbonded Parameters C6**	**Nonbonded Parameters C12**	**Notes**
	CH0 – CH0[1]		0.1545[3]	7.1500E+6[1]	C, CHn - C, CHn[1]	0.0023970816[1]	0.0002053489[1]	GROMOS code: gb_27[1] Bond length modified from 0.153 to 0.1545 nm for a better representation of diamond[3]
	CH0 – OA[1]		0.1430[1]	8.1800E+6[1]	CHn – OA[1]	0.0023285376[1]	1.5763E-5[1]	GROMOS code: gb_18[1] Bond length previously calculated as 0.142 nm.[11]
	OA – H[1]		0.1000[1]	1.5700E+7[1]	H – OA[1]	0[1]	0[1]	GROMOS code: gb_01[1] Bond length previously calculated as 0.0995 nm.[11]
	Bond-Angle Bending (2 = G96 angle)[2]		**Ideal bond angle (degree)**	**Force constant (kJ mol^{-1})**	**Example Usage[1]**			**Notes**
	CH0 – CH0 – CH0[1]		109.5[1]	520[1]	CHn, C – CHn – C, CHn, OA, OM, N, NE[1]			GROMOS code: ga_13[1] Tetrahedral => sp3 hybridization
	CH0 – CH0 – OA[1]		109.5[1]	520[1]	CHn, C – CHn – C, CHn, OA, OM, N, NE[1]			
	CH0 – OA – H[1]		109.5[1]	450[1]	X – OA, SI – X[1]			GROMOS code: ga_12[1] Angle previously calculated as 109.7°.[11]
	Torsional Dihedral-Angle (Type 1 = proper dih.)[2]	**Phase Shift (deg)**	**Force constant (kJ mol^{-1})**	**Multiplicity (m)**	**Example Usage[1]**			**Notes**
	CH0 – CH0 – CH0 – CH0[1]	0[1]	5.92[1]	3[1]	- CHn, SI – CHn -[1]			GROMOS code: gd_34[1]
	CH0 – CH0 – CH0 – OA[1]	0[1]	5.92[1]	3[1]	- CHn, SI – CHn -[1]			
	CH0 – CH0 – OA – H[1]	0[1]	1.26[1]	3[1]	- CHn – OA - (no sugar)[1]			GROMOS code: gd_23[1]

***Table A4**: Parameters for the OH-terminated (111) diamond model.*

SURFACE	PARAMETERS							
(100)-H	Atom type[1] (1 = LJ)[2]	Partial Charge (e)	Mass in a.m.u.[1]	Mass atom type code[1]	Description[1]	C6[1] [kJ mol^{-1} nm^{6}]	C12[1] [kJmol^{-1} nm^{12}]	Notes
	CH0[1] (C1/C2/bulk)	0	12.011[1]	6[1]	Bare sp3 carbon, 4 bound heavy atoms[1]	0.0023970816[1]	0.0002053489[1]	Partial charges were calculated as ~0.073 – 0.083 e based on estimated C-H dipole moments[4,5] and bond lengths.[6,7]
	CH1[1]	0	13.019[1]	6	Aliphatic or sugar CH-group[1]	0.00606841[1]	9.70225E-5[1]	CH1 (united atoms): carbon (CH0) and surface hydrogen (HC) combined into a single atom.[1]
	Bond Stretching (Type 2 = G96 bond)[2]		**Ideal Bond Length (nm)**	**Force constant (10^{6} kJ mol^{-1} nm^{-4})**	**Example Usage[1]**	**Nonbonded Parameters C6**	**Nonbonded Parameters C12**	**Notes**
	C1 – C1		0.1630[10]	7.1500E+6[1]	C, CHn - C, CHn[1]	0.0023970816[1]	0.0002053489[1]	GROMOS code: gb_27[1] Bond lengths modified by surface reconstruction geometry.[8,10] Carbon notation: CH1 surface carbons and hydrogens, C1 first layer below surface, C2 second layer below surface, CH0 all subsequent layers.
	C1 – C2		0.1595[10]	7.1500E+6[1]	C, CHn - C, CHn[1]	0.0023970816[1]	0.0002053489[1]	
	C2 – CH0[1]		0.1545[3]	7.1500E+6[1]	C, CHn - C, CHn[1]	0.0023970816[1]	0.0002053489[1]	
	CH0 – CH0[1]		0.1545[3]	7.1500E+6[1]	C, CHn - C, CHn[1]	0.0023970816[1]	0.0002053489[1]	
	CH0 – CH1[1]		0.1545[3]	7.1500E+6[1]	C, CHn – C, CHn[1]	0.003813984[1]	0.0001411505[1]	
	Bond-Angle Bending (2 = G96 angle)[2]		**Ideal bond angle (degree)**	**Force constant (kJ mol^{-1})**	**Example Usage[1]**			**Notes**
	CH0 – CH0 – CH0[1]		109.5[1]	520[1]	CHn, C – CHn – C, CHn, OA, OM, N, NE[1]			GROMOS code: ga_13[1] Tetrahedral => sp3 hybridization
	CH0 – CH0 – CH1[1]		109.5[1]	520[1]	CHn, C – CHn – C, CHn, OA, OM, N, NE[1]			
	Torsional Dihedral-Angle (Type 1 = proper dih.)[2]	**Phase Shift (deg)**	**Force constant (kJ mol^{-1})**	**Multiplicity (m)**	**Example Usage[1]**			**Notes**
	CH0 – CH0 – CH0 – CH0[1]	0[1]	5.92[1]	3[1]	- CHn, SI – CHn -[1]			GROMOS code: gd_34[1]
	CH0 – CH0 – CH0 – CH1[1]	0[1]	5.92[1]	3[1]	- CHn, SI – CHn -[1]			

***Table A5**: Parameters for the H-terminated (100) diamond model.*

SURFACE	PARAMETERS							
(100)-O-ether	Atom type[1] (1 = LJ)[2]	Partial Charge (e) (*ab initio* calculation using Compound 3)	Mass in a.m.u.[1]	Mass atom type code[1]	Description[1]	C6[1] [kJ mol^{-1} nm^{6}]	C12[1] [kJmol^{-1} nm^{12}]	Notes
	CH0[1] (bulk)	0	12.011[1]	6[1]	Bare sp3 carbon, 4 bound heavy atoms[1]	0.0023970816[1]	0.0002053489[1]	C-OA dipole moment is ~0.17 eÅ.[8]
	CH0[1]	+0.670[1]	12.011[1]	6[1]	Bare sp3 carbon, 4 bound heavy atoms[1]	0.0023970816[1]	0.0002053489[1]	
	OE[1]	-0.670	15.999[1]	8[1]	Ether or ester oxygen[1]	0.0022619536[1]	1.21E-6[1]	
	Bond Stretching (Type 2 = G96 bond)[2]		**Ideal Bond Length (nm)**	**Force constant (10^{6} kJ mol^{-1} nm^{-4})**	**Example Usage[1]**	**Nonbonded Parameters C6**	**Nonbonded Parameters C12**	**Notes**
	CH0 – CH0[1]		0.1545[3]	7.1500E+6[1]	C, CHn - C, CHn[1]	0.0023970816[1]	0.0002053489[1]	GROMOS code: gb_27[1] Bond length modified from 0.153 to 0.1545 nm for a better representation of diamond.[3]
	CH0 – OE[1]		0.1430[1]	8.1800E+6[1]	CHn – OE[1]	0.0023285376[1]	1.5763E-5[1]	GROMOS code: gb_18[1] Bond length of C – O previously calculated as 0.150 nm.[6]
	Bond-Angle Bending (2 = G96 angle)[2]		**Ideal bond angle (degree)**	**Force constant (kJ mol^{-1})**	**Example Usage[1]**			**Notes**
	CH0 – CH0 – CH0[1]		109.5[1]	520[1]	CHn, C – CHn – C, CHn, OA, OM, N, NE[1]			GROMOS code: ga_13[1] Tetrahedral => sp3 hybridization
	CH0 – CH0 – OE[1]		109.5[1]	520[1]	CHn, C – CHn – C, CHn, OA, OM, N, NE[1]			
	CH0 – OE – CH0[1]		109.5[1]	450[1]	X – OA, SI – X[1]			GROMOS code: ga_12[1] Angle was previously calculated as 113°.[10]
	Torsional Dihedral-Angle (Type 1 = proper dih.)[2]	**Phase Shift (deg)**	**Force constant (kJ mol^{-1})**	**Multiplicity (m)**	**Example Usage[1]**			**Notes**
	CH0 – CH0 – CH0 – CH0[1]	0[1]	5.92[1]	3[1]	- CHn, SI – CHn -[1]			GROMOS code: gd_34[1]
	CH0 – CH0 – CH0 – OE[1]	0[1]	5.92[1]	3[1]	- CHn, SI – CHn -[1]			
	CH0 – OE – CH0 – CH0[1]	0[1]	1.26[1]	3[1]	- CHn – OA - (no sugar)[1]			GROMOS code: gd_23[1]
	CH0 – OE – CH0 – OE[1]	0[1]	1.26[1]	3[1]	- CHn – OA - (no sugar)[1]			

***Table A6**: Parameters for the O-ether-terminated (100) diamond model.*

SURFACE	PARAMETERS							
(100)-O-ketone	Atom type[1] (1 = LJ)[2]	Partial Charge (e) (*ab initio* calculation using Compound 4)	Mass in a.m.u.[1]	Mass atom type code[1]	Description[1]	C6[1] [kJ mol^{-1} nm^{6}]	C12[1] [kJmol^{-1} nm^{12}]	Notes
	CH0[1] (bulk)	0	12.011[1]	6[1]	Bare sp3 carbon, 4 bound heavy atoms[1]	0.0023970816[1]	0.0002053489[1]	C=O dipole moment is ~0.17 eA.[8]
	C[1]	+0.58	12.011[1]	6[1]	Bare carbon[1]	0.0023406244[1]	4.937284E-6[1]	
	O[1]	-0.58	15.999[1]	1[1]	Carbonyl oxygen (C=O)[1]	0.0022619536[1]	1E-6[1]	
	Bond Stretching (Type 2 = G96 bond)[2]		**Ideal Bond Length (nm)**	**Force constant (10^6 kJ mol^{-1} nm^{-4})**	**Example Usage[1]**	**Nonbonded Parameters C6**	**Nonbonded Parameters C12**	**Notes**
	CH0 – CH0[1]		0.1545[3]	7.1500E+6[1]	C, CHn - C, CHn[1]	0.0023970816[1]	0.0002053489[1]	GROMOS code: gb_27[1] Bond length modified from 0.153 to 0.1545 nm for a better representation of diamond.[3]
	CH0 – C[1]		0.1545[3]	7.1500E+6[1]	C, CHn - C, CHn[1]	0.0023686848[1]	3.184126E-5[1]	
	C – O[1]		0.1230[1]	1.6600E+7[1]	C – O[1]	0.0023009528[1]	2.222E-6[1]	GROMOS code: gb_05[1] Bond length previously calculated is 0.119 nm.[10]
	Bond-Angle Bending (2 = G96 angle)[2]		**Ideal bond angle (degree)**	**Force constant (kJ mol^{-1})**	**Example Usage[1]**			**Notes**
	CH0 – CH0 – CH0[1]		109.5[1]	520[1]	CHn, C – CHn – C, CHn, OA, OM, N, NE[1]			GROMOS code: ga_13[1] Tetrahedral => sp3 hybridization
	CH0 – CH0 – C[1]		109.5[1]	520[1]	CHn, C – CHn – C, CHn, OA, OM, N, NE[1]			
	CH0 – C – O[1]		121[1]	685[1]	O – C – CHn, C CH3 – N – CHn[1]			GROMOS code: ga_30[1] Trigonal planar => sp2 hybridization
	Torsional Dihedral-Angle (Type 1 = proper dih.)[2]	**Phase Shift (deg)**	**Force constant (kJ mol^{-1})**	**Multiplicity (m)**	**Example Usage[1]**			**Notes**
	CH0 – CH0 – CH0 – CH0[1]	0[1]	5.92[1]	3[1]	- CHn, SI – CHn -[1]			GROMOS code: gd_34[1]
	CH0 – CH0 – CH0 – C[1]	0[1]	5.92[1]	3[1]	- CHn, SI – CHn -[1]			
	CH0 – CH0 – C – O[1]	0[1]	0.418[1]	2[1]	O – CH1 – CHn – no O[1]			GROMOS code: gd_17[1]

***Table A7**: Parameters for the O-ketone-terminated (100) diamond model.*

A.1 References

[1] C. Oostenbrink, A. Villa, A. E. Mark, W. F. Van Gunsteren, *J. Comput. Chem.* **2004**, *25*, 1656-1676.

[2] D. van der Spoel, E. Lindahl, B. Hess, A. Van Buuren, E. Apol, P. Meulenhoff, D. Tieleman, A. Sijbers, K. Feenstra, R. van Drunen, **2008**, 117-150.

[3] J. Donohue, *Structures of the Elements*, Wiley, New York, US., **1974**.

[4] R. S. Sussmann, *CVD Diamond for Electronic Devices and Sensors., Vol. 149*, John Wiley & Sons, Chichester, UK., **2009**.

[5] L. Ley, J. Ristein, F. Meier, M. Riedel, P. Strobel, *Physica B Condens Matter.* **2006**, *376*, 262-267.

[6] G. Vidali, M. Cole, W. Weinberg, W. Steele, *Phys. Rev. Lett.* **1983**, *51*, 118.

[7] C. Nebel, J. Ristein, *Thin-Film Diamond II (Semiconductors and Semimetals), Vol. 77*, Elsevier B. V., Amsterdam, Netherlands., **2004**.

[8] C. Nebel, J. Ristein, *Thin-Film Diamond I (Semiconductors and Semimetals), Vol. 76*, Elsevier B.V., Amsterdam, Netherlands., **2003**.

[9] D. Horinek, A. Serr, M. Geisler, T. Pirzer, U. Slotta, S. Lud, J. Garrido, T. Scheibel, T. Hugel, R. Netz, *Proc. Natl. Acad. Sci.* **2008**, *105*, 2842-2847.

[10] D. Petrini, K. Larsson, *J. Phys. Chem. C* **2007**, *111*, 795-801.

[11] S. Zhao, K. Larsson, *J. Phys. Chem. C* **2014**, *118*, 1944-1957.

[12] F. Liu, J. Wang, B. Liu, X. Li, D. Chen, *Diamond Relat. Mater.* **2007**, *16*, 454-460.

[13] L. A. Hutton, J. G. Iacobini, E. Bitziou, R. B. Channon, M. E. Newton, J. V. Macpherson, *Anal. Chem.* **2013**, *85*, 7230-7240.